

KAUNAS UNIVERSITY OF TECHNOLOGY

DAMIRA SMAGULOVA

DEVELOPMENT OF ULTRASONIC METHOD
FOR NON-DESTRUCTIVE EVALUATION OF
DISSIMILAR MATERIAL JOINTS

Doctoral dissertation
Technological Sciences, Measurement Engineering (T 010)

Kaunas, 2022

This doctoral dissertation was prepared at Kaunas University of Technology, at Prof. Kazimieras Baršauskas Ultrasound Research Institute during the period of 2017–2021. The studies were supported by the Research Council of Lithuania.

Scientific Supervisor

Prof. Dr. Elena JASIŪNIENĖ (Kaunas University of Technology, Technological Sciences, Measurement Engineering, T 010).

Edited by: English language editor Dr. Armandas Rumšas (Publishing House *Technologija*), Lithuanian language editor Violeta Meiliūnaitė (Publishing House *Technologija*)

Dissertation Defence Board of the Measurement Engineering Science Field:

Prof. Dr. Vaidotas MAROZAS (Kaunas University of Technology, Technological Sciences, Measurement Engineering, T 010) – **chairperson**;

Prof. Dr. Maria Giuseppina LIMONGELLI (Politecnico di Milano, Italy, Technological Sciences, Measurement Engineering, T 010);

Prof. Dr. Spiros PANTELAKIS (Patras University, Greece, Technological Sciences, Measurement Engineering, T 010);

Dr. Vytautas PETKUS (Kaunas University of Technology, Technological Sciences, Measurement Engineering, T 010);

Prof. Dr. Renaldas RAISUTIS (Kaunas University of Technology, Technological Sciences, Measurement Engineering, T 010).

The official defence of the dissertation will be held at 10.00 a.m. on 17 June 2022 at the public meeting of Dissertation Defence Board of the Measurement Engineering Science Field in Dissertation Defense Hall at Kaunas University of Technology.

Address: Donelaičio 73-403, Kaunas LT-44249, Lithuania.

Phone (+370) 37 300 042; fax. (+370) 37 324 144; e-mail doktorantura@ktu.lt

The doctoral dissertation was sent out on 17 May 2022.

The doctoral dissertation is available on the internet at <http://ktu.edu> and at the library of Kaunas University of Technology (Donelaičio 20, Kaunas LT-44239, Lithuania).

KAUNO TECHNOLOGIJOS UNIVERSITETAS

DAMIRA SMAGULOVA

ULTRAGARSINIO METODO SKIRTINGŲ
MEDŽIAGŲ SUJUNGIMŲ PATIKRAI
SUKŪRIMAS

Daktaro disertacija
Technologijos mokslai, matavimų inžinerija (T 010)

Kaunas, 2022

Disertacija rengta 2017–2021 metais Kauno technologijos universiteto Prof. K. Baršausko ultragarso mokslo institute. Mokslinius tyrimus rėmė Lietuvos mokslo taryba.

Mokslinis vadovas

prof. dr. Elena JASIŪNIENĖ (Kauno technologijos universitetas, technologijos mokslai, matavimų inžinerija, T 010).

Redagavo: anglų kalbos redaktorius dr. Armandas Rumšas (leidykla „Technologija“), lietuvių kalbos redaktorė Violeta Meiliūnaitė (leidykla „Technologija“).

Matavimų inžinerija mokslo krypties disertacijos gynimo taryba:

prof. dr. Vaidotas MAROZAS (Kauno technologijos universitetas, technologijos mokslai, matavimų inžinerija, T 010 – **pirmininkas(-ė)**;

prof. dr. Maria Giuseppina LIMONGELLI (Politecnico di Milano, Italija, technologijos mokslai, matavimų inžinerija, T 010);

prof. dr. Spiros PANTELAKIS (Patras University, Graikija, technologijos mokslai, matavimų inžinerija, T 010);

dr. Vytautas PETKUS (Kauno technologijos universitetas, technologijos mokslai, matavimų inžinerija, T 010);

prof. dr. Renaldas RAIŠUTIS (Kauno technologijos universitetas, technologijos mokslai, matavimų inžinerija, T 010).

Disertacija bus ginama viešame Matavimų inžinerijos mokslo krypties disertacijos gynimo tarybos posėdyje 2022 m. birželio 17 d. 10 val. Kauno technologijos universiteto Disertacijų gynimo salėje.

Adresas: K. Donelaičio g. 73-403, Kaunas LT-44249, Lietuva.

Tel. (+370) 37 300 042; faks. (+370) 37 324 144; el. paštas doktorantura@ktu.lt

Disertacija išsiųsta 2022 m. gegužės 17 d.

Su disertacija galima susipažinti interneto svetainėje <http://ktu.edu> ir Kauno technologijos universiteto bibliotekoje (K. Donelaičio g. 20, Kaunas LT-44239).

TABLE OF CONTENTS

INTRODUCTION	9
1. ULTRASONIC INSPECTION OF DISSIMILAR MATERIAL JOINTS....	15
1.1. Joining of dissimilar materials	15
1.2. Adhesive bonding: method description, type of defects	16
1.3. Evaluation of boundary characteristics	18
1.4. Nondestructive testing of adhesively bonded materials	22
1.4.1. Inspection of joints of similar materials	22
1.4.2. Inspection of joints of dissimilar materials	28
1.5. Model-assisted probability of detection	32
1.6. Conclusion of the chapter and outline of the research task	38
2. DEVELOPMENT OF A METHOD FOR THE IMPROVEMENT OF DETECTION PROBABILITY IN DISSIMILAR MATERIAL JOINTS	40
2.1. Investigation method	40
2.1.1. Theoretical analysis of multiple reflections and boundary characteristics	42
2.1.2. Sensitivity analysis	47
2.1.3. Ultrasonic inspection simulations	55
2.1.4. Signal modelling in layered structure and optimization of parameters	61
2.2. Development of the post-processing algorithm to increase detectability	65
2.3. Conclusion of the chapter	68
3. EXPERIMENTAL INVESTIGATIONS AND APPLICATION OF THE DEVELOPED ALGORITHM	70
3.1. Experimental investigations of dissimilar material joints and investigation results	70
3.1.1. Description and experimental investigation of bonded steel-CFRP component	70
3.1.2. Description and experimental investigation of bonded aluminium- CFRP component	75

3.2. Comparison of the obtained modelled and experimental results.....	79
3.3. Application of the developed post-processing algorithm and discussion of the results	81
3.4. Conclusion of the chapter.....	95
4. RELIABILITY OF ULTRASONIC NDT TECHNIQUE AND UNCERTAINTY MEASUREMENT	96
4.1. Evaluation of model-assisted probability of detection	96
4.1.1. Signal response analysis of disbond detection before algorithm employment.....	98
4.1.2. Signal response analysis of disbond detection after algorithm employment.....	100
4.2. Uncertainty measurement.....	101
4.3. Conclusion of the chapter.....	106
GENERAL CONCLUSIONS	107
FUTURE SCOPE OF RESEARCH.....	108
SUMMARY.....	109
REFERENCES	149
INFORMATION ABOUT AUTHOR.....	158
LIST OF PUBLICATIONS	159

NOMENCLATURE AND ABBREVIATIONS

AE	Acoustic emission
A_{1n}	Amplitudes of aluminium-air multiple reflections
A_{2n}	Amplitudes of adhesive-air and adhesive-GFRP multiple reflections
CFRP	Carbon fiber reinforced plastics
DB	Data Base
EPAT	Electromagnetic-pulse-induced acoustic testing
F	Focal distance
FBH	Flat bottom hole
FBT	Fokker bond tester
FE	Finite element
FRP	Fiber reinforced polymer
FT	Fourier transform
FT^{-1}	Inverse Fourier transform
f	Frequency
f_1	Frequency of lower cut-off
f_2	Frequency of upper cut-off
Δf	Width of the filter function fronts
GFRP	Glass fiber reinforced thermosetting plastic
H_k	Thickness of materials
$H(t)$	Transfer function arbitrary unit
$H(f)$	Transfer function of filter
$h(t)$	Theoretical pulse response in multi-layered components
HYPER	Hybrid penetrative reinforced
K_1, K_2	Coefficients of peak-to-peak amplitudes
K_R	Reflection coefficient
K_T	Transmission coefficient
k	Material type
LISA	Local interaction simulation approach
M_D	Material depth
M_n	Peak-to-peak amplitudes of interface multi-reflections
MAPOD	Model-assisted probability of detection
n	Number of multi-reflections
NDT	Non-destructive testing
ρ_k	Material density
PFA	Probability of false alarms
POD	Probability of detection
PE	Polyethylene
QSA	Quasi-Static Approximation
Re	Real part
ROC	Receiver Operating Characteristics
SHM	Structural Health Monitoring
t_s	Time moment of signal reflected from the object surface

$t_{i1}-t_{4i}$	Time moments of aluminium-adhesive multi-reflections
$t_{1ad,air}-t_{4ad,air}$	Time moments of adhesive-air multi-reflections
$t_{1ad,GFRP}-t_{4ad,GFRP}$	Time moments of adhesive-GFRP multi-reflections
$t_{GFRP,CFRP}-t_{2GFRP,CFRP}$	Time moments of GFRP-CFRP multi-reflections
t_k	Propagation time of ultrasonic waves in the structure layers
$t_{n1,k}$	Arrival time of the signal reflected from surface at set threshold
t_{nk}	Propagation time of the signal multiple reflected in the layer
t_{n1}	Time moment of first sample above the threshold U_{th}
$t_{0,k}$	Time moment of the signal transiting zero crossing point
$U_F(f)$	Filtered frequency spectrum
$u_F(t)$	Filtered signal
$U(f)$	Frequency spectrum
$u(t)$	Modelled signal
U_{th}	Threshold for time alignment
$u'_k(t_n)$	Shifted in time signals
$u_k(t_{n1})$	Digitised signal
$u_k(t_n)$	Digitised signal for all time moments above the threshold
UT	Ultrasound testing
V_{tm}	Ultrasound velocity in the testing material
V_w	Ultrasound velocity in the water
V_k	Ultrasound velocity in the layers of the structure
XCT	X-ray Computed Tomography
W_p	Distance between the transducer and surface of the object
y_{ref}	Reference signal measured with reference block
Z_k	Acoustic impedance of particular structure material
Z_1	Acoustic impedance of 1 st material
Z_2	Acoustic impedance of 2 nd material

INTRODUCTION

Motivation and relevance of work

A combination of the requirements for improved performance and the functional needs of structural parts, environmental safety, the safety of people's lives and health as well as economic benefits in such industries as aerospace, automotive, civil, and marine industries have been motivating researchers to work and develop new advanced materials and their joints. The joining technology of different materials is essential in the design of components [1]. The bonding method based on adhesives in comparison to such traditional mechanical joining as riveting or bolting enables the weight reduction of the structure and the even distribution of mechanical stress [2]. The current tendency of development implies the substitution of metal components by advanced composite materials. Composites are the key materials which are characterised by structure lightening and the reduction of CO₂ emission [3]. Besides the potential of weight savings, composites are popular due to their advanced mechanical properties compared to metal alloys. The anisotropic properties of composite materials allow manufacturing strong and stiff structures; it also leads to the superior aerodynamic characteristics of construction, better structure performance, and enhanced fuel efficiency. Composites are widely used in the primary and secondary structures of aircraft, both in civil and military applications [4], [5], [6]. However, not all metals can be replaced in the structure because of the low bearing strength and the stiffness of composites, their dependence on the laminate structure and the environmental conditions which can change the mechanical behaviour of the component. That is why the joints of metal-to-composite are being used [5]. Additionally, the structural repair of integrity can be conducted by using patches of composite or metal materials providing in conjunction dissimilar strength and stiffness [7]. Usually, damaged metal structures are repaired by using composite patches [8]. Bonded dissimilar materials, such as aluminium to carbon fiber reinforced plastics (CFRP), provide better structure enhancement and are denoted by superior characteristics of fatigue life, impact resistance, and residual strength. These hybrid materials have been attracting high interest and are being increasingly used in the aircraft fuselage, wing boxes and nacelles [4], [5]. The adhesive bonding technology is fairly recent, and, therefore, there is still no reliable method for the quality control of such assembly. Therefore, the traditional fasteners are still required in the critical parts of, for example, aircraft constructions [2].

Ultrasonic non-destructive testing is a widely used method for the inspection of various materials and structures [3]. Many researchers have used this technique to characterise the adhesion quality of bonded materials [2]. However, the number of studies is limited, and the absence of a single reliable method which would be suitable for the investigation of dissimilar material joints is an urgent scientific issue. Particularly, much attention has been paid to the evaluation of the adhesive quality of similar materials, but there is still a limited amount of works performed in the field of adhesively bonded dissimilar materials [9].

The overall quality of adhesively bonded joints depends on the presence and development of various defects between material interfaces, such as disbonds, voids, surface contamination, porosity, etc. The most critical area of such joints is the bonding area where internal defects, such as delaminations and disbonds, can appear. The defects can be generated during the manufacturing process or in the course of exploitation. The main reason for the appearance of defects during the service life of the structure is impacts. However, even low energy impacts can stimulate the generation of internal defects without any modification of the top surface of the component. Such defects are very dangerous since they are invisible but can strongly influence the quality of the bonding and lead to the failure of the structure [4]. The presence of a defect and its further growth can cause great damage to the entire construction structure in general. Usually, the size of the defect which has to be detected starts at 5 mm, since defects of smaller sizes are not critical in terms of the structural reliability and do not pose danger in the aircraft industry in particular. However, the detection of such defects in general is still problematic because there is no reliable inspection method to determine the integrity of the adhesive joints. Thus, the safety of life, environment and economic costs are strongly dependent on the structural health of such bonded constructions.

The ultrasonic inspection offers a great potential to ensure the quality of structural integrity of bonded joints of similar and dissimilar materials due to such capabilities as the detection of delaminations, air bulbs and deviations in the geometry of the component, its layers and defects [3]. Therefore, this work focuses on the ultrasonic detection of such critical defects as disbonds in the adhesive layer between the bonded metal/composite materials with the objective to evaluate the quality of bonding.

Scientific and technological problem

The main problem of the quality control of the bonding area in adhesively bonded dissimilar materials stems from the complexity of detecting adhesive defects due to the absence of a reliable method with the high probability of detection. The factors causing the difficulty of detecting disbond-type defects are as follows: component multi-layering, complex geometry, different elastic and acoustic properties. A prominent difference in the acoustic impedance of metals and composites leads to a sufficiently high value of the reflection coefficient on the metal/composite, metal/adhesive, or adhesive/metal interfaces. This means that the major share of the amount of ultrasonic energy will be reflected on the boundary of dissimilar material joints. However, the disbond-type defects located in these interfaces are filled with air; they also exhibit a high reflection coefficient. As a result, the ultrasonic wave will be reflected from both the defective and the defect free region of the interface, which will complicate the detection of defects located at the metal/adhesive interface due to the high reflection amplitude which can be similar to the amplitude of reflection of a non-defective interface. In addition, in the case of dissimilar joints, ultrasonic waves poorly penetrate in the structure, and the detection of defects on the opposite interface is even more complicated. Another

quite significant problem of the quality control is the very thin components, and especially the adhesive layer. The thickness of the adhesive can start from 0.1 mm. This leads to the problem of distinguishing reflections of each interface due to their overlap in the time domain [4], [6], [9]. This complicates the detection of defective interfaces by comparing the signals reflected from the defective and the defect-free interfaces of a layered structure of dissimilar materials.

Working hypothesis

An advanced processing algorithm based on the non-destructive testing technique, theoretical analysis of wave-defect interactions, qualitative and quantitative evaluations as well as signal modelling and parameters optimisation, which allows increasing the probability of disbond/delamination detection in the adhesive layer of the joint of dissimilar materials, can be developed. By using the developed technique, it should be possible to detect defects bigger than 5 mm with 1 mm uncertainty.

Objective and tasks

The objective of the thesis is to develop an advanced technique for the detection of disbond-type defects in the joints of dissimilar materials with the improved probability of detection (POD) and to measure its performance so that to monitor the structural integrity in the bonding area. The following tasks were formulated to achieve the objective:

1. To perform literature analysis in order to evaluate the existing methods applied for the inspection of layered structures, their advantages and disadvantages as well as to select the appropriate methods and techniques which can be used to achieve the objective of the work and solve the assigned tasks.

2. To investigate the fundamentals of wave-disbond interactions in adhesive joints, including the waves reverberation within a structure, the phase change, and the reflection magnitudes; to perform qualitative evaluation of the ultrasonic inspection in order to determine the major factors influencing the detection of disbonds in layered structures of dissimilar material joints.

3. To develop a model based on the arrival time of ultrasonic waves and the selection of time gates; to extract the valuable features from the theoretical, quantitative and qualitative evaluations which can be used for the improvement of disbond detection in dissimilar material joints according to the developed method of investigation.

4. To develop a data post-processing algorithm based on the extracted features in order to increase the performance of the selected NDT technique improving the probability of disbond detection.

5. To verify the proposed technique by estimating the detected defect sizes and to evaluate its uncertainties. To evaluate the POD of the inspection technique before and after the application of the improved post-processing algorithm.

Scientific novelty

The novelty of the thesis is the new methodology which enables improved probability of the detection of disbonds in the adhesive layer between two dissimilar materials.

1. After performing sensitivity analysis and conducting the evaluation of the probability of detection curves based on meta-model generation for the selected technique of ultrasonic inspection of disbonds in dissimilar material joints, the following most critical factors affecting the detection of disbonds were determined: the component surface curvature, the distance between the transducer and the object as well as the defect depth location in the adhesive layer.

2. The investigation process based on qualitative and quantitative evaluations, the theoretical analysis and signal modelling can extract valuable features (the time moments and time intervals of the reflected signals, the amplitude change and the ratio coefficients of amplitudes of the selected time intervals) which are required for the development of the improved disbond detection method.

3. A novel post-processing algorithm to improve the detectability of disbond type defects in the adhesive layer between dissimilar materials, such as bonded metals to composites, was developed and implemented successfully.

Practical value of the work

1. The proposed methodology can be used as a basis for the analysis of multi-layered structures of bonded similar and dissimilar materials aiming to detect debonding in the interface. It contributes to the development of a universal, cost-effective, and reliable inspection technique by increasing the probability of detection.

2. The proposed approaches of signal processing can play the essential role in detecting defects in the adhesive layer of multilayered structures, especially in such complex joints as those involving dissimilar materials.

3. The proposed signal processing algorithms can be used as a part of an intelligent computer program of a measurement system in the evaluation of the structural integrity of bonded similar and dissimilar materials.

4. The results obtained in the research can contribute to the further study of integrity of adhesively bonded dissimilar materials, the development of new ideas of such structural investigations, which can facilitate the possibility of the widespread use of adhesively bonded dissimilar materials in such constructions as aircraft which require exceptional reliability and safety levels.

Results presented for the defence of the thesis

1. Steps of the investigation method for the extraction of valuable features in order to develop the method serving the objective to improve disbond detection. The method consists of inspection simulations, signal modelling, theoretical analysis and qualitative evaluations.

2. Sensitivity analysis based on meta-model computation has been developed to determine the major influencing factors on the detection of disbonds in the structures of the selected NDT technique.

3. The main steps of the developed post-processing algorithms based on the extracted features and the obtained results from the investigation method have been demonstrated.

4. The experimental investigation of the samples and the implementation of the developed algorithms as well as the defect size and the uncertainty measurement for the verification and demonstration of the achieved results have been conducted.

5. The process used for the evaluation of the POD curves and the determination of the detection threshold in order to obtain reliable results of the defect sizes which can be detected by the NDT technique before and after applying the developed post-processing algorithm has been described.

Approbation

The obtained results during the period of the research were published in 6 publications: 3 publications were published in international journals from the database of *Thomson Reuters ISI Web of Science* with the impact factor, 1 publication was presented in the peer-reviewed proceedings of an international conference indexed in the *Web of Science* without the impact factor, and 2 other publications were delivered in reviewed proceedings of international conferences. In addition, the results were presented in 6 international scientific conferences which took place in Gothenburg, Palanga, Vilnius, Athens, Paris, and in 2 virtual international conferences. In 2020, the doctoral scholarship was provided by the Research Council of Lithuania for the study results. In 2018–2019, the scholarship for the most active PhD student was granted by Kaunas University of Technology.

Structure and content of the thesis

The thesis consists of the introduction, four chapters, general conclusions, the future scope of research, a list of references and the author's scientific publications. Overall, there are 160 pages, including 72 figures, 22 tables, 50 mathematical formulas and 116 bibliographic references. The chapters of the thesis are organised as follows:

1. The first chapter discusses the currently available methods of testing, the techniques and methodologies which can be applied for the investigation of multi-layered structures aiming to detect flaw(s) in the interfaces. The main goal of the literature review is the analysis of the state-of-arts and recently developed methods, the evaluation of the advantages and disadvantages as well as the possibility to apply them for the investigation of structures containing dissimilar materials.

2. The second chapter describes the developed method of investigation required for the full analysis of the selected NDT technique, the objects under investigation, the possibilities they offer along with their limitations in order to extract valuable features for the development of the algorithm to improve disbond detectability.

3. The third chapter demonstrates the results obtained after the experimental investigation of the samples of dissimilar material joints representing the complexity of disbond detectability. Further, the effectiveness of the developed post-processing

algorithm for the improvement of defect detection was demonstrated by measuring the sizes of the detected defects.

4. In the fourth chapter, the evaluation of detection probability was performed for the selected ultrasonic technique based on the meta-model generation before and after the application of the developed post-processing algorithm. The value which characterises the improvement was presented.

1. ULTRASONIC INSPECTION OF DISSIMILAR MATERIAL JOINTS

The goal of this chapter is to analyse the currently available methods and techniques of the inspection of dissimilar materials, to find out their advantages and disadvantages with respect to the feasibility of their application for multilayered structures and the detection of debonding in the adhesive layer and thereby to select the most suitable approaches. In order to achieve the goal, the literature analysis of the field of interest was performed.

1.1. Joining of dissimilar materials

The requirements imposed on constructions to possess such characteristics as the light weight, increased performance and functionality leads to the use of multilayered hybrid structures [10]. Nowadays, constructions of dissimilar materials have become popular and are being widely applied in the industry, namely, by virtue of bonding of metals to composites [11]. The manufacturing of dissimilar material joints leads to the savings of energy and resources. Different properties of different materials in conjunction can provide improved performance of the structure. However, the joining process is a challenging task since dissimilar materials may have relatively different physical properties and individual chemical compositions [10]. The appropriate joining technique has to be selected in order to preserve the advantageous characteristics of the bonded metal-to-composite materials and to fully exploit the benefits of the construction [11].

There are three joining techniques of composite components to metal ones, specifically, *adhesive bonding*, *mechanical fastening*, and a *combination* of these two techniques. The selection of the joining technique largely depends on the geometrical arrangement of the dissimilar materials. Overlapped components, comeld joints and hybrid penetrative reinforced (HYPER) joints are considered to be state-of-the-art. Adhesive bonding is a technique which is suitable for joining of any similar and dissimilar materials. Adhesive bonding is flat and uniformly distributed on the surface of the components in the place of the bondline; also, it is denoted by the advantage of the fiber-safe load. In addition, such bonding prevents corrosion between dissimilar materials. However, there is dependence of the durability of joints on the adhesive strength and the degradation of bonded materials over time. Before joining, the surfaces of the materials have to be prepared for the gluing and curing processes. Moreover, special attention should be paid to the temperature and humidity [11]. In general, the performance of the adhesive bond is defined by the chemical and physical properties of the adhesive, the preparation of the adherents' surfaces for bonding, their wettability and the design of the joint where the appropriate adhesive has to be selected [10]. Mechanical fastening is still being widely used in the aircraft and automotive industries. However, hole drilling interrupts the health of the fusion zone and can thus become the source of the defect occurrence. Usually, bolts and rivets are used in order to provide high joining strength of materials. Titanium foil embedded to the bonding zone can increase the mechanical strength. Nevertheless, the life of the joint is influenced by the fiber

damage, the polymer matrix in the place of the embedded bolts, as well as the decrease of the clamping load of the bolt. Another disadvantage is the cost of fasteners and the process of fastening. Hole-clinching is a more time- and cost-efficient method of the mechanical joining methods which is mostly suitable to join composites with brittle metal materials. Despite that, this method suffers from such a disadvantage as the high introduced load which does not allow avoiding fiber damage and residual strength in metal materials. HYPER joints contain small pins on the surface of metal materials which are integrated into uncured composite materials. This method provides additional adhesion around the pins. However, this technology is costly and time-consuming as it requires additive and subtractive manufacturing [11].

The main attention in the joining technologies is focused on the mechanical strength. The bearable stress is an important characteristic of bonded components as well as the static and dynamic loading, fatigue, torsion, tension, bending, and the clamp load.

As a result, all the joining techniques are denoted by their own advantages and disadvantages. However, nowadays, the requirements in the aircraft and automotive industries for lightweight constructions, fuel saving, and environmental aspects are leading to the use of adhesives used to join different materials as well as the replacement of metal materials with lightweight composites.

1.2. Adhesive bonding: method description, type of defects

The adhesive bonding technology is highly used in the constructions of the aerospace industry serving the objective of joining similar and dissimilar materials. The main advantages of this method are the possibility to reduce the weight of constructions and to achieve uniform distribution of stress. There are also several design configurations for the adhesively bonded joints as lap joints, scarf and butt joints [12], [13]. Thorough research has been carried out for the failure of similar bonded materials as metals and composites, but there is still lack of research on bonded dissimilar materials [14], [15], [16], [17]. The bonding area is the weakest point, and it is subjected to failures because of the weaker adhesive strength in comparison to the adherends of the joints and the unusual concentration of the shear and peel stress on the edges of the bondline [12], [13]. Therefore, the joint configuration of dissimilar materials is essential because of the importance of the strength and stress distribution which has to be examined. Kanani *et al.* [13] used finite element analysis and experimental studies in order to evaluate the difference of performance of four different joint configurations (half-lap splice joints, scarf joints, single-lap, and stepped-lap joints). It was found out that the scarf joint offered the best performance comparing to all other joint configurations. Another configuration which could spread the damage more evenly is the single-lap joint. In addition, by increasing the length of the overlap, the peak stresses increase as well as the end of the bondline of joints. The overlap length increase delivers significant benefits as an increase of the load-carrying capacity only for certain designs and combinations of adherends. Khashaba *et al.* [18] found out in their research that the

thickness and the angle of composites of adhesive scarf joints produces a relatively significant effect. The strength of the joint decreases when the thickness of the composites is increased, and the scarf angle is decreased. The bonding strength also depends on the surface preparation, etching, the thickness of the adhesion layer, etc. Saikaew *et al.* [19] presented the research results where the type of the surface preparation and the adhesive application time had a significant impact on the bonding strength. Also, the quality of the surface preparation or the surface topography can improve the bond strength [20]. Therefore, the surface treatment before joining exerts great impact on the joining when using adhesives, and it can even be improved by different techniques [21]. Furthermore, it was found that adhesive thickness is one of the most significant parameters, and that it has a great effect on the overall strength of the bonded structure. The load bearing capacity of the lap joints increases when the thickness of the adhesive decreases [22], [23].

The main critical type of defects in adhesively bonded similar and dissimilar materials is the bonding defects having a negative impact on the distribution of shear stress in the layer of the adhesive. Debondings, zero-volume disbonds, weak bonding and voids are the types of defects which can occur in the adhesive layer. The conducted research proved that, by the increase of the size of these defects, the strength of the joint decreases [24], [25]. The resulting stresses of debonds and voids are concentrated on the edges of large defects. Shear stresses reach the maximum values near the defects because high stress concentration occurs in these areas [24], [26]. Zero-volume disbonds or kissing bonds are the defects which characterise the bonded interface, but the bond strength is not ensured. The material properties of kissing bonds are similar to the surrounding medium; therefore, these defects do not show sufficient contrast in order to be detected. These defects mainly occur due to the curing lack of the adhesive, physical damage, or surface contamination [27], [28], [29]. The reliability of adhesive bonding is mostly influenced by the presence and location of the defects as well as by the preparation of the adherends' surfaces before the gluing and curing process and such other factors as the environment which is hard to control. Therefore, the study of the influence of adhesive defects is an important task [24]. In the case of dissimilar material joints, the materials can also have their own defects separately. For example, in the composites, such defects as delamination and fiber damages can occur at the manufacturing, bonding (especially mechanical joining) and exploitation stages [13]. Different types of defects which can occur in layered adhesive structures are presented in Fig. 1.1 below [30]:

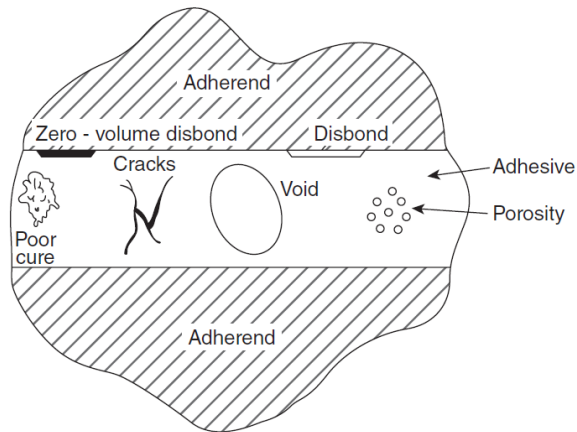


Fig. 1.1 Types of defects in bonded structures [30]

As a result, the bonding area is the weakest place in multilayered structures which has to be controlled and reliably checked. The adhesive integrity depends on the adhesive strength, stress distributions, the design configuration of bonded joints as well as the bonding defects. In this work, the integrity of manufactured adhesively bonded plates of dissimilar materials, as well as the single lap-joint with artificial disbonds in the interface of the structures were investigated.

1.3. Evaluation of boundary characteristics

Ultrasonic reflection and transmission characteristics are used in NDT and in the evaluation of the properties of adhesive bonding. The thickness of the adhesive as well as elastic properties of the material can be identified by ultrasonic wave reflections. In addition, when using this method, the strength or degradation of the bonding between the adherend-adhesive can be evaluated quantitatively and qualitatively [31].

Metal-to-composite and composite-to-composite bonded joints are denoted by more complicated ultrasonic wave propagation characteristics compared to metal-to-metal bonded joints due to the different sequence of the type of materials [31]. Kumar *et al.* [32] in their studies of the degradation in adhesively bonded composites carried out experimental and theoretical investigations of the samples with various conditions of interfacial and cohesive properties. The ultrasonic inspection of oblique incidence demonstrated that bonding degradation can be measured by the change in the amplitude of reflections and by the shift in the minima of the spectrum of the reflected signals. It was determined that there is a correlation between the bonding strength and the frequency shift in the spectrum minimum. There is high influence on the shift in the spectrum minimum in the case of bulk adhesive degradation and more significant influence for interfacial degradation [32]. The research regarding investigation of thick adhesive layers was also performed where the double-interface model was introduced, and the effect on the reflection and transmission behaviour in the joints was studied [33]. However,

the comprehensive research was conducted to isotropic bonded materials. Extended research to anisotropic materials and a combination of isotropic and anisotropic materials is still required [31].

He *et al.* [31] performed theoretical analysis with the objective to evaluate the bonding of a FRP-to-FRP (Fiber Reinforced Polymer) sample with a thick adhesive layer. The schematic of the sample immersed in liquid is shown in Fig. 1.2.

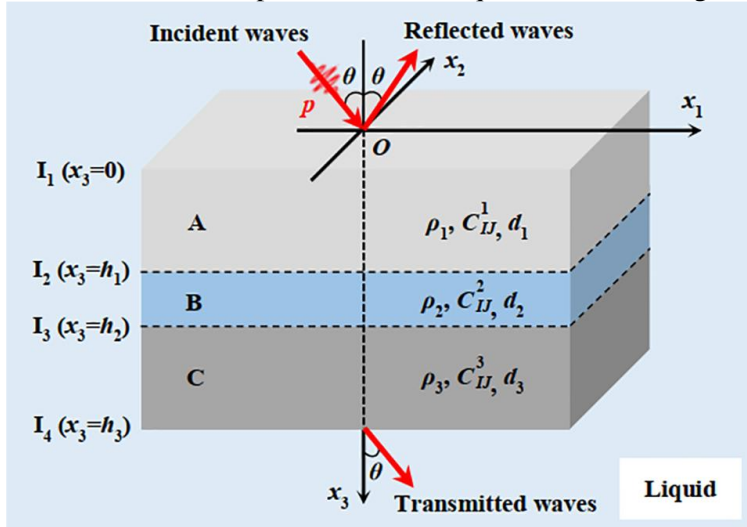


Fig. 1.2 Adhesively bonded FRP-to-FRP with a thick adhesive layer [31]

In the schematic of the FRP-to-FRP sample, d_1 , d_2 , d_3 are the thicknesses of the FRP layers A and C and the adhesive layer B. Attenuation was not considered in the research. There are also four interfaces (I_1 , I_2 , I_3 , I_4) with the appropriate coordinates (0 , h_1 , h_2 , h_3) and densities with the elastic constants for each layer ρ_1 , C_{IJ}^1 , ρ_2 , C_{IJ}^2 , ρ_3 , C_{IJ}^3 where $I, J=1,2,\dots,6$. Incident waves are travelling from the liquid into the layered structure at an angle θ . The same angle defines the reflected and transmitted waves. All the vectors of wave propagation are perpendicular to the bonding layers in accordance with the Snell's Law. Displacement u_i , ε_{ij} , σ_{ij} , strain and stress components as well as the elastic constant C_{ijkl} and material density ρ were calculated from the basic mechanical equation for solid layers, the liquid domain. Also, the boundary conditions for liquid-solid interfaces and solid-solid interfaces were calculated. As a result, the method of the global matrix was applied for the joint of FRP-to-FRP due to such advantages as robustness and the ability to be used in various solutions, for example, in liquid, vacuum or solid half. The global matrix (Equation 1.1) includes all boundary conditions as well as the reflection R and transmission T coefficients.

$$\begin{aligned}
& \begin{bmatrix} [M^2(0)] & [G(0)] \\ [M^4(h_3)] & [H(h_3)] \\ [M^2(h_1)] & [-D(h_1)] \\ [M^3(h_2)] & [-F(h_2)] \end{bmatrix}_{20 \times 20} \cdot \begin{bmatrix} \{Q_i^1/A_0\} \\ \{Q_i^2/A_0\} \\ \{Q_i^3/A_0\} \\ \{A_R/A_0\} \\ \{A_T/A_0\} \end{bmatrix}_{20 \times 1} \\
& = \begin{bmatrix} \beta \\ K_w j k (1 + \beta^2) \\ \{0\}_{18 \times 1} \end{bmatrix}_{20 \times 1}, \quad i \in \{1, 2, 3, 4, 5, 6\}
\end{aligned} \tag{1.1}$$

If $M^2(0)$, $M^4(h_3)$ are characteristic matrices of liquid-solid interfaces, $M^2(h_1)$, $M^3(h_2)$ are characteristic matrices of solid-solid interfaces, $G(0)$, $H(h_3)$, $-D(h_1)$, $-F(h_2)$ are segmented matrices of appropriate interfaces, Q_i^n is the expansion coefficient for partial waves, A_0 , A_R , A_T are the amplitudes of incident, reflected and transmitted waves, $\beta = \cot\theta$, K_w is compressibility.

The results of theoretical analysis show that the angular and frequency spectrums of the reflection coefficients can be acquired by changing the frequency and the incident angle. Afterwards, the evaluation of degradation for several models of the FRP-to-FRP joint was carried out according to theoretical analysis. In the case of the single and dual bonding interface, while the interfacial stiffness decreases, the extreme points in the frequency spectrum shift to the lower frequency, whereas, in the angular spectrum, these points shift to the side of the larger angle. In addition, the key factor that has to be considered while analysing the shift of extreme points is the symmetry of the bonded materials. As a result, this method is a theoretical foundation for the joints of composite-to-composite with a thick adhesive layer [31].

Studies on the interface condition in multilayered structures using guided waves were also conducted [34], [35], [36]. Ding *et al.* [37] in the research deduced the reflection and transmission coefficients of the SH mode (SH0) of ultrasonic guided waves in a multilayered structure with adhesive bonding from the basis of equations of wave propagation and coefficient of tangential stiffness K_T . Afterwards, adhesively bonded aluminium to aluminium with a different quality level of the interface (the perfect bond, the weak bond, and the debond) were investigated in order to analyse effects of the changes in frequency-thickness characteristics, the incident angle, and the tangential stiffness. The schematic of SH wave propagation mode is shown in Fig. 1.3.

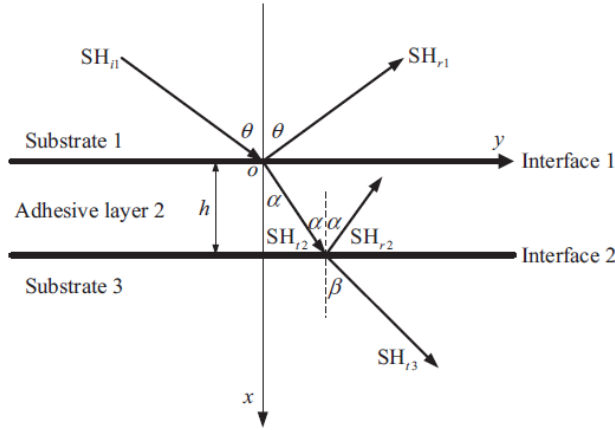


Fig. 1.3 Propagation of SH mode wave in adhesively bonded aluminium materials [37]

Substrate 1 and substrate 3 are aluminium materials in an adhesive layered structure. Substrate 2 is an adhesive layer of h thickness. All the medias are isotropic elastic solid. SH_{i1} is the incident wave, SH_{r1} and SH_{r2} are reflected waves in media 1 and 2. α is the angle of propagation in the adhesive, θ and β are the incidence angle and the transmitted wave angle, respectively.

The expression of reflection and transmission coefficients of the SH wave mode in adhesively bonded aluminium materials (3-layered structure) is presented in Equations 1.2 and 1.3.

$$R = \frac{B_1}{A_1} = \frac{\mu_1 Q_1 F - \mu_2 K_T^{(1)} Q_2 (H - 1)}{\mu_1 Q_1 F + \mu_2 K_T^{(1)} Q_2 (H - 1)}; \quad 1.2$$

$$T = \frac{A_3}{A_1} = \frac{2\mu_1 K_T^{(1)} K_T^{(2)} Q_1 (H + e^{-2ikQ_2 h}) e^{-ik(Q_3 - Q_2)h}}{[K_T^{(2)} + ik\mu_3 Q_3] [\mu_2 K_T^{(1)} Q_2 (H - 1) + \mu_1 Q_1 F]}; \quad 1.3$$

Here, A_i is the amplitude of the incidence wave, A_3 and B_1 are unknown numbers of amplitudes of the transmitted waves in adherend 3 and the reflected waves in the adhesive layer which are expressed by A_i and the tangential stiffness coefficients $K_T^{(1)}$, $K_T^{(2)}$, μ_1 , μ_2 and μ_3 are the Lamé constants of each structure layer, Q_1 , Q_2 and Q_3 are phase velocities in 3 layers, h is the thickness of the adhesive, i is the real part, k is the wave number, $H = \frac{[(K_T^{(2)} + ik\mu_3 Q_3)\mu_2 Q_2 + \mu_3 Q_3 K_T^{(2)}]}{[(K_T^{(2)} + ik\mu_3 Q_3)\mu_2 Q_2 - \mu_3 Q_3 K_T^{(2)}]} e^{-2ikQ_2 h}$, $F = K_T^{(1)}(H + 1) + ik\mu_2 Q_2 (H - 1)$.

As a result, it was determined that, by increasing the frequency-thickness characteristics, multi-order resonance occurs in the curves of reflection and transmission coefficients in the wave of the SH mode under the perfect and weak bonds. As the result of the paper, it was concluded that the proper values for the incident angle and the frequency-thickness characteristics have to be selected in

order to differentiate each adhesive layer condition – that is, whether it has perfect bonding, weak bonding, or debonding [37].

Loukkal *et al.* [38] in their research numerically evaluated the properties of the adhesive in order to study their influence on the behaviour of guided waves. The sample under investigation constituted adhesively bonded aluminium and steel layers. Epoxy resin was used for the adhesion of materials. The reflection coefficient was used in this study since it gives resonance modes which correspond to the guided wave modes. The condition of interface of the multilayered structure was assessed by the viscoelastic parameter $\omega\tau$ as well as by the normal and transverse stiffness of interface K_n and K_t . Thus, the magnitudes of the reflection coefficient as well as the dispersion curves of guided waves are influenced by the condition of the adhesive interface of the layered structure.

There is also research done on the evaluation of the normal and shear stiffness for the characterisation of the interface condition by analysing the amplitudes of the reflection and transmission coefficients [39], [40], [41].

As a result, the material properties of each layer of the multilayered structure can be evaluated in order to assess the integrity. Ultrasonic reflection coefficients can be calculated in layered structures by taking into account the thickness of the adhesive layer for the further evaluation of bonding degradation. However, in the case of very thin adhesive layers, when the thickness is lower than the wavelength in the material, the quality of the bonding interface can be evaluated by ultrasonic bulk and guided waves with the use of Quasi-Static Approximation (QSA) [31]. The proposed evaluation of the interface condition of a layered structure by using ultrasonic guided waves can be applied for the samples with the sufficient surface length for the propagation of guided waves. Overall, the basic methodology of the reflection and transmission coefficients which are influenced by the bonding area condition can be applied for the inspections using bulk as well as guided waves.

1.4. Nondestructive testing of adhesively bonded materials

The currently available nondestructive methods for the investigation of multilayered structures of adhesively bonded similar and dissimilar materials are described in this section.

1.4.1. Inspection of joints of similar materials

The state-of-the-art and other acoustic methods for the nondestructive inspection of adhesively bonded joints of similar materials were developed in [42], [43], [44], [45], [46], [47], [48]. However, not all the techniques can be easily applied to all structures due to their difference of geometry, the thickness of the layers and the adhesive as well as the types of the materials. The pulse-echo ultrasonic techniques of a high frequency were used to visualise the defects in the interface of adhesively bonded joints [49], [50]. In the case of disbond being present, the reflection coefficient of the bonding interface of the metal and adhesive layers is fairly high, and the acoustic images of the defective interface can be obtained with sufficient contrast to distinguish them. However, the large difference of acoustic

impedances of metals and adhesives results in high amplitude reflections and produces strong wave reverberations in the first metal layer. In addition, in such structures, the reflected waves from the adhesive and second adherend bonding or defect can be masked by these strong reverberations, which makes the detection of a defect in the interface more complicated [50], [51], [52], [53], [54]. The quality of adhesion of layered structures can also be tested with the proposed ultrasonic resonance spectroscopy methods [55], [56], [57]. The amplitude and the frequency value of the through-thickness resonance of the system of the transducer bonded to the sample are measured. The change of these values can be characterised by the defective adhesion and the condition of bonded materials in the sample [50], [57]. The electrical impedance of the transducer is measured in the narrowband ultrasonic spectroscopy with the objective to detect the defects in the layered structures due to the dependence on acoustic impedance [55], [56].

Titov *et al.* [50] proposed a method for the detection of voids and disbonds in adhesively bonded materials. The reference waveform was recorded for only the first metal layer in order to eliminate the strong response produced by the ultrasonic wave reverberation in the first metal layer of the adhesively bonded structure. The elimination was required since the output waveform is the sum of signal reflections from the metal-adhesive and the adhesive-metal interfaces. The decomposition algorithm was developed and applied to the sample's inspection of bonded aluminium and steel with different thicknesses of the adhesive layer. The proposed method is based on the calculation of the amplitudes of multiply reflected waves from the interfaces of interest (metal-adhesive and adhesive-metal) which will be received by the transducer after propagation through the layers of the sample. The model under analysis is shown in Fig. 1.4.

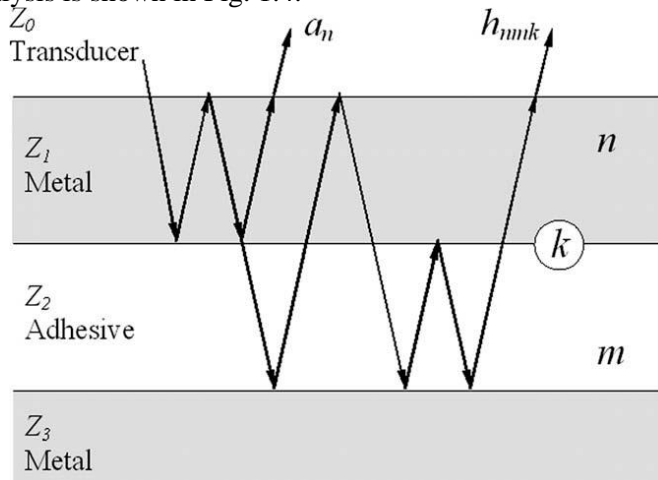


Fig. 1.4 Schematic of ultrasonic wave propagation paths vs. time [50]

In this research, the measured waveform and the recorded reference one was compared. Then, in order to detect disbonds at appropriate interfaces, the deviation parameter r was calculated for the first metal-adhesive interface:

$$r = \left[\int_{t_1}^{t_2} (s(t) - s_{R1}(t))^2 dt \right]^{1/2}; \quad 1.4$$

Here, $s(t)$ is the waveform output for the metal-adhesive interface, $S_{R1}(t)$ is the reference waveform recorded for bare metal material; $[t_1, t_2]$ is the time range of the data window.

Disbonds at the adhesive-metal interface were detected by using phase inversion of the reflected pulses. In the case of a good contact between these layers, pulses are inverted. The polarity of the pulses was determined by the sign of the correlation function $g(t)$. The negative value characterised the inversed phase and the absence of disbonds. However, this method is only applicable for perfectly flat and smooth surfaces and interfaces of the samples [50].

Recently, Yilmaz *et al.* [58] in their work proposed a technique to detect the weak bond in the joint of adhesively bonded composite materials. The method of acoustic spectroscopy of high frequency and high resolution was used for this purpose. The single-lap joint of bonded CFRPs with a different bonding quality – debonding and the weak bond – were evaluated. The algorithm of shape-based feature extraction was developed for the detection of the weak bond, and the high frequency in acoustic microscopy provides great visualisation of the bonding quality. In the case of a thin bonded structure of composites, post-processing plays an important role for the evaluation of the bonding quality. A diagram of the multi-level post-processing algorithm is shown in Fig. 1.5.

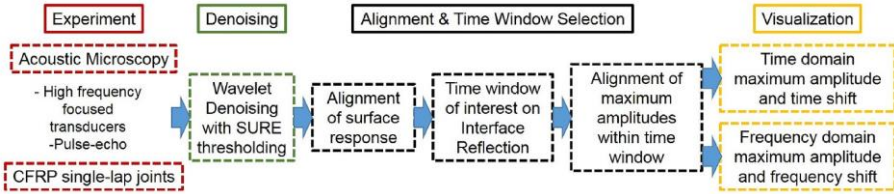


Fig. 1.5 Diagram of the developed post-processing algorithm for weak bond detection [58]

The Structural Health Monitoring (SHM) inspection techniques were also applied for the evaluation of bonding qualities of layered structures. SHM makes it possible to monitor the condition of the structure and to build a history database of the structure life [59]. Nicassio *et al.* [59] in their work proposed a novel SHM technique based on the interference of elastic waves for the detection of disbond defects. The sample under investigation was bonded to thin plates of aluminium. However, the mechanical properties do not affect the validity of the method since the study is performed for the wave propagation through the adhesive layer. The interference of elastic waves is generated by the piezo sensors and waves travelling along the aluminium plates and through the adhesive layer. In the case of debonding, the wave speed changes. These changes affect the reflection of the wave from the bonding area of the presence of a disbond and the further interference of the reflected waves with the main wave which is travelling along the bonded plates. The condition of destructive interference is dependent on the length of the disbond. As a

result, such tasks as numerical simulation and the comparison to analytical models of wave propagation through the sample as well as the comparison with experimental results were performed, and reliable results were provided.

Another work of Zhang and Zhou [60] describes the detection of disbonds in multilayered structures of adhesively bonded composites by laser ultrasonic guided waves. Due to the investigation of the interaction of guided waves with disbonds, the optimal distance between the source and the receiver was determined for the detection accuracy and the efficiency of the method. The size of defects was measured by using the proposed -8 dB method, and the relative errors were estimated at about 8%. As a result, laser ultrasonic guided waves and the quantitative method proposed to facilitate the visualisation of disbonds and to provide accurate information of bonding quality. In the resulting C-scan image, the modelled defects (in white circles) along with other natural defects were detected and shown in Fig. 1.6.

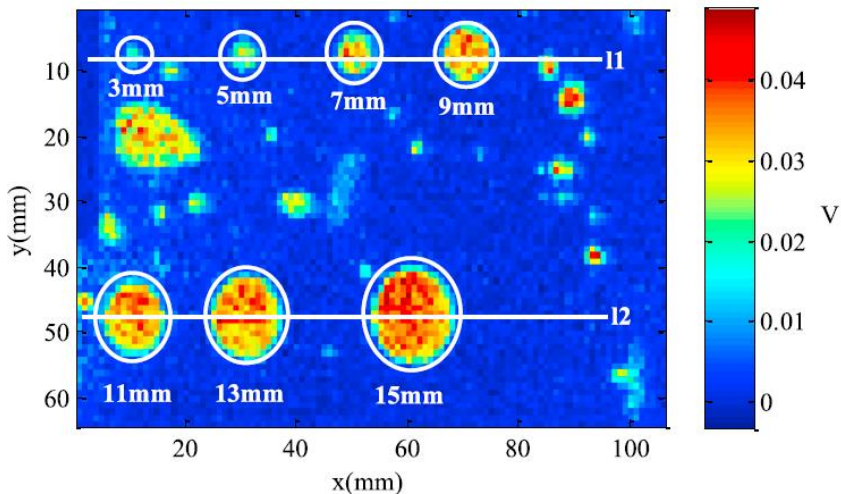


Fig. 1.6 C-scan of the detected disbonds in a layered structure of lead-adhesion-steel [60]

The method of defect sizing of -8 dB was proposed according to the simulation results of the relationship between the size of disbonds and the relative sensitivity, which is shown in Fig. 1.7.

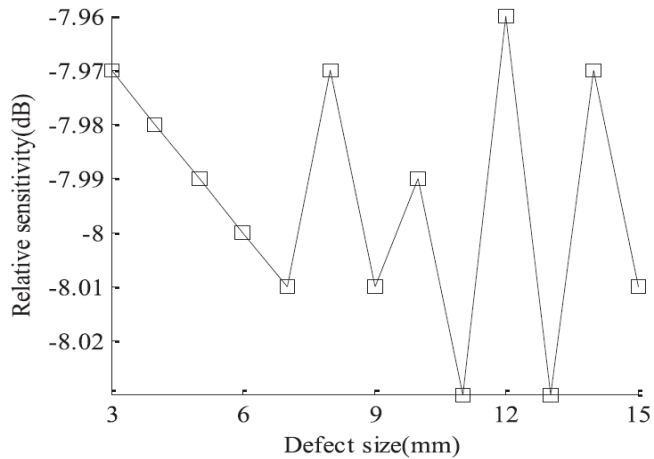


Fig. 1.7 Simulation results of relationship between defect sizes and relative sensitivity [60]

Pyzik *et al.* [61] proposed the laser ultrasound method for disbond detection in adhesively bonded metals. This method showed high performance for carbon reinforced composites; however, in the case of metals, the excitation of longitudinal waves was not efficient. For this case, the generation of shear acoustic waves was proposed. A multilayered structure of three adhesively bonded aluminium plates was under investigation. Disbonds were created by using the Teflon film. For the experimental investigation, a laser ultrasound system with a high repetition rate laser for the excitation of shear waves and a highly sensitive interferometer *Sagnac* were used. The schematic of the sample under investigation along with snapshots of the velocity wavefields are presented in Fig. 1.8.

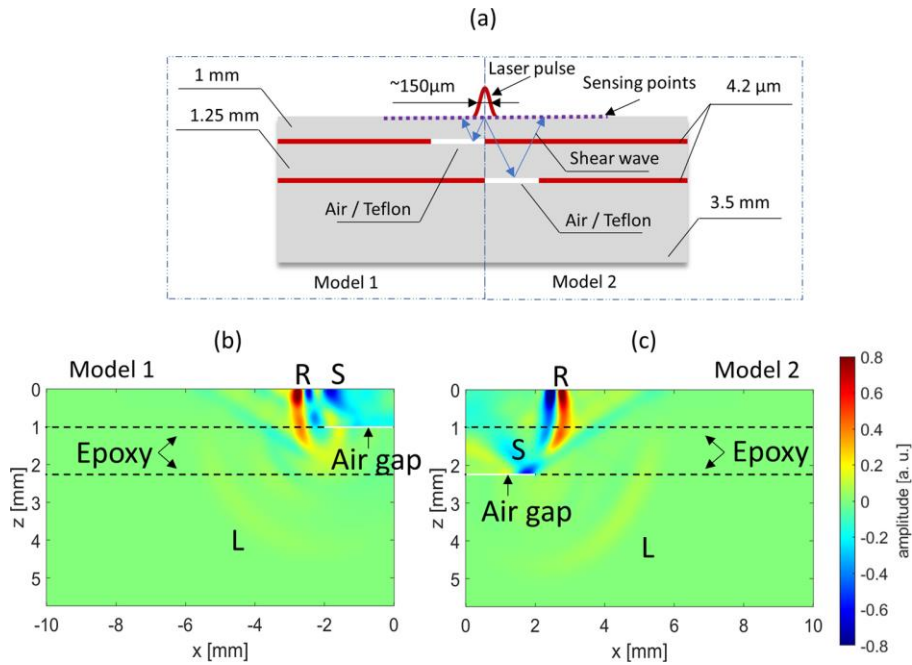


Fig. 1.8 Schematic of a multilayered structure of adhesively bonded aluminium materials with disbonds on first and second adhesive layers (a). Snapshots of velocity wavefield for Model 1 (b) and Model 2 (c). Generated waves: longitudinal (L), shear (S) and Rayleigh (R) [61]

The stand-off distance between the interferometer and the source maximises the amplitude of the received signal. Therefore, the local interaction simulation approach (LISA) was used for the accurate estimation of the distance. In addition, the inverse filter which was based on the reference signal obtained from the undamaged area was used to remove the undesirable wave modes from the response. As a result, both defects were easily detected, and the proposed technique was proven to be suitable for the industrial use and environment [61].

Palumbo *et al.* [62] in their research characterised the adhesive joints of glass fiber reinforced thermosetting plastic (GFRP) by using ultrasonic imaging and lock-in thermography. Firstly, ultrasonic testing in the pulse-echo mode was performed. The coupling of ultrasound testing (UT) probes was performed with water-driven jets in order not to leave the specimen in the water so that to avoid the influence on the physical and chemical characteristics of the specimen. A 1 MHz frequency immersion probe and the *LabView* measurement system were used for the inspection. The UT inspection was performed for the joints before and after 4-year aging. The resulting C-scans represented the bonding quality where lower amplitudes indicated areas which could have been associated with defects. However, after 4-year aging, no variation appeared in the bonding quality. The lock-in thermography which is based on the generation of thermal waves in the specimen

was applied as well (Fig. 1.9). Debonding areas were determined from the phase images which were obtained with the appropriate modulation frequency.

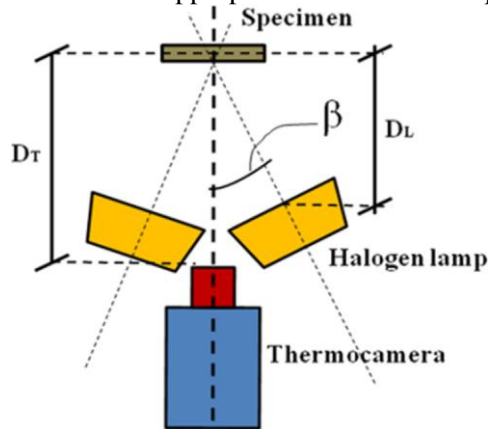


Fig. 1.9 Set-up of lock-in thermography for adhesively bonded composite plates [62]

The conclusions of the ultrasonic testing and lock-in thermography were compared, and good agreement of the results of both techniques was obtained. The rupture test of the sample was performed as evidence of the obtained results of nondestructive testing [62]. Katsiropoulos and Pantelakis [63] in their work investigated the bonding quality of composite-adhesive U-joints by using ultrasonic C-scan inspection and the mechanical test as the *InterLaminar Shear Strength*. The resulting C-scan demonstrated defected bonding in several places, mainly voids.

Ehrhart and Valeske [30] in their research made a review of the state-of-the-art non-destructive testing techniques applicable for adhesively bonded composite materials. The following methods can be applied for the assessment of the bonding quality – visual inspection, leak and tap tests, the Fokker bond tester (FBT), X-ray, shearography, infrared thermography, acoustic emission (AE), and ultrasonic testing.

There are more works which were carried out for the evaluation of bonding quality by using different NDT techniques as well as the determination of the chemical and physical properties. Various ultrasonic techniques were used with various adhesion levels, Lamb waves and SH waves, nonlinear ultrasonic, laser ultrasonic, etc., strategies, see [64], [65], [66], [67], [68], [69], [70], [71].

1.4.2. Inspection of joints of dissimilar materials

Despite the extensive work performed for adhesively bonded similar materials, which still requires reliable testing techniques for the detection of disbond, the evaluation of the adhesive bonding quality in dissimilar material joints is a challenging task. There is lack of research performed for the inspection of such multilayered structures. However, below, the currently available works are described. A reliable NDT technique still has to be developed in order to detect the disbond type defects in the bonding line of dissimilar materials.

Jasiuniene *et al.* [72] in their work applied ultrasonic testing for the adhesive bonding evaluation of the hybrid-metal-to-composite joints. Due to the geometrical structure and the characteristics of the sample, there is scattering, attenuating and overlapping of the reflected ultrasonic signals from the layers. The sample under investigation was bonded titanium with pins and CFRP materials (Fig. 1.10).

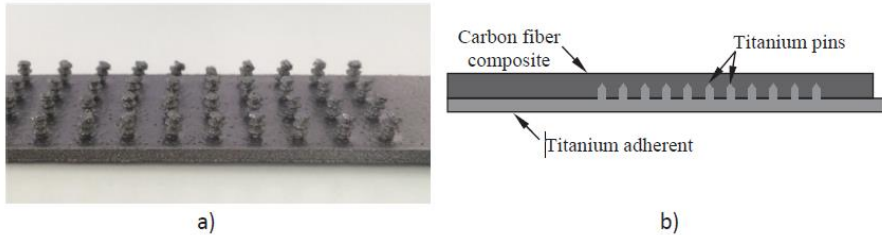


Fig. 1.10 Dissimilar material joints of titanium to CFRP [72]

After the determination of the appropriate side for the sample inspection (composite), the pulse-echo ultrasonic inspection in the immersion mode with a 10 MHz focused transducer was applied for the sample investigation. A signal post-processing algorithm for the reconstruction of the data was developed in order to eliminate the influence on the detectability of a rough surface and the non-parallel layers of the structure. By using this technique, the defects and their positions were identified. The post-processing algorithm consists of the following steps [72]:

1. Denoising of the signals by the Gaussian filter.
2. Calculations of the spectrum mean frequency.
3. Estimation of the arrival times of the signals reflected from the interface.
4. Linear interpolation for the positions of the arrival time which contains zeros or sharp spikes.
5. Signal shift in the time domain according to the estimated arrival time.
6. Denoising of the reflected signals from the interface by the Gaussian filter.
7. Calculation of the envelope of each signal.
8. Calculation of the maximum values for the signals for 3D imaging.

Summa *et al.* [73] proposed *in situ* passive thermography for the investigation of interfacial stress relaxation in the hybrid structures of bonded metal and CFRP. A metal plate is inserted in the central plies of the CFRP material. Then, the thermoplastic layer is placed between these hybrid components, and a tight fit is provided. The damages which can occur during the mechanical loading were studied. The inserted thermoplastic mostly generated such defects as delamination and cracking. The experimental and modelling results showed that, by the decrease of thermoplastic stiffness, the stresses are distributed more increasingly. As a result, *in situ* thermography located the origins of the damages. The set-up of the NDT technique is shown in Fig. 1.11.

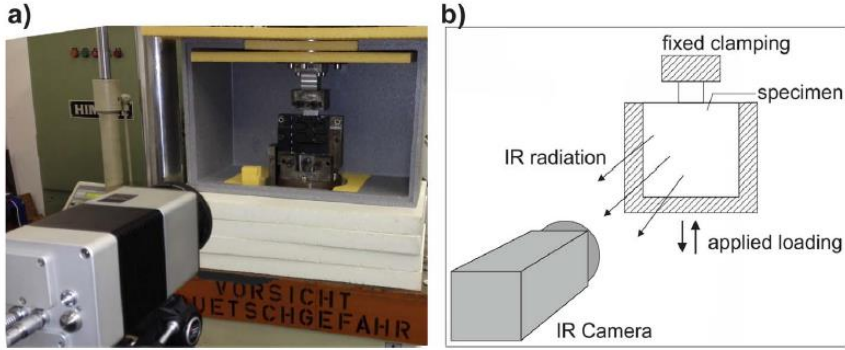


Fig. 1.11 Set-up of *in situ* passive thermography of the hybrid structure of bonded dissimilar materials with thermoplastic insert: (a) Picture, (b) Schematic diagram of experimental investigation with specimen and IR camera [73]

Moradi *et al.* [74] proposed a thermography non-destructive method for the edge disbond detection between the carbon-epoxy patch used on aluminium for repair. Usually, composite patches are used to repair damages in aerospace metal constructions. Therefore, in such structures, the dangerous defects are disbonds which usually develop from the edge of the patch. In this work, different image post-processing methods were proposed for the quantitative evaluation of the defects – Fourier transform and 1D and 2D Daubechies wavelet transforms. The 3D wavelet transform was used for the optimisation of results in terms of the time processing and the signal-to-noise ratio. Finite element modelling (FEM) was also performed for the better understanding of the heat transfer and the establishment of the experimental set-up.

The patch contains 8 disbonds and is shown in Fig. 1.12. The Phase Fourier Analysis which was used in the post-processing algorithm is a powerful tool of the pulse thermography which transforms thermal images from the time domain to the frequency domain:

$$F_n = \Delta t \sum_{k=0}^{N-1} T(k\Delta t) e^{-\frac{j2\pi kn}{N}} = \text{Re}_n + i\text{Im}_n; \quad 1.5$$

Here, $j = \sqrt{-1}$ is the imaginary number, the N -number of frequency, n is the evaluated frequency ($n=0,1,\dots,N$), Δt is the interval of the sampling time, Im and Re are the imaginary and the real part of the Fourier transform, respectively.

The initial signal was decomposed by the 1D wavelet:

$$W_f(S, B) = \int_{-\infty}^{+\infty} f(t) h_{SB}^*(t) dt = \text{Re} + i\text{Im}; \quad 1.6$$

Here, W_f is the wavelet transform, S is the factor of scaling, B is the factor of translation, * characterises complex conjugation, h_{SB} is the daughter wavelet.

2D wavelet transform is similar to 1D wavelet transform; the estimation and decomposition were only made on the 2D signal. The wavelet decomposition for 2D signal is described as follows:

$$I(x, y) = s_j(x, y) + \sum_{j=1}^j D_j^V(x, y) + \sum_{j=1}^j D_j^H(x, y) + \sum_{j=1}^j D_j^D(x, y); \quad 1.7$$

Here, S_j , D_j^V , D_j^H , D_j^D are the functions of the approximation and the initial image horizontal, diagonal, vertical coefficients. J characterises the numbers of N levels ($N=2^J$), j is the present level.

As a result, the 3D wavelet image analysis demonstrated the enhancement of the image in the spatial as well as in the time domains [74].

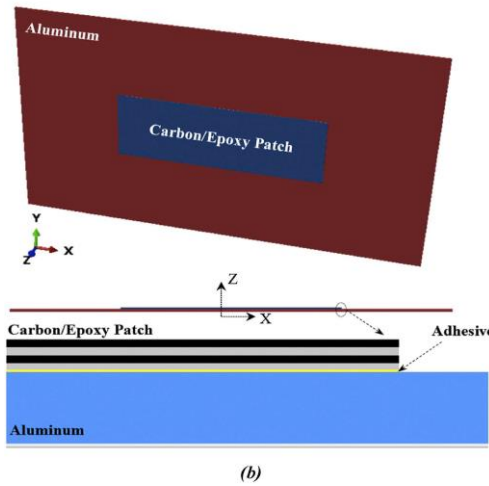
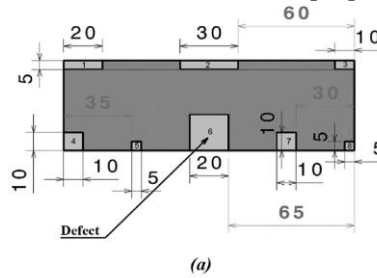


Fig. 1.12 Schematic diagram of a sample of aluminium repaired with the carbon patch with adhesive: (a) Patch with 8 disbonds, (b) Model of the entire sample of aluminium and patch [74]

Recently, Sun *et al.* [75] in their work investigated a sample of composite-metal adhesive bonding by the nondestructive electromagnetic-pulse-induced acoustic testing (EPAT). In the research, hydrogen tanks were investigated. To ensure the safe use of these tanks, nondestructive evaluation was performed on the adhesive bonding area of the plastic composite-metal components. The proposed

EPAT method uses generated guided waves in the adhesive bonding line for the disbond detection. The principle of this method is shown in Fig. 1.13.

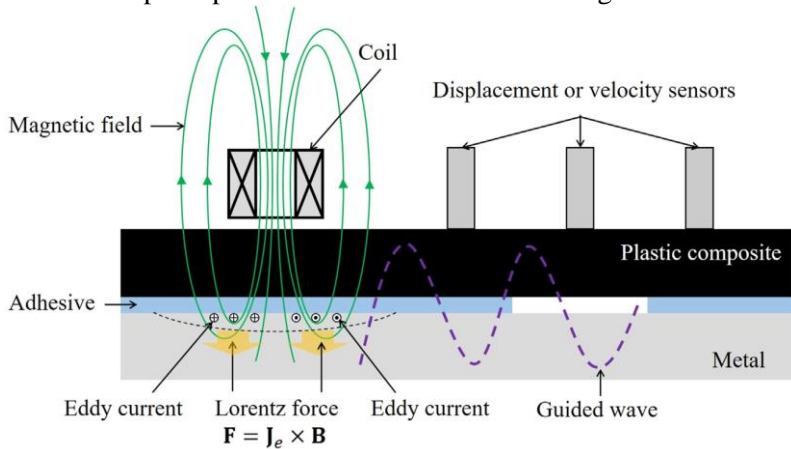


Fig. 1.13 EPAT method principle [75]

The EPAT method applies noncontact forces as Lorentz to metal components due to interaction of pulsed current and magnetic field. Therefore, guided waves of antisymmetric mode are generated. Guided waves propagate in the inner adhesive layer of the component as well as in the plastic composite and metal. In the case of the presence of any debonding type defect, the change of the signal of elastic waves occurs [75].

On the grounds of the above discussed methods, some techniques and algorithms can be applied for the sample under investigation in this work. The study of the polarity of the pulses as well as multiple reflections from the interface of bonded materials can be applied in this research of dissimilar material joints. However, for investigating thin joints, samples with rough and non-parallel surfaces and interfaces, the post-processing algorithms for the interface quality visualisation can be an essential part of the research which enables to eliminate the effect on the result of these sources.

When considering the NDT technique selection for the inspection of the appropriate specimen, there are many factors which influence it. Depending on the geometry of the sample, its design, the thickness of the layers, the type of material, as well as the area under interest, the defect type has a great effect on the choice of the NDT technique. In this work, guided waves were not considered due to the lack of the sample length for wave propagation. Thermography is also a very attractive method for the detection of the adhesive defect in the joints of similar and dissimilar materials.

1.5. Model-assisted probability of detection

The reliability of the NDT technique can be quantified by the evaluation of the Probability of Detection (POD) curves [76]. POD describes the probability of the detection of a defect of a certain size in the structure. The model-assisted POD

(MAPOD) approach has a great potential to determine POD curves without performing expensive and time-consuming experiments. Due to the simulation of POD curves, the performance of the inspection can be evaluated. However, many factors are influencing the POD, such as the material type, the structure geometry, the defect, the selected inspection technique, or the environment [76], [77]. As a result, the size of the detectable defect can be estimated by the POD curves. The methodology of the model-assisted POD curves assessment is the same as for the experimental one which is described in the military handbook MIL-HDBK-1823A and the ENIQ report [78].

The response of any inspection system is dependent on the influential parameters of the inspection method. This relationship is expressed as follows:

$$y = f(a, X); \quad 1.8$$

Here, y is the inspection system response, a is the characteristic value of the defect (dimension), X represents uncertain parameters.

The characteristic parameter represents the harmfulness of the defect. Usually, the defect dimension of length, width or height is selected as the characteristic value according to the type of the defect. In the case of disbonds, the characteristic value which identifies the harmfulness is the length of the defect. When calculating the POD curves, the correct statistical model of the data has to be provided. This can be ensured when the Berens hypothesis has been verified, and the statistical sampling captures all the variable parameters of the inspection [78]. In addition, basic assumptions of the POD curve have to be fulfilled. The POD has to be an increasing function with the increase of the size of the defect (the characteristic value), and it has to reach 100% with a certain size of the defect [79]. Moreover, the confidence intervals which measure the degree of uncertainty or certainty of the sampling method should be introduced when analysing the POD curves. The disbond size a_{90} describes the size with 90% probability of detection, the size $a_{90/95}$ denotes 95% confidence level for the size a_{90} detected with 90% POD [78], [80], [81]. Mostly, there is a requirement, especially in the aerospace industry, to determine the minimum size of the defect which can be detected in 90% cases of inspections with 95% confidence level. In this work, the length of the disbond, $a_{90/95}$, was determined [80], [82], [83].

There are two approaches to assess the POD curves – the Hit/Miss analysis and the Signal Response (\hat{a} vs. a). Both approaches can be used in order to evaluate the POD of disbonds in dissimilar material joints. The Hit/Miss approach, or the Bernoulli data analysis, is a measure of qualitative information which determines the presence or absence of a defect. The outcomes of the inspection are 1 describing a hit, and 0 describing a miss. Usually, this method is used when there is no knowledge of signal amplitudes, no obvious linearity between the raw data and the defect size a , or the hypotheses of the Signal response approach are not satisfied. The *Logit* function can be used in the Hit/Miss analysis to fit the data [80], [84], [85], [78].

$$\log \left(\frac{POD(a)}{1 - POD(a)} \right) = \beta_0 + \beta_1 \cdot a; \quad 1.9$$

Here, $\log \left(\frac{POD(a)}{1 - POD(a)} \right)$ is the logarithm of the odds, $\left(\frac{POD(a)}{1 - POD(a)} \right)$ are the corresponding odds, where $POD(a)$ is the probability of the defect ‘hit’, $1 - POD(a)$ is the probability of the defect ‘miss’, a is the selected characteristic value (the disbond size), β_0 and β_1 are the parameters of the model, β_1 describes how quickly the probability will change by changing the defect size a .

As a result, the obtained $POD(a)$ which increases continuously with the growth of the defect size and gives values [0;1] is expressed as follows:

$$POD(a) = \frac{e^{\beta_0 + \beta_1 \cdot a}}{1 + e^{\beta_0 + \beta_1 \cdot a}}; \quad 1.10$$

Here, $e=2.718$, and it denotes the base of the natural logarithm.

However, in the case of the Hit/Miss analysis, the quantity of samples has to be not less than 60 in order to obtain a reliable POD curve. This is due to the fact that POD is based on binary results and does not have enough information about the correlation of the defect size and the signal strength response [79].

The signal response (\hat{a} vs. a) approach was also used for the evaluation of the POD curves. The signal response approach is a quantitative measure based on the relationship between the defect size and the sensor response [86]. In the case of the selected ultrasonic inspection for the layered structure investigation, the amplitude of the response (\hat{a} represents the measured sensor response) depends on the size of the defect (a is the characteristic value or the defect size). If comparing to the Hit/Miss approach, the Signal response allows evaluating the POD curve with a significantly lower data amount. This method is based on the linear model when the data has to fulfil the assumptions called the ‘Berens hypothesis’ [78]. According to the Berens hypothesis, the data has to fulfil 4 criteria as follows:

1. The linearity of data behaviour.
2. Homoscedasticity or constant dispersion which implies a straight-line scattering around the regression for all sizes of defects.
3. Normality corresponding to the Gaussian distribution law for scattered data.
4. Independent data set for non-correlated data.

The measured value \hat{a} in the Signal Response analysis is denoted as:

$$\hat{a} = \beta_0 + \beta_1 \cdot a + \delta; \quad 1.11$$

Here, δ is an error which is characterised by the standard deviation σ_δ .

The POD curve is defined as a density fraction of the scattered data which is above the detection threshold.

$$\begin{aligned} POD(a) &= Prob(\hat{a} > \hat{a}_0) = 1 - \Phi_{norm} \left(\frac{\hat{a}_0 - (\beta_0 + \beta_1 \cdot g(a))}{\sigma_\delta} \right) \\ &= \Phi_{norm} \left(\frac{g(a) - \mu}{\sigma} \right); \end{aligned} \quad 1.12$$

Here, \hat{a}_0 is the detection threshold, $\Phi_{norm}(z)$ is the standard cumulative density function of scattered data according to the normal distribution law; parameters μ and σ were used to ease computations, where $\mu = \frac{(\hat{a}_0 - \beta_0)}{\beta_1} = a_{50}$ and corresponds to the defect size with POD=50%, $\sigma = \frac{\sigma\delta}{\beta_1}$ corresponds to the POD curve steepness, $g(a) = a = \log(a)$.

However, in the case of the Berens hypothesis being violated, another methodology has to be applied.

Since noise presence is observed in all NDT inspections, the level which defines the output with a defect or without a defect has to be established. This level is characterised by the detection threshold \hat{a}_0 . Generally, the detection threshold is determined as the highest level of the background noise in the case of measurements when there is no defect in the structure. Since the detection threshold is the highest level of the noise in the defect free region, therefore, it is important to correctly define the threshold for the layered structure. In the case of disbond defect detection which is located on the interface of dissimilar material joints, the maximum amplitude of the defect-free region of the interface is taken as the highest level of the background noise in the inspection. Meanwhile, the threshold value depends on the contrast of the amplitude of the disbond echo and the disbond free interface echo. However, there is a high possibility to classify the defect-free region as damaged if the strong background noise level exceeds the detection threshold. The POD curve is denoted by high dependence on the selected detection threshold and is valid only for this detection level. Therefore, in order to determine a more accurate value of the detection threshold, POD and the probability of false alarms (PFA) can be plotted on the diagram with the goal to maximise POD and minimise PFA. PFA is the probability when the system detects defects when there is none in the structure; see [86], [87], [88], [82], [78], [89].

Extensive work was done for the reliability assessment of the NDT techniques for various structures under inspection. Some of the works are described and analysed in this chapter. Rental *et al.* [77] in their study demonstrated the MAPOD approach of ultrasonic inspection. A cylindrical block made of Ti-6Al-4V with volumetric defects was under inspection. The ultrasonic response from the Flat Bottom Hole (FBH) defects of different sizes was generated numerically. The flowchart of MAPOD of the inspection is shown in Fig. 1.14.

In this study, the validation of the mathematical model was performed. The peak-to-peak amplitudes and the time of flight between the backwall echoes were estimated and compared to the experimental results. All the sizes of cracks were generated according to the lognormal distribution, and the POD of each size was evaluated. The regression of the data for POD curves generation was performed in order to calculate the mean and the standard deviation.

$$\text{Mean, } m = \frac{\log(\hat{a}_{dec}) - \beta_0}{\beta_1}, \quad 1.13$$

$$\text{Standard Deviation, } \sigma = \frac{\delta}{\beta_1}; \quad 1.14$$

Here, \hat{a}_{dec} is the signal response decision threshold value, β_0 is the regression line intercept, β_1 is the regression line slope, β_1 is an error.

As a result of the study, the value of defects detected with 90% probability and 95% confidence level is increased with the increase of the level of the decision threshold which depends on the signal noise level or/and the false call rate [77].

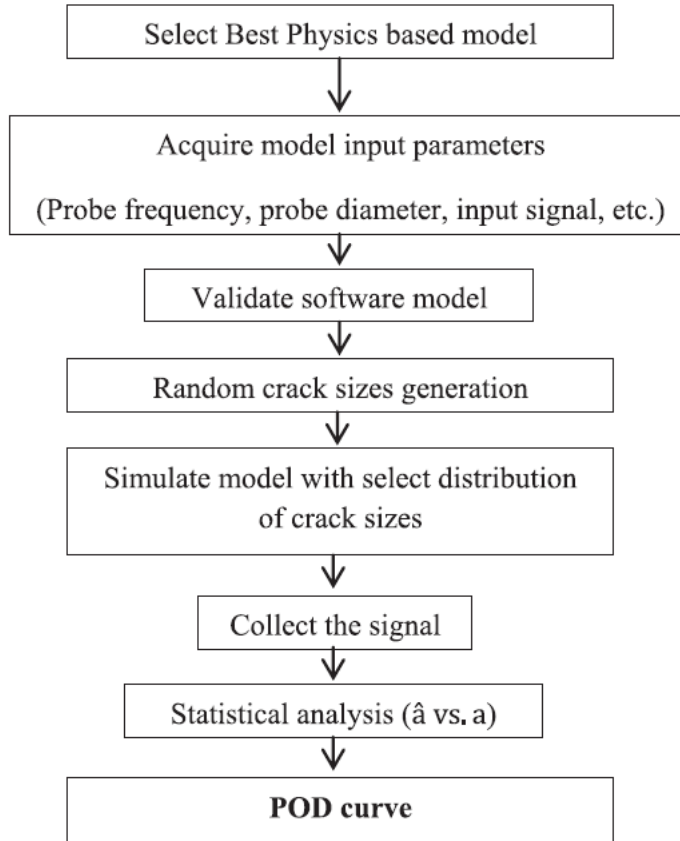


Fig. 1.14 Flowchart of MAPOD of ultrasonic testing of Ti-6Al-4V cylindrical block [77]

Bato *et al.* [90] in their work also suggested experimental and numerical approaches for the calculation of eddy current NDT for the POD curves. Multiple experimental inspections were carried out in order to take into account the human factor influence and the impact of various devices. These, along with defined uncertainties, were used as the inputs for the simulation model. The POD curves were calculated numerically and experimentally, and then compared to each other with the purpose to replace experimental tests by model-assisted ones (Fig. 1.15).

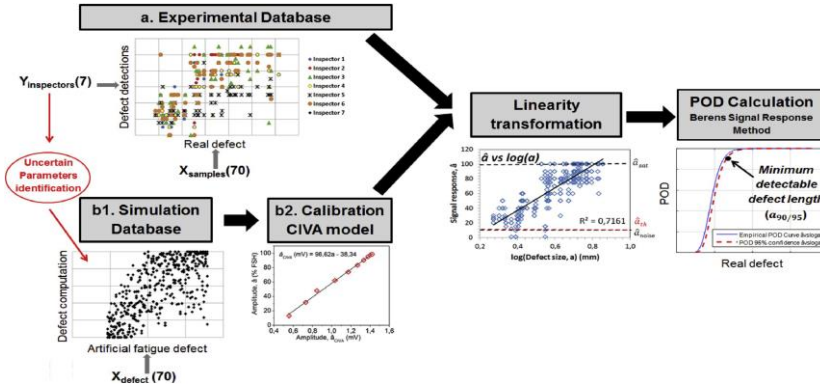


Fig. 1.15 Steps for the determination of POD curves according to the signal response method from experimental and modelled results [90]

Kurz *et al.* [91] in their work showed the results of POD determination of the inspection of real cracks by using ultrasound phased arrays. Different test specimens with such defects as austenitic, ferritic, dissimilar materials welds and cladded specimens were manufactured. Signal response analysis was used for the POD evaluation.

There has been more research performed in the evaluation of the reliability of the NDT techniques involving the calculation of the POD curves [92], [77], [93], [94], i.e., Duan *et al.* [95] quantitatively compared the reliability of pulsed thermography and the ultrasonic inspection of the impact damage in a CFRP specimen. In the work of Kim *et al.* [96], the probability of the detection of additive manufacturing flaws by using X-ray Computed Tomography (XCT) was determined empirically by using specimens and by a simulation model where signal response analysis was implemented. The empirical measurements of POD were close to the simulated results. However, the simulation model for POD evaluation could consider such factors as the flaw size, its location and orientation – those which were not assessed by the experimental approach. As a result, the incorporation of experimental and simulation results was performed by the multi-level Bayesian method. Junyan *et al.* [97] presented a work for the POD study of a lock-in thermography method applied for CFRP materials. The detected and undetected defects were determined by the hit/miss method. The capability of defect detection and the reliability of the thermography NDT were estimated.

$$\text{Hit/Miss} = \begin{cases} 1, & \text{if } |\overline{Ph}_{S_1} - \overline{Ph}_{S_3-S_2}| \geq \Delta Ph_{decision} \\ 0, & \text{if } |\overline{Ph}_{S_1} - \overline{Ph}_{S_3-S_2}| < \Delta Ph_{decision} \end{cases} \quad 1.15$$

Subair *et al.* [98] presented finite element (FE) Simulations for POD curves to perform the assessment of the ultrasonic inspection of stainless-steel plates and welds. The uncertain parameters which affect the ultrasonic inspection were identified. The FE simulations were performed for each combination of varying parameters. As a result of the research, the simulated results were compared to experimental measurements.

POD for various NDT techniques, such as ultrasonic inspection, thermography, eddy current, XCT, SHM and others by experimental and modelling approaches was performed in the research [99]. Further in this paper, the POD of disbonds in a multilayered structure will be evaluated. Model assisted probability of detection is a useful tool which avoids the use of expensive and time-consuming experimental calculations of POD curves, provides a close match to the experimental results and is able to analyse more influential parameters which cannot be considered in the experimental approach. The hit/miss and signal response approaches will be studied and used for computing POD curves.

1.6. Conclusion of the chapter and outline of the research tasks

Various NDT techniques can be used for the inspection of adhesively bonded materials. Table 1.1 presents a summary of the possible NDT techniques which can be applied for the investigation, together with their drawbacks and benefits. There are, also, other techniques and methods with different configurations. However, the main ones are summarised in the table below; all of these are recent or can be applied for the inspection of layered structures in order to detect interfacial defects.

However, the situation of the inspection of adhesively bonded dissimilar materials, such as metals bonded to composites, is a more challenging task. Along with the NDT techniques, the development of post-processing algorithms should be performed in most cases. The most attractive NDT techniques for the inspection of dissimilar material joints is the ultrasound inspection using bulk or guided waves, high frequency acoustic microscopy, and thermography. The most recently performed works describe the use of EPAT, guided waves, and a fusion of NDT techniques as well as the methods of image reconstruction.

According to the findings of the performed literature analysis, the following tasks were formulated for the development of the methodology of inspection of adhesively bonded dissimilar materials and for the disbond detection in the interface:

- To investigate and compare NDT techniques which are suitable for the disbond detection in adhesively bonded metal and composite materials.
- To provide theoretical analysis and calculation of boundary characteristics of the sample; to investigate the influential factors and parameters on the inspection of the joint of dissimilar materials with respect to disbond detection.
- To model the signals for different cases of the sample interface condition and to compare the results to the ones obtained theoretically. To extract the valuable feature(s) for the use in the development of the processing algorithm by performing theoretical, qualitative, and quantitative evaluations.
- To propose and develop the processing algorithm for the improvement of disbond detectability according to the extracted valuable features and the results of the investigations.
- To inspect experimentally the joints of dissimilar materials and to verify the developed algorithms for the improvement of the detection probability by the defect sizing and the uncertainty measurement; also, to evaluate the probability of defect detection before and after the application of the developed technique.

Table 1.1. Comparative analysis of the methods for inspection of layered structures

	Principle and defect sizes	Benefits	Drawbacks
Ultrasonic inspection	Pitch catch mode (oblique incidence), generation of shear waves on the interface [32]	Detection of interfacial degradation by amplitude change, shift in the frequency minimum and interfacial transverse stiffness [32]	High sensitivity of reflection minima to bondline thickness, surface roughness, environmental conditions, inspection method for adhesively bonded similar materials [32]
	Pulse-echo mode (immersion), amplitude of multiple reflection, change in the frequency spectrum and time domain. Disbond of 20 mm [50]	Detection of disbonds and voids, elimination of non-parallel layers and rough surface by reconstruction algorithm [50]	Only for flat and smooth sample interfaces, amplitude trend, overlapping, etc., inspection method for adhesively bonded similar materials [50]
Acoustic Spectroscopy	High frequency waves, algorithm of shape-based feature extraction. Debonding of 12.7 mm, weak bond [58]	Detection of debonding and weak bonds with great visualisation [58]	High cost, high attenuation, applicable for thin layers of the sample, inspection method for adhesively bonded similar materials [58]
Ultrasonic guided waves	Interference of elastic waves. Disbond of 7.5 mm [59]	Disbond detection, no dependence on mechanical properties [59]	Dependence of sample thickness and geometry, transducers placement, etc, inspection method for adhesively bonded similar materials [59], [60]
	Interaction of laser ultrasonic guided waves with defect [60]	Disbond detection by evaluation of displacement amplitude, high sizing accuracy [60]	
	Study of reflection, transmission and tangential stiffness coefficients of SH mode guided waves. Analysis of perfect, weak and debonding states [37]	Detection of perfect bond, weak bond and slip/debonding [37]	High sensitivity to the change of incidence angle, frequency, etc., inspection method for adhesively bonded similar materials, high dependence on the incidence angle and frequency [37]
Thermography	Generation of thermal waves, Fourier transform, 1D and 2D Daubechies wavelet transform, 3D wavelet transform [74]	Detection of debonds, delaminations, cracks by phase change and thermoplastic stiffness. Higher defect quantification by post-processing algorithms [74]	High reflecting metals, environmental conditions, high dependence on angle of radiation, etc. [74]

2. DEVELOPMENT OF A METHOD FOR THE IMPROVEMENT OF DETECTION PROBABILITY IN DISSIMILAR MATERIAL JOINTS

The goal of this chapter is to develop a post-processing algorithm which will increase the probability of the disbond type defect detection in the adhesive layer of dissimilar material joints. In order to achieve this goal, the components of layered structures were investigated theoretically, by using numerical simulations, and the modelling of the signal; also, a parametric study was performed. The investigation method presented in the work describes each step of the action to achieve the set objectives.

2.1. Investigation method

Interfaces are the most critical area of bonded structures. Defects in the adhesive layer are common. Due to that, the detection of such defects as disbonds and delaminations is important to ensure the integrity of the bonded area. Two samples of adhesively bonded dissimilar materials were used for the study in order to develop a technique of the detection probability improvement for the joints of dissimilar materials. The components of bonded metals to CFRP are usually used in aircraft structures in such segments as hulls; in the automobile industry, they are used in roof segments, and also they are common in the energy field and in mechanical engineering for rotor blade elements, etc. [100], [11], [10], [62], [101]. The samples under investigation are the plate having thicker layers of dissimilar materials and one single-lap joint with thinner layers which can be the reason of the defect detection becoming more complicated. In order to achieve the aim of the work, the investigation was performed as follows:

1. Analysis of multiple reflections and boundary characteristics.
2. Determination of the influential parameters through sensitivity analysis.
3. Numerical study of signal parameters and characteristics useful for the improvement of detection probability.
4. Optimisation of parameters to detect the essential time intervals for defect detection.
5. Development of post-processing algorithms.
6. Experimental investigation and application of the developed algorithms.
7. Evaluation of model-assisted POD curves of the selected ultrasonic NDT technique before and after the improvement of the probability of defect detection.
8. Measurement of uncertainty

The scheme of the investigation method steps is shown in Fig. 2.1. This method describes the full process of the study of dissimilar material joints, the detection of defects in the adhesive layer and the steps for the development of algorithms for detectability improvement.

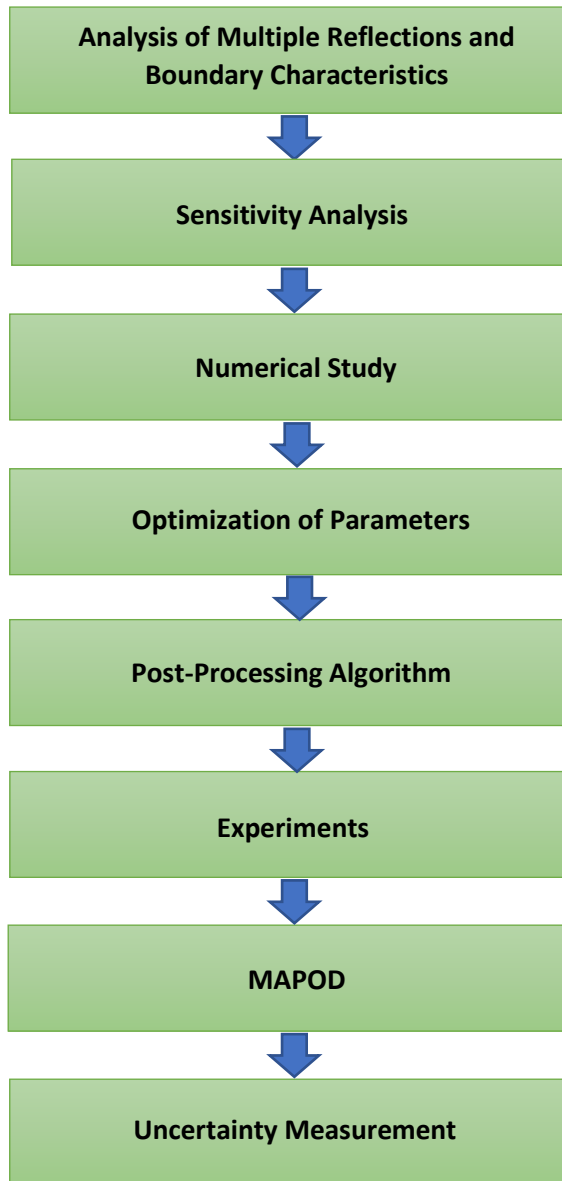


Fig. 2.1 Steps of the Investigation Method

In order to detect disbands in dissimilar material joints, theoretical evaluations of boundary characteristics and the calculation of the amount of energy received by the transducer after ultrasonic wave propagation in the structures were studied. Sensitivity analysis was performed with the objective to determine the most influential parameters regarding the inspection for the further development of the technique to increase the probability of disbond detection in the layered structure of dissimilar material joints. Inspection simulations were performed by using a semi-

analytical finite element to study the ultrasonic wave behaviour and the propagation through the layers of the samples of different adhesive conditions and defect locations in the adhesive. In addition, the evaluation, and comparison of the amplitude reflections of different cases was performed. The analysis is required to discover the possible techniques and to develop a post-processing algorithm to improve the detectability of disbonds in adhesively bonded dissimilar materials. Moreover, signal modelling was performed by using a custom developed program in *MatLab* with the aim to create the signal which should be maximally close to the experimental one. A comparison of the different condition of the modelled layered structures can give valuable information on how each layer affects the ultrasonic wave propagation and the signal form as well as to determine the time intervals with the most prominent amplitude change in the case of the defect presence in epoxy.

After the analysis of dissimilar material joints and the development of the technique to increase the defect detectability, the validation of the proposed techniques should be implemented by conducting experimental investigations and applying the developed post-processing algorithms. The model-assisted PoD shows the size of the defect which can be detected with the selected ultrasonic technique in 90% of the inspections at a 95% confidence level. In addition, the uncertainty of the measured defect sizes was calculated.

2.1.1. Theoretical analysis of multiple reflections and boundary characteristics

The goals of this part of the work are to evaluate the boundary characteristics of dissimilar material joints in order to learn the behaviour of ultrasonic waves in a layered structure, to study the propagation and reflection paths from the sample boundaries so that to determine the time instances of each of those and to calculate the values of the amplitudes of signals multiply reflected from the certain interfaces in the case of a different defect location in the adhesive layer. This procedure allowed assessing the impact of the defect location in the adhesive layer on the detection probability of the inspection technique. In order to achieve the outlined goals, an aluminium-CFRP sample of adhesively bonded materials was considered for the study. The sample consists of 3 layers: aluminium with the thickness size of 1.6 mm, an adhesive of 0.22 mm, and a CFRP layer of 5.11 mm. The CFRP plate consists of 41 layers where first and the last layers are GFRP, whereas the other layers are CFRP. Since the GFRP sub-layers are relatively thin, the entire composite plate is called CFRP. The ultrasonic wave propagation paths in the sample of dissimilar material joints were determined and shown in Fig. 2.2. The ultrasound velocity in aluminium, CFRP and in the adhesive was measured experimentally by using the appropriate NDT techniques. The contact pulse-echo technique and the *Olympus Omniscan MX* measurement system with a 15MHz conventional transducer were used for the aluminium and CFRP materials. In the case of the ultrasound velocity measurement in a relatively thin adhesive layer, a scanning acoustic microscopy measurement system (*KSI GmbH*) and a 50MHz focused transducer was used. The ultrasound velocities in aluminium, CFRP and in the adhesive were calculated according to the following equation:

$$V = \frac{2 \cdot H}{\Delta t}; \quad 2.1$$

Here, H is the thickness of the material, the time of flight interval $\Delta t = t_n - t_{n-1}$, t_n is the time of flight of a certain reflection from the bottom of the sample, the number of reflections is $n=1,2,\dots,5$.

The propagation time of ultrasound in each layer of the structure was calculated according to Equation 2.2. Moreover, in order to calculate the propagation time of the ultrasonic waves multiply reflected from the certain interfaces of the structure, Equation 2.3 was used [9]. The explanation of the indices of the time instances which are used in this section is presented in Table 2.1.

$$t_k = \frac{2 \cdot H_k}{V_k}; \quad 2.2$$

Here, H_k is the thickness of the layers, V_k is the ultrasound velocity in a certain material, k stands for the type of material(s) [9].

$$t_{nk} = \sum_{k=1}^K \sum_{n=1}^{N_k} \frac{2 \cdot H_{nk}}{V_{nk}}; \quad 2.3$$

Here, K is the type of the material layer, k is the number of a certain layer, $n=$ from 1 to N stands for the number of multiple reflections from the boundary, H_{nk} is the thickness of the layer K , V_{nk} is the ultrasound velocity in the layer K .

Table 2.1. Description of the indices of time instances

Reflection from boundary	Description
t_s	Reflection from surface or water-metal boundary
t_{1i}	1 st reflection from metal-adhesive interface
$t_{1adh,air}$	Reflection from adhesive-defect boundary after t_{1i}
$t_{1adh,GFRP}$	Reflection from adhesive-GFRP sub-layer after t_{1i}
t_{2i}	2 nd reflection from metal-adhesive interface
$t_{2adh,air}$	Reflection from adhesive-defect boundary after t_{2i}
$t_{2adh,GFRP}$	Reflection from adhesive-GFRP sub-layer after t_{2i}
t_{3i}	3 rd reflection from metal-adhesive interface
$t_{3adh,air}$	Reflection from adhesive-defect boundary after t_{3i}
$t_{3adh,GFRP}$	Reflection from adhesive-GFRP sub-layer after t_{3i}
t_{4i}	4 th reflection from metal-adhesive interface
$t_{4adh,air}$	Reflection from adhesive-defect boundary after t_{4i}
$t_{4adh,GFRP}$	Reflection from adhesive-GFRP sub-layer after t_{4i}

Ultrasonic wave propagation paths in the layered structure allow learning the sequence and order of the expected signal reflections from the interfaces or defects of interest from the ultrasonic A-scans. Further investigation of the signal, specifically, a comparison of the signal reflections from the defective and non-defective interfaces can provide useful information for disbond detection, for the influencing factors, and for the improvement of detection probability.

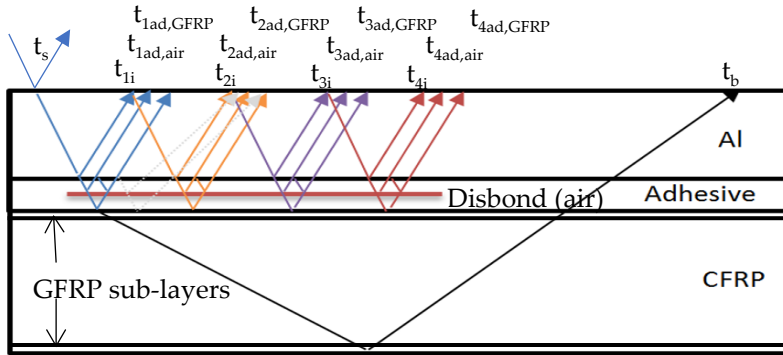


Fig. 2.2 Paths of ultrasonic waves propagating in a layered structure of adhesively bonded aluminium-CFRP joint [9]

In order to calculate the energy which is received by the transducer of ultrasonic wave propagation and multiple reflection from certain interfaces for the further comparison, three models of the structure were created – the disbond location between aluminium and the adhesive, the disbond location in the middle of the adhesive layer, and the bonding without defect (‘perfect bonding’). To achieve the goal, firstly, such boundary characteristics as the acoustic impedance (Z_k) of each material was calculated (Equation 2.4). The material characteristics are presented in Table 2.2.

$$Z_k = V_k \cdot \rho_k; \quad 2.4$$

Here, V_k is the ultrasound velocity in a certain material, ρ_k is the density of a certain material, k stands for the type of material(s).

Table 2.2. Calculated values of wavelength in materials of layered structures

No	Materials	Density, kg/m ³	Ultrasound velocity, m/s	Acoustic impedance, MRayl
1	Water	997.98	1 485	1.48
2	Aluminium	2 710	6 363	17.24
3	CFRP	1 800	2 800	5.04
4	GFRP	1 900	3 000	5.70
5	Adhesive film AF163	1 270	2 315	2.94
6	Air	1.225	330	0.000429

The reflection (K_R) and transmission (K_T) coefficients were calculated according to the following equations:

$$K_R = \frac{Z_2 - Z_1}{Z_2 + Z_1}; \quad 2.5$$

$$K_T = \frac{2 \cdot Z_2}{Z_2 + Z_1}; \quad 2.6$$

Here, Z_1 and Z_2 are acoustic impedances of the medias along the propagation path of the ultrasonic wave.

The amplitude values of signal reflections and multi-reflections from the sample boundaries were estimated according to Equation 2.7 for the model with the disbond between aluminium and the adhesive (the aluminium-disbond boundary) as well as based on Equation 2.8 for the models with the disbond in the middle of the adhesive layer (the adhesive-air boundary) and the perfect bonding (the adhesive-GFRP boundary) [9].

$$A_{1n} = K_{T12} \cdot K_{T21} \cdot K_{R23}^n \cdot K_{R21}^{n-1}; \quad 2.7$$

$$A_{2n} = K_{T12} \cdot K_{T23} \cdot K_{T32} \cdot K_{T21} \cdot K_{R34}^n \cdot K_{R32}^{n-1}; \quad 2.8$$

Here, n is the degree or the number of multi-reflections from a certain boundary, K_T is the transmission coefficient, K_R is the reflection coefficient; the numeric indices are the numbers of the component layers.

The three developed models for the investigation of different boundary conditions are shown in Fig. 2.3. The layers of materials of the modelled structure are presented not to scale. Air determines the disbond in the models. The propagation paths of ultrasonic waves in the layered structures of different boundary conditions are illustrated, and certain reflection coefficients are identified. Theoretical calculations to obtain the pulse responses in the structure for each reflection from the boundary were performed. The obtained plots of impulses characterise the arrival time of the signals reflected from the different boundaries of the sample. $H(t)$, a.u. characterises the transfer function with an arbitrary unit. Multiple reflections t_{1i} - t_{4i} , $t_{1ad,air}$, and $t_{1ad,GFRP}$ for each case of the boundary condition – aluminium-disbond, adhesive-disbond and adhesive-GFRP sub-layer – were plotted. The positive and negative polarity of the pulses is characterised by the different acoustic impedances of the structure materials and the phase change.

The amplitude values of multi-reflections of interest for each model case – aluminium-disbond, adhesive-disbond and adhesive-GFRP sub-layer – were calculated and presented in Table 2.3. As a result, more sensitive reflections for the disbond detection are the ones which follow after the first interface reflection.

According to the values from the presented table, it can be observed that the energy of reflections from the disbond located in the middle of the adhesive layer is relatively lower comparing to the defect location between aluminium and the adhesive. This fact confirms that there is an impact of the defect depth location in the adhesive on the disbond detectability. Furthermore, the difference between the amplitudes of the first reflection from the aluminium-disbond and the adhesive-disbond boundaries $A1$ is close to 2 times (6 dB). When analysing the fourth multiple reflections of these boundaries, the ratio is 3.3 (10 dB). In order to compare the amplitudes of defective and non-defective boundaries (adhesive-disbond and adhesive-GFRP), the ratio of the first reflection is ca. 10 dB, for the second reflection, the ratio is ca. 20 dB, whereas, for the fourth multiple reflections, it is ca.

40 dB. As a result, more information about the presence of a defect can be acquired by the analysis of a possibly bigger number of a particular multi-reflection. This technique can significantly increase the disbond detectability in layered structures.

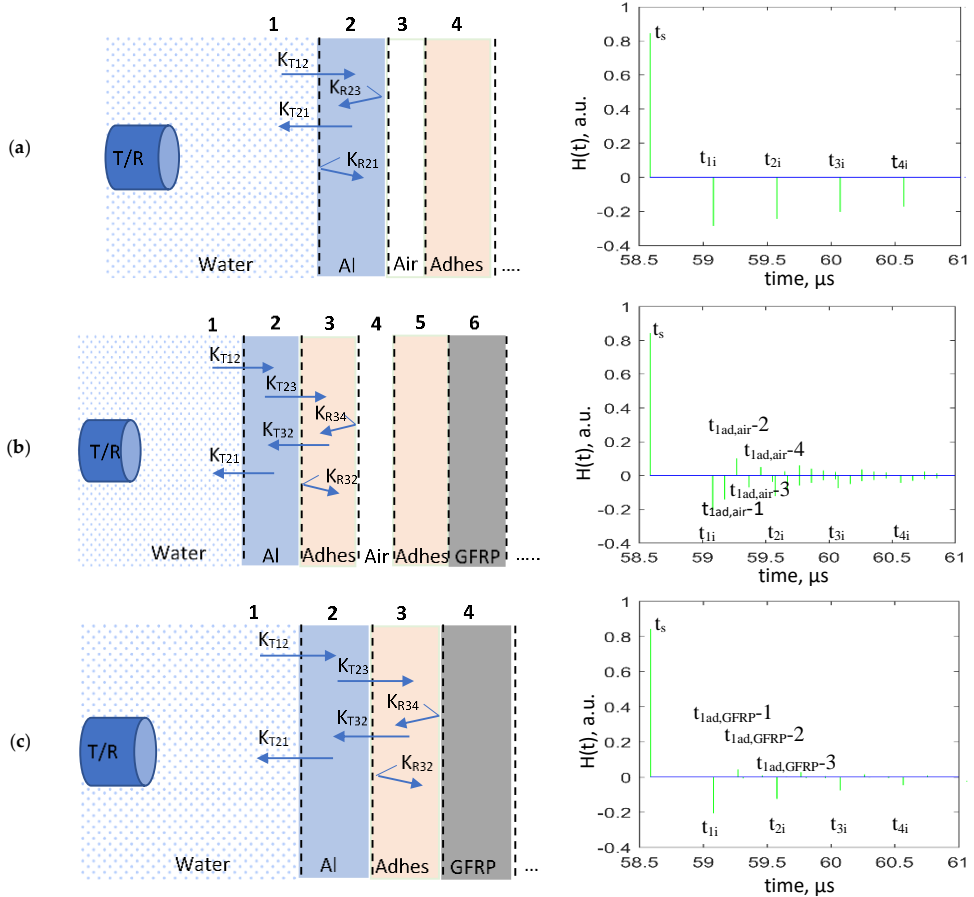

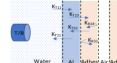



Fig. 2.3 Models of different boundary conditions: (a) debonding at aluminium-adhesive interface, (b) debonding between two adhesive tapes, (c) perfect bonding [9]

Table 2.3. Calculated amplitude values of multiple reflections from different boundary condition of the structure

Amplitude of multiple reflections	Aluminium-disbond	Adhesive-disbond	Adhesive-GFRP
			
	$t_{1i}, t_{2i}, t_{3i}, t_{4i}$	$t_{1ad,air-1}, t_{1ad,air-2}, t_{1ad,air-3}, t_{1ad,air-4}$	$t_{1ad,GFRP-1}, t_{1ad,GFRP-2}, t_{1ad,GFRP-3}, t_{1ad,GFRP-4}$
A_1	-0.2915	-0.1451	0.0468
A_2	-0.2424	0.1020	0.0106
A_3	-0.2016	-0.0717	0.0024
A_4	-0.1676	-0.0504	0.00054

2.1.2. Sensitivity analysis

The NDT technique performance is affected by the parameters which vary due to the environmental and operational conditions. Therefore, in order to assess the reliability of the inspection technique, the relevant influential parameters have to be studied according to the applied NDT technique and the defects to be detected [78].

The goal of this section is to study the influential parameters and to determine whichever of these exert a major impact on the results of the selected inspection technique and its performance. The knowledge of the main parameters affecting the detection of defects in the structure of bonded dissimilar materials can be used at the stage of the post-processing algorithm development, and it gives understanding wherever the focus should be applied during the inspection so that to improve the detectability of disbonds.

In order to achieve the goal, sensitivity analysis was performed by using semi-analytical finite element software *CIVA* with the objective to determine the major influential parameters which have an impact on the detection of disbonds while using the selected techniques. Sensitivity analysis consists of 2 main stages: calibration and meta-model computation. Calibration is required to determine the reference amplitude of the signal which is reflected from the defective interface and has the maximum value of the amplitude. The value of the amplitude is used in the meta-model computation part as the reference amplitude; see [78], [90], [80], [87]. Meta-model computation is a powerful fast calculation engine which provides a set of pre-computed data with the established interpolation functions depending on the calculated values. Thus, the meta-model approach gives access to a large number of results for any combination of parameters at a defined range.

Calibration configuration was discovered in order to obtain the reference amplitude. The model of adhesively bonded aluminium to CFRP was created with the same geometrical parameters as the manufactured sample under investigation whose detailed characteristics are presented in Chapter 3. The number of 41 unidirectional layers, the thicknesses of each of them and the orientation of the laminates corresponds to the sample characteristics. The ultrasonic pulse-echo technique in the immersion mode and a 10MHz focused transducer were applied to the inspection simulation. The parameters of the transducer were set the same as the parameters of the one used in the experimental investigation (Table 2.4). In addition, the signal form of the transducer was created close to the real one from the transducer passport. Modelled signal form of a 10MHz focused transducer is shown in Fig. 2.4. The transducer was mounted at such a distance from the component so that it could focus the ultrasound beam on the interface of the layered structure. The distance between the transducer and the sample surface focusing on the interface is 44.03 mm, which was calculated according to Equation 2.9.

Table 2.4. Parameters of 10MHz focusing transducer

No	Transducer parameters	Value/description
1	Crystal shape	Circular
2	Crystal diameter	9.525 mm
3	Focusing surface type	Spherical
4	Focusing radius	50.8 mm

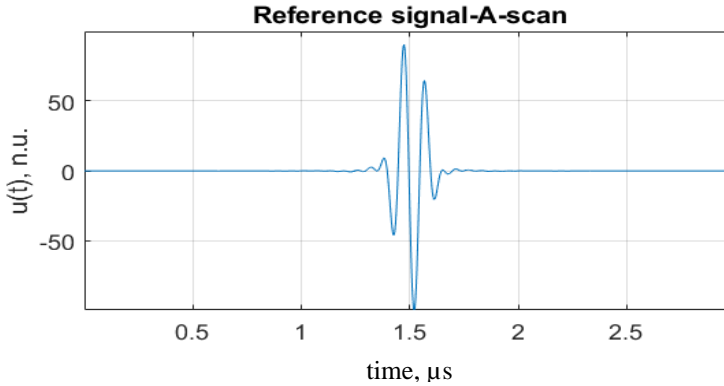


Fig. 2.4 Signal waveform of 10MHz focused transducer

$$W_p = F - M_D \left(\frac{V_{tm}}{V_w} \right); \quad 2.9$$

Here, F is the focal distance, M_D is the depth of the material, V_{tm} is the velocity of ultrasound in the tested material, and V_w is the velocity of ultrasound in water.

A rectangular type defect which characterises the disbond was placed between the aluminium and adhesive layers. A visualisation of the created model for calibration is shown in Fig. 2.5.

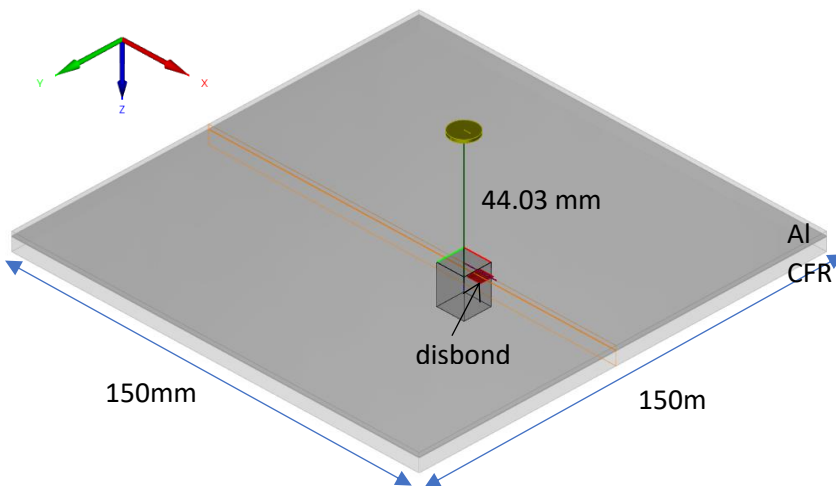


Fig. 2.5 Visualisation of the model configuration for calibration

The interactions of the interface and the defect were taken into account in the computation based on the detection threshold which is dependent on the contrast between the disbond echo amplitude and the interface echo amplitude in the case of a layered structure and the type of the defect under interest. The calibration results of inspection simulation on the rectangular-type defect are shown in Fig. 2.6. The influence of multiple reflections was taken into account as well.

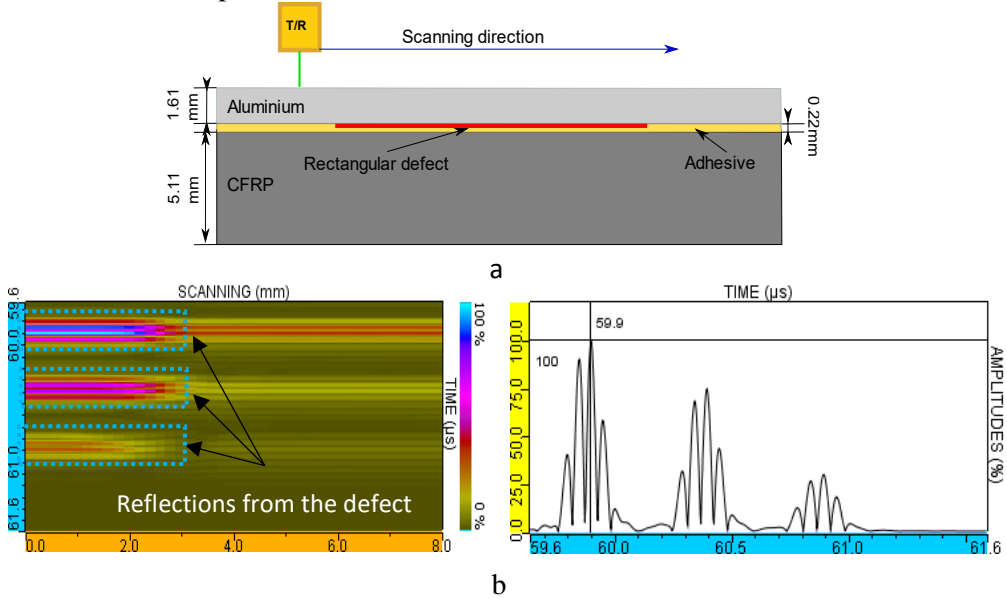


Fig. 2.6 Calibration results of the inspection simulation: (a) Computation set-up, (b) B-scan and A-scan with the identified reference amplitude

The maximum amplitude of 100% of the signal reflected from the defect was used as the reference amplitude for meta-model generation. The meta-model approach provides profound study of the influential parameters. The flowchart of the process of meta-model generation is shown in Fig. 2.7, and it was used in this work.

The analysis of different uncertain parameters was performed according to the selected inspection technique and the sample structure. The parameters with a very slight impact, such as the ultrasound velocity in the adhesive layer, CFRP and water, the transducer position along the x axis and the density of the material(s) compared to other material(s) were excluded from the statistical analysis for time saving purposes in the course of the calculations. The variation ranges of these uncertain parameters were selected according to the modelling results of the ultrasound signal which was passed through the sample interfaces while comparing to the experimentally received results [78]. The final list of the identified parameters is as follows: the longitudinal ultrasound velocity in aluminium, the defect length along the x axis, the defect depth position in the adhesive layer, the ‘water path’ which describes the distance between the transducer and the surface of the object, the thickness of the aluminium adherend and the incidence angle or the angle of the

transducer beam which, also, characterises the possible curvature of the sample. The ultrasound velocity in the aluminium material as well as its thickness are correlated and were taken into account automatically by the software while conducting meta-model generation.

The next important step of the meta-model generation in order to perform the sensitivity analysis of each influential parameter is the assignment of statistical distribution to every parameter which can be normal, uniform, etc., as well as the determination of the variation ranges [78]. The maximum and minimum values of the longitudinal wave velocity, the thickness of the aluminium and the water path between the sample surface and the transducer were identified by statistical analysis, multiple experimental measurements, scientific knowledge, as well as by modelling the signal close to the experimental one and the optimisation of parameters. The standard deviation is calculated according to Equation 2.10.

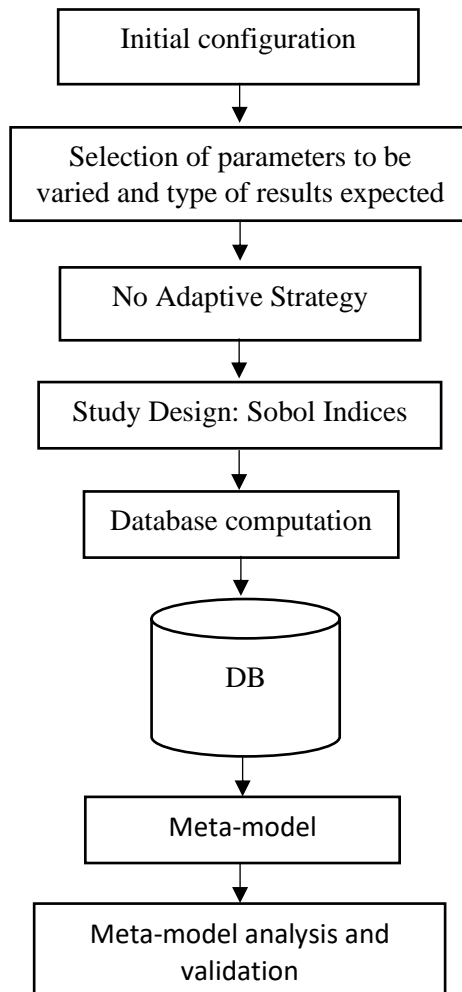


Fig. 2.7 Flowchart of the process of meta-model generation (DB is the Data Base)

$$\sigma = \sqrt{\frac{1}{N-1} \sum_{i=1}^N (x_i - \bar{x})^2}; \quad 2.10$$

Here, x_i is the measured value, \bar{x} is the mean value, N is the number of measurements.

The variation range of the incidence angle was determined by the numerical evaluations of the ultrasonic wave propagation through the sample interfaces by adjusting the transducer position at a different angle (Fig. 2.8). In the case of the defect depth uncertain parameter, the variation range is limited by the thickness of the adhesive layer. The range for the defect dimension depends on the analysis of the beam spot size. The focal spot size and the focusing length are shown in Fig. 2.9.

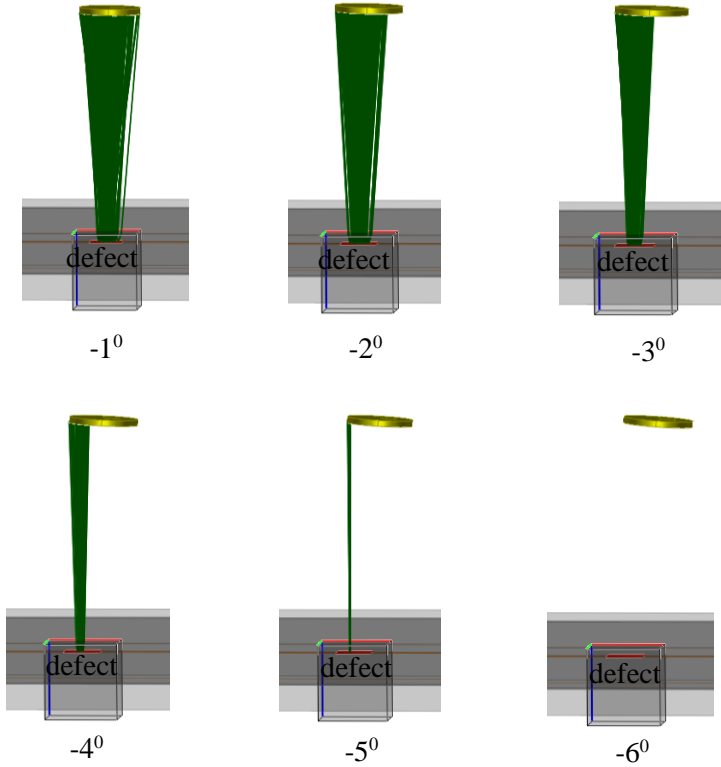


Fig. 2.8 Beam of rays reflected from the defect and received by transducer at a different angle of incidence

The beam spot's size of the transducer is 1x1mm at the -6dB threshold. When the defect gets larger than the beam, there will not be much variability of the disbond response since the flaw will not reflect more energy. Uncertain parameters with defined variation ranges and distribution laws are presented in Table 2.5.

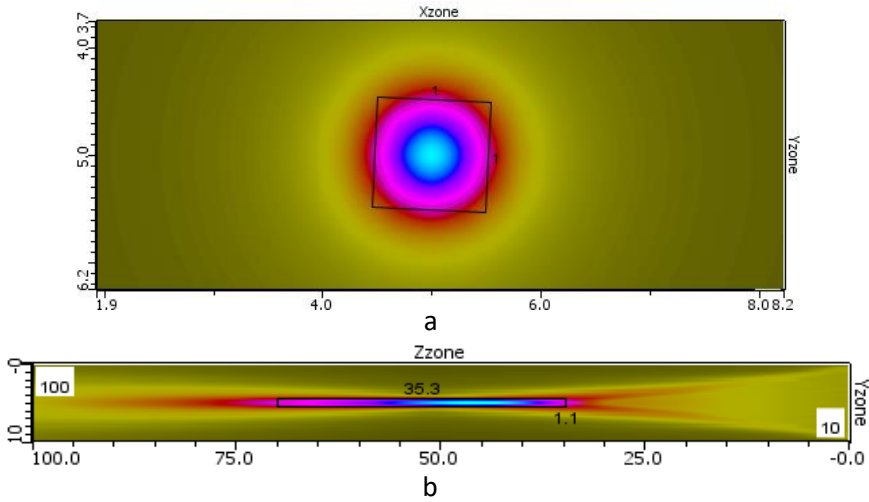


Fig. 2.9 Analysis of beam spot size: (a) Focal spot size at -6dB level, (b) Focusing length

Table 2.5. Variation ranges and distribution laws of uncertain parameters

Parameters	Mean value	Variation range	Statistical distribution law
Longitudinal velocity of ultrasound in aluminium	6 363 m/s	[6 313 m/s; 6 500 m/s]	Normal
Defect length along the x axis	2.625 mm	[0.25 mm; 5 mm]	Constant/ Characteristic value
Defect depth position in adhesive	1.72 mm	[1.61 mm; 1.82 mm]	Uniform
Water path between sample surface and transducer	44.03 mm	[43.5 mm; 44.03 mm]	Uniform
Thickness of aluminium	1.61 mm	[1.60 mm; 1.61 mm]	Normal
Incidence angle	0°	$[-6^\circ; 0^\circ]$	Uniform

The ‘No Adaptive’ strategy was used with the fixed number of cases to compute the meta-model in order to save on the time of calculations. The statistical method of Sobol indices was applied, and the Kriging interpolator was selected. Sobol indices characterise the portion of variance which is associated to each or to a subset of the input parameters. In addition, when selecting the Kriging interpolator, the relative error decreases. In order to build a consistent meta-model, 768 cases of simulation were performed. The parallel plot which represents the calculated simulations for our meta-model generation is shown in Fig. 2.10. The reliability of the meta-model is analysed from the computed simulations (‘true’) and the meta-model’s value (‘predicted’) regression and error distribution graphs (Fig. 2.11). As a result, there is about 0.02% of relative error in nearly 76% of cases.

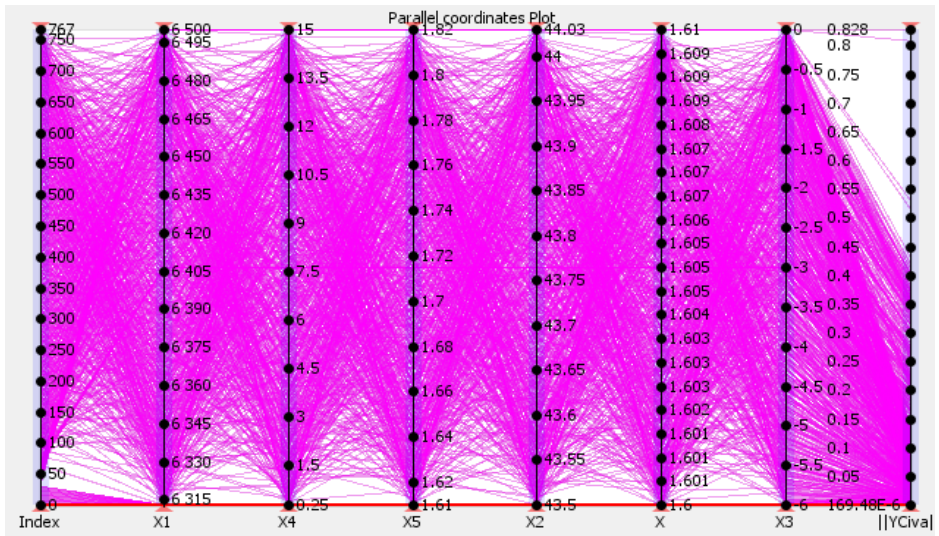


Fig. 2.10 Parallel plot of calculated simulations

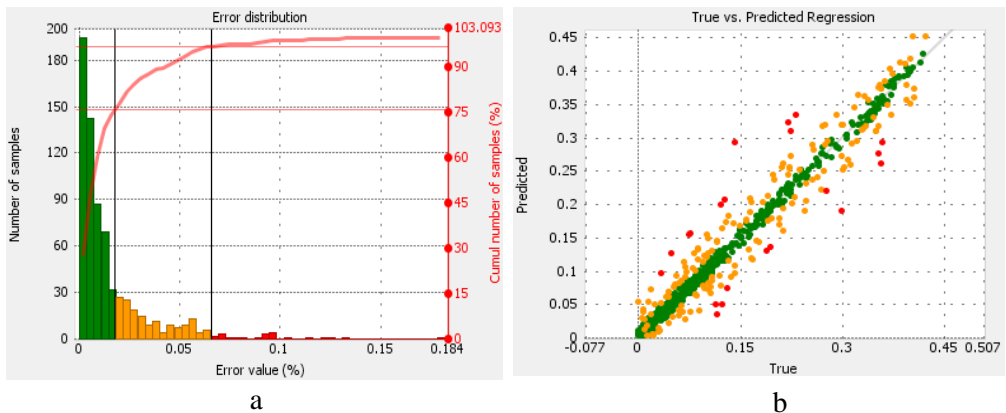


Fig. 2.11 Error distribution and ‘true’ vs. ‘predicted’ regression

In Table 2.6, the values of sensitivity and the proportion of impact of each uncertain parameter are presented. The Sobol indices diagram is shown in Fig. 2.12. The diagram of sensitivity analysis demonstrates that there are two critical uncertain parameters which mostly influence the results of the ultrasonic inspection: the water path between the transducer and the component surface, and the incidence angle of the transducer. The defect depth position has an impact on the result as well. However, comparing to the water path and the incidence, the influence of defect depth position is much less prominent. The uncertain parameters, such as the longitudinal velocity of the ultrasound, and the thickness of the aluminium layer, have insignificant influence on the detectability of disbonds in layered structures. Such uncertain parameters as the water path and the incidence angle of the

transducer are related to the set-up of inspection. In addition, the water path and the transducer incidence angle depend on the surface curvature. In the case of changing the angle of the beam rays, the time of flight of ultrasonic waves changes as well. Since the factor of the incidence angle and the water path exert significant impact on the results of inspection, the attention should mainly be paid to the adjustment of the experiment or to the development of a certain technique for the inspection. As a result, the alignment of the signals reflected from the curved surface of the sample and arriving at the transducer plays a significant role in the detection of disbonds. The alignment of the signals according to their arrival time can eliminate the curvature impact and increase the probability of defect detection.

Table 2.6. Values of sensitivity and proportion of impact of each uncertain parameter

Uncertain parameters	Sensitivity, Sobol indices	Proportion value, %
Longitudinal wave velocity	0.04	0.03
Defect depth	3.53	2.95
Water path	46.90	39.18
Thickness of aluminium	0.03	0.02
Incidence angle	69.21	57.82

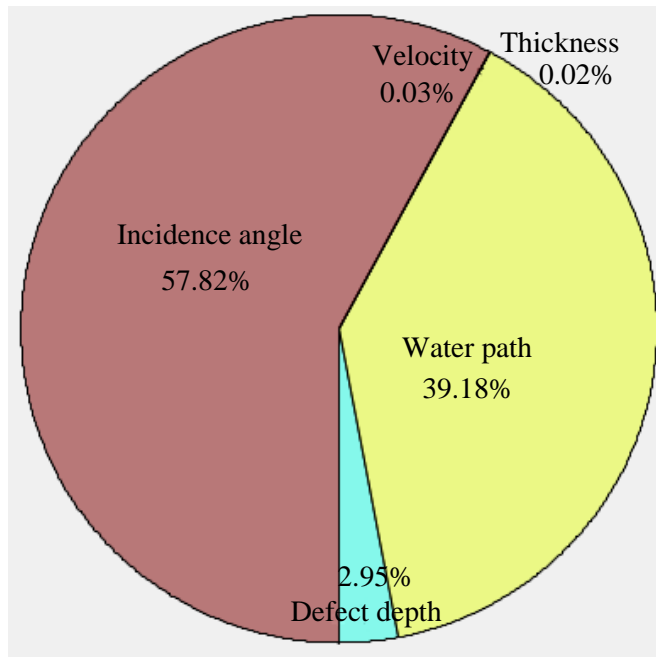


Fig. 2.12 Sobol indices diagram of sensitivity analysis

2.1.3. Ultrasonic inspection simulations

The goal of this section is to perform simulations of ultrasonic inspections of dissimilar material joints in order to study the behaviour of ultrasound propagation through the layers of bonded dissimilar materials, to select the side of the sample for the inspection, to obtain the resulting A and B-scans, to evaluate the amplitude values of the signals reflected from the defective and non-defective areas, as well as to compare the results for the further determination of the possible techniques which can potentially be valuable for the improvement of the probability of disbond detection. In addition, numerical evaluation allows studying the performance of the selected technique. In order to achieve the goal, the *CIVA* software which was developed by *CEA* (the French *Atomic Energy Commission*) was used for all simulations. The ultrasonic pulse-echo technique in the immersion mode as well as the focusing transducers were selected for the investigation of dissimilar materials.

The ultrasonic inspection from the metal side seems to be more appropriate since the composite is a more attenuating material which absorbs ultrasonic waves more quickly. There is, also, the scattering of the waves in the composite due to the different orientation of laminates. However, the most suitable side for the inspection of the samples was studied and attested by using quantitative evaluations. For the inspection simulation, the joints of adhesively bonded aluminium to CFRP, and steel to CFRP were modelled. Furthermore, the appropriate frequency range of the transducer has to be selected for each sample under investigation in order to create a high performance NDT method. In order to achieve this goal, the wavelength of the ultrasound was calculated. The calculated values of the wavelength in each material are presented in Table 2.7 for the focusing transducers as follows: 2.25MHz, 10MHz, 25MHz.

$$\lambda = \frac{V_m}{f}; \quad 2.11$$

Here, V_m is the ultrasound velocity in a material, f is the frequency of a transducer.

Table 2.7. Calculated values of wavelength in materials of layered structures

Sample	Material	Velocity, m/s	Wavelength, λ , mm			
			2.25 MHz	5 MHz	10 MHz	25 MHz
Al-CFRP	Aluminium	6 363	2.83	1.27	0.64	0.25
	CFRP	2 800	1.24	0.56	0.28	0.11
	Adhesive	2 315	1.03	0.46	0.23	0.09
Steel-CFRP	Steel	5 985	2.66	1.20	0.60	0.24
	CFRP	3 100	1.38	0.62	0.31	0.12

According to the results of the wavelength and by considering the thicknesses of the materials, the frequency range for the aluminium-CFRP sample has to be equal to or higher than 10 MHz. The frequency of 10 MHz was selected for

inspection simulations with the further use in experimental investigations. In the case of joints of steel-CFRP, the appropriate frequency range is 5–10 MHz. This frequency range enables to inspect dissimilar material joints while avoiding attenuation in materials. However, a higher frequency will provide a better detection probability, but such measurements are more expensive. Therefore, the 10 MHz frequency was selected in order to consider the lowest limit that can be used for such components as well as to avoid expensive measurement techniques, such as acoustic microscopy in our pursuit to make the method available for broad use in the industry. The increase of the frequency range up to 75 MHz is possible in order to receive ultrasonic waves reflected from the adhesive interface in the case of inspection from the metal side. Since the metal and adhesive layers are fairly thin and the attenuation in these materials does not exceed the limit, therefore, such high frequencies can be applied.

In order to achieve the goals of this section, inspection configurations were built in a semi-analytical finite element. In addition, three different options of the disbond depth location in the adhesive layer were modelled in order to study and compare the influence of the defect position on the detectability in the structure of bonded aluminium-CFRP. The smallest size of the defect of 5x5 mm was selected for the inspection. Moreover, according to the manufacturing report, the disbonds were placed between two adhesive tapes. Since the manufacturing conditions are not ‘ideal’, the position of each defect in the adhesive layer can differ. The location of defects in the modelled adhesive layer is shown in Fig. 2.13. A focusing transducer of 10MHz with the same parameters and the signal waveform as presented in Table 2.4 and Fig. 2.4 was defined in the inspection configuration. As determined by Equation 2.9, the focusing length is 44.03 mm between the transducer and the aluminium surface, and 41.30 mm between the transducer and the CFRP surface.

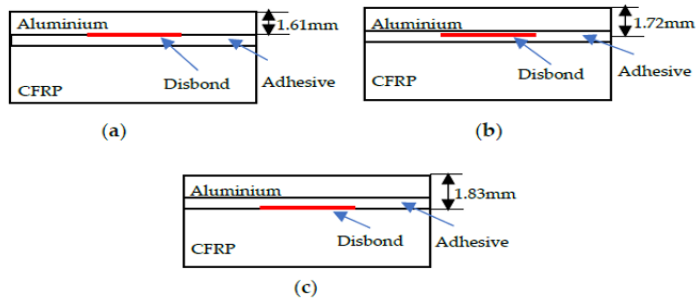


Fig. 2.13 Disbond location in the adhesive layer of aluminium-CFRP joint: (a) top interface (between aluminium and adhesive), (b) middle interface (in the middle of the adhesive layer), (c) bottom interface (between adhesive and CFRP)

In order to ensure that the modelling results are close to the experimental ones, the measured values of ultrasound velocities and the attenuation in materials of the sample were taken into account. Since attenuation is frequency dependent, the power attenuation law was used to define attenuation in aluminium according to [102], [103], [104]:

$$\alpha(f) = \alpha_0 \times \left(\frac{f}{f_0}\right)^p ; \quad 2.12$$

Here, $\alpha_0 = -\frac{20}{x} \log\left(\frac{A_x}{A_0}\right)$ is the attenuation coefficient measured at frequency f_0 . A_0 is the initial amplitude of the wave, A_x is the amplitude of the wave at distance x , p is the power of the dependency on frequency f .

The attenuation coefficient was determined by measuring the amplitude decrease of the signal reflections along the path of wave propagation. The amplitude of signal reflections in the aluminium layer was measured experimentally at 15 MHz frequency. As a result, it was determined that the signal attenuation in aluminium is 0.3 dB/mm at $f=10$ MHz. In the case of CFRP, the attenuation was set according to the stiffness matrix of the elastic properties of a material. The set-ups of the inspection configurations are shown in Fig. 2.14.

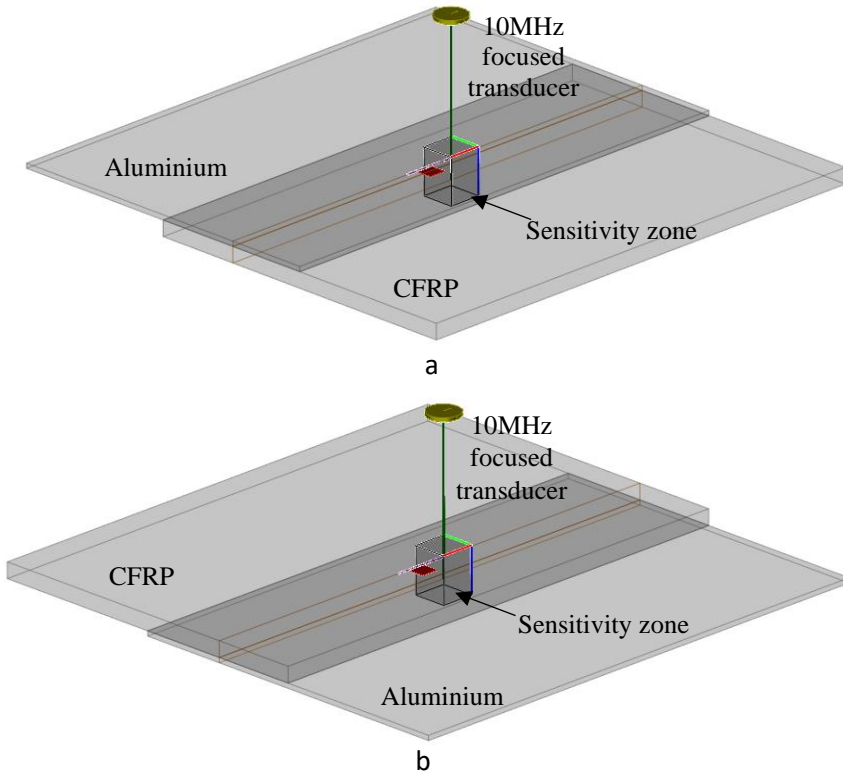


Fig. 2.14 Set-up of inspection configurations for aluminium-CFRP joint: (a) inspection from the aluminium side, (b) inspection from the CFRP side

The resulting A- and B-scans of multiple reflections from the structure in the case of the disbond location between aluminium and adhesive, in the middle of the adhesive, and between adhesive and CFRP are shown in Fig. 2.15 and Fig. 2.16, respectively, for the metal and composite side inspections.

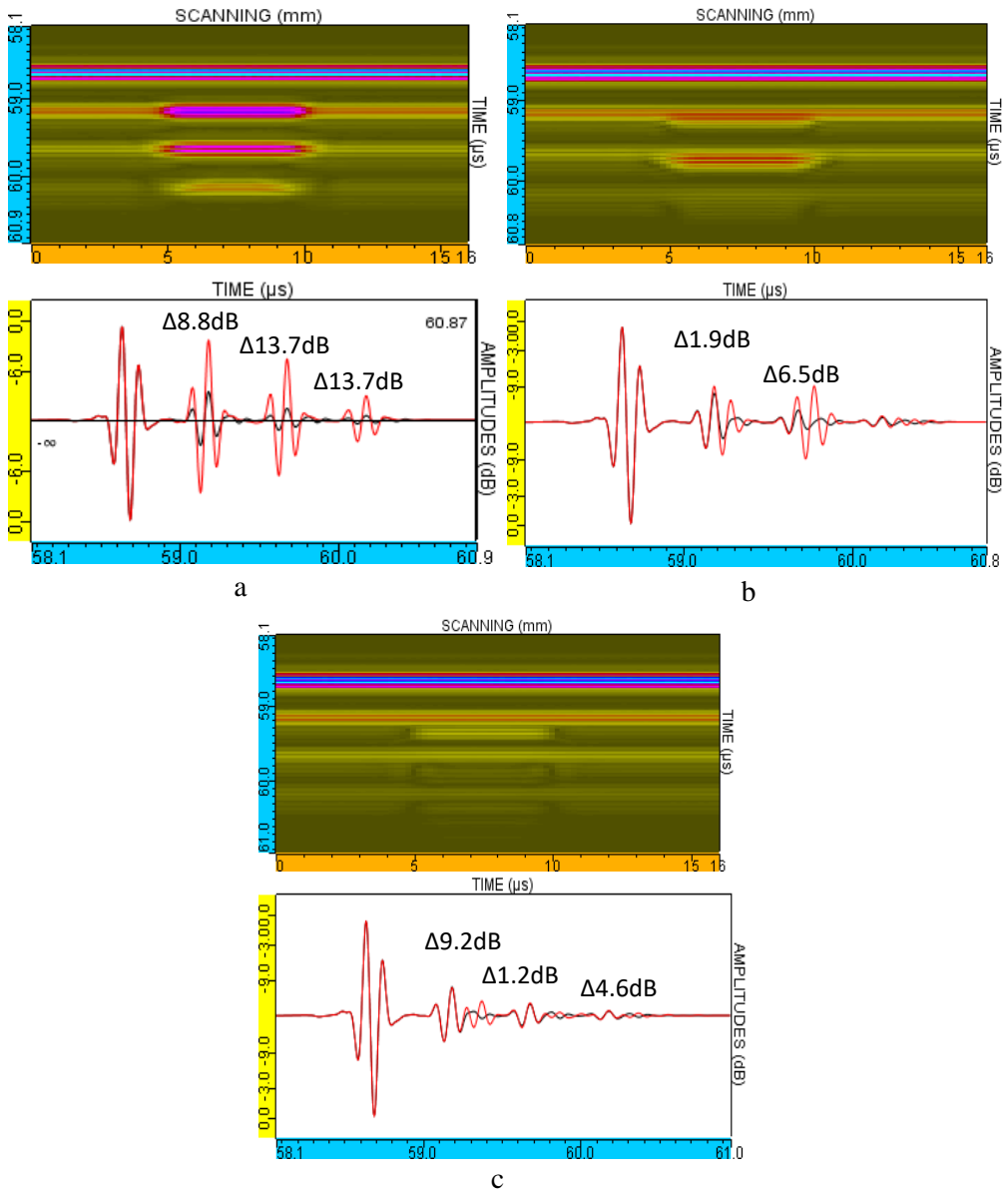


Fig. 2.15 A- and B-scans of inspection simulation from the metal side in the case of different depth location of disbond in adhesive (the red colour line is the reflection from the defect, the black line comes from the non-defective interface): (a) disbond location between aluminium and adhesive, (b) disbond location in the middle of adhesive, (c) disbond location between adhesive and CFRP

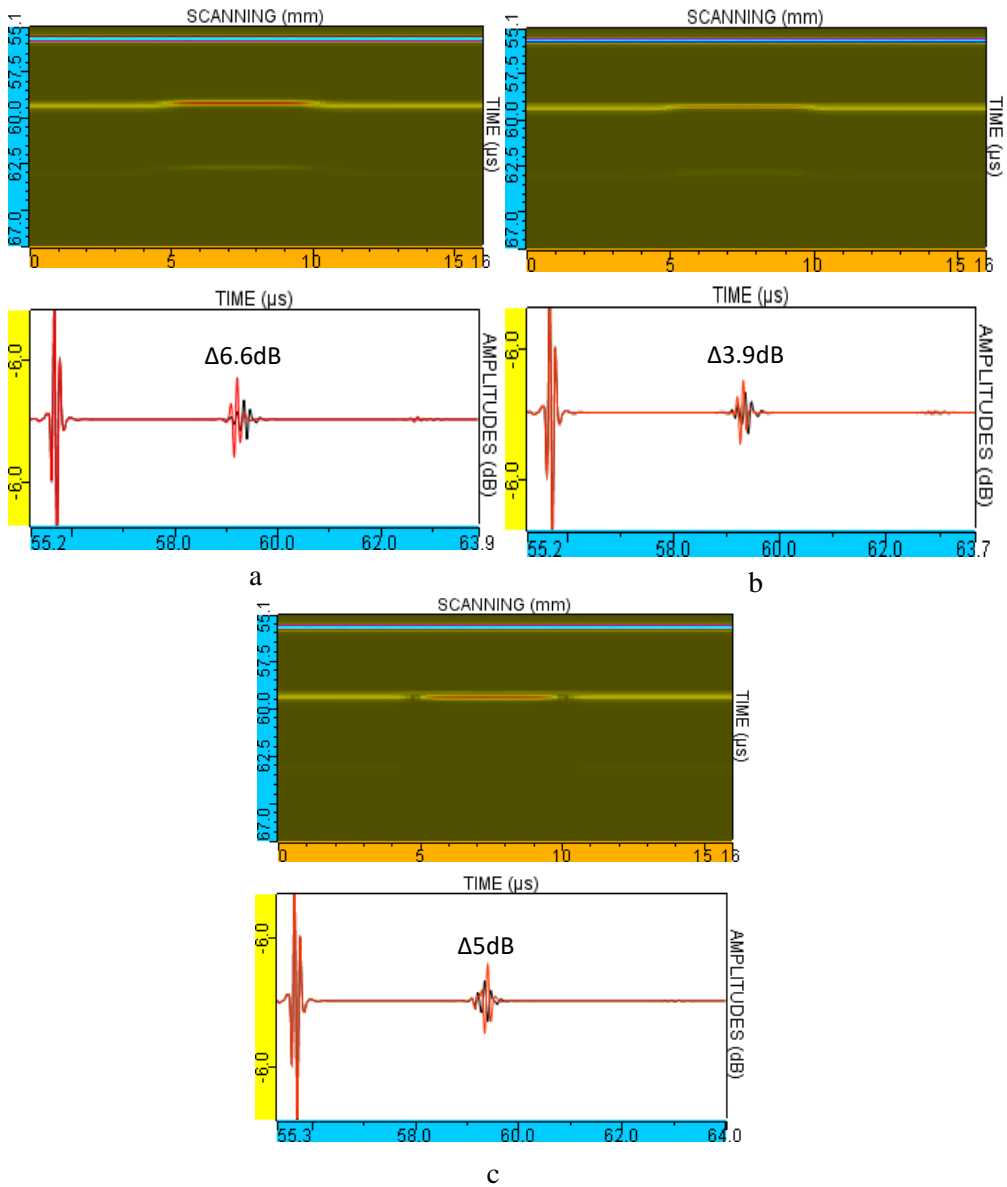


Fig. 2.16 A- and B-scans of inspection simulation from the composite side in the case of different depth location of disbond in adhesive (the red colour line is the reflection from the defect, the black line comes from the non-defective interface): (a) disbond location between aluminium and adhesive, (b) disbond location in the middle of adhesive, (c) disbond location between adhesive and CFRP

From the resulting A- and B-scans, it can be seen that it is hard to detect disbonds at adhesive interfaces, and also to detect delamination which can occur inside the adhesive. The amplitude of the reflection from the interface without a

defect is still relatively high since metal-adhesive joints involve dissimilar materials which are denoted by different acoustic impedances. In addition, the inspection simulation was performed for the perfect condition of the inspection, method, and object without considering any influencing factors. It was also found that the probability of disbond detection decreases when the defect is located deeper in the adhesive layer. In the case of the defect location in the middle of the adhesive layer or at the adhesive-composite interface, the overlapping of the signals reflected from aluminium and adhesive, the defect, and adhesive and composite is observed. This fact, which is caused by the relatively thin adhesive layer, and by the attenuation in epoxy, also affects the disbond and delamination detectability. The overlapping effect and attenuation depends on the frequency selected for the inspection, the adhesive thickness, and the defect depth location in the adhesive. This means that, in the case of the perfect bonding, the overlapping of signals reflected from metal-adhesive, and adhesive-composite, is also applicable. However, in the case of the disbond location on the metal-adhesive interface, the disband can be detected best among other options of the defect position in the adhesive layer. Despite this, the problem of dissimilar materials still persists. In the experimental part of this research, the deeper position of the defect in the adhesive layer (in the middle of the adhesive) was the focus in order to investigate a more complicated situation. The most complicated situation of the detection of a defect located at the adhesive-composite (opposite) interface was not investigated experimentally due to the absence of such a sample. Furthermore, the resulting A- and B-scans of the inspection simulations show that the analysis of multiple reflections gives valuable information of the presence of a defect. Due to multi-reflections, the presence and the position of a disbond can be determined. When comparing the difference of the amplitude of the signals multiply reflected from the defective (the red colour signal on A-scans) and non-defective (the black colour signal on A-scans) areas, it was observed that the value of the amplitude difference increases with each subsequent multiple reflection. As a result of the data obtained from inspection simulations, the most promising assessment of disbond detection in dissimilar material joints has to be based on the analysis of multiple reflections from the interface of the structure and used for the development of the algorithm to increase the detection probability. What concerns the inspection side selection, it was determined from Fig. 2.16 that probability of detection of a disbond from composite side is smaller than in the case of the inspection from the aluminium side, and, also, because of the high attenuation in the composite material, the analysis of multiple reflections is not applicable. Therefore, the inspection from the metal side was selected as the more appropriate option.

In order to confirm the effectiveness of the analysis of multi-reflections, a steel-CFRP structure was investigated as well. The immersion ultrasonic pulse-echo method and a 10MHz focused transducer were used for the inspection simulations. The set-up of the inspection simulation from the metal side for the steel-CFRP sample is shown in Fig. 2.17. The disbond is located between steel and the adhesive

layer. The resulting A-scans of the comparison of multiple reflections from the defective and non-defective areas are shown in Fig. 2.18.

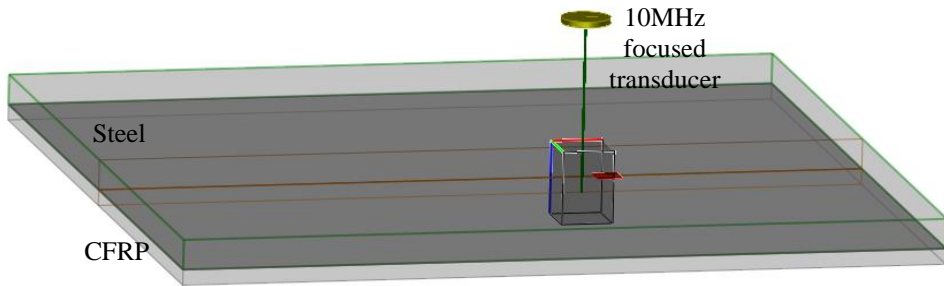


Fig. 2.17 Set-up of inspection simulation of steel-CFRP sample of dissimilar material joints when using the immersion pulse-echo method and 10MHz focused transducer

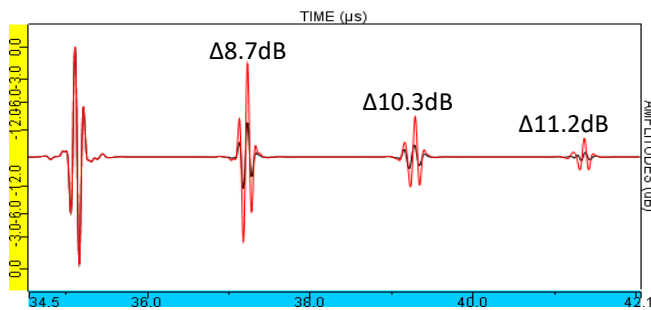


Fig. 2.18 A-scan comparison of reflections from defective and not defective areas of samples of steel-CFRP joints (the red colour line is reflection from the defect, the black colour line comes from non-defective interface)

When investigating the effect of the analysis of multiple reflections on the detectability of the disbond type defects, this strategy was also proven to be applicable in the case of steel-CFRP reflections. As a result, the detectability of disbands increases with the analysis of multi-reflections. The obtained results of inspection simulations were used for the development of a post-processing algorithm so that to improve disbond detectability of the ultrasonic NDT technique.

2.1.4. Signal modelling in layered structure and optimisation of parameters

The goal of this section is to determine the time instances of the signal where the maximum amplitude change is observed in the case of the presence of a disbond in the structure. In order to achieve this goal, signals reflected from the perfect bonding and from the defective interface were modelled in a custom-developed program in *MatLab*. In addition, the analysis of the modelled signals allows studying the signal propagation through the layers of the structure, the form of the signals reflected from the sample surfaces and interfaces, and also to study the impact of the thin adhesive layer on the signal reflection waveform as well as the influence of the reverberation which was observed in the experimentally obtained signal. The main idea is to create signals as close as possible to the signals which are received

experimentally. For this case, the reference signal was used. The flat aluminium block was used to record the signal reflected from the sample surface. The measurement was performed in a tank of water by using the ultrasonic pulse-echo technique and a 10 MHz focused transducer. The reference signal used for the modelling is shown in Fig. 2.19.

Additionally, the optimisation of the model parameters was required in order to achieve the best fit of the experimental and modelled signals. The following parameters were optimised manually in the program so that to provide the best match: the ultrasound velocity in the materials of the structure, the thickness values of the layers, and the densities of the materials. The time of flight for each signal reflection from the boundaries as well as the acoustic impedances and the reflection and transmission coefficients were calculated according to Equations 2.2–2.6 in the program. The results of the values of parameters after optimisation are presented in Table 2.8.

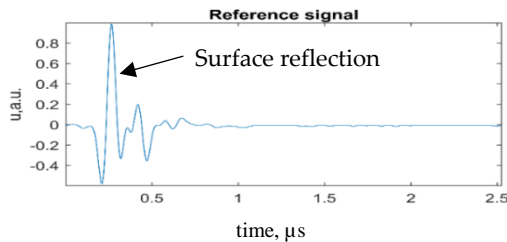


Fig. 2.19 A-scan of the reference signal of 10MHz focused transducer

Table 2.8. Optimised parameters of a modelled structure and ultrasound to achieve the match between the modelled and experimental signal

Type of material	Thickness, mm	Density, kg/m ³	Ultrasound velocity, m/s
Water	43.5	997.98	1 485
Aluminium	1.61	2 710	6 500
Adhesive	0.22	1 270	2 315
Glass prepreg	0.06	1 900	3 000
CFRP	4.99	1 800	2 800
Air	10	1.225	330

In order to determine the time instances where the most significant amplitude change is observed, the signals reflected from the defective and non-defective interfaces have to be compared. Therefore, the models of perfect bonding (aluminium-adhesive-composite) and delamination in the middle of the adhesive layer (aluminium-adhesive-defect) were created, and signals $u(t)$ were modelled according to the following Equation [9]:

$$u(t) = y_{ref}(t) \otimes h(t); \quad 2.13$$

Here, y_{ref} is the reference signal recorder experimentally using the reference block, $h(t)$ is the pulse response calculated theoretically in the sample of a layered structure.

The plots of pulse responses and the A-scans of the modelled signals for the cases of perfect bonding and delamination in the adhesive with the identified time instances for surface reflections and multi-reflection from the interface of the sample are shown in Fig. 2.20 and Fig. 2.21. The time instances of each reflection from the sample structure were described and presented in Table 2.9 and Table 2.10.

As a result, it can be observed from the modelled signal that the detection of disbands in dissimilar material joints is a fairly complicated task. The reverberation which is present on the generation signal has an impact on the whole signal, and, therefore, it can hide the useful information of the presence of the disbond. In addition, due to the thin layers of the structure, especially in the case of the adhesive where the disbond is located, the effect of overlapping was observed. This fact complicates the detectability as well. However, the time instances of each reflection and the multi-reflections of the layered structure were identified for the further use in the development of post-processing algorithms.

Table 2.9. Description continuation of the indices of time instances

Reflection from boundary	Description
$t_{1adh,GFRP-1}$	1 st reflection from adhesive- GFRP sub-layer boundary
$t_{1adh,GFRP-2}$	2 nd reflection from adhesive- GFRP sub-layer boundary
$t_{1GFRP,CFRP}$	Reflection from GFRP sub-layer-CFRP boundary after t_{1i}
$t_{1adh,GFRP-3}$	3 rd reflection from adhesive- GFRP sub-layer boundary
$t_{1adh,air-1}$	1 st reflection from metal-defect boundary
$t_{1adh,air-2}$	2 nd reflection from metal-defect boundary
$t_{1adh,air-3}$	3 rd reflection from metal-defect boundary
$t_{1adh,air-4}$	4 th reflection from metal-defect boundary
$t_{1adh,air-5}$	5 th reflection from metal-defect boundary t_{3i}

Table 2.10. Time instances of the signal reflected from defective and non-defective sample

Aluminium-adhesive-composite (perfect bonding)		Aluminium-adhesive-defect (delamination)	
Reflection from certain boundary	Time of flight, μs	Reflection from certain boundary	Time of flight, μs
t_s	58.59	t_s	58.59
t_{1i}	59.08	t_{1i}	59.08
$t_{1adh,GFRP-1}$	59.27	$t_{1adh,air-1}$	59.18
$t_{1adh,GFRP-2}$	59.46	$t_{1adh,air-2}$	59.27
$t_{1GFRP,CFRP}$	59.31	$t_{1adh,air-3}$	59.37
$t_{1adh,GFRP-3}$	59.65	$t_{1adh,air-4}$	59.46
t_{2i}	59.58	$t_{1adh,air-5}$	59.56
t_{3i}	60.07	t_{2i}	59.58
t_{4i}	60.57	t_{3i}	60.07
		t_{4i}	60.57

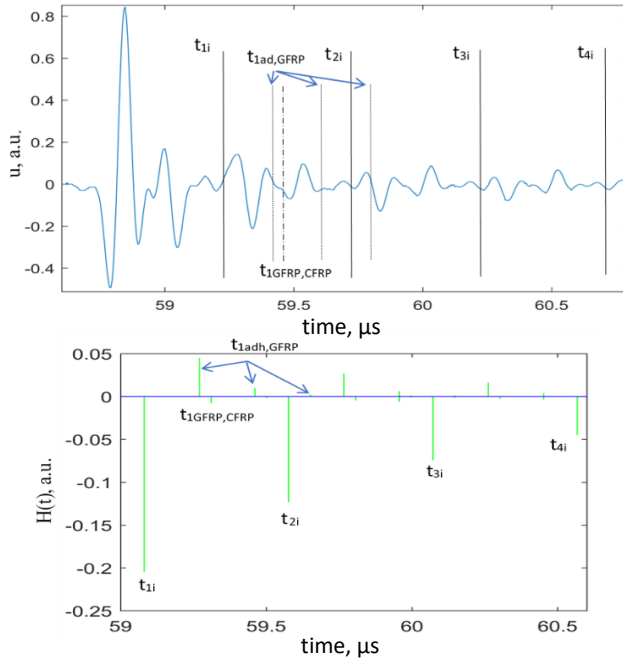


Fig.2.20 A-scan and plot of pulse responses for the signal reflected from a non-defective layered structure (aluminium-adhesive-composite)

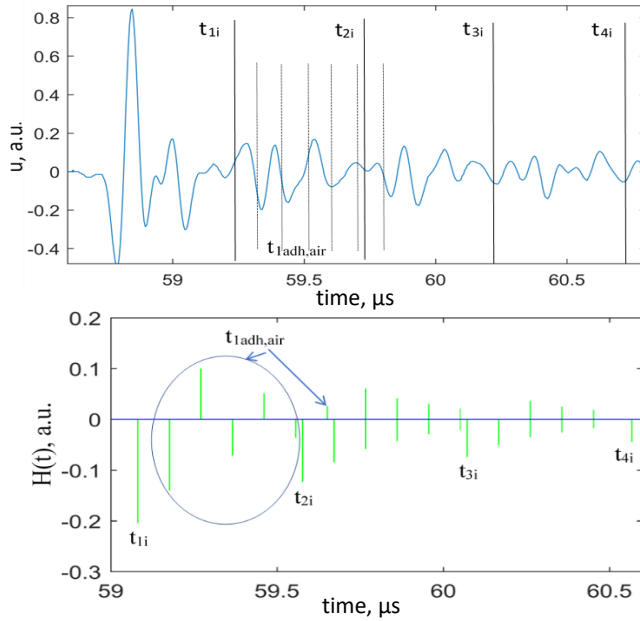


Fig.2.21 A-scan and plot of pulse responses for the signal reflected from a defective layered structure (aluminium-adhesive-defect) where air characterises the defect

2.2. Development of the post-processing algorithm to increase detectability

The developed post-processing algorithms can significantly improve the performance of the NDT technique; therefore, the focusing of attention towards the development of algorithms was applied in this work. The goal of this section is to develop a method to increase the detectability of disbonds in dissimilar material joints based on the results received from the theoretical calculations, the investigation of various samples of dissimilar materials, the modelling results and inspection simulations while taking into account all the possible limitations and influencing factors on the inspection technique and the expected results.

Usually, the objects which need to be inspected are not ideally flat. In addition, there are, always, some misalignments during the scanning process. These facts have an impact on the determination of the time gates of reflections from the layered structures. Therefore, the detection of disbonds in such objects and the inspection in general can be more complicated. The sample which was investigated in this work – adhesively bonded aluminium and CFRP – is not perfectly flat, either. The sample is curved along both axes x and y . An advanced post-processing algorithm was developed in order to increase the detectability of disbonds in adhesively bonded dissimilar materials and to overcome the main reasons affecting the probability of defect detection. According to the investigation of dissimilar joints in the previous sections, there are the following main reasons which affect the detectability of disbonds: the considerable difference of acoustic impedances of dissimilar materials, which leads to a relatively high value of the signal reflected from the defect-free interface region, the relatively small thicknesses of the structure layers, especially wherever it concerns the adhesive layer where the disbonds appear, the overlapping of signal reflections from different boundaries, the disbond depth location in the adhesive layer, imperfectly flat surfaces or interfaces of the structures, signal reverberations and the noise, attenuation in materials as well as other influential factors. The following main steps were performed in order to develop the post-processing algorithm:

1. Collection of the output data after the experimental inspection.
2. Filtering of the signal with a filter selected in such a way as not to lose the important signal information.
3. Determination of the time instance (moment) and its gate adjustment at the signal reflected from the object's surface.
4. Determination of the time gates of the multiple reflections from the sample interface where the maximum amplitude change is observed.
5. Assessment of the peak-to-peak amplitudes in time intervals of multiple reflections.
6. Calculation of the ratio of the obtained peak-to-peak amplitudes for multiple reflections.

The functional block of the proposed algorithm which describes the main steps is shown in Fig. 2.22.

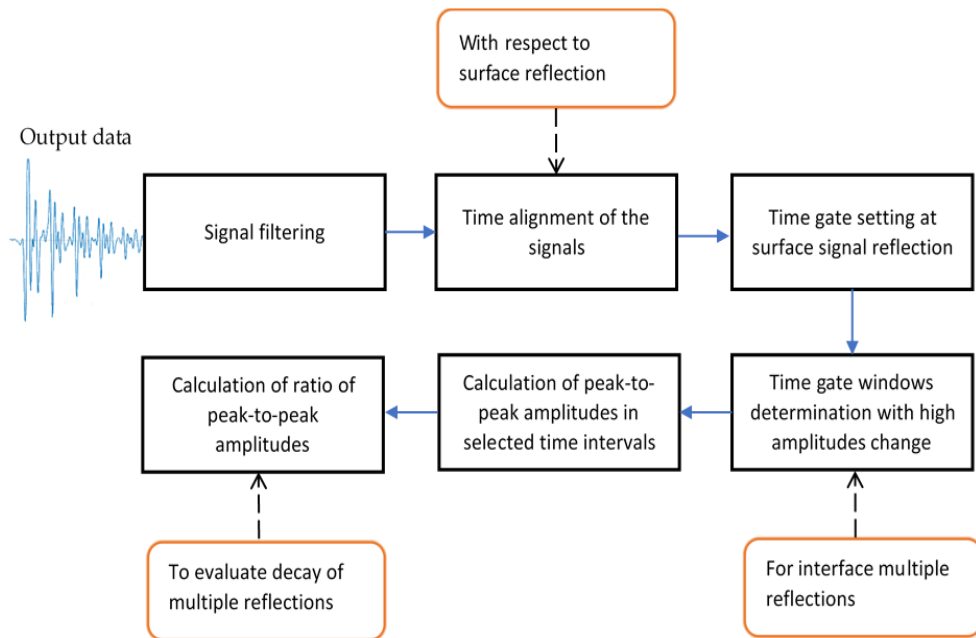


Fig. 2.22 Functional block diagram of the proposed algorithm for the improvement of detectability [9]

In order to obtain the best value of the signal-to-noise ratio, the signal output has to be filtered. To achieve this goal, the employment of various filters can be used [105], [106]. However, the band-pass filter was selected and used in this work. The spectrum of the filtered and unfiltered signal with the selected filter characteristic as well as the A-scan comparison of the filtered and unfiltered signals is shown in Fig. 2.23.

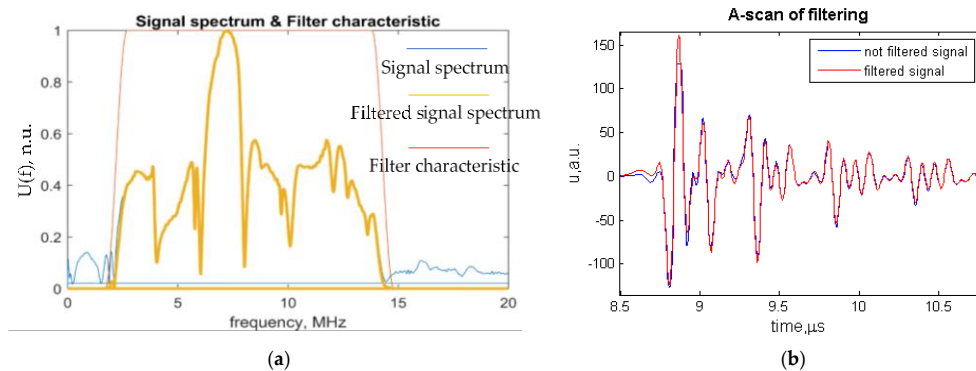


Fig. 2.23 Signal denoising when using band-pass filter: (a) Signal spectrum with filter characteristic, (b) A-scan comparison of filtered and unfiltered signals [9]

The steps of the filtering process are as follows:

1. Firstly, the measurement of the frequency spectra of the signal was performed.

$$U(f) = \text{FT}[u(t)]; \quad 2.14$$

Here, FT is the Fourier transform.

2. Filtering of the frequency spectrum by using the band-pass filter.

$$U_F(f) = U(f) \cdot H(f); \quad 2.15$$

Here, $H(f)$ is the transfer function of the filter.

3. Reconstruction of the signal filtered by using the inverse Fourier transform.

$$u_F(t) = \text{Re}(\text{FT}^{-1}[U_F(f)]); \quad 2.16$$

Here, Re is the real part, and FT^{-1} is the inverse Fourier transform.

The calculation of the filter characteristic was performed according to Equation 2.18 [9].

$$H(f) = \begin{cases} 1, & f_1 + \frac{\Delta f}{2} \leq f \leq f_2 - \frac{\Delta f}{2} \\ \sin\left(\frac{(f - f_1) \cdot \pi}{2 \cdot \Delta f}\right) + 0,5, & f_1 - \frac{\Delta f}{2} < f < f_1 + \frac{\Delta f}{2}; \\ \sin\left(\frac{(f_2 - f) \cdot \pi}{2 \cdot \Delta f}\right) + 0,5, & f_2 - \frac{\Delta f}{2} < f < f_2 + \frac{\Delta f}{2} \\ 0, & \text{in other cases} \end{cases} \quad 2.17$$

Here, f is the frequency, f_1 is the lower cut-off frequency which is 2.2MHz, f_2 is the upper cut-off frequency which is 14.3MHz, Δf is the width of the filter function fronts.

The next step is the alignment of the arrival time of the signals reflected from the object's surface which was conducted as follows:

1. The threshold was set for the object surface reflections. Next, the arrival time instances of each signal reflected from the surface at a set threshold U_{th} were determined [9].

$$t_{n_1,k} = \min\{\arg[u_k(t_{n_1}) > U_{th}]\}; \quad 2.18$$

Here, $u_k(t_{n_1})$ is a digitised signal where $k =$ from 1 to K , K is the states for the number of the recorded signals reflected from the surface, and t_{n_1} is the time instance of the first sample which exceeds U_{th} .

2. The time moments of the first signal's transition through the zero-crossing point exceeding t_{n_1} were determined [9].

$$t_{0,k} = \min\{\arg[u_k(t_n) = 0]\}; \quad 2.19$$

Here, all the time moments are $t_n > t_{n_1}$, and $u_k(t_n)$ represents all the digitised signals reflected with the time moments t_n greater than t_{n_1} .

The time alignment of all the signals was performed by shifting the signal (Equation 2.21) according to the determined time intervals [9].

$$u'_k(t_n) = u_k(t_n + t_{0,k}); \quad 2.20$$

The zero-crossing technique for the time alignment of each signal's reflections from the object surface was used in this work. The detailed description is presented in the article of Mazeika *et al.* [107] where the analysis of the technique was performed. As a result, all the signals were aligned, and the impact of the object's curvature and the imperfect scanning process was eliminated.

The next step of the post-processing algorithm development was to set the time gate at the surface reflections. Then, according to the comparison results of the modelled signals reflected from the defective and non-defective areas, the time instances and the time intervals with the highest amplitude change were determined. Therefore, the peak-to-peak amplitudes in the determined time intervals with a significant amplitude change were calculated [9].

$$M_n = \max(u(t)) - \min(u(t)); \quad 2.21$$

Here, n is the number of the multi-reflections from the interface, $n =$ from 1 to N , t represents the determined time intervals.

In addition, the decay law of the interface multi-reflections can determine the quality of the adhesion of dissimilar joints. Based on this, the ratio coefficients of the peak-to-peak amplitudes of the selected time intervals for interface multi-reflections were calculated so that to assess the quickness of signal decay [9].

$$K_1 = \frac{M_n}{M_{n+1}}; \quad 2.22$$

$$K_2 = \frac{M_{n+1}}{M_n}; \quad 2.23$$

Here, M_n is the peak-to-peak amplitudes in the determined time intervals of multi-reflections, and n is the number of the interface multi-reflections where $n =$ from 1 to N .

As a result, the post-processing algorithm was developed based on the results of the investigation of dissimilar material joints. The application of the algorithm is demonstrated in the following chapter of the experimental results and the application of the developed algorithm.

2.3. Conclusion of the chapter

1. The investigation method containing the steps of the process and serving the objective to study the objects of dissimilar materials while employing the selected ultrasonic inspection method was created in order to develop a method for the detectability improvement in dissimilar material joints. The method of our investigation has allowed determining and evaluating the influential factors on the inspection system; we can also extract the valuable features from the obtained results for the further use while pursuing the algorithm development.

2. In particular, the sensitivity analysis has provided us with the opportunity to define and evaluate the major factors having the impact on the detection of disbonds.

The incidence angle and the water path characterising the curvature of the component surface are the major uncertain parameters which were taken into account for the development of the post-processing algorithms. The alignment according to the arrival time of the signals reflected from the component surface is able to eliminate the curvature impact.

3. Ultrasonic inspection simulations and the calculation of the boundary characteristics as well as the amplitude values which were received after determining the ultrasonic wave propagation through the layered structure were performed, and they allowed determining the effectiveness of the analysis of multiple reflections from the sample interfaces. The obtained results showed that the detectability of disbonds increases with the analysis of a higher number of particular multi-reflections.

4. The performed signal modelling and the optimisation of parameters in order to receive a signal which is close to the experimentally obtained values demonstrates the complexity of the disbond detection due to such factors as the overlapping and reverberation of the signals. However, the comparison of signals modelled for the defective and defect-free regions allowed defining the time intervals with the significant amplitude change caused by the presence of a disbond. The obtained results of the analysis were used for the algorithm development.

5. The post-processing algorithm serving the objective to improve the detectability of disbonds in dissimilar material joints was developed; it was based on the six main steps including the signal filtering, the alignment of the arrival time of all the signals, the determination of the required time instances and time intervals, the assessment of the peak-to-peak amplitudes and the evaluation of the quickness of the signal decay.

3. EXPERIMENTAL INVESTIGATIONS AND APPLICATION OF THE DEVELOPED ALGORITHM

In this chapter, the results of our experimental investigations of the components under investigation, the results of the comparison of the experimental and modelled data, the proposed methodology as well as the demonstration of the application of the developed algorithm are presented. These results describe and demonstrate the complexity of inspection of adhesively bonded materials while focusing on dissimilar material joints. The steps of the developed algorithm serving to improve the disbond detection probability in the adhesive layer of dissimilar material joints are represented.

3.1. Experimental investigations of dissimilar material joints and investigation results

The goal of this section is to demonstrate the results obtained in the course of the experimental inspection of dissimilar material joints when using ultrasonic nondestructive techniques. In order to achieve this goal, two samples of dissimilar material joints – steel-CFRP and aluminium-CFRP – were inspected by using the selected ultrasonic methods. The complexity of the disbond type defect detection in layered structures of dissimilar materials was proven by the obtained experimental results.

3.1.1. Description and experimental investigation of bonded steel-CFRP component

A sample of bonded steel to CFRP was under investigation where two plates had thicker layers of dissimilar materials. The image of the sample is shown in Fig. 3.1.

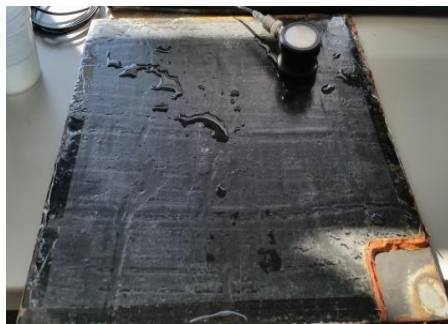


Fig. 3.1 Image of the sample of steel-CFRP under investigation

The sample of steel-CFRP features the rectangular planar shape. In the joint, there are also 3 artificial defects located between the adhesive and steel. The defects were made of polyethylene (PE) tape by using oil to prevent bonding between the plate and epoxy. The CFRP composite material consists of 4 unidirectional sub-layers of carbon/epoxy *prepreg* (the joint of steel-CFRP) which are arranged at

different angles (90°, 45°, 0°, -45°). The geometric characteristics of the samples are presented in the Table 3.1 and shown in Fig. 3.2.

Table 3.1. Geometric characteristics of steel-CFRP dissimilar material joints

No	Characteristics	Steel/CFRP
1	Thickness	9.32 mm
2	Thickness of metal	6.14 mm
3	Thickness of composite	3.18 mm
4	Thickness of adhesive	0.1 mm
5	Sample dimension	300 mmx300 mm
6	Quantity of defects	3
7	Dimension of defects	20 mmx20 mm; 15 mmx15 mm; 25 mmx25 mm
8	Metal/composite plate dimension	300 mmx300 mm
9	Bonded part dimension	300 mmx300 mm
10	Defect's location	Between epoxy and the metal plate
11	Unidirectional prepregs	4 layers of carbon prepregs

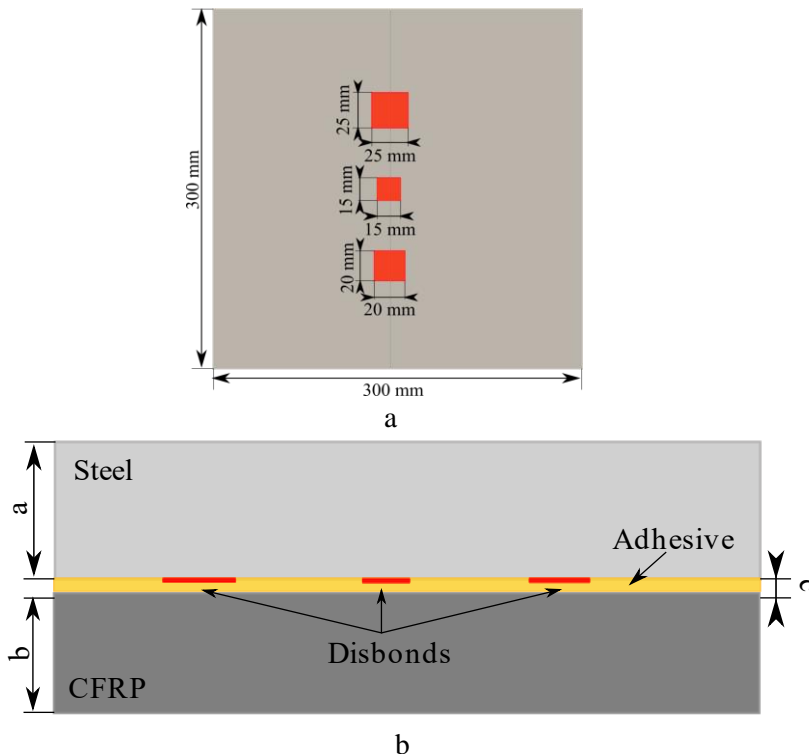


Fig. 3.2 Joint of dissimilar materials of bonded steel-CFRP and defects: (a) top view, (b) cross-sectional view, where a=thickness of steel, b=thickness of CFRP, c= thickness of adhesive layer

The orientation of the laminates is shown in Fig. 3.3. According to the micromechanics of lamina, the generalised Hook's law of anisotropic materials relates stresses to strains and is expressed as given in [108]:

$$\sigma_i = C_{ij}\varepsilon_j, \quad ij = 1,2, \dots,6; \quad 3.1$$

Here, σ_i are the components of stress, C_{ij} is the stiffness matrix, and ε_j is the component of strain.

The stiffness matrices of the composite material are presented in Table 3.2.

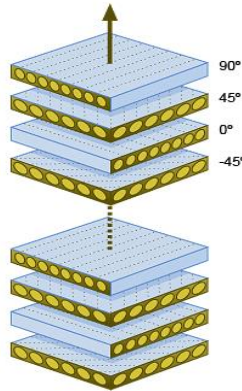


Fig. 3.3 Orientation of laminates in bonded steel-CFRP sample

Table 3.2. Stiffness matrix C_{ij} of steel-CFRP structure

249.856	106.856	146.229	0	0	0
106.856	249.856	146.229	0	0	0
146.229	146.229	218	0	0	0
0	0	0	107.478	0	0
0	0	0	0	107.478	0
0	0	0	0	0	71.5

The automated *TecScan* measurement system (*TecScan Systems, Inc.*) and a 10MHz focused transducer were selected for the ultrasonic pulse-echo inspection of the steel-CFRP structure. 3D testing is available in the measurement systems due to the *TecView* software. The selected focused transducer *Olympus V375-SU* with the focus distance in the water of 2 inches (50.8 mm) was manufactured by *Olympus Scientific Solutions Americas Incorporation*. In the pulse-echo ultrasonic method, the transducer was used as the emitter and the receiver. The components were immersed into the tank of water and fixed on the system turntable. The transducer was also fixed to the scanner and immersed into the water. The transducer was adjusted perpendicularly to the components' surfaces. The incidence of the ultrasound beam was aligned in a way so that to receive the maximum amplitude reflected from the surface. According to the theoretical analysis and the results of inspection simulations, the metal side of the structures was selected for the inspection. Since the area of interest is the interface of the structures, the transducer

was focused respectively according to Equation 2.9 to increase the detectability. As a result, in order to focus the signal on the interface between the metal and the adhesive, the distance between the transducer and the component's surface is 26.1 mm for the steel-CFRP structure. The scanning area along the y and z axes was set with the scanning step of 1 mm (steel-CFRP). The set-up of the inspection is shown in Fig. 3.4.

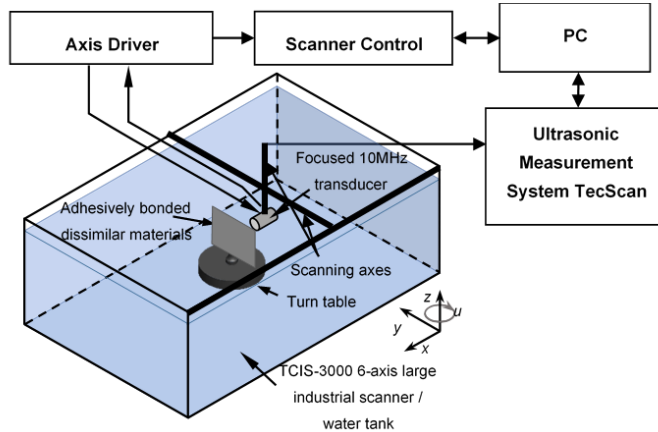


Fig. 3.4 Set-up of ultrasonic pulse-echo inspection in the immersion model of structures of dissimilar material joints [9]

The obtained results describe the problematic area of the inspection of adhesively bonded dissimilar materials and the influential factor as the surface curvature of the object. The C-scans of the *TecScan* experimental investigation of the steel-CFRP structure when using a 10 MHz focused transducer in the pulse-echo mode are presented in Fig. 3.5. In this case, the time gates were set in order to cover the part of the first reflection from the surface of the object. The obtained C-scans demonstrate the curvature of the sample surface. This factor has a strong impact on the detection of disbonds.

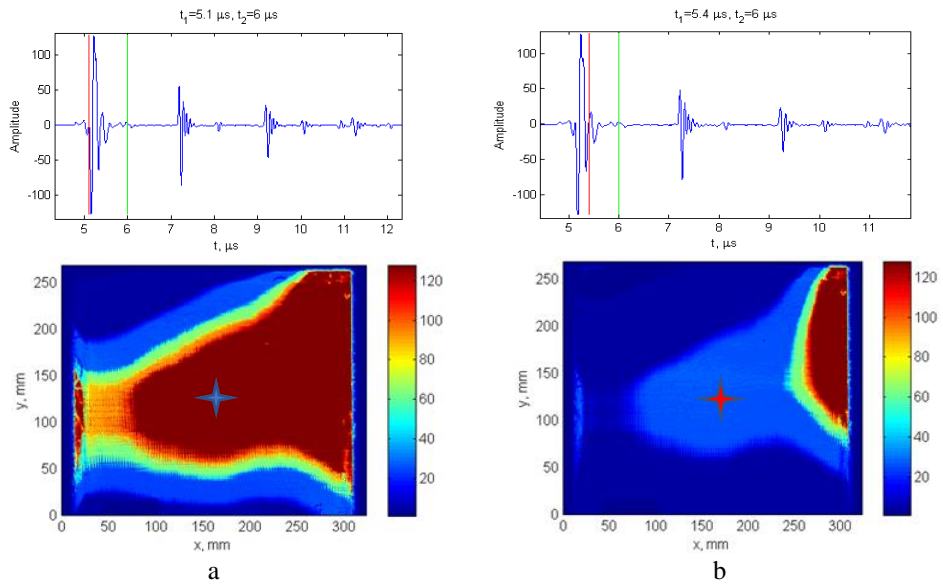


Fig. 3.5 A- and C-scans of the steel-CFRP structure displaying the signals starting at different time instances: (a) for time interval of 5.1–6 μs , (b) for time interval of 5.4–6 μs

The post-processing of the obtained data was performed in order to display the reflection from the interface of the structure since the disbands are located between the metal and the adhesive. The time gates were set respectively. According to the modelling and simulation results, the probability of the detection of disbands should increase with the analysis of multi-reflections. Therefore, the time gates were set manually in order to analyse multiple reflections from the interface. The best results of the detected disbands were obtained when studying the 3rd reflection from the steel-adhesive bonding. The A-scans with the selected time intervals to display the top view of the structure interface as well as the C-scans are shown in Fig. 3.6.

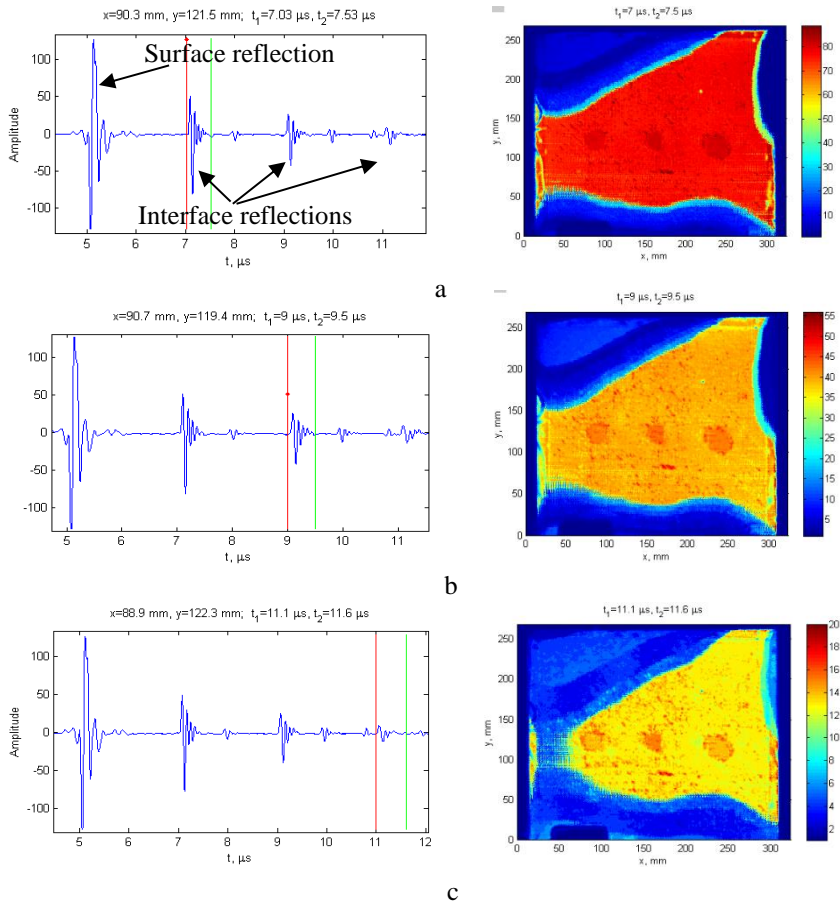


Fig. 3.6 Inspection of steel-CFRP structure: (a) A- and C-scans of the signal with selected time gates of 1st interface reflection, (b) A- and C-scans of 2nd multiple reflection from the interface as per selected time gates, (c) A- and C-scans of 3rd multiple reflection from the interface

The manual selection of the time instances is not appropriate; hence, the technique of the post-processing algorithm has to be applied for disbond detection. However, the obtained experimental results confirm the increase in the probability of the detection of disbonds by the analysis of the bigger number of the subsequent multi-reflections from the interface.

3.1.2. Description and experimental investigation of bonded aluminium-CFRP component

The single-lap joint of bonded aluminium to CFRP is under investigation as well. Thinner layers of materials of the component can be the reason of a more

complicated defect detection process. The image of the sample is shown in Fig. 3.7.

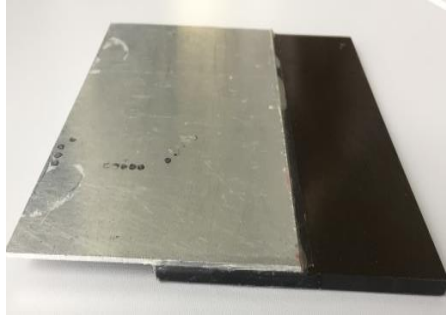


Fig. 3.7 Image of aluminium-CFRP sample under investigation

The sample of adhesively bonded aluminium and CFRP is a single lap joint manufactured in *COTESA GmbH*, Germany. Aluminium and CFRP were bonded by using 2 layers of the structural adhesive film *3M Scotch-Weld AF163-2 K* red. In the joint, there are 3 artificial disbonds placed between 2 layers of the adhesive film. The disbonds were made from 2 layers of the *Wrightlon® 4600* polyolefin copolymer release film. The CFRP plate of the sample consists of 41 units of unidirectional layers where the first and the last layers are GFRP. The orientation of the laminates is: 45° , -45° , 0° , 90° . The geometric characteristics of the sample are presented in Table 3.3 and shown in Fig. 3.8. The stiffness matrix of the composite material is presented in Table 3.4.

Table 3.3. Geometric characteristics of aluminium-CFRP dissimilar material joints

No	Characteristics	Aluminium/CFRP
1	Thickness	6.94 mm
2	Thickness of metal	1.61 mm
3	Thickness of composite	5.11 mm
4	Thickness of adhesive	0.22 mm
5	Sample dimension	150 mm × 150 mm
6	Quantity of defects	3
7	Dimension of defects	5 mm × 5 mm; 10 mm × 10 mm; 15 mm × 15 mm;
8	Metal/Composite plate dimension	100 mm × 150 mm
9	Bonded part dimension	50 mm × 150 mm
10	Defect's location	Between 2 layers of adhesive film
11	Unidirectional layers	41 layers (0–41): 40 CFRP, 2 GFRP

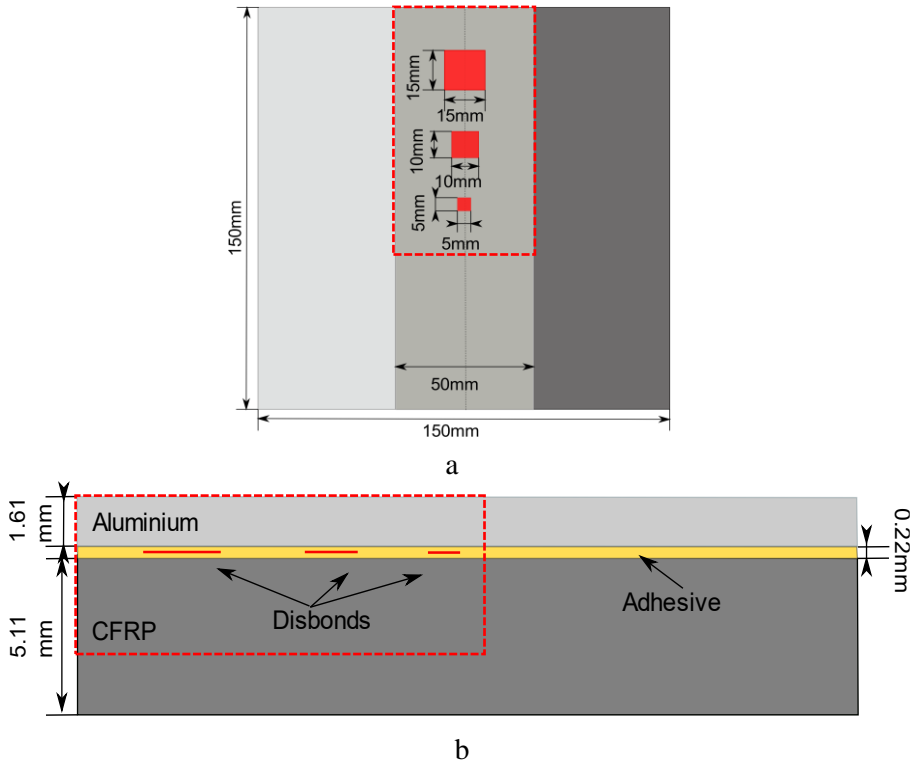


Fig. 3.8 Joint of dissimilar materials of bonded aluminium to CFRP and defects: (a) top view, (b) cross-sectional view

Table 3.4. Stiffness matrix C_{ij} of aluminium-CFRP structure

112.767	71.869	5.317	0	0	0
71.869	113.288	5.167	0	0	0
5.317	5.167	12.568	0	0	0
0	0	0	3.9	0	0
0	0	0	0	3.9	0
0	0	0	0	0	20.579

The *TecScan* measurement system (*TecScan Systems, Inc.*) and a 10MHz focused transducer were used for the ultrasonic pulse-echo inspection of the aluminium-CFRP structure as well. The transducer was focused on the interface, and the distance was calculated according to Equation 2.9. As a result, the distance between the transducer and the component's surface is 44.03 mm. The scanning area along the y and z axes was set with the scanning step of 0.5 mm. The set-up of the inspection is shown in Fig. 3.4.

In the case of the inspection of the aluminium-CFRP structure, the disbond detection is more complicated since the defects are in the middle of the adhesive

layer between two tapes. This makes the defects comparable to a cohesive failure of the structure. The C-scan of the experimental investigation of the joint of aluminium and CFRP is shown in Fig. 3.9. The obtained B-scan also demonstrates the curvature of the sample surface along the x axis. In this case, the influential factor of the sample curvature complicated the detection of disbonds on the structure interface. The highest time difference observed due to the surface curvature is $1\mu\text{s}$. The defects and their sizes cannot thus be measured. However, the method based on the manual selection of time intervals cannot be applied for other samples of dissimilar materials. So, there is a requirement for the development of a single method for all types of samples of dissimilar materials with a layered structure so that to eliminate the influence of the sample's curvature (i.e., the non-ideal geometry). The post-processing algorithm developed in Chapter 2 of this work has to eliminate this influencing factor on defect detection.

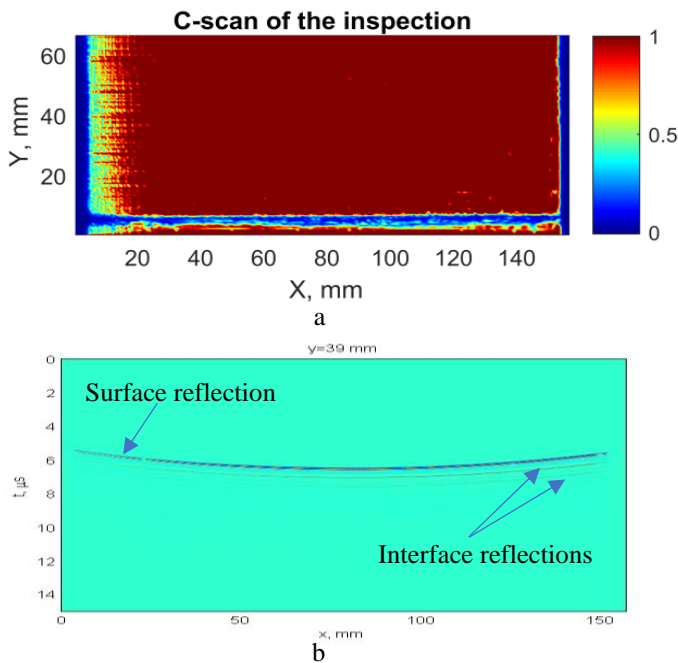


Fig. 3.9 Ultrasonic pulse-echo inspection of aluminium-CFRP structure: (a) C-scan, (b) B-scan demonstrating the component curvature

Thus, all the results of the experimental investigations of different samples of dissimilar materials demonstrate the main problem aspect of the disbond detection caused by different acoustic impedances of dissimilar materials. In addition, the immersion technique is the best selection for such components to be inspected with the further use of post-processing algorithms for the elimination of influential factors.

3.2. Comparison of the obtained modelled and experimental results

The goal of this section is to obtain the time moments and time intervals of the interface multi-reflections with the most significant amplitude change caused by the debonding according to the technique described in Section 2.2.4. The first step of the technique which was developed is the optimisation of the parameters in order to obtain the modelled signal propagating through the layered structure of aluminium-CFRP materials as close as possible to the signal obtained experimentally. After parameter optimisation, the best fit of the modelled and experimental signals was achieved. The A-scan comparison of these signals reflected from the non-defective interface for the model and the experiments is shown in Fig. 3.10. The gates of the calculated time instances of the reflections from the layered structure are indicated on the A-scan.

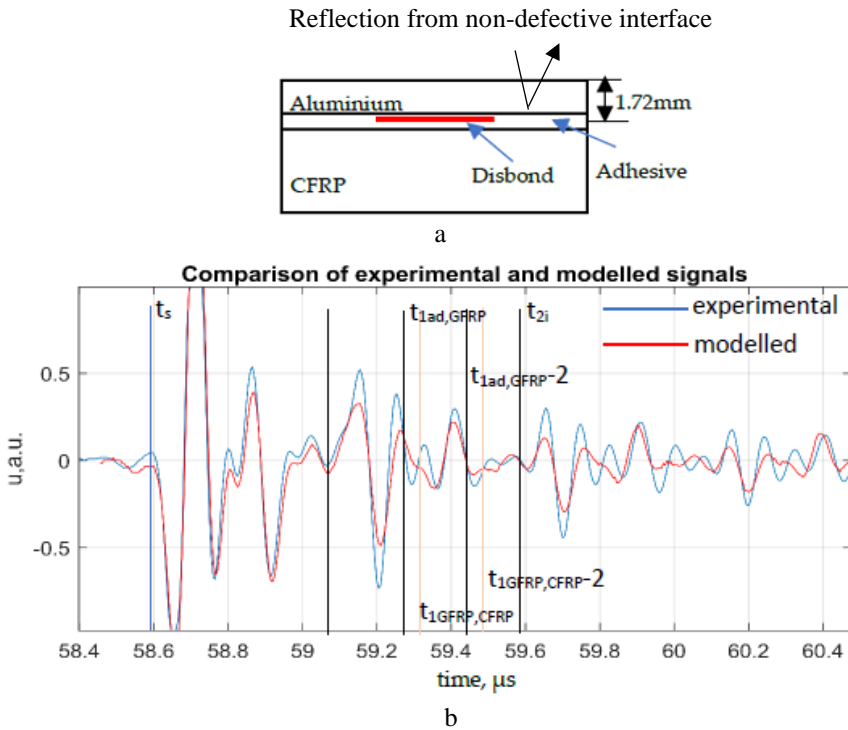


Fig. 3.10 Comparison of modelled and experimental signals for the case of ‘healthy’ state of interface: (a) Section view of the structure, (b) A-scan comparison [9]

As a result, the modelled signal perfectly fits the experimental one along the time of the signal reflection from the boundaries. The reverberation is present on the surface and the interface reflections in both signals. According to the characteristics from the transducer documentation, the pulse duration is 0.49 μs . Therefore, from the A-scan, it is determined that the signals reflected from the aluminium-adhesive interface t_{1i} , and the signals reflected from the adhesive-GFRP $t_{1ad,GFRP}$ and GFRP-

CFRP $t_{1\text{GFRP,CFRP}}$ boundaries as well as their multi-reflections are overlapping due to the low thicknesses of the layers. This effect of overlapping makes the detection of disbonds more complicated since the amplitude difference between the signals reflected from the defective and defect-free regions can be hidden. Also, there is an impact of reverberation.

However, the modelling of the signals reflected from the defective (delamination located between two adhesive tapes) and defect-free areas was performed with the aim to determine the theoretical time of the most prominent amplitude change by comparing these signals. Since in the experimental investigation many factors, such as the surface, the interface curvature of the sample, the signal overlapping and reverberations due to thin adhesive layers, the amplitude trend, etc. can affect the results, the amplitude difference between the signals reflected from the defective and the defect-free interfaces can be not obvious and constant; also, it can yield opposite results. The A-scan comparison of the modelled signals is shown in Fig. 3.11.

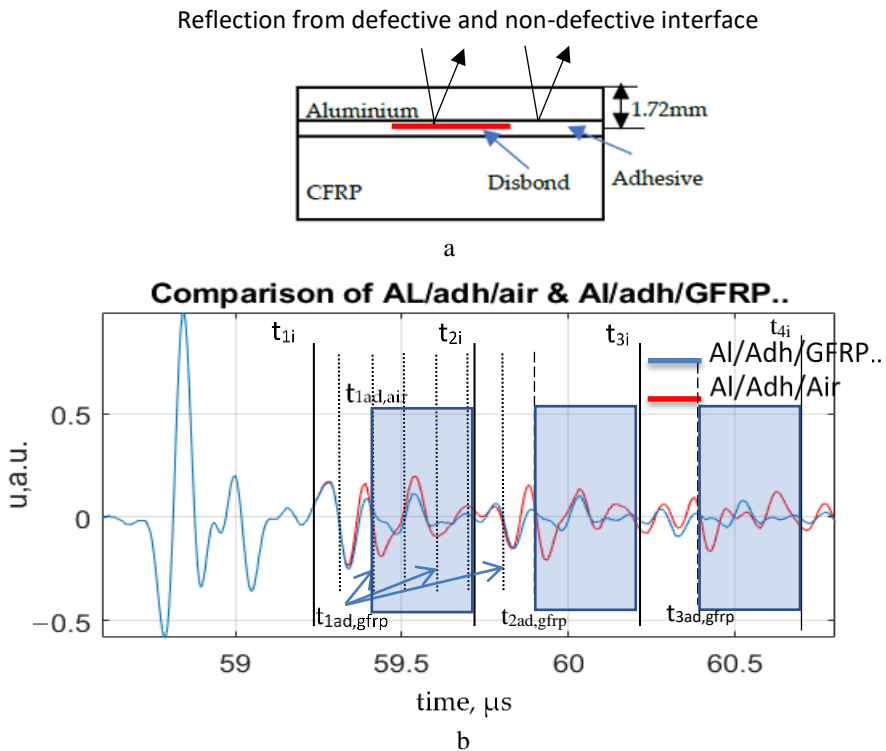


Fig. 3.11 Comparison of modelled signals: (a) Section view of the structure, (b) A-scan comparison [9]

From the A-scan comparison of the modelled signals reflected from the perfect bonding (aluminium-adhesive-composite) and debonding (aluminium-adhesive-air/defect), the time instance of the appropriate reflection was defined.

When considering the time interval of the 1st reflection from the interface, the maximum amplitude change was observed after the second reflection from the disbond $t_{1ad,air}$ or at the time instance of the first reflection from the bottom interface $t_{1ad,gfrp}$ at the time interval $t_{1i}:t_{2i}$. This technique was applied in order to increase the probability of the detection of disbonds in dissimilar material joints. The time moment of the signal reflected from the bottom interface or the adhesive-composite coincides with the doubled time of the signal reflected from the defect. Since the study of multiple reflections serves well regarding detection probability, the time instances and time intervals with the high amplitude change were defined for each time interval ($t_{1i}:t_{2i}$, $t_{2i}:t_{3i}$, $t_{3i}:t_{4i}$, $t_{4i}:t_{5i}$) of the interface multi-reflections, respectively. This means that, when considering any point from the C-scan, the defined time intervals will remain the same. The selected time intervals are demonstrated on the A-scan in Fig. 3.11. The peak-to-peak amplitudes in these time intervals of the experimental signals were calculated in order to obtain the C-scans of the inspection. In Table 3.5, the time intervals with the highest change of amplitude values are presented.

Table 3.5. Selected time intervals and peak-to-peak amplitudes

Peak-to-peak amplitudes	Time intervals with the maximum amplitude change
M_1	$t_{1ad,GFRP}:t_{2i}$
M_2	$t_{2ad,GFRP}:t_{3i}$
M_3	$t_{3ad,GFRP}:t_{4i}$
M_4	$t_{4ad,GFRP}:t_{5i}$

The defined time intervals and the calculation of the peak-to-peak amplitudes were used in the developed post-processing algorithm for the improvement of the probability of disbond detection.

3.3. Application of the developed post-processing algorithm and discussion of results

The goal of this section is to apply the developed post-processing algorithm for the disbond detectability improvement in the joints of adhesively bonded dissimilar materials. In order to achieve this goal, the data obtained from the experimental investigation of the aluminium-CFRP layered structure was post-processed according to the developed algorithm.

Firstly, the band-pass filter was used for the denoising of the collected signals. Then, the zero-crossing technique was applied to align the arrival time of the signals reflected from the object's surface. The A-scans and B-scans of the signals before the alignment of the arrival times after the time alignment of the surface reflection as well as the comparison of the signals before and after filtering are shown in Fig. 3.12.

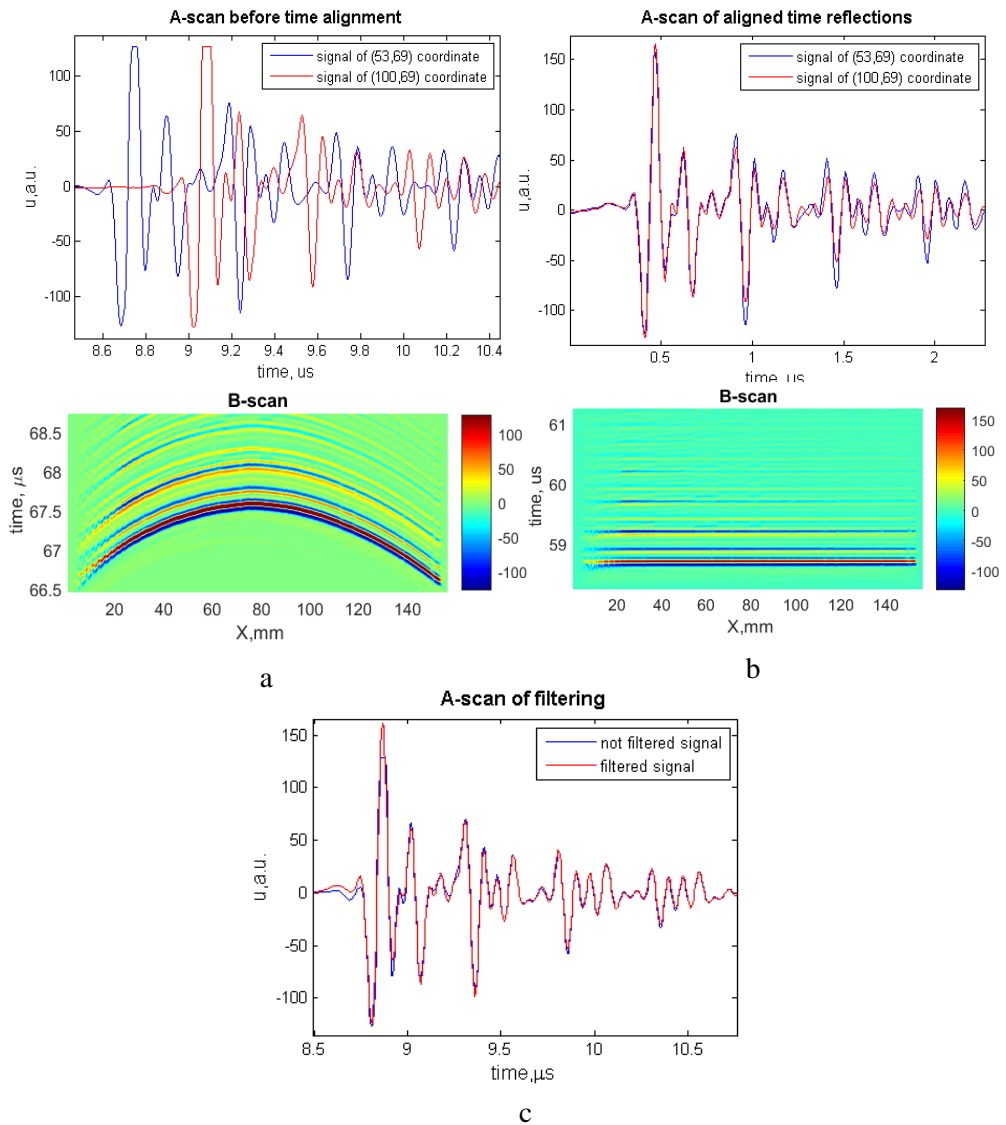


Fig. 3.12 A- and B-scans of the signals: (a) B-scan and A-scan comparison of two signals reflected from different coordinate points of the sample surface before time alignment, (b) B-scan and A-scan comparison of two signals reflected from the different coordinate points of the sample surface after time alignment, (c) A-scan comparison of filtered and non-filtered signals

According to the presented A- and B-scan (a), the time difference between two signal reflections selected from the same y coordinate point and 2 different points of the x coordinate was observed due to the object surface curvature. The A- and B-scans (b) represent the same signals after applying the zero-crossing

technique in order to align the time arrival of the reflected signals. The A-scan (c) demonstrates the band-pass filtering of the signal. The signals on the A-scan were presented before the adjustment of the time axis according to the distance between the transducer and the object's surface. During the experimental inspection, a gate-like window was applied for the reflected signal; therefore, there is a 50 μs delay. This value was used in the post-processing in order to display the correct time axis of the A-scans; otherwise, 0 μs will be at the start time of the threshold applied as well as the after time alignment as shown in Fig. 3.12 (b).

For the further data post-processing, the experimentally obtained signal was studied in order to indicate the type of signal reflections and the time instances of each reflection according to the obtained results from signal modelling. The A-scan of the filtered signal is shown in Fig. 3.13. As a result, the time moments for the four multiple reflections from the aluminium-adhesive, adhesive-disbond and adhesive-composite (GFRP sub-layer) contacts were indicated in the A-scan.

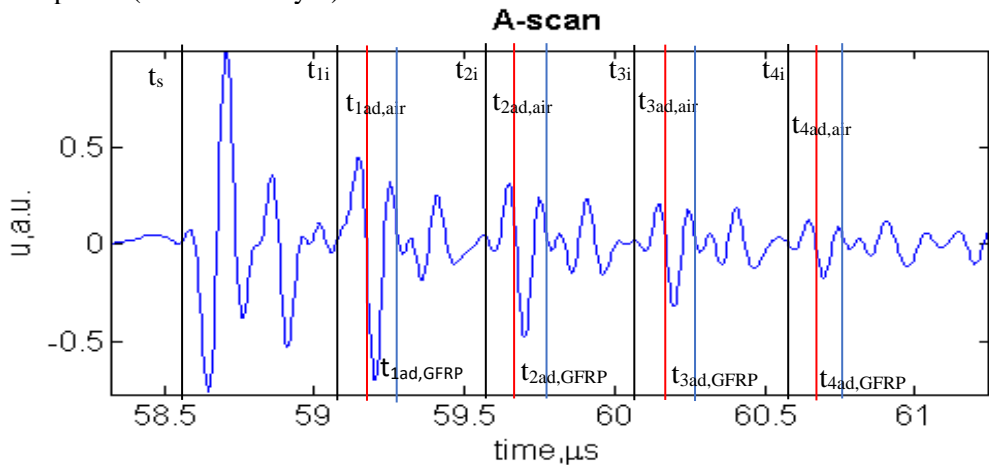


Fig. 3.13 A-scan of the signal with the indicated reflection types for the determined time instances

After the 3rd step of the developed post-processing algorithm of the adjustment of time instances for the surface reflections, the correct time intervals of the multiple interface reflections were determined for the analysis. The length of the signal duration according to the used transducer references is 0.49 μs at the -40 dB level. The subsequent multi-reflections from the interface repeat in 0.506 μs according to the theoretical and modelling calculations. The A-scan with the defined windows of time intervals for the four multiple interface reflections $t_{1i}:t_{2i}$ (Interface 1), $t_{2i}:t_{3i}$ (Interface 2), $t_{3i}:t_{4i}$ (Interface 3), $t_{4i}:t_{5i}$ (Interface 4) is shown in Fig. 3.14 (a). The C-scans for each multiple interface reflection were displayed. As a result, the major influencing factor of the object curvature on the system disbond detectability was partially eliminated. All the disbonds which existed in the layered structure interface were detected with different detectability due to the trend and also, possibly, due to the different depth location in the adhesive layer of each defect. When taking into account the biggest disbond, the detectability of it increases

with the analysis of the subsequent multiple reflections. However, it was hard to distinguish between the other two disbonds in the 1st and 2nd multiple reflections. Yet, the highest detectability was observed at the time interval of the 4th multiple reflection $t_{4i}:t_{5i}$ for all the disbonds shown in Fig. 3.14 (e).

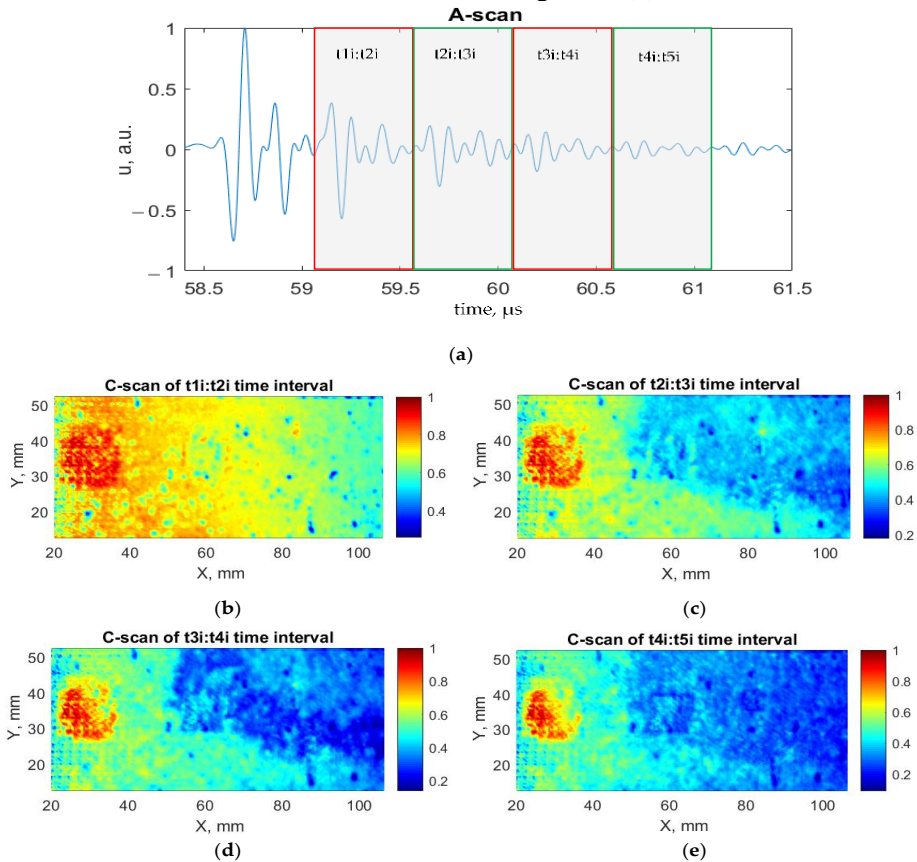


Fig. 3.14 A-scan and C-scans of interface multiple reflections: (a) A-scan with the indicated time intervals for each multi-reflection, (b) C-scan of 1st interface reflection of $t_{1i}:t_{2i}$ time interval, (c) C-scan of 2nd interface reflection of $t_{2i}:t_{3i}$ time interval, (d) C-scan of 3rd interface reflection of $t_{3i}:t_{4i}$ time interval, and (e) C-scan of 4th interface reflection of $t_{4i}:t_{5i}$ time interval [9]

Furthermore, the quantification of the improvement of the disbond detection was performed by using the -6 dB drop method after each step of the developed algorithm for the C-scan demonstration. As a result, the sizes of the biggest defect for the 4 multiple interface reflections and the size of the middle and smaller defects detected on the 4th interface reflection were determined. The C-scans and slices of the intensity variation in the selected coordinate of the defects along the x and y axes are presented in Fig. 3.15 and Fig. 3.16. The sizes of the defects are presented in Table 3.6.

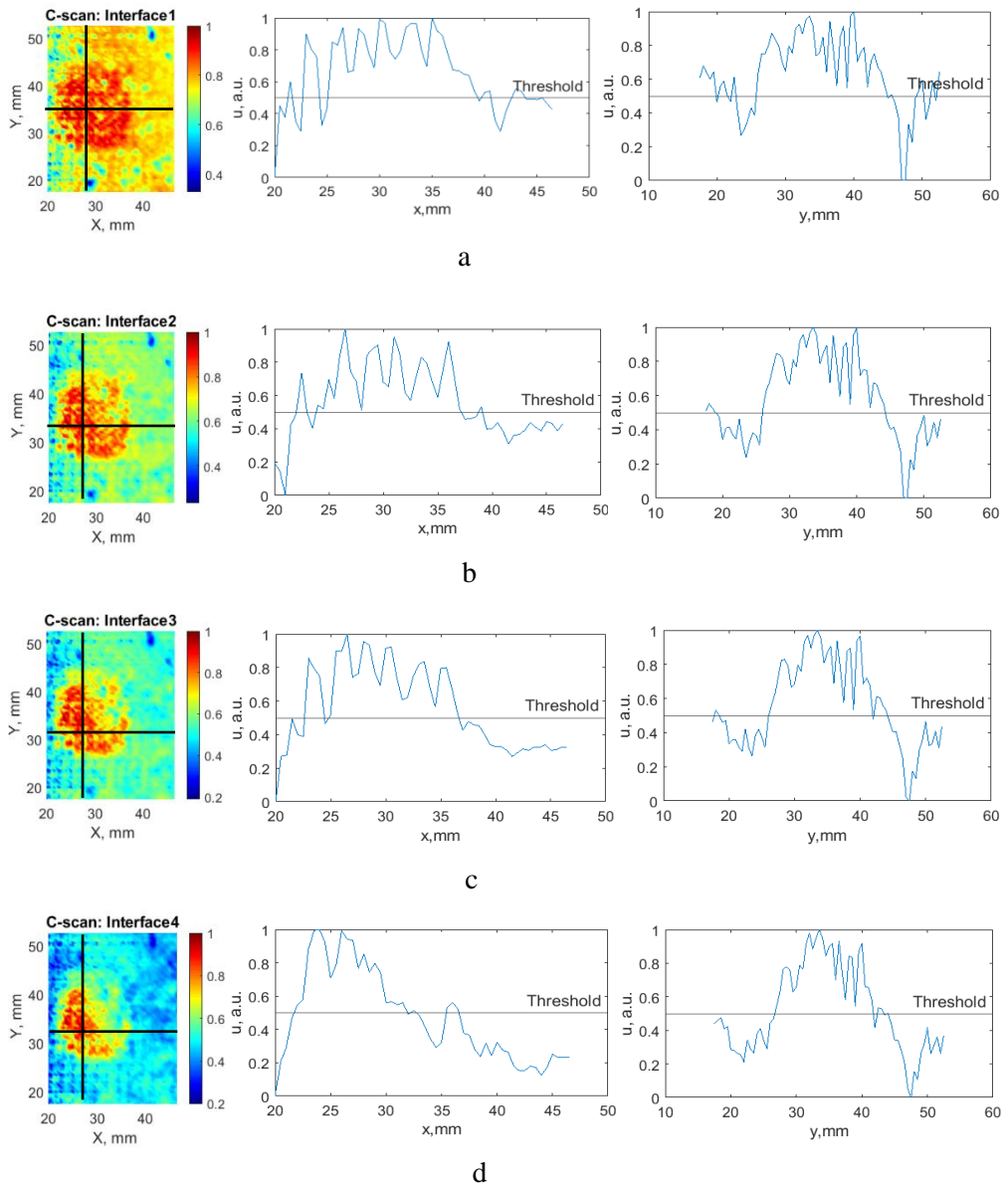


Fig. 3.15 C-scans and slices of intensity variations according to x and y axes of -6dB drop method for the biggest defect: (a) Reflection from Interface 1 ($t1:t2i$), (b) Reflection from Interface 2 ($t2:t3i$), (c) Reflection from Interface 3 ($t3:t4i$), (d) Reflection from Interface 4 ($t4:t5i$).

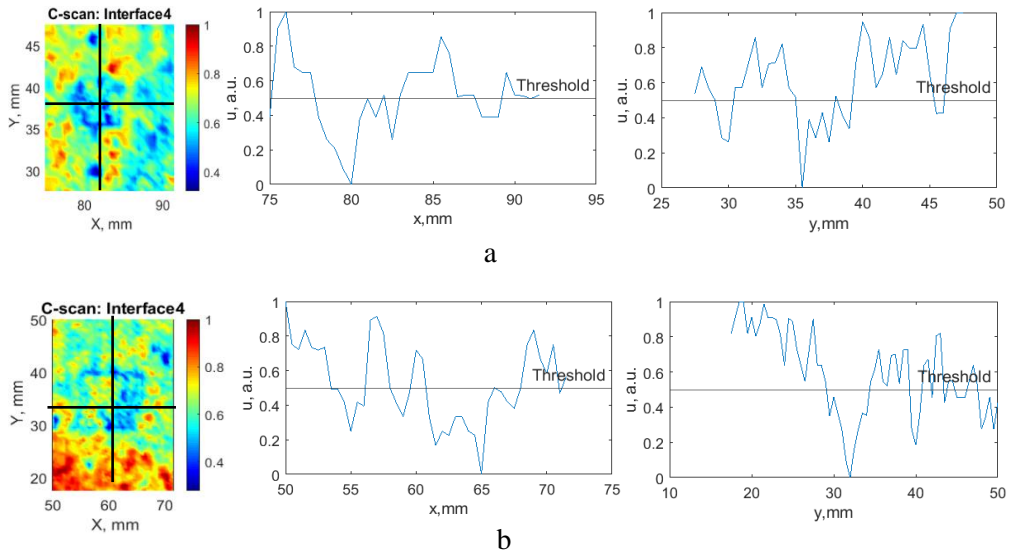


Fig. 3.16 C-scans and slices of intensity variations according to x and y axes of -6dB drop method for the medium and the smallest defects: (a) the smallest defect, (b) middle-sized defect

Table 3.6. Sizes of defects measured by using the -6dB drop method

Interface reflection	Slice along	Big defect size, mm	Medium defect size, mm	Small defect size, mm
Interface 1	X axis	14.2	-	-
	Y axis	19.3	-	-
Interface 2	X axis	13.4	-	-
	Y axis	18.3	-	-
Interface 3	X axis	11.9	-	-
	Y axis	16.0	-	-
Interface 4	X axis	10.3	5.2	4.2
	Y axis	15.1	5.1	2.9

The study of multiple reflections from the interface of the component made it possible to detect the biggest defect. The subsequent interface reflections demonstrate better results regarding the biggest defect size. The two smaller defects could be detected by studying the 4th multiple interface reflection. However, the measured sizes do not correspond to the theoretical ones provided by the manufacturer mainly due to the influence of the amplitude trend.

The detected disbands after the analysis of multiple reflections allow selecting the coordinate points for the signals reflected from the perfect bonding and debonding of the experimental data for the comparison of the A-scans. The experimentally obtained signals reflected from the disbands and from the defect-free interface were compared in order to study the change of the amplitude for both interface conditions. The C-scans with the selected coordinates of the signals were compared; also, the A-scan comparison is shown in Fig. 3.17 and Fig. 3.18.

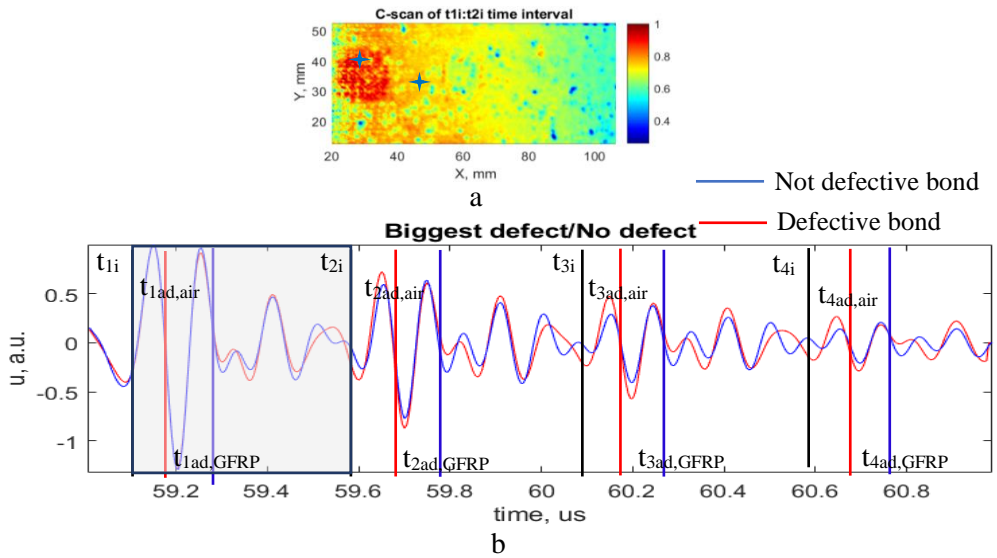


Fig. 3.17 C-scan and A-scans of the signal reflected from perfect bonding and debonding in the structure: (a) C-scan with the marked selected coordinate points of signals, (b) A-scan comparison of two signals where the blue line is the reflection from the perfect bond, and the red line is the reflection from debond

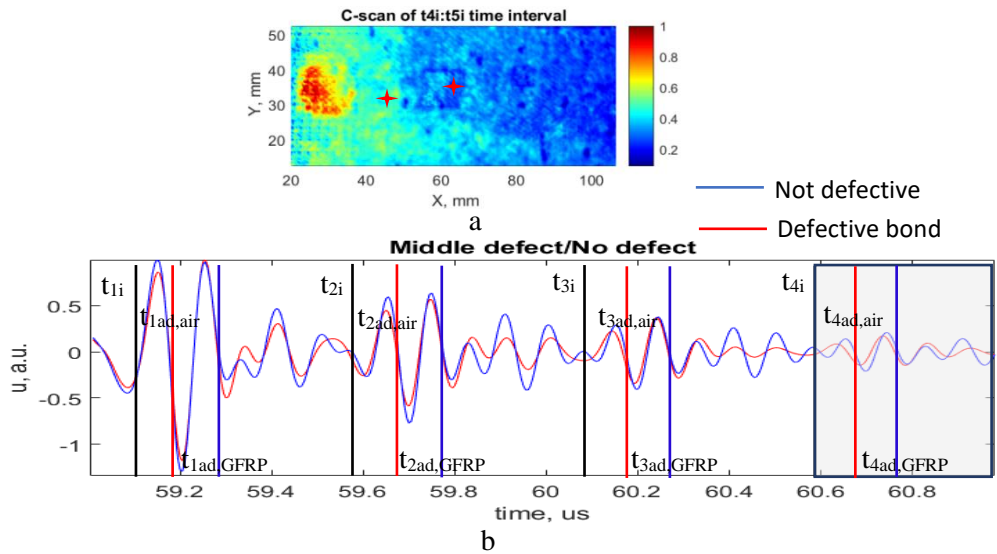


Fig. 3.18 C-scan and A-scans of the signal reflected from perfect bonding and debonding in the structure: (a) C-scan with the marked selected coordinate points of signals, (b) A-scan comparison of two signals where the blue line is the reflection from the perfect bond and the red line is the reflection from debond

The comparison of the A-scans of the signal reflections from the defect-free and defective areas in Fig. 3.17 demonstrates the slight increase of the amplitude in the time intervals of the interface reflections; however, in Fig. 3.18, the amplitude of the perfect interface reflections is higher if compared to the defective area. It was determined that the correct amplitude change cannot be determined in the experimentally obtained signals due to the main factor as a trend which is observed on the C-scans. In addition, spectral analysis was performed which, also, did not provide any valuable insight regarding the difference between the reflections from perfect bond and debonding. Therefore, the fourth step of the developed post-processing algorithm was applied for the data. In this case, the time gates of the interface multiple reflections were determined where the significant amplitude change was observed between the defective and defect-free results obtained by modelling. The determined time gates were applied for the experimental results. Then peak-to-peak amplitudes were calculated in the selected time intervals (M_1 - M_4) in order to display the C-scans (Fig. 3.19).

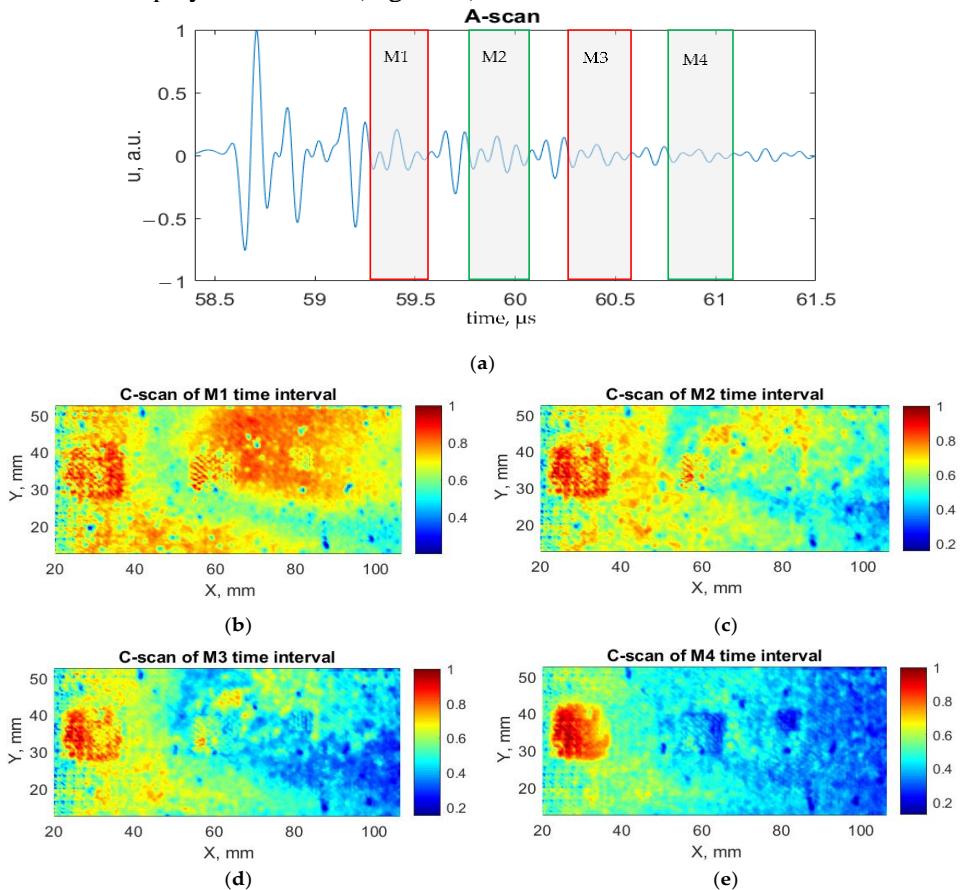


Fig. 3.19 A-scan and C-scans of the selected interface multiple reflections: (a) A-scan, (b) C-scan of M1 time interval, (c) C-scan of M2 time interval, (d) C-scan of M3 time interval, and (e) C-scan of M4 time interval [9]

As a result, applying the selected time gates for C-scan visualisation provided the detection of all disbands in the structure. Two smaller defects are observed more clearly. The first and fourth interface reflections M1 and M4 are provided with sharper contours of the shape of all the three defects. In addition, the C-scans demonstrate the increase in the defect detection by studying the subsequent multiple reflections. Therefore, the sizes of the defects were measured from the C-scan of the M4 time interval (Fig. 3.20). In order to determine the sizes of the defects, the decibel drop method was applied as well. The measured defect dimensions are presented in Table 3.7.

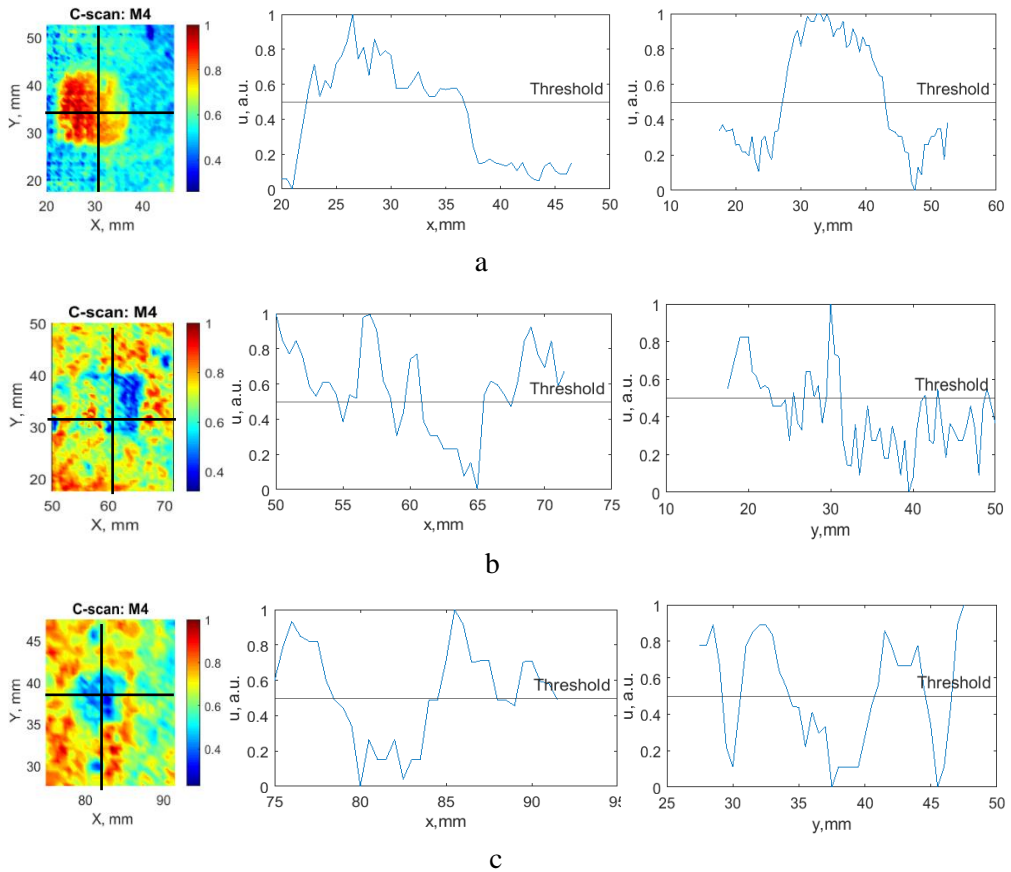


Fig. 3.20 C-scans and slices of intensity variations according to the x and y axes of the -6dB drop method for the defects: (a) the biggest defect, (b) middle size defect, (c) the smallest defect

Table 3.7. Sizes of defects measured by using -6dB drop method

Interface reflection	Slice along	Big defect size, mm	Medium defect size, mm	Small defect size, mm
M4	X axis	14.3	4.7	6
	Y axis	15.7	10.2	6.4

As a result, the measured sizes of the defects in this case are closer to the reference ones compared to the results of the interface reflections of the full-time intervals, such as $t1:t2i$ and others.

Moreover, the ratio of the peak-to-peak amplitudes of the defined time intervals M1-M4, which corresponds to step 6 of the developed post-processing algorithm, were calculated. The best coefficients of the amplitudes relations providing the best detection probability of disbonds are shown in Fig. 3.21. The obtained C-scans demonstrate all the disbonds of the structure which were detected with the improved detectability. Two smaller defects were clearly detected where distinct contours of the shape are observed even in the case of the smallest disbond of 5x5 mm of size.

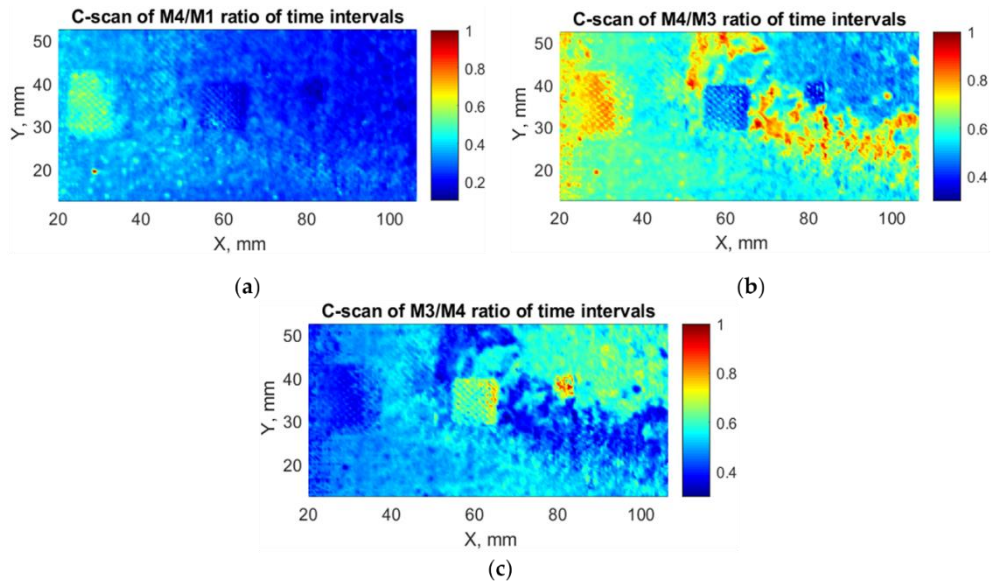


Fig. 3.21 C-scans of selected interface multiple reflections: (a) C-scan of M4/M1 ratio, (c) C-scan of M4/M3 ratio, (d) C-scan of M3/M4 ratio [9]

The C-scan of the M4/M1 ratio of time interval demonstrates the detection of the biggest defect. The C-scans of M4/M3 and M3/M4 represent a higher probability of the detection of two smaller defects with sharper contours of the defect geometry. The sizes of the defects were measured and presented in Table 3.8. The C-scans and slices of the intensity variation of the defects along the x and y axes are presented in Fig. 3.22 – Fig. 3.28.

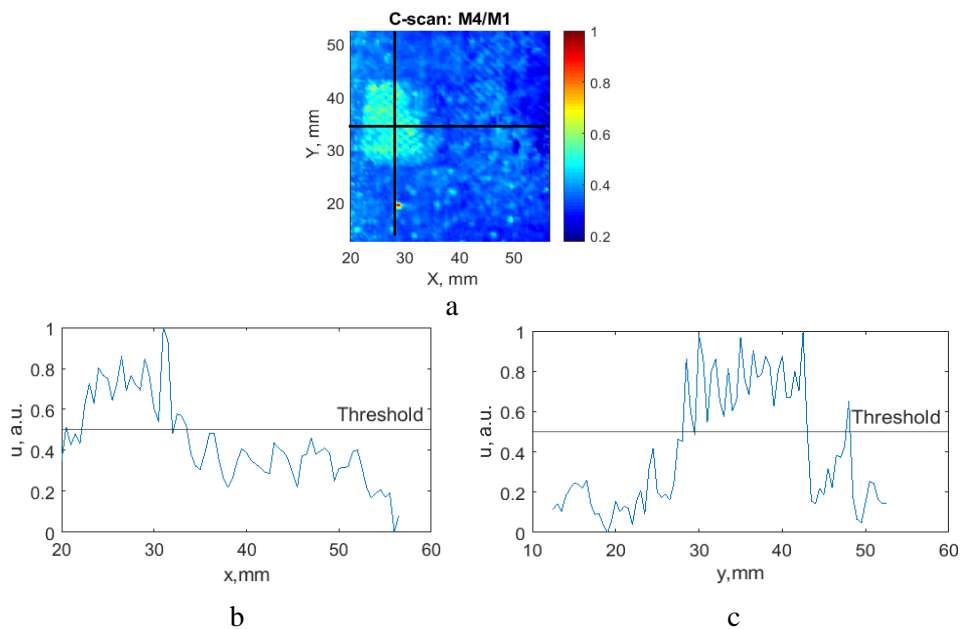


Fig. 3.22 C-scan and slices of intensity variation: (a) C-scan of the biggest defect of M4/M1 ratio coefficient, (b) slice along x axis, (c) slice along y axis

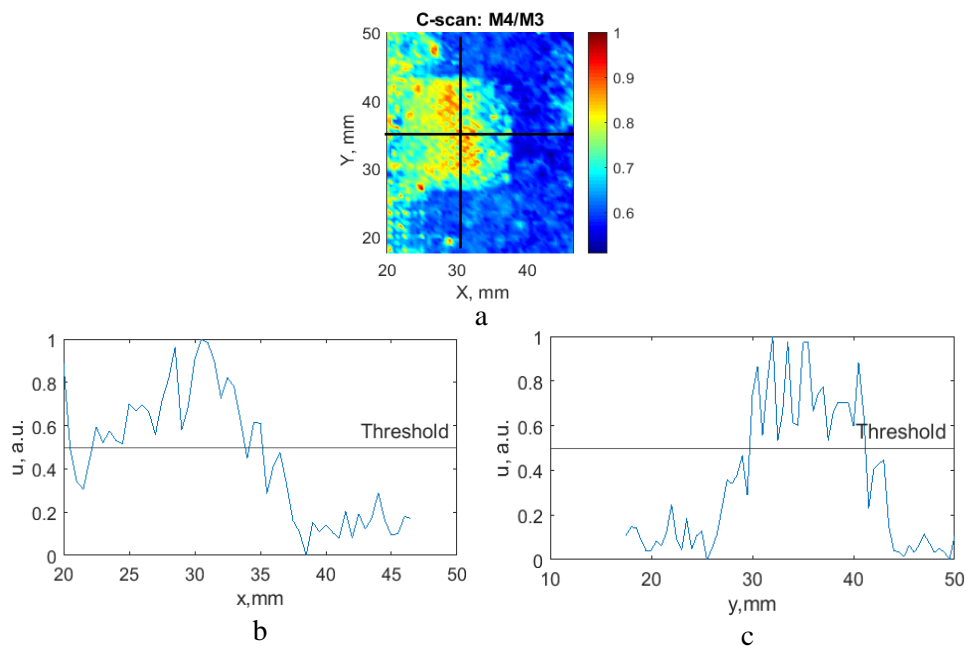


Fig. 3.23 C-scan and slices of intensity variation: (a) C-scan of the biggest defect of M4/M3 ratio coefficient, (b) slice along x axis, (c) slice along y axis

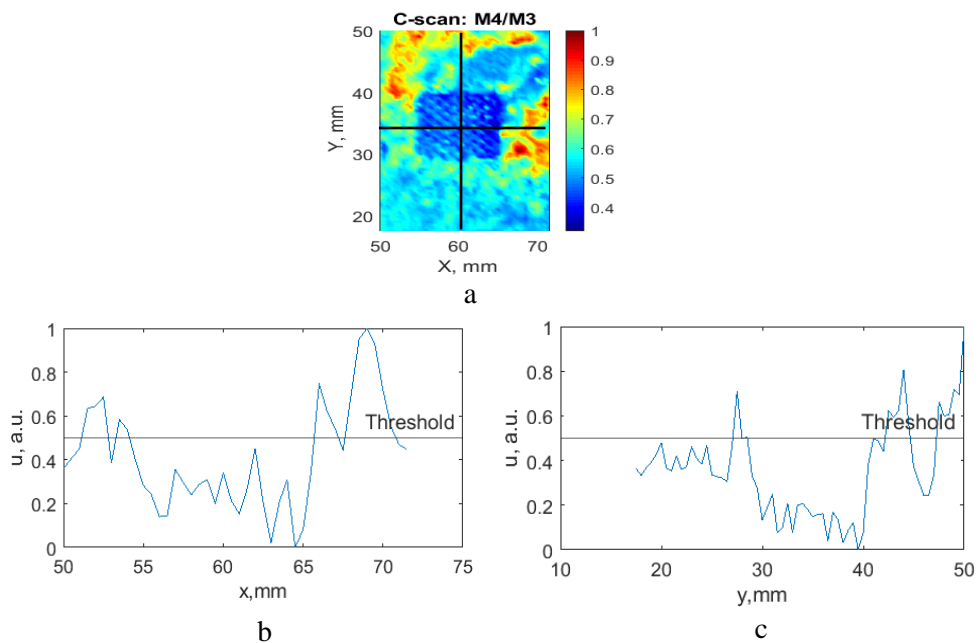


Fig. 3.24 C-scan and slices of intensity variation: (a) C-scan of the medium defect of M4/M3 ratio coefficient, (b) slice along x axis, (c) slice along y axis

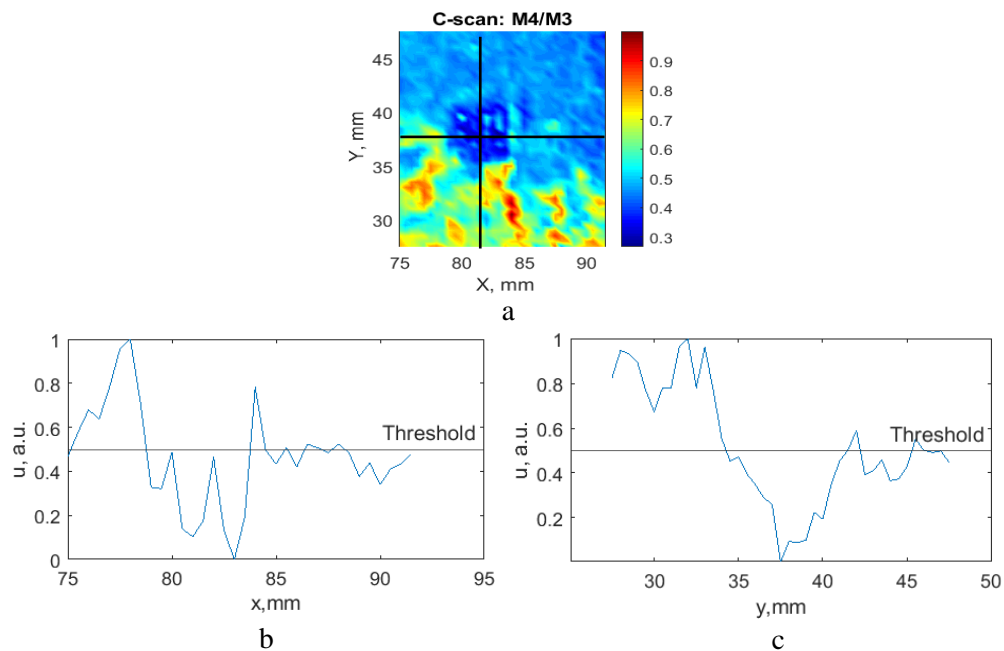


Fig. 3.25 C-scan and slices of intensity variation: (a) C-scan of the smallest defect of M4/M3 ratio coefficient, (b) slice along x axis, (c) slice along y axis

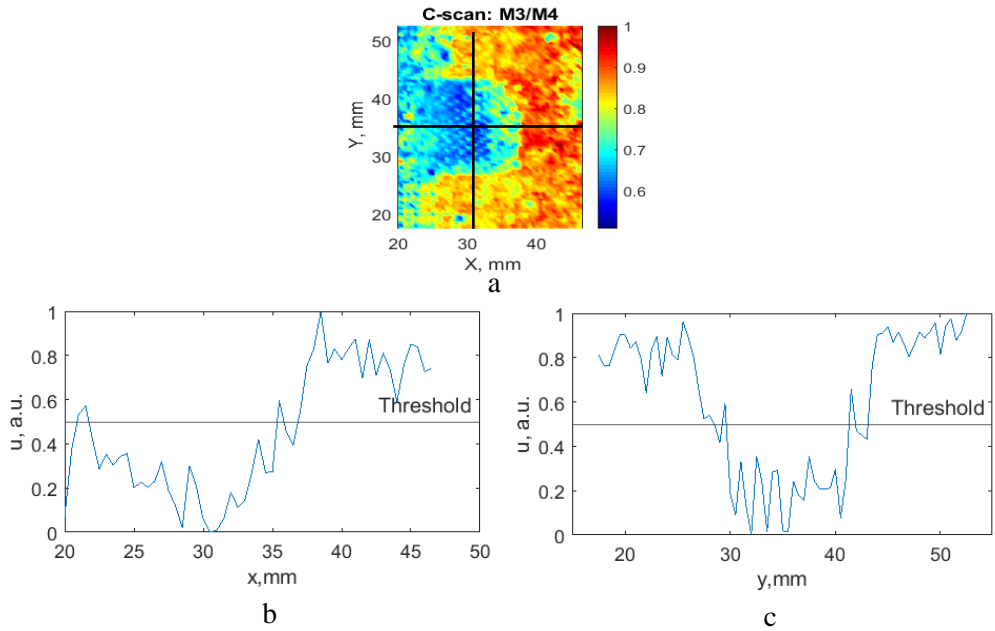


Fig. 3.26 C-scan and slices of intensity variation: (a) C-scan of the biggest defect of M3/M4 ratio coefficient, (b) slice along x axis, (c) slice along y axis

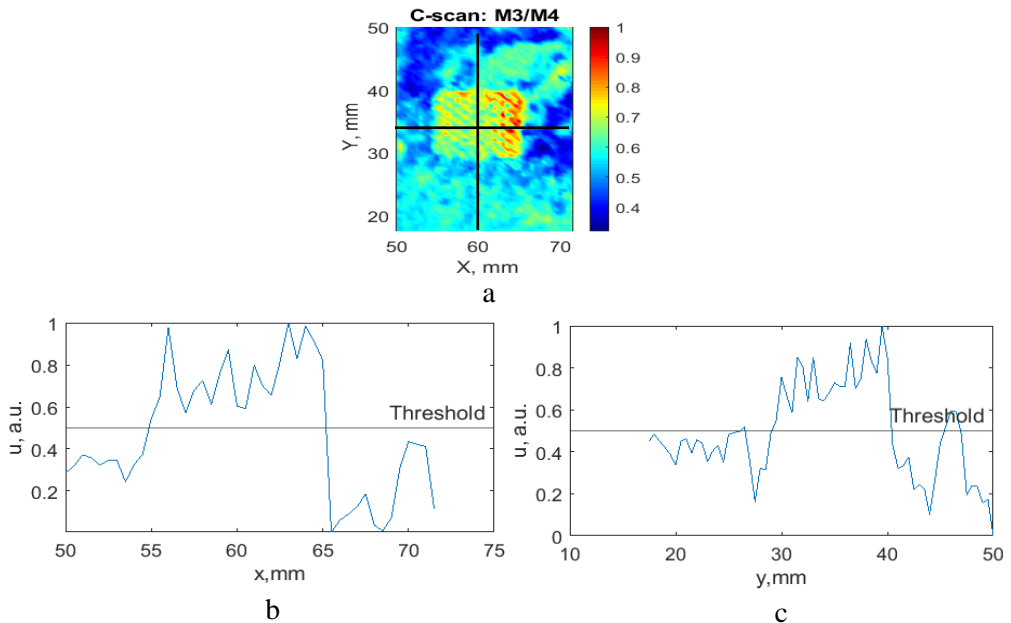


Fig. 3.27 C-scan and slices of intensity variation: (a) C-scan of the medium defect of M3/M4 ratio coefficient, (b) slice along x axis, (c) slice along y axis

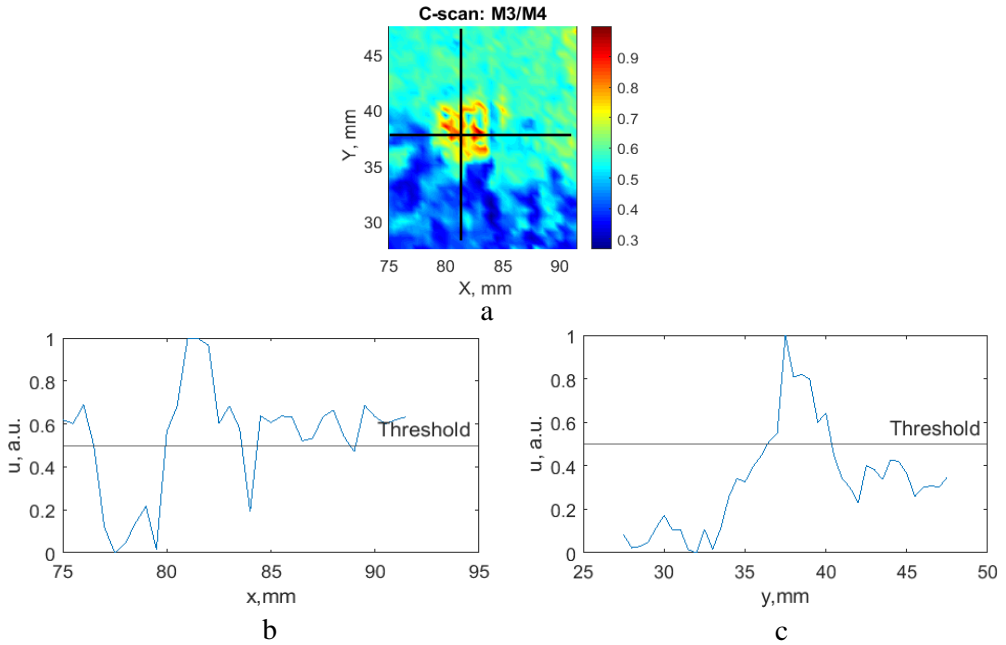


Fig. 3.28 C-scan and slices of intensity variation: (a) C-scan of the smallest defect of M4/M3 ratio coefficient, (b) slice along x axis, (c) slice along y axis

Table 3.8. Sizes of defects measured by using -6dB drop method

Interface reflection	Slice along	Big defect size, mm	Medium defect size, mm	Small defect size, mm
M4/M1	X axis	9.8	-	-
	Y axis	13.5	-	-
M4/M3	X axis	11.6	11.5	4.9
	Y axis	11.6	13.5	6.2
M3/M4	X axis	13.6	10.3	3.8
	Y axis	11.8	11.4	3.9

As a result, the experimental investigations of the components of dissimilar materials were performed, and the complexity of disbond detection was proven on the grounds of the obtained results. Time intervals with the significant amplitude change between the reflections from the perfect bonding and debonding were determined according to the modelling of the signals and their comparison. The developed post-processing technique for the improvement of the disbond detection probability and the defined time intervals was applied on the data collected by experimental inspection. The effectiveness of the developed algorithm was proven in practice by detecting all disbands in the adhesive layer of the structure of bonded dissimilar materials with an increased performance of detect detection. The best result for the detection of the biggest defect was demonstrated by the C-scan of the M4 time interval with the following dimensions: 14.3x15.7 mm. In the case of the

medium defect, the best results were demonstrated by the C-scan of M3/M4 with the 10.3x11.4 mm dimensions, whereas, for the smallest defect, the C-scan of M4/M3 with the 4.9x6.2 mm dimension was the most appropriate.

3.4. Conclusion of the chapter

1. The experimental investigation of the structures of bonded dissimilar materials was performed by using selected techniques. The obtained results demonstrated the complexity of detecting the disbond type defects in such multi-layered structures. The curvature of the surface was identified as the most influential factor beside the effect of overlapping, the defect depth location in the adhesive layer and the amplitude trend having the impact on the disbond detection.

2. The comparison of the modelled and experimental signals as well as the comparison of two modelled signals reflected from the defective and defect-free interfaces was performed. Due to that, the values of the time moments and time intervals with the most prominent amplitude change caused by the defective interface were determined and used in the process of the post-processing algorithm application.

3. The developed post-processing algorithm was applied for the collected data of experimental investigations following the steps presented in Chapter 2. The obtained C-scans successfully demonstrated the improvement of the probability of disbond detection in the structures of bonded dissimilar materials. The defect sizing performance was studied at each step of the algorithm and subsequently compared. The best results which were closest to the reference sizes given by the manufacturer were measured. As a result, the defects were detected, and the probability of their detection was increased by using the developed post-processing algorithm.

4. RELIABILITY OF ULTRASONIC NDT TECHNIQUE AND UNCERTAINTY MEASUREMENT

The reliability of the ultrasonic non-destructive technique in order to detect disbands in dissimilar material joints can be quantified by using the probability of detection (POD) approach [76], [83]. The estimation of POD ensures the accurate size of the defect which can be detected by using a particular NDT technique. Since the POD assessment requires a large number of the same inspections with similar specimens, model-assisted POD is a more appropriate approach to avoid evaluation experimentally and to mitigate the high costs of samples for statistical purposes; see [109], [110], [111].

The goal of this chapter is to estimate the size of the disbond type defect in a layered structure of dissimilar material joints which is possible to detect by using the selected ultrasonic NDT technique before and after the employment of the developed post-processing algorithm enabling to increase the probability of detection.

4.1. Evaluation of model-assisted probability of detection

The POD of disbands in the layered structure of dissimilar material joints was evaluated according to the general methodology of using the numerical models [78]. The numerical models describe the variability of the output of the NDT inspection system which is under the influence of uncertain parameters. The meta-model approach described in Chapter 2 was used for the evaluation of the POD curves. The process of the POD curve evaluation based on inspection simulations is shown in Fig. 4.1 [78].

Firstly, the initial configuration was defined describing all the necessary information of the inspection. Then, the sources of variability were determined and characterised along with their statistical distributions. The sampling of statistical distributions of the determined variable parameters was performed by the Monte Carlo algorithm. The corresponding simulations were calculated. As a result, the POD curves were computed from the obtained results. The reliability of the ultrasonic NDT technique before and after the employment of the developed post-processing algorithm was evaluated by determining the POD of disbands and reported in [78]. The performance of the developed algorithm on the improvement of the disbond detection was assessed by comparing these results.

The three initial steps of the process of the POD curve evaluation were performed in the chapter on the sensitivity analysis where the meta-model was generated. After the meta-model analysis, the POD curves were computed, and the POD parameters were adjusted. The Signal Response method was selected for statistical processing. The defect length (the value of characteristics) is considered as the abscissa of the POD curve. The values of the influential parameters with the similar statistical distributions mentioned in the meta-model analysis were defined (Table 2.5).

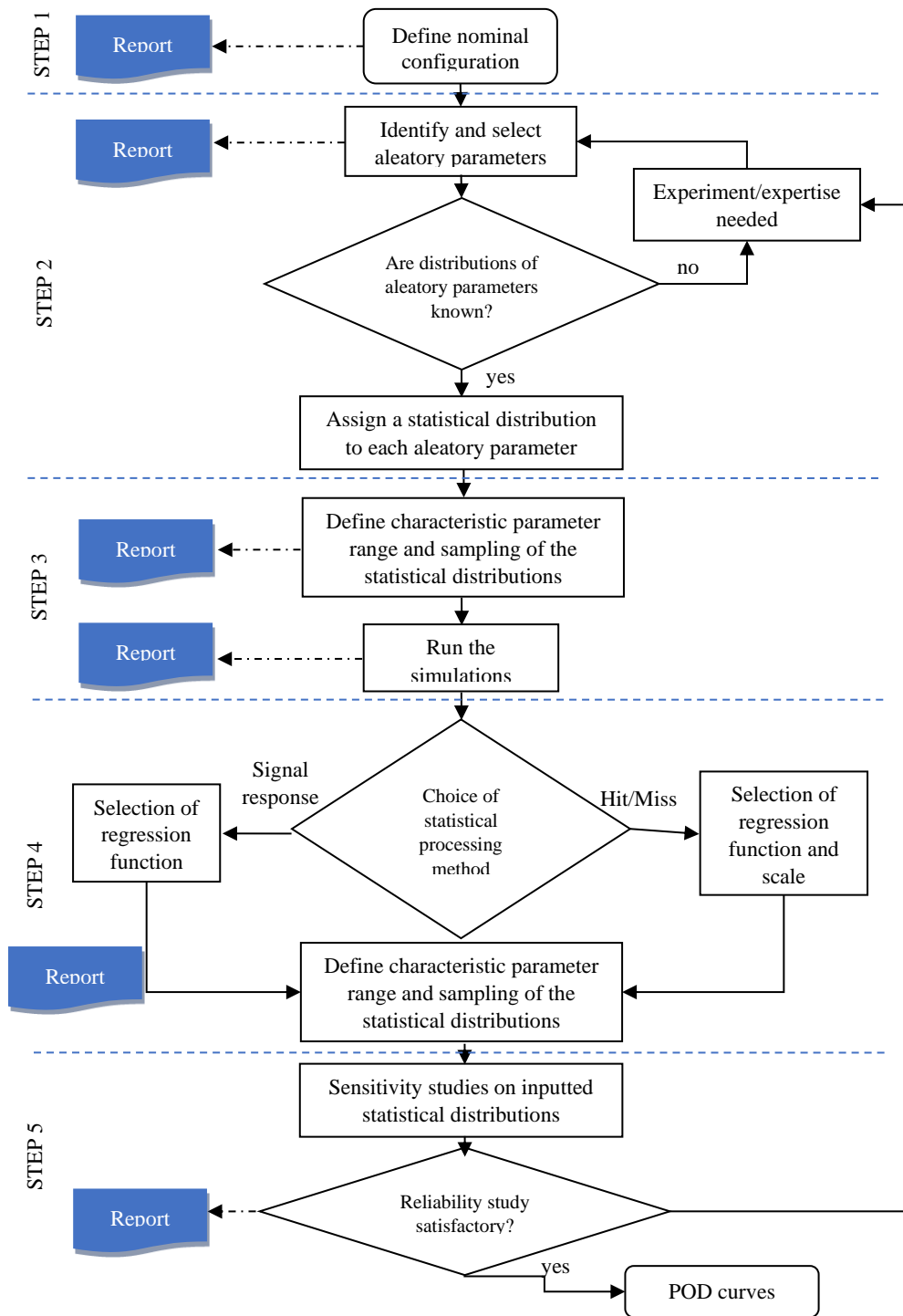


Fig. 4.1 Flowchart of the process of POD curve evaluation [84]

4.1.1. Signal response analysis of disbond detection before algorithm employment

In the case of the Signal Response POD curve computation, 16 characteristic values and 5 samples were defined. The detection threshold was obtained from the analysis of the inspection simulation. The maximum amplitude reflected from the defect-free interface was manually determined. The level of the detection threshold was -9.1dB , which represents the highest level of background noise (the defect-free interface reflection). The noise and saturation thresholds were adjusted in order to fulfil the *Berens* validity criteria and to obtain consistent results regarding the normality and the constantness of variance. The 95% confidence level was defined, the logarithm representation for the X value (the defect length) was selected. Plot \hat{a} vs. a of data representation with the Log data transformation of X as well as the residuals plot is shown in Fig. 4.2.

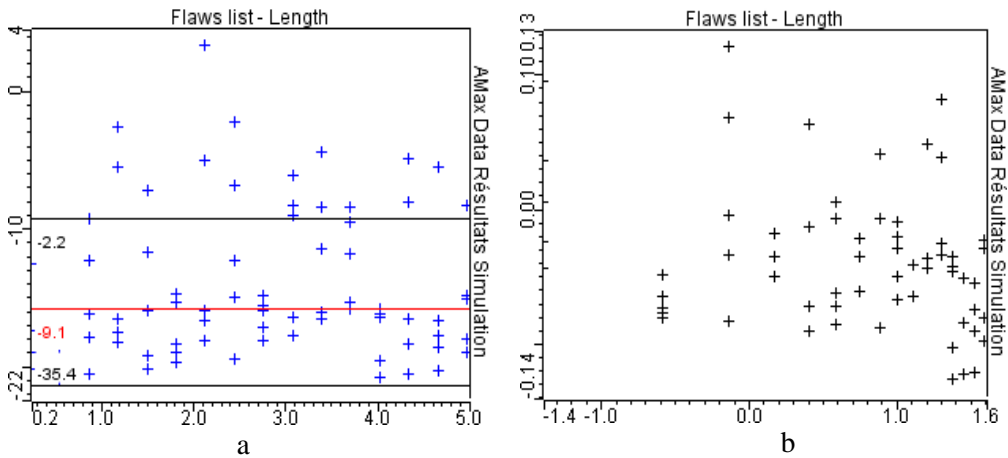


Fig. 4.2 Data representation plots: (a) Plot \hat{a} vs. a with log data transformation, (b) residual plot

The obtained Signal Response POD curve is shown in Fig. 4.3. As a result, no defect can be detected on the component surface in 90% of the inspections with the 95% confidence level. The probability curves which do not reach the 100% probability of detection are not consistent. However, when analysing the obtained POD curve, there is a probability of about 53% that the defect of 5 mm size can be detected. This probability is very low and does not correspond to the measurement requirements, especially in the aerospace industry. This can be caused by the factors which strongly influence the defect detection using the inspection technique.

Therefore, other cases of POD curves were also studied in order to evaluate the probability of defect detection according to the change of the transducer incidence angle and the water path between the transducer and the surface of the component. The obtained POD curves of the Signal Response case are presented in Fig. 4.4 and Fig. 4.5. In these cases, the incidence and the water path were selected as the characteristic values and considered as the abscissa of the POD curves.

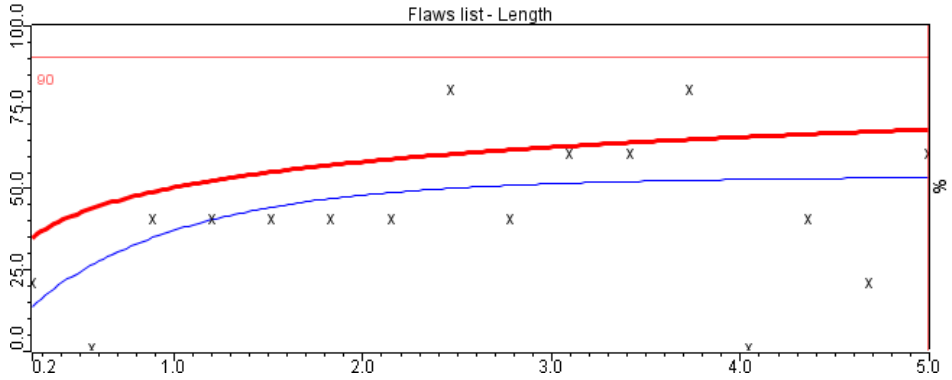
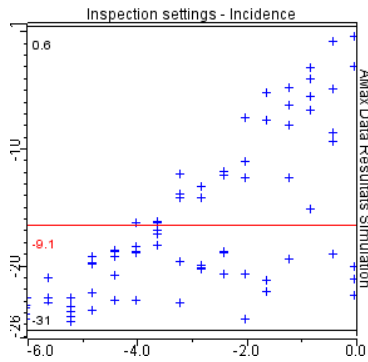
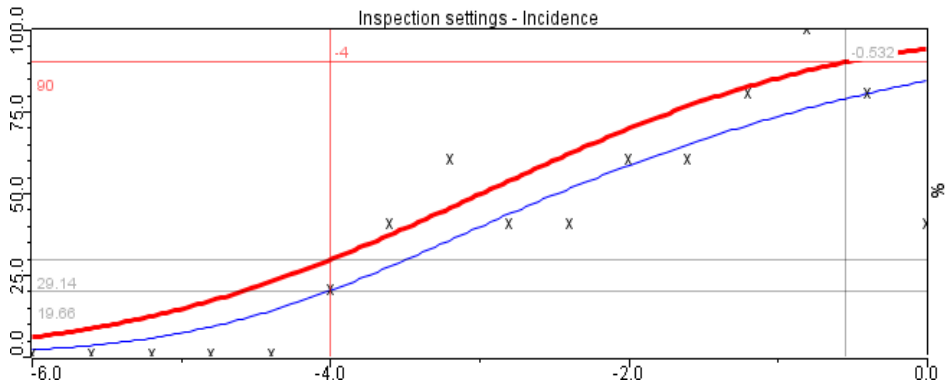


Fig. 4.3 Signal Response POD curve with Log/Lin data for the inspection before algorithm employment (defect length)



a



b

Fig. 4.4 Signal Response POD curve with Lin/Lin data for the inspection before algorithm employment (incidence angle): (a) Plot \hat{a} vs. a with log data transformation, (b) POD curve

As a result of studying the POD curve, it was determined that the disbond within the range of 0.25 mm to 5 mm can be detected with 90% probability in the case of transducer deviation at 0.53° .

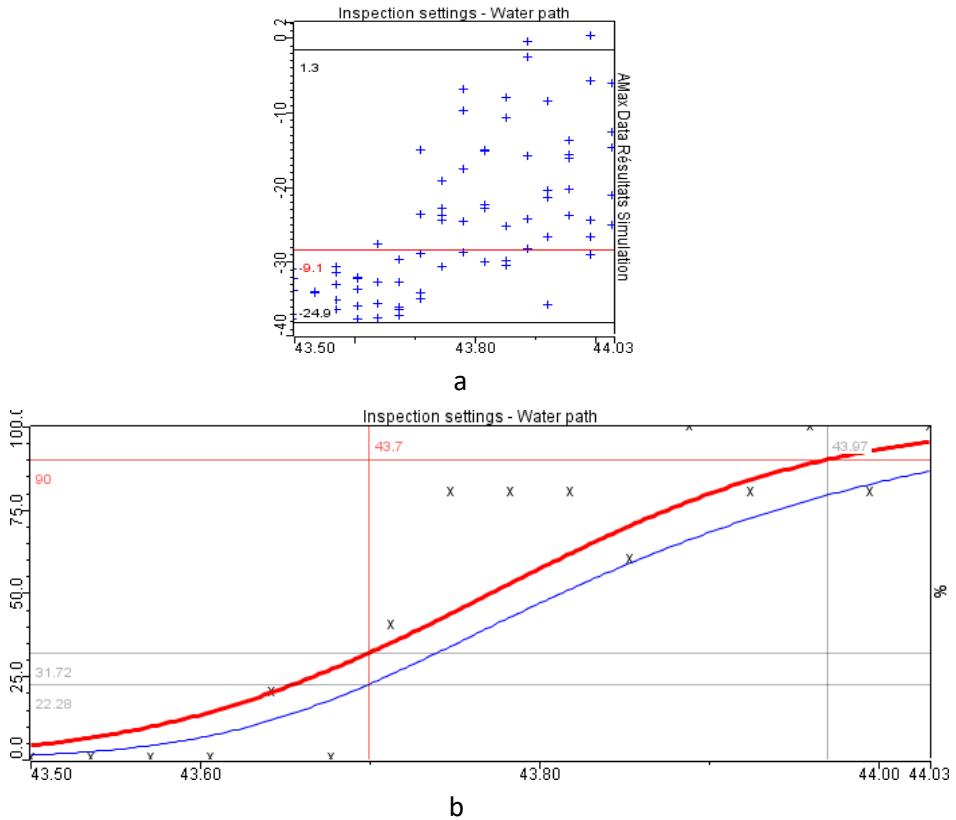


Fig. 4.5 Signal Response POD curve with Lin/Lin data for the inspection before algorithm employment (water path): (a) Plot \hat{a} vs. a with log data transformation, (b) POD curve

According to the analysis of the obtained POD curve, the disbond within the size range of 0.25 mm to 5 mm can be detected with 90% probability in the case of the water path between the surface and the transducer being not less than 43.97 mm.

As a result, the reason of the inability to detect disbands in the interface of the layered structure is within the high possible range of influential factors.

4.1.2. Signal response analysis of disbond detection after algorithm employment

The post-processing algorithm was developed in order to be able to detect disbands in the adhesive layer of dissimilar material joints and to increase the probability their detection. The algorithm was applied for the experimental investigations, and the disbands were detected. In this part, the performance of the developed technique was evaluated according to the assessment of the POD curve for disbond detection. The main factors, such as the angle incidence and the water path, were eliminated with the technique; therefore, these factors were not included

as uncertain parameters for the POD assessment. In addition, the time gates were set in order to cover the subsequent multiple reflection from the interface. The defect length is selected as the characteristic value and considered as the abscissa of the POD curve. The estimated POD curve is presented in Fig. 4.6.

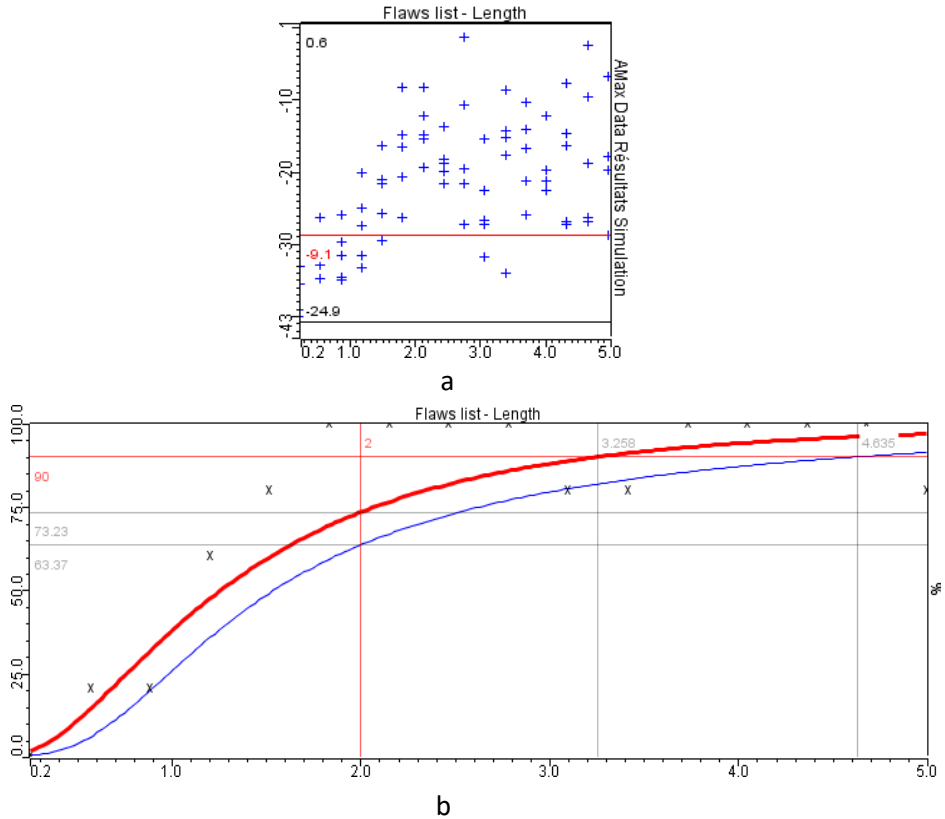


Fig. 4.6 Signal Response POD curve with Log/Log data for the inspection after algorithm employment (defect length): (a) Plot \hat{a} vs. a with log data transformation, (b) POD curve

As a result, a consistent POD curve was obtained by eliminating the most influencing error factors. The length of the disbond a_{90} is 3.26 mm, and it can be detected with 90% probability of detection. The length of the disbond $a_{90/95}$ is 4.64 mm, and it can be detected in 90% of the inspections with the 95% confidence level. The uncertainty value according to the confidence intervals is 1.38 mm.

4.2. Uncertainty measurement

In this section, the uncertainty of the measured defect sizes after applying the developed post-processing algorithm for the disbond detection and the improvement of their detection probability was measured. The measurement uncertainty has to be considered when such numerical criteria as the defect length are applied. Thus, the final results are complete and correct.

Firstly, the mathematical model has to be identified for the uncertainty measurement. In order to calculate the uncertainty of the defect length along the x and y axes, the formula is expressed as given in [112]:

$$Y = f(X_1, X_2, \dots, X_n); \quad 4.1$$

Here, Y is the measurand of the defect length, X_i, \dots are the input quantities (the sources of errors) on which the output quantity Y depends, where $i=1,2,\dots,n$, f is the function of the measurement process.

The ultrasonic testing was performed in the *TecScan* measurement system using an immersion focused transducer, the specimen which is under investigation, and the post-processing of the collected data. While scanning the sample in the system, the averaging number of inspections of 64 was applied. Repetitive measurements allow reducing the errors. The defects in the component were determined by ultrasonic waves, and the sizes were measured by the -6 dB drop method. The measurement was based on the evaluation of the time of flight of ultrasonic waves to the defects and the estimation of the amplitudes of these signals. The time of flight depends on the ultrasonic velocity, whereas the amplitude values depend on the frequency of the transducer, the material thickness, etc. In turn, these parameters are also dependent on the derivative factors of influence.

The main factors influencing the defect detection and the determination of their size were identified in the sensitivity analysis subsection of Chapter 2 and are as follows: the ultrasound velocity in aluminium, the defect depth position in the adhesive layer, the water path between the transducer and the surface of the component, the thickness of aluminium and the surface curvature. Surface curvature as the source of an error was not taken into account for the calculation of uncertainty since this factor was eliminated during post-processing. The ultrasound velocity in aluminium depends on the thickness of the material, the time of flight of ultrasonic waves, and the wavelength which further depends on the excitation frequency. The water path between the transducer and the component surface depends on the focal distance of the transducer, the ultrasound velocity in aluminium and in water, which further depends on the thickness of the media and the time of flight. The thickness of aluminium was measured by using a calliper, and it depends on the instrument resolution. There are other uncertain parameters, such as the room temperature, the operator, the quantisation, the discretisation errors, the electrical noise, etc. However, only the main influencing factors were studied which could potentially have the major effect on the final result comparing to the other factors with insignificant influence. In addition, the method of -6dB drop for sizing the defects does not involve any systematic error.

The standard uncertainty of each influencing factor was quantified by type A and type B uncertainty evaluation. Type A is based on the statistical analysis of independent direct measurements. Type B is based on indirect measurements taken from previous measurements, on experience, or on the general knowledge and sources, etc.; see [112], [113], [114], [115], [116]. As a result, the influencing factors or the sources of errors, their derived factors as well as the appropriate uncertainty type and measurement model for each are presented in Table 4.1.

Table 4.1. Influencing factors and mathematical models

No	Sources of errors	Uncertainty type	Model
1	Velocity of ultrasound in aluminium, V_{al}	B	$V_{al} = \left(\frac{2H_{al}}{t_{al}}\right)$;
2	Thickness of aluminium, H_{al}	A	Statistical analysis
3	Resolution of calliper, r_c	B	Instrument values, $r_c=0.01$
4	Time of flight to aluminium-adhesive bond and back, t_{al}	A	Statistical analysis
5	Wavelength of ultrasound in aluminium, λ_{al}	B	$\lambda_{al} = \left(\frac{V_{al}}{f_{freq}}\right)$;
6	Transducer frequency, f_{freq}	B	Technical documentation
7	Defect depth position in adhesive layer, D_d	A	Statistical analysis
8	Water path between transducer and surface, W_p	B	$W_p = F - M_D \left(\frac{V_{al}}{V_w}\right)$;
9	Focal distance, F	B	Technical documentation
10	Ultrasound velocity in water, V_w	B	$V_w = \left(\frac{2H_w}{t_w}\right)$;
11	Thickness of water medium, H_w	A	Statistical analysis
12	Time of flight to water-aluminium bond and back, t_w	A	Statistical analysis

The measurement of ultrasound velocity in water was performed several times. Thus, the evaluation of thickness of the medium and the time of flight was calculated by statistical analysis. In the case of direct measurements performed by statistical analysis, the mean values of multiple independent observations were calculated according to the following Equation:

$$\bar{x} = \frac{1}{N} \sum_{i=1}^N x_i ; \quad 4.2$$

Here, N is the number of independent measurements, x_i is the measured value.

The next step is to calculate the standard uncertainty for direct measurements which is expressed as:

$$u(x_i) = \sqrt{\frac{1}{N(N-1)} \sum_{i=1}^N (x_i - \bar{x})^2} ; \quad 4.3$$

Here, N is the number of independent measurements, x_i is the measured value.

In order to calculate the standard uncertainty for instrument resolution, the uniform or rectangular distribution law has to be applied, and it is expressed as:

$$u(r_c) = \frac{r_c/2}{\sqrt{3}} ; \quad 4.4$$

Here, r_c is the resolution of the instrument.

The equation for the combined uncertainty which considers the resolution amendment was calculated according to the following Equation:

$$u(y) = \sqrt{u(x_i)^2 + u(r_c)^2}; \quad 4.5$$

In the case of the B type measurement, the standard uncertainty is calculated as follows (the uniform distribution law is considered for the equal probability of the range of the values):

$$u(x_i) = \frac{\Delta}{\sqrt{3}}; \quad 4.6$$

Here, Δ is the error of resolution.

The next step is to estimate the influence coefficient $W(x)$ of the x value of the mathematical model:

$$W(x_i) = \frac{\partial f}{\partial x_i}; \quad 4.7$$

Here, f is the mathematical model of uncertainty measurement.

Furthermore, the combined uncertainty for the indirect type measurements is determined according to Equation 4.8:

$$u(y) = \sqrt{\sum_{i=1}^n u(x_i)^2 \cdot W(x_i)^2}; \quad 4.8$$

There was a correlation between the thickness and the time of flight while the measurement of the ultrasound velocity was performed. The correlation provides an additional uncertainty component which has to be considered:

$$r(x_i, x_j) = \frac{u(x_i, x_j)}{u(x_i) \cdot u(x_j)}; \quad 4.9$$

Here, $r(x_i, x_j)$ is the correlation coefficient of the values x_i, x_j , $u(x_i, x_j)$ is the covariance of the input values.

The correlation coefficient changes within the range [-1; 1]. In this case, the value is positive and equals to 1 since, in the relation of two variables, both of them move in the same direction in which an increase of the thickness is associated with the increase of the time of flight. As a result, the equation of combined uncertainty which considers the additional component of correlation is expressed as follows:

$$u(y) = \sqrt{\sum_{i=1}^n u(x_i)^2 W(x_i)^2 + 2 \sum_{i=1}^n \sum_{j=1}^n W(x_i) W(x_j) r(x_i, x_j) u(x_i) u(x_j)}; \quad 4.10$$

The results of the calculated standard uncertainties, influence coefficients and combined uncertainties of various mathematical models are presented in Table 4.2.

Table 4.2. Results of calculated standard and combined uncertainties

Mathematical model, f	Sources of errors, x_i	Standard uncertainty, $u(x_i)$	Influence coefficient, $W(x_i)$	Combined uncertainty, $u(y)$
H_{al}	H_{al}	0.0035 mm	-	0.0450 mm
	r_c	0.0029 mm	-	
$V_{al} = \left(\frac{2H_{al}}{t_{al}}\right)$	H_{al}	0.0450 mm	$3.95 \mu\text{s}^{-1}$	0.1828 mm/ μs
	t_{al}	0.0034 μs	$-12.58 \text{ mm}/\mu\text{s}^2$	
$\lambda_{al} = \left(\frac{V_{al}}{f_{freq}}\right)$	V_{al}	0.1828 mm/ μs	0.1 MHz^{-1}	0.0234 mm
	f_{freq}	0.2309 MHz	$0.0636 \text{ mm}/\mu\text{sMHz}^2$	
$V_w = \left(\frac{2H_w}{t_w}\right)$, including $r(x_i, x_j)$	H_w	0.1934 mm	$0.0341 \mu\text{s}^{-1}$	0.0007 mm/ μs
	t_w	0.2537 μs	$-0.0257 \text{ mm}/\mu\text{s}^2$	
$W_p = F - M_D \left(\frac{V_{al}}{V_w}\right)$	V_{al}	0.1828 mm/ μs	$-1.0835 \mu\text{s}$	0.3540 mm
	V_w	0.0007 mm/ μs	$4.6459 \mu\text{s}$	
	F	0.2933 mm	1	
D_d	D_d	0.0635 mm	-	0.0635 mm

The value of the material depth M_D is constant since it is selected by the operator depending in which depth the transducer beam is desired to be focused. The summarised uncertainty was calculated for all the sources of error which exert influence on the length of the defects located in the interface of the component. The combined uncertainty was expanded to the confidence level of 95% and expressed as determined by Equation 4.11:

$$u_{exp} = k \cdot u(y); \tag{4.11}$$

Here, $k = 2$ is the coverage number selected from the Student's table (the normal distribution law).

As a result, the expanded uncertainty for the detected defect length along the x and y axes is 0.88 mm. The final metrological results for every defect with the calculated uncertainty are presented in Table 4.3.

Table 4.3. Final metrological results

Defect	Length along x axis, mm	Length along y axis, mm	Uncertainty, mm
Biggest defect	14.3	15.7	± 0.88
Medium defect	10.3	11.4	
Smallest defect	4.9	6.2	

As a result, the complete results of the length of disbonds detected by the ultrasonic measurement system and the applied post-processing algorithm were measured by the estimation of uncertainty.

4.3. Conclusion of the chapter

1. The evaluation of the POD curves was performed by using the Signal Response analysis based on the meta-model generation and the detection threshold which corresponds to the highest level of the noise (defect-free interface reflection in the case of layered structures). The obtained results demonstrated that it is not possible to detect disbonds by the ultrasonic NDT technique in the adhesive of the layered structure of dissimilar material joints. The probability of detection is only 50%, which is very low.

2. The most influential parameters according to the sensitivity analysis were studied, and the limit values of the range at which the defects can be detected were assessed. In the case of the incidence angle uncertain parameter, the deviation should not exceed 0.5° in order to be able to detect a defect with 90% probability. For the water path factor, the range should be from 43.9 mm to 44.03 mm in order to be able to detect a defect with 90% probability.

3. The application of the developed post-processing technique made it possible to detect disbonds in the adhesive layer of various sizes. The defect size of 3.26 mm can be detected in 90% of the inspections with the 95% confidence level. Therefore, when using this technique, the defects smaller than 5 mm (the smallest defect existing in the component under investigation) can be detected.

4. The uncertainty of the defect sizes detected and measured in the experimental part when using the developed post-processing algorithm was assessed, and it equals to 0.88 mm of the 95% confidence level.

GENERAL CONCLUSIONS

1. Ultrasonic non-destructive testing, evaluation of reflection and transmission coefficients, data post-processing as well as the study of influential factors and the evaluation of probability of detection were selected in order to create a methodology which will enable disbond type defects to be detected in dissimilar material joints with improved detectability.

2. The analysis of multiple reflections from the interface significantly increases the probability of disbond detection due to the increase in the amplitude difference of the signals reflected from defect-free and defected regions. The main factor influencing defect detection in components with layered structures is the surface/interface curvature which is characterised by such uncertain parameters as the angle of incidence of the ultrasonic beam and the water path. These parameters have an impact of 57% and 39%, respectively.

3. Modelling based on the arrival time of ultrasonic waves allowed to identify the time intervals where the maximum amplitude change is observed by comparing the modelled signals reflected from the defective and defect-free areas. The method for the investigation of adhesively bonded dissimilar material joints was created to extract valuable features for the development of the post-processing algorithm in order to increase the probability of defect detection in the adhesive layer. The extracted features are as follows: the time of flight and the time intervals of the reflected signals while taking into account multiple interface reflections, the amplitude change and the ratio coefficients of amplitudes of the selected time intervals. The investigation method includes the following steps: analysis of multiple reflections and boundary characteristics, sensitivity analysis, numerical study, and the optimisation of parameters.

4. The developed data post-processing algorithm includes the zero-crossing technique for the time alignment of signals reflected from the sample surface, analysis of the subsequent multiple reflections, the determination of time instants for the identification of time gates and the ratio coefficients of the peak-to-peak amplitudes

5. By using the developed algorithm, all the disbonds/delaminations in the adhesive layer of dissimilar material joints were detected (without using the algorithm, the detection is not possible at all), and their dimensions were estimated: 14.3x15.7 mm \pm 0.88 mm (the largest defect), 10.3x11.4 mm \pm 0.88 mm (the medium-sized defect), 4.9x6.2 mm \pm 0.88 mm (the smallest defect). The developed technique can detect disbonds/delaminations in the adhesive layer after applying the developed algorithm in the inspection in 90% of inspections with the 95% confidence level according to the results of the MAPOD evaluation. In comparison, there was no possibility to detect the defects in dissimilar material joints in the case of ultrasonic inspection without applying the algorithm.

FUTURE SCOPE OF RESEARCH

In the performed study, the probability of detection is increasing in general for the adhesive layer. However, future research could concentrate on the increase in the detection probability of the defect location at the metal adhesive, in the middle of the adhesive and adhesive-composite separately for each bonding under interest. In addition, the procedure for selecting the arrival time and the time gates can be automated for other metal and adhesive layer thicknesses.

SANTRAUKA

Darbo aktualumas

Nuolat tobulėjančiame pasaulyje atsiranda naujų reikalavimų, siekiant pagerinti konstrukcijų, technikos, metodų ir kt. efektyvumą ir patikimumą. Aerokosminėje, automobilių, civilinėje ir jūrų pramonėje keliami įvairūs reikalavimai eksploatacinėms konstrukcijų savybėms, atsižvelgiant į žmonių gyvybės ir sveikatos saugą, aplinkosaugą bei ekonominę naudą. Todėl patikros sistemų patikimumas yra svarbus norint įgyvendinti šiuos reikalavimus. Reikalavimas pagerinti konstrukcijų eksploatacines savybes paskatino mokslininkus dirbti ir kurti naujas pažangias medžiagas ir jų sujungimus [1, 2]. Dabartinė tendencija rodo, kad vis dažniau metaliniai komponentai yra pakeičiami pažangiomis kompozitinėmis medžiagomis, užtikrinančiomis mažą konstrukcijos svorį bei leidžiančioms sumažinti CO₂ emisiją [3]. Kompozitai populiarūs ne tik dėl galimybės sumažinti svorį, bet ir dėl geresnių mechaninių savybių, lyginant su metalų lydiniais. Kompozitinių medžiagų anizotropinės savybės leidžia gaminti tvirtas ir standžias konstrukcijas, taip pat pagerina konstrukcijos aerodinamines bei eksploatacines savybes ir degalų sunaudojimo efektyvumą. Tačiau kompozito laminato ir jo struktūrų priklausomybė nuo aplinkos sąlygų neleidžia visų metalinių komponentų pakeisti kompozitinėmis medžiagomis, todėl reikalingi ir plačiai naudojami metalo-kompozito sujungimai. Sujungtos skirtingos medžiagos, pavyzdžiui, aliuminis ir anglies pluoštu armuotas plastikas (angl. CFRP), sustiprina struktūrą ir pasižymi geresnėmis nuovargio charakteristikomis, atsparumo smūgiams ir liekamojo stiprumo savybėmis. Šie skirtingų medžiagų sujungimai kelia didelį susidomėjimą ir yra plačiai naudojami gaminant lėktuvų fiuzeliažus, sparnų konstrukcijas ir variklius [4, 5, 6].

Šių medžiagų sujungimo technologija yra labai svarbi ir turi didelę įtaką visam konstrukcijos svoriui. Pavyzdžiui, mechaniniam sujungimui būdingas varžtų, kniedžių ir kitų tvirtinimo elementų naudojimas, kuris turi įtakos ne tik konstrukcijos svoriui, bet ir sluoksnių vientisumui. Kai medžiagos sujungiamos klizais, išsaugomas konstrukcijos vientisumas, taip pat sumažinamas konstrukcijos svoris ir tolygiai paskirstomi mechaniniai įtempiai [2]. Kritiškiausia tokių jungčių vieta yra sukibimo zona. Defektai dviejų sluoksnių riboje gali atsirasti gamybos proceso arba eksploatacijos metu. Tokie defektai labai pavojingi, nes yra nematomi, tačiau gali stipriai paveikti sujungimo kokybę ir lemti konstrukcijos gedimą [4]. Klizais sujungtų skirtingų medžiagų naudojimas konstrukcijose vis dar yra ribotas, nes nėra universalus ir patikimo sujungimo kokybės įvertinimo metodo.

Ultragarsiniai neardomieji bandymai yra plačiai taikomi įvairioms medžiagoms ir konstrukcijoms tikrinti. Ultragarsinė patikra turi didelį potencialą įvertinant struktūrinį klizuočių sujungimų vientisumą bei siekiant aptikti tokius defektus kaip atsiskuoksniaivimas, sukibimo pažeidimai (angl. *disbonds*), poros ir komponento geometrijos nuokrypiai [3]. Daugelis tyrėjų šį metodą taikė siekdami apibūdinti klizuojamų medžiagų sukibimo kokybę [2]. Kita vertus, nėra vieno

patikimo metodo, kuris būtų tinkamas skirtingų medžiagų sujungimams tirti [7]. Šiame darbe ultragarsinė patikra naudojama kritiniams defektams, pavyzdžiui, metalo ir kompozitinės medžiagos atsiluoksniavimui, aptikti.

Mokslinė ir technologinė problema

Pagrindinė problema atliekant skirtingų medžiagų klijavimo srities kokybės kontrolę yra ta, kad sunku nustatyti sukibimo defektus, nes nėra patikimo metodo, kuris leistų aptikti defektus su didele tikimybe. Kljais sujungtų skirtingų medžiagų kokybės ultragarsinių tyrimų kompleksiškas yra tas, kad tai daugiasluoksnės struktūros, turinčios sudėtingą geometriją, skirtingas elastines ir akustines savybes. Didelis metalų ir kompozitų akustinės varžos skirtumas lemia gana reikšmingą atspindžio koeficientą metalo ir kompozito, metalo ir klijų arba klijų ir metalo ribose. Tai reiškia, kad didžiausias ultragarso energijos kiekis atspindės skirtingų medžiagų jungčių sandūroje. Tačiau šiuose sujungimuose esantys sukibimo pažeidimai yra užpildyti oru ir taip pat pasižymi dideliu atspindžio koeficientu. Dėl to ultragarso banga atspindės ir nuo defektų turinčių, ir nuo defektų neturinčių sujungimo vietų, todėl dėl didelės atspindžio amplitudės, kuri gali būti panaši į defektų neturinčios ribos atspindžio amplitudę, yra sunku aptikti defektus, esančius metalo ir klijų riboje. Be to, skirtingų medžiagų sujungimų atveju ultragarso bangos sunkiai skverbiasi į struktūrą, todėl defektų nustatymas priešingoje sujungimo vietoje yra dar sudėtingesnis. Kita gana didelė kokybės kontrolės problema yra labai ploni komponentai, ypač klijų sluoksnis. Klijų storis gali būti nuo 0,1 mm storio. Dėl to iškyla problema atskirti atspindžius nuo atskirų sluoksnių ribų dėl jų persidengimo laiko srityje. Dėl to sunku aptikti defektinius sujungimus lyginant signalus, atsispindinčius nuo defektinių ir nedefektinių sujungimų sluoksniuotose struktūrose, sudarytose iš skirtingų medžiagų [4, 6, 7, 9].

Darbo hipotezė

Naudojant neardomųjų bandymų metodą, teorinę bangų ir defektų sąveikos analizę, kokybinius ir kiekybinius vertinimus, taip pat signalų modeliavimą ir parametrų optimizavimą, galima sukurti pažangų apdorojimo algoritmą, kuris leistų padidinti sukibimo defektų / delaminacijos aptikimo tikimybę skirtingų medžiagų sujungimo klijų sluoksnyje. Naudojant sukurtą metodą turėtų būti įmanoma aptikti didesnius nei 5 mm defektus su 1 mm neapibrėžtimi.

Tikslas ir uždaviniai

Disertacijos tikslas – sukurti pažangos metodiką, skirtą aptikti sukibimo defektus skirtingų medžiagų sujungimuose su padidinta aptikimo tikimybe (POD), ir įvertinti jos efektyvumą kontroliuojant struktūrinį vientisumą sujungimo srityje. Šiam tikslui pasiekti buvo suformuluoti tokie uždaviniai:

1. Atlikti literatūros analizę, siekiant įvertinti esamus metodus, taikomus sluoksniuotų konstrukcijų patikrai, jų privalumus ir trūkumus, bei atrinkti tinkamiausius metodus, kurie galėtų būti naudojami darbo tikslui pasiekti ir nustatytiems uždaviniams spręsti.

2. Ištirti bangų ir defektų sąveikos principus adheziniuose sujungimuose, įskaitant bangų reverberaciją struktūroje, fazės pokytį ir atspindžio dydį. Atlikti ultragarsinių tyrimų kokybinį vertinimą, siekiant nustatyti pagrindinius faktorius, turinčius įtakos defektų aptikimui sluoksniuotose struktūrose, skirtingų medžiagų sujungimuose.

3. Sukurti modelį, pagrįstą ultragarso bangų atsklidimo laiku ir laiko intervalų parinkimu. Nustatyti kriterijus, kurie galėtų būti naudojami defektų aptikimui pagerinti skirtingų medžiagų sujungimuose pagal sukurtą tyrimo metodą, apimančią teorinius, kokybinius ir kiekybinius vertinimus.

4. Sukurti signalų apdorojimo algoritmą, pagrįstą atrinktais parametrais, siekiant padidinti pasirinkto neardomojo bandymo metodo efektyvumą ir pagerinti defektų aptikimo tikimybę.

5. Verifikuoti siūlomą metodiką įvertinant aptiktų defektų dydį ir jų neapibrėžtį. Įvertinti defektų aptikimo tikimybę prieš ir po signalų apdorojimo algoritmo taikymo.

Mokslinis naujumas

Disertacijos naujumas – nauja metodika, leidžianti nustatyti defektus klijų sluoksnyje tarp dviejų skirtingų medžiagų ir užtikrinti geresnį jų aptikimo patikimumą.

1. Atlikus jautrumo analizę ir įvertinus defektų aptikimo tikimybės kreives pagal sudarytą metamodelį pasirinktam ultragarsiniam patikros metodui, taikomam skirtingų medžiagų sujungimams, nustatyti šie svarbiausi faktoriai, turintys įtakos defektų aptikimui: objekto paviršiaus kreivumas, atstumas tarp keitiklio ir objekto bei defekto gylis klijų sluoksnyje.

2. Kokybiniais ir kiekybiniais vertinimais, teorine analize ir signalų modeliavimu pagrįstas tyrimo procesas leidžia išgauti vertingas charakteristikas (atspindėtų signalų laiko momentus ir laiko intervalus, amplitudės pokyčius ir pasirinktų laiko intervalų amplitudžių santykius), reikalingas norint sukurti patobulintą sukibimo defektų nustatymo metodą.

3. Sukurtas ir sėkmingai įgyvendintas naujas signalų apdorojimo algoritmas, kuriuo siekiama pagerinti defektų aptikimą klijų sluoksnyje tarp skirtingų medžiagų, t. y. metalų ir kompozitinių medžiagų.

Praktinė darbo vertė

1. Siūloma metodika gali būti naudojama kaip pagrindas daugiasluoksnių struktūrų analizei. Ji leidžia aptikti kelių medžiagų riboje esančius defektus, skatina universalaus, ekonomiško ir patikimo testavimo metodo kūrimą, kadangi padidina defektų aptikimo tikimybę.

2. Siūlomi signalų apdorojimo metodai gali būti labai svarbūs nustatant defektus klijų sluoksnyje, ypač sudėtinguose skirtingų medžiagų sujungimuose.

3. Siūlomi signalų apdorojimo algoritmai gali būti panaudojami kaip matavimo sistemos dalis vertinant skirtingų medžiagų konstrukcijos vientisumą.

4. Tyrimo rezultatai gali prisidėti prie tolesnių klįjais sujungtų skirtingų medžiagų vientisumo tyrimų.

Gynimui pateikiami rezultatai

1. Tyrimo proceso etapai, atliekami siekiant gauti vertingų kriterijų, kurie bus naudojami algoritme, siekiant pagerinti nesukibimo aptikimą. Metodas susideda iš tyrimo modeliavimo, signalų modeliavimo, teorinės analizės ir kokybinio įvertinimo.

2. Jautrumo analizė, pagrįsta metamodelio skaičiavimu, siekiant nustatyti pagrindinius faktorius, darančius įtaką defektų aptikimo galimybei konstrukcijose, naudojant pasirinktą neardomojo bandymo metodą.

3. Pagrindiniai sukurtų apdorojimo algoritmų etapai grindžiami išskirtomis savybėmis ir tyrimo metodu gautais rezultatais.

4. Eksperimentinis objektų tyrimas ir sukurtų algoritmų įgyvendinimas, taip pat defektų dydžių ir jų neapibrėžties matavimas, siekiant patikrinti ir pademonstruoti pasiektus rezultatus.

5. Procesas, naudojamas POD kreivėms įvertinti ir aptikimo ribai nustatyti, kad būtų gauti patikimi defektų dydžių rezultatai, kuriuos galima aptikti NDT metodu, prieš ir po to, kai buvo pritaikytas sukurtas apdorojimo algoritmas.

Aprobavimas

Tyrimo metu gauti rezultatai paskelbti šešiose publikacijose: trys publikacijos išspausdintos tarptautiniuose žurnaluose, priklausančiuose *Thomson Reuters ISI Web of Science* duomenų bazei, turinčiuose įtakos faktorių, viena publikacija atspausdinta recenzuojamuose tarptautinių konferencijų leidiniuose, indeksuojamuose *Web of Science*, be įtakos faktoriaus, o kitos dvi publikacijos išleistos recenzuojamuose tarptautinių konferencijų leidiniuose. Taip pat rezultatai buvo pristatyti šešiose tarptautinėse mokslinėse konferencijose, kurios vyko Geteborge, Palangoje, Vilniuje, Atėnuose, Paryžiuje, bei dvi virtualiose tarptautinėse konferencijose. 2020 m. doktorantūros stipendiją už studijų rezultatus skyrė Lietuvos mokslo taryba. 2018–2019 m. stipendiją doktorantei skyrė Kauno technologijos universitetas.

Disertacijos struktūra ir turinys

Disertaciją sudaro įvadas, keturi skyriai, bendrosios išvados, būsimų tyrimų apimtis, literatūros sąrašas ir autorės mokslinių publikacijų sąrašas. Iš viso yra 160 puslapių, įskaitant 72 paveikslus, 22 lentelių, 50 matematines formules ir 116 bibliografinių nuorodų.

Pirmajame skyriuje aptariami esami bandymų metodai, būdai ir metodikos, kurie gali būti taikomi daugiasluoksniams konstrukcijoms tirti, siekiant aptikti defektus klįjų sluoksnyje.

Antrajame skyriuje aprašomas nustatytas tyrimo metodas, reikalingas išsamiai išanalizuoti metodiką ir tyrimo objektus, išnagrinti jų galimybes ir apribojimus, kad būtų išskirtos informatyvios charakteristikos defektų nustatymo algoritmui tobulinti.

Trečiajame skyriuje pateikiami rezultatai, gauti atlikus eksperimentinį tyrimą su skirtingų medžiagų sujungimo objektais, kurių defektus sunku aptikti. Be to, po

apdoravimo sukurto defektų aptikimo algoritmo veiksmingumas buvo įrodytas matuojant aptiktų defektų matmenis.

Ketvirtajame skyriuje įvertinama pasirinkto ultragarsinio metodo aptikimo tikimybė, pagrįsta metamodelio sukūrimu prieš ir po sukurto apdoravimo algoritmo taikymo. Taip pat pateikiama vertė, apibūdinanti defektų aptikimo pagerėjimą.

1. SKIRTINGŲ MEDŽIAGŲ SUJUNGIMŲ ULTRAGARSINĖ DEFEKTOSKOPIJA

Literatūros analizė atlikta siekiant išanalizuoti esamus metodus ir būdus, kurie naudojami skirtingų medžiagų sujungimams tikrinti arba kurie gali būti taikomi tokiems objektams tirti.

1.1. Skirtingų medžiagų sujungimas

Reikalavimai, kad konstrukcijos pasižymėtų tokiomis savybėmis kaip mažas svoris, didesnis efektyvumas ir funkcionalumas, skatina naudoti daugiasluoksnės hibridines konstrukcijas [10]. Kompozitinių komponentų sujungimo su metalais būdai yra trys: klijavimas, mechaninis tvirtinimas ir šių dviejų būdų derinys. Klijavimas – tai metodas, kuris tinka bet kokioms vienodoms ir skirtingoms medžiagoms sujungti. Klijų sujungimas yra plokščias ir tolygiai pasiskirstantis komponentų paviršiuje, esančiame tarp dviejų medžiagų. Kita vertus, jungčių ilgaamžiškumas priklauso nuo klijų stiprumo ir sujungtų medžiagų degradacijos laikui bėgant. Apskritai klijų efektyvumą apibūdina klijų cheminės ir fizikinės savybės, sukibusių paviršių paruošimas klijavimui ir sujungimo konstrukcija. Mechaninis tvirtinimas vis dar plačiai naudojamas lėktuvų ir automobilių pramonėje. Tačiau skylės grėžimas sutrikdo sujungimo zonos būklę ir gali tapti defektų atsiradimo priežastimi, nors jie suteikia aukštą medžiagų sujungimo stiprumą. Kiti trūkumai – didelės išlaidos tvirtinimo detalėms ir tvirtinimui, taip pat pridėtinis konstrukcijos svoris [10, 11]. Taigi visi sujungimo būdai turi savų privalumų ir trūkumų. Tačiau šiuo metu lėktuvų ir automobilių pramonėje keliami reikalavimai mažai konstrukcijos masei, degalų taupymui ir aplinkos apsaugai. Tai skatina įvairių medžiagų sujungimui naudoti klijus, taip pat metalo konstrukcijas pakeisti lengvesnėmis kompozitinėmis medžiagomis ar kompozito ir metalo hibridais [11].

1.2. Klijų sujungimas: metodo aprašymas, defektų tipas

Pagrindiniai šio metodo privalumai – galimybė sumažinti konstrukcijų svorį ir tolygiai paskirstyti apkrovas. Tokio sujungimo silpniausia vieta yra sukibimas ir dėl silpnesnio klijų stiprumo joje gali kilti problemų, lyginant su metalais ar kompozitais ir jų sujungimais [12, 13]. Išsamūs tyrimai atlikti siekiant nustatyti sujungtų vienodų medžiagų gedimus, pvz., metalų ir kompozitų, tačiau vis dar trūksta tyrimų su sujungtomis skirtingomis medžiagomis [14, 15, 16, 17]. Buvo atlikti įvairūs tyrimai, tokie kaip baigtinių elementų analizė ir eksperimentiniai tyrimai, siekiant įvertinti keturių skirtingų jungčių konfigūracijų eksploatacinių

savybių skirtumus. Nustatyta, kad jungčių konfiguracijos, perdengimo ilgis, kompozitų storis ir kampas turi didelę įtaką sujungimo stiprumui [12, 13].

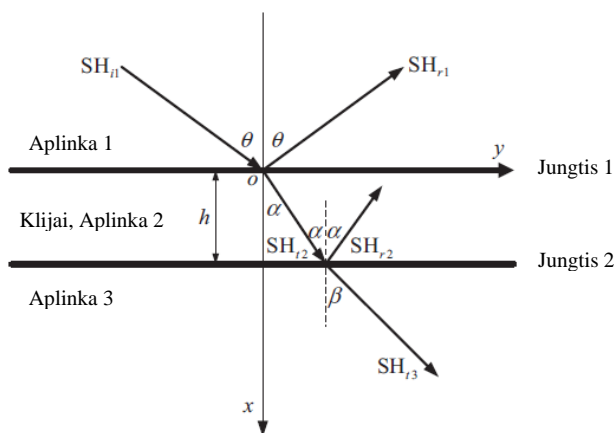
Pagrindinis kritinis defektų tipas kljais sujungtose vienodose ir skirtingose medžiagose yra sukibimo defektai, kurie turi neigiamos įtakos šlyties įtempių pasiskirstymui kljų sluoksnyje. Kljų sluoksnyje gali atsirasti tokių defektų kaip atsisluoksniavimas, sukibimo defektas, silpnas sukibimas ir oro intarpai. Atlikus tyrimus įrodyta, kad didėjant šių defektų dydžiui mažėja jungties stiprumas [24, 25, 26]. Kljų sujungimo patikimumui didžiausią įtaką turi defektų atsiradimas ir jų vieta, taip pat medžiagų paviršių paruošimas prieš kljavimą ir kietėjimo proceso kontrolė. Atsiradę defektai yra vienas svarbiausių veiksnių, sumažinančių sujungimo patikimumą, todėl jų įtakos tyrimas yra svarbus uždavinys [19, 20].

Sukibimo vieta yra silpniausia daugiasluoksnių konstrukcijų vieta, kurios kokybę reikia patikrinti ir įvertinti. Kljų vientisumas priklauso nuo kljų stiprumo, įtempių pasiskirstymo, konstrukcinės sujungimų konfiguracijos ir sukibimo defektų. Kljavimo stiprumas taip pat priklauso nuo paviršiaus paruošimo, apdirbimo, kljų sluoksnio storio ir kt. Be to, nustatyta, kad kljų storis yra vienas iš svarbiausių parametrų, darančių didelę įtaką bendram konstrukcijos stiprumui. Sujungtų medžiagų laikomoji galia padidėja, kai sumažėja kljų storis [19, 20, 24]. Šiame darbe buvo tiriamos kljais sujungtos plokštės, pagamintos iš skirtingų medžiagų su dirbtiniais defektais kljų sluoksniuose.

1.3. Ribinių charakteristikų vertinimas

Ultragarsinės atspindžio ir perdavimo charakteristikos naudojamos neardomuosiuose bandymuose kljų sukibimo savybėms įvertinti. Kljų storį ir medžiagos elastines savybes galima nustatyti pagal ultragarso bangų atspindžius. Be to, taikant šį metodą galima kiekybiškai ir kokybiškai įvertinti kljų sukibimo stiprumą arba degradaciją. Metalas-kompozitas ir kompozitas-kompozitas suklijuotų jungčių ultragarso bangų sklidimo charakteristikos yra sudėtingesnės, palyginus su metalas-metalas suklijuotomis jungtimis, nes skiriasi medžiagų tipų seka [31].

Buvo atlikti eksperimentiniai ir teoriniai sujungimo degradacijos tyrimai kompozitiniuose bandiniuose analizuojant tarpfazines ir kohezines savybes. Atliekant ultragarsinę patikrą įstrižais kampais, paaiškėjo, kad sukibimo degradaciją galima įvertinti pagal atspindžių amplitudės pokytį ir pagal atspindėto signalo spektro minimumo poslinkį [32]. Taip pat buvo atlikti storų kljų sluoksnių tyrimai, kuriuose buvo įvestas modelis su dviguba riba ir ištirtas poveikis atspindžio ir perdavimo elgsenai sujungimuose [33]. Taip pat buvo atlikti daugiasluoksnių konstrukcijų vidinės ribinės būklės tyrimai naudojant nukreipiamąsias bangas [34, 35, 36]. Ding ir kiti [37] savo tyrime iš bangų sklidimo lygčių ir tangentinio standumo koeficiento K_T išvedė ultragarsinių bangų SH režimo (SH0) atspindžio ir perdavimo koeficientus daugiasluoksneje konstrukcijoje su kljais. Siekiant išanalizuoti dažnio-storio charakteristikos, kritimo kampo ir tangentinio standumo pokyčius, buvo tiriamas dviejų aliuminio plokščių sujungimas su skirtingomis vidinės ribos kokybėmis (tobulas sukibimas, silpnas sukibimas ir atsisluoksniavimas). SH bangos sklidimo režimo schema pateikta 1.1 pav.



1.1 pav. SH režimo bangos sklidimas tarpusavyje sujungtose aliuminio medžiagose [37]

Aplinka 1 ir aplinka 3 yra aliuminio medžiagos, sudarytos iš sluoksniuotos klijų struktūros. Aplinka 2 yra h storio klijų sluoksnis. Visos medžiagos yra izotropiniai tamprūs kietieji kūnai. SH_{i1} yra krintančioji banga, SH_{r1} ir SH_{r2} yra atspindėtosios bangos 1 ir 2 aplinkoje. α – sklidimo kampas klijuose, θ ir β – ultragarsinės bangos kritimo ir praėjimo kampai.

SH bangos režimo atspindžio ir perdavimo koeficientų išraiška tarpusavyje sujungtose aliuminio medžiagose (3 sluoksnių struktūra) pateikta 1.1 ir 1.2 lygtyse.

$$R = \frac{B_1}{A_1} = \frac{\mu_1 Q_1 F - \mu_2 K_T^{(1)} Q_2 (H - 1)}{\mu_1 Q_1 F + \mu_2 K_T^{(1)} Q_2 (H - 1)}; \quad 1.1$$

$$T = \frac{A_3}{A_1} = \frac{2\mu_1 K_T^{(1)} K_T^{(2)} Q_1 (H + e^{-2ikQ_2 h}) e^{-ik(Q_3 - Q_2)h}}{[K_T^{(2)} + ik\mu_3 Q_3] [\mu_2 K_T^{(1)} Q_2 (H - 1) + \mu_1 Q_1 F]}; \quad 1.2$$

kur A_1 – krintančios bangos amplitudė, A_3 ir B_1 – bangos amplitudė, perduodama į 3 medžiagą bei klijų sluoksnį, yra nežinomieji. Jie išreiškiami A_1 ir tangentinio standumo koeficientais $K_T^{(1)}$, $K_T^{(2)}$, μ_1 , μ_2 ir μ_3 kiekvieno konstrukcijos sluoksnio Lamé konstantos, Q_1 , Q_2 ir Q_3 – faziniai greičiai 3 sluoksniuose, h – klijų storis, i – realioji dalis, k – bangų skaičius, $H = \frac{[(K_T^{(2)} + ik\mu_3 Q_3)\mu_2 Q_2 + \mu_3 Q_3 K_T^{(2)}]}{[(K_T^{(2)} + ik\mu_3 Q_3)\mu_2 Q_2 - \mu_3 Q_3 K_T^{(2)}]} e^{-2ikQ_2 h}$, $F = K_T^{(1)}(H + 1) + ik\mu_2 Q_2(H - 1)$.

Buvo nustatyta, kad didinant dažnio ir storio charakteristikas, atspindžio ir perdavimo koeficientų kreivėse SH bangos režime, esant tobulam ir silpnam jungimui, atsiranda kelių eilių rezonansas. Tyrimo apraše buvo padaryta išvada, kad reikia parinkti tinkamas kritimo kampo ir dažnio bei storio charakteristikų vertes, kad būtų galima atskirti kiekvieno klijų sluoksnio būklę, t. y. tobulai sukibęs, silpnai sukibęs arba atsiklijavęs [37].

Todėl galima įvertinti kiekvieno sluoksnio medžiagos savybes. Taip bus įmanoma įvertinti konstrukcijos vientisumą. Ultragarso atspindžio koeficientus

galima apskaičiuoti sluoksniuotose struktūrose, atsižvelgiant į kiekvieno sluoksnio storį. Tačiau esant itin ploniems sukibimo sluoksniams, kurių storis yra mažesnis už medžiagos bangos ilgį, sukibimo ribos kokybę galima įvertinti naudojant ultragarsines tūrines ir nukreiptąsias bangas, taikant kvazistatinę aproksimaciją (QSA) [31]. Metodiką, pagal kurią nustatomi atspindžio ir perdavimo koeficientai, priklausantys nuo sukibimo ploto būklės, galima taikyti tiek tūrinių, tiek nukreiptųjų bangų tyrimams.

1.4. Kljais sujungtų medžiagų neardomasis bandymas

Šiame skyriuje aprašomi ultragarsiniai neardomieji metodai, skirti daugiasluoksniams konstrukcijoms tirti.

1.4.1. Vienodų medžiagų sujungimų tikrinimas

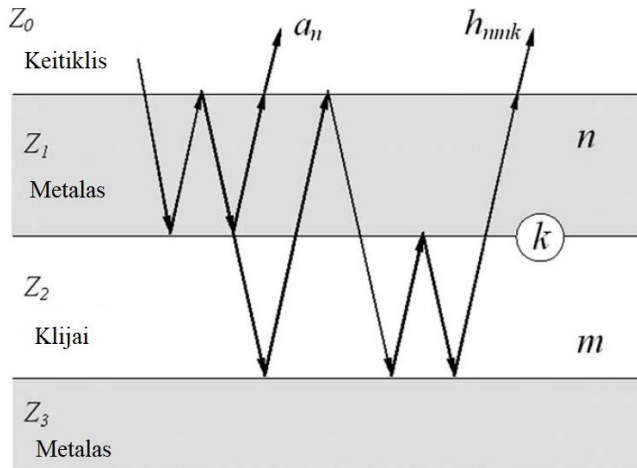
Egzistuoja įvairūs šiuolaikiniai ir kiti akustiniai metodai, skirti neardomajai patikrai atlikti kljais sujungtose medžiagos jungtyse [42, 43, 44, 45, 46, 47, 48]. Tačiau ne visi metodai gali būti lengvai pritaikomi visoms konstrukcijoms, nes skiriasi jų geometrija, sluoksnių ir kljų storis bei medžiagų rūšys [49, 50].

Titov ir kiti [50] pasiūlė tuštumų ir atsluoksniavimų aptikimo metodą kljais sujungtose medžiagose, kuriame išėjimo bangos forma yra signalo atspindžių nuo metalo ir kljų bei kljų ir metalo ribų suma. Buvo sukurtas dekompozicijos algoritmas ir pritaikytas bandiniams iš suklijuoto aliuminio ir plieno su skirtingais kljų sluoksnio storiais tikrinti. Siūlomas metodas pagrįstas daugkartinių bangų amplitudžių apskaičiavimu, atsispindėjusių nuo nagrinėjamos ribos (metalas-kljai ir kljai-metalo), kurias sklisdamas per bandinio sluoksnius priima keitklis. Nagrinėjamo modelio schema parodyta 1.2 paveiksle. Šiame tyrime buvo lyginama išmatuota ir įrašyta etaloninė bangos forma. Tada, siekiant aptikti defektus atitinkamose ribose, buvo apskaičiuoti pirmosios metalo ir kljų ribos nuokrypio parametrai r :

$$r = \left[\int_{t_1}^{t_2} (s(t) - s_{R1}(t))^2 dt \right]^{1/2} ; \quad 1.3$$

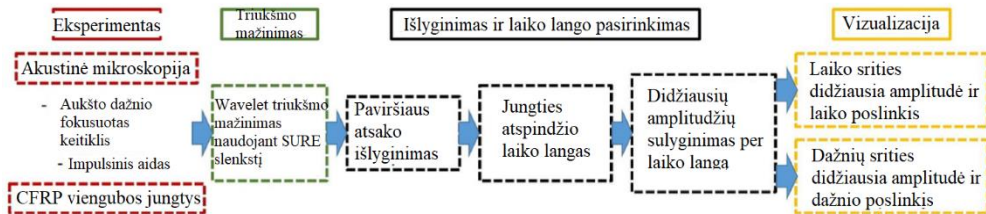
kur $s(t)$ yra išėjimo bangos forma metalo ir kljų ribos atveju, $S_{R1}(t)$ – etaloninė bangos forma, $[t_1, t_2]$ – duomenų lango laiko intervalas.

Kljų ir metalo riboje esantys defektai buvo aptikti naudojant atspindėtų impulsų fazės inversiją. Esant geram kontaktui tarp šių sluoksnių impulsai invertuojami. Impulsų poliariskumas buvo nustatomas pagal koreliacijos funkcijos $g(t)$ ženklą. Neigiama reikšmė apibūdina inversinę fazę ir defektų nebuvimą. Tačiau šis metodas taikytinas idealiai lygiems ir glotniems bandinių paviršiams bei riboms [50].



1.2 pav. Ultragarso bangų sklidimo kelio priklausomybės nuo laiko schema [50]

Yilmaz ir kiti [58] savo darbe pasiūlė metodą, skirtą aptikti nekokybišką jungtį klijais sujungtose kompozitinėse medžiagose. Šiam tikslui buvo naudojamas aukšto dažnio ir didelės skiriamosios gebos akustinės spektroskopijos metodas. Buvo vertinama vienguba klijuotų CFRP plokščių jungtis su skirtinga sukibimo kokybe (atsiluoksniavimu ar silpnu sukibimu). Silpno sukibimo aptikimui buvo sukurtas formos ypatybių išskyrimo algoritmas. Aukšto dažnio akustinė mikroskopija leidžia puikiai vizualizuoti sukibimo kokybę. Vertinant sujungimo kokybę sujungtose plonų kompozitų struktūrose ypač svarbus signalų apdorojimas. Daugiasluoksnio apdorojimo algoritmo schema parodyta 1.3 pav.



1.3 pav. Sukurtas apdorojimo algoritmas silpnaiems junginiams aptikti [58]

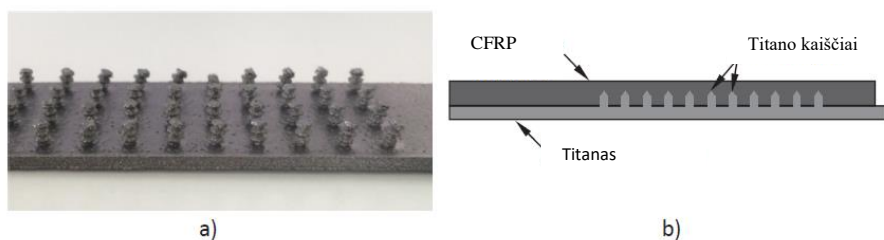
Atlikta ir daugiau darbų, skirtų sujungimo kokybei įvertinti, naudojant įvairius neardomuosius bandymų metodus (rentgeno spinduliuotę, infraraudonųjų spindulių termografiją, akustinę emisiją (AE)), taip pat siekiant nustatyti chemines ir fizikines savybes. Struktūroms su skirtingu sukibimo lygiu patikrinti buvo naudojami įvairūs ultragarso metodai, pavyzdžiui, Lamb ir SH bangos, netiesinis ultragarsas, lazerinis ultragarsas ir kt. [64, 65, 66, 67, 68, 69, 70, 71].

1.4.2. Skirtingų medžiagų sujungimų tikrinimas

Šiuo metu vis dar atlikta nepakankamai daugiasluoksnių struktūrų tikrinimo tyrimų. Esami sujungtų skirtingų medžiagų tikrinimo metodai aprašyti toliau šioje

dalyje. Todėl, norint aptikti defektus, esančius skirtingų medžiagų klijų sluoksnio sukibimo linijoje, vis dar reikia sukurti patikimą neardomojo tikrinimo metodą, tinkantį šioms struktūroms ir defektams tirti.

Jasiūnienė ir kiti [72] taikė ultragarsinį bandymą hibridinių metalo ir kompozito jungčių sukibimui įvertinti. Dėl bandinio geometrinės struktūros ir savybių vyksta sluoksnių atspindėtų ultragarsinių signalų sklaida, slopinimas ir persidengimas. Tiriamasis bandinys buvo titano plokštės su kaiščiais ir CFRP medžiagos sujungimu (1.4 pav.). Tyrimo metu nustatyta, kad matavimus sujungimo kokybės įvertinimui geriau atlikti iš kompozito pusės, tam buvo taikytas impulsinis echoskopinis ultragarsinis tyrimas imersiniu režimu su 10 MHz fokusuotu keitikliu. Siekiant pašalinti nelygaus paviršiaus ir nelygiagrečių konstrukcijos sluoksnių sukeltus signalų iškreipimus buvo sukurtas adaptyvus signalo apdorojimo algoritmas.



1.4 pav. Titano plokštė su kaiščiais (a) ir titano plokštės su CFRP sujungimu brėžinys (b) [72]

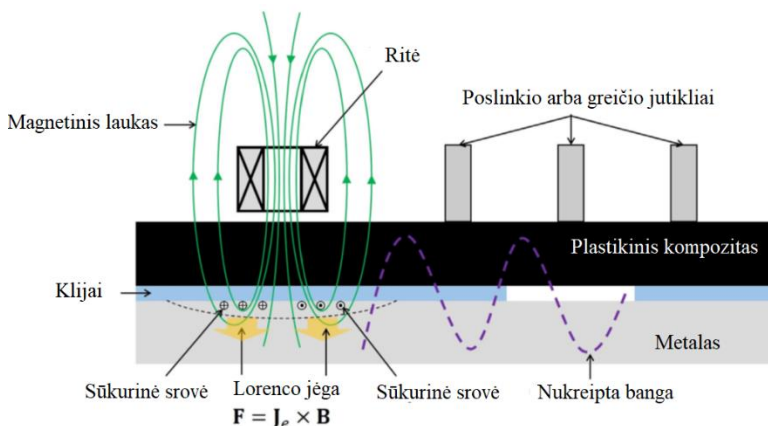
Naudojant šį metodą buvo nustatyti sujungime esantys defektai ir jų vieta. Apdorojimo algoritmą sudaro šie etapai [72]:

1. signalų filtravimas Gauso filtru;
2. spektro vidutinio dažnio skaičiavimai;
3. signalų, atsispindėjusių nuo vidinės ribos, priėmimo laiko įvertinimas;
4. signalo priėmimo laiko tiesinė interpoliacija pozicijoms, kuriose yra nulių arba ryškių smailių;
5. signalo poslinkis laiko srityje pagal įvertintą atvykimo laiką;
6. nuo ribos atsispindėjusių signalų filtravimas Gauso filtru;
7. kiekvieno signalo gautinės (angl. *envelope*) apskaičiavimas;
8. didžiausių signalų verčių apskaičiavimas 3D vaizdavimui.

Summa ir kiti [73] pasiūlė *in situ* pasyviąją termografiją tarpfazinių įtempių relaksacijai tirti hibridinėse konstrukcijose iš sujungto metalo ir CFRP. Eksperimento ir modeliavimo rezultatai parodė, kad mažėjant termoplasto standumui įtempiai pasiskirsto vis plačiau. Šiuo metodu pavyko nustatyti pažeidimų kilmės vietas *in situ*. Moradi ir kiti [74] pasiūlė termografijos neardomąjį metodą krašto defektams aptikti tarp aliuminio ir anglies epoksidinio pleistro, naudojamo jo remontui. Šiame darbe kiekybiniam defektų įvertinimui buvo pasiūlyti skirtingi vaizdų apdorojimo metodai – Furjė transformacija ir 1D bei 2D Daubechie bangelių

(angl. *wavelet*) transformacijos. Siekiant optimizuoti rezultatus pagal apdorojimo laiką ir signalo bei triukšmo santykį, buvo naudojama 3D bangelių transformacija.

Sun ir kiti [75] savo darbe tyrė kompozito ir metalo klijų sujungimo bandinį naudodami neardomąjį elektromagnetinių impulsų sukeltą akustinį bandymą (angl. EPAT). Buvo atliktas neardomasis tyrimas plastikinio kompozito ir metalo komponentų klijų sujungimo zonoje. Siūlomas EPAT metodas generuoja nukreiptą bangą klijų sukibimo zonoje, siekiant aptikti atsisluoksniavimą. Šio metodo principas parodytas 1.5 pav. Nukreiptosios bangos sklinda vidiniame klijų sluoksnyje, taip pat plastiko kompozite ir metalo. Esant bet kokiam defekto tipui, tampriųjų bangų signalas pasikeičia [75].



1.5 pav. EPAT metodo taikymo principas [75]

Remiantis išvardintais tyrimais, kai kuriuos metodus ir algoritmus galima taikyti šiame darbe tiriamam bandiniui. Impulsų poliarizavimo tyrimas, taip pat daugkartiniai atspindžiai nuo vidinio sluoksnio gali būti taikomi šiame tyrime atliekant skirtingų medžiagų sujungimų kokybės įvertinimą. Tačiau tiriant plonus sujungimus, bandinius su šiurkščiais ir nelygiagrečiais paviršiais bei vidiniais sluoksniais, esminė tyrimo dalis yra apdorojimo algoritmai, skirti klijų sluoksnių kokybės vizualizacijai, kurie leidžia pašalinti neigiamą šių šaltinių įtaką rezultatuose.

1.5. Modeliu pagrįsta aptikimo tikimybė

Neardomųjų bandymų metodo patikimumą galima kiekybiškai įvertinti pagal tikimybės aptikimo kreives [76]. Aptikimo tikimybė apibūdina tam tikro dydžio defekto aptikimą struktūroje. Matematinio modeliu paremtas aptikimo tikimybės metodas (angl. MAPOD) turi galimybę suskaičiuoti POD kreives neatliekant brangių ir daug laiko reikalaujančių eksperimentų. Modeliuojant POD kreives galima įvertinti patikros efektyvumą. Tačiau aptikimo tikimybės įvertis priklauso nuo daugelio faktorių, pavyzdžiui, medžiagos tipo, konstrukcijos geometrijos, defektų tipo, pasirinktos patikros technikos, matavimo aplinkos [76, 77]. Dėl to pagal POD kreives galima įvertinti aptinkamo defekto dydį. POD kreivių įvertinimo

pagal modelį metodika yra tokia pati kaip ir eksperimentinė, aprašyta MIL-HDBK-1823A kariniame vadovėlyje ir ENIQ ataskaitoje [78].

Bet kurios valdymo sistemos atsakas priklauso nuo įtakojančių valdymo metodo parametrų. Šią priklausomybę išreiškiame taip:

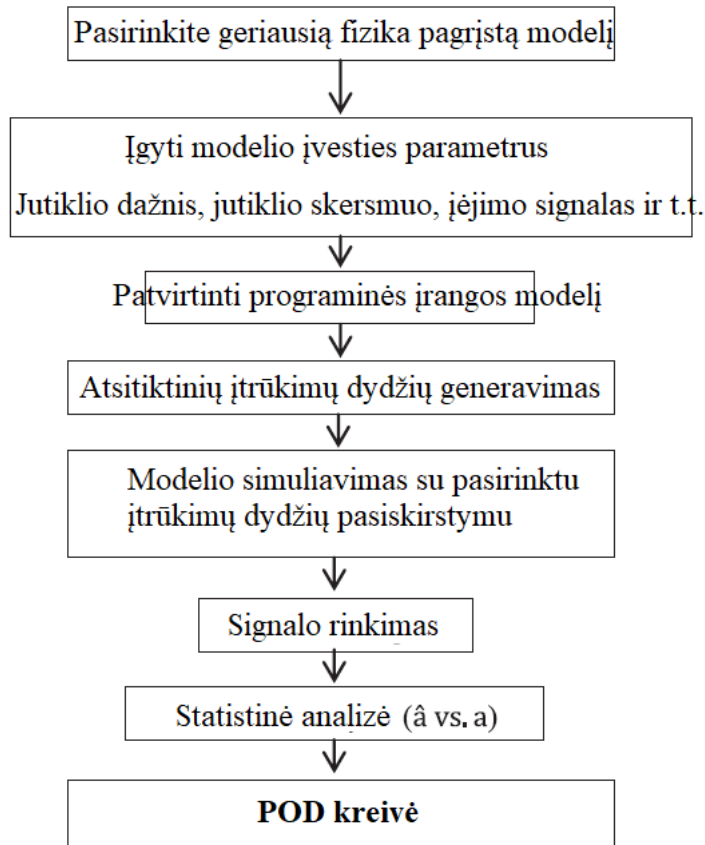
$$y = f(a, X); \quad 1.4$$

kur y – tikrinimo sistemos reakcija, a – defekto dydžio charakteristika (dydis), X – neapibrėžtumo parametrai.

Charakteristinis parametras parodo defekto kenksmingumą. Paprastai kaip charakteristinę vertę pasirenkamas defekto dydis: ilgis, plotis arba aukštis, priklausomai nuo defekto tipo. POD kreivėms įvertinti taikomi du metodai – pataikymo / nepataikymo analizė (ang. Hit / Miss) ir signalo atsakas (\hat{a} priklausomybė nuo a). Abu metodai gali būti naudojami POD kreivėms įvertinti skirtingų medžiagų sujungimuose. Hit / Miss metodas arba Bernulio duomenų analizė – tai kokybinės informacijos matas, pagal kurį nustatomas defekto buvimas arba nebuvimas. Testo rezultatas yra 1, reiškiantis pataikymą, ir 0, reiškiantis nepataikymą. POD kreivėms įvertinti taip pat naudojamas signalo atsako (\hat{a} – priklausomybė nuo a) metodas. Signalo atsakas yra kiekybinis matas, pagrįstas santykiu tarp defekto dydžio ir keitiklio atsako [86]. Atliekant ultragarsinę patikrą sluoksniuotai struktūrai tirti, atsako amplitudė (\hat{a} – išmatuotas keitiklio atsakas) priklauso nuo defekto dydžio (a yra charakteringoji vertė arba defekto dydis).

Kadangi triukšmas yra visuose neardomuosiuose bandymuose, turi būti nustatytas lygis, kuris apibrėžia rezultatą su defektu arba be jo. Šiam lygiui būdinga aptikimo riba \hat{a}_0 . Paprastai aptikimo riba apibrėžiama kaip didžiausias foninio triukšmo lygis atliekant matavimus, kai konstrukcijoje nėra defektų [86, 87, 88, 82, 78, 89].

Rentalis ir kiti [77] savo tyrime pademonstravo modeliais paremtą POD metodą ultragarsiniam testavimui. Skirtingų skersmenų plokščiosios dugno skylės (angl. *Flat Bottom Hole*, FBH) defektai buvo generuojami skaitmeniniu būdu. Tikrinimo MAPOD schema pateikta 1.6 pav. Šiame tyrime atliktas matematinio modelio patikrinimas: buvo apskaičiuotos ir su eksperimentiniais rezultatais palygintos amplitudės maksimumo vertės bei signalo sklidimo laiko skirtumas tarp atspindžių nuo priekinės ir galinės sienelės. Įvairių matmenų defektai buvo generuojami pagal lognormalųjį pasiskirstymą ir buvo įvertinta kiekvieno defekto aptikimo tikimybė. Atlikus tyrimą nustatyta, kad defektų, aptiktų su 90 % tikimybe ir 95 % patikimumo lygiu, vertė didėja didėjant ribinei vertei (angl. *detection threshold*), kuri priklauso nuo signalo triukšmo lygio ir (arba) nuo klaidingų pranešimų skaičiaus (angl. *false calls*) [77].



1.6 pav. Ti-6Al-4V cilindrinio bloko ultragarsinio bandymo modelio paremta POD schema[77]

Bato ir kiti [90] savo tyrime pasiūlė eksperimentinius ir kiekybinius metodus POD kreivių skaičiavimui atliekant testavimą sūkurinių srovių metodu. Siekiant atsižvelgti į žmogaus veiksnio įtaką ir skirtingų prietaisų poveikį, buvo atlikti keli eksperimentiniai bandymai. Šie nustatyti neapibrėžtumai buvo naudojami kaip imitacinio modelio duomenys. POD kreivės buvo apskaičiuotos remiantis skaitmeniniu modeliu bei eksperimentiniu būdu ir palygintos tarpusavyje.

Daugiau tyrimų atlikta vertinant neardomųjų bandymų metodų patikimumą skaičiuojant POD kreives [92, 77, 93, 94]. Atliekant tyrimus [95], eksperimentiniais ir modeliuojamaisiais metodais buvo nustatytos aptikimo tikimybės įvairiems neardomojo tikrinimo metodams: ultragarsiniam skenavimui, termografijai, sūkurinėms srovėms, XCT, SHM ir kt. [95]. Toliau šiame darbe bus vertinama defektų aptikimo tikimybė daugiasluoksnėje struktūroje. Modeliu paremtos aptikimo tikimybės panaudojimas leidžia išvengti brangių ir daug laiko reikalaujančių eksperimentinių POD kreivių skaičiavimų, užtikrinančių gerą eksperimentinių rezultatų atitikimą ir leidžiančių analizuoti daugiau įtakos turinčius parametrus, į kuriuos negalima atsižvelgti taikant eksperimentinį metodą.

Daugeliu atvejų kartu su neardomųjų bandymų metodais turėtų būti pateikiami signalų apdorojimo algoritmai. Patraukliausi neardomųjų bandymų metodai, skirti skirtingų medžiagų sujungimams tikrinti, yra ultragarsinis tikrinimas naudojant tūrinės arba nukreiptąsias bangas, aukšto dažnio akustinė mikroskopija, termografija. Naujausiuose atliktuose darbuose aprašomas EPAT, nukreiptųjų bangų ir neardomųjų tyrimų metodų sintezės naudojimas bei vaizdų rekonstrukcijos metodai.

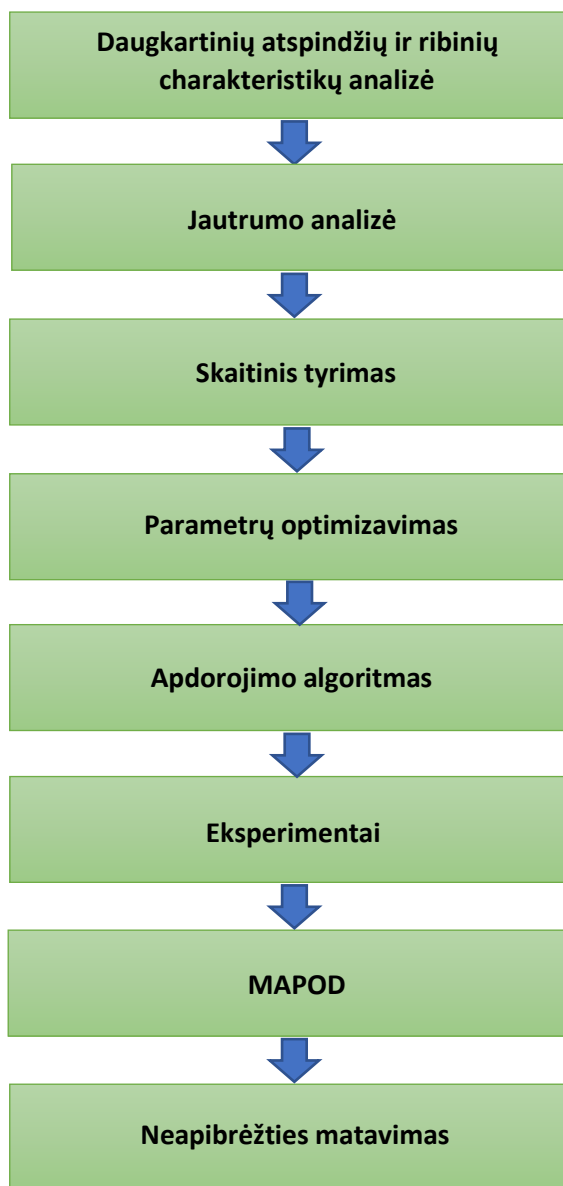
2. METODO, SKIRTO APTIKIMO GALIMYBĖS PAGERINIMUI SKIRTINGŲ MEDŽIAGŲ SUJUNGIMUOSE, SUKŪRIMAS

Šio skyriaus tikslas – sukurti apdorojimo algoritmą, kuris padidintų tikimybę aptikti defektus skirtingų medžiagų klijų sluoksnių sujungimuose. Siekiant šio tikslo, sluoksniuotų struktūrų komponentai buvo ištirti teoriškai, taikant skaitmeninį modeliavimą, signalų modeliavimą ir atliekant parametrinį tyrimą. Šiame darbe pateiktas tyrimo metodas apibūdina kiekvieną veiksmo etapą, skirtą pasiekti tikslams.

2.1. Tyrimo metodas

Sujungimo zonos yra svarbiausia klįjuojamų konstrukcijų sritis. Defektai klijų sluoksnyje pasitaiko dažnai. Todėl, siekiant užtikrinti sujungimo vietos vientisumą, svarbu aptikti defektus, pvz., sukibimo pažeidimus ir atsiskuoksniavimus [100, 11, 10, 62, 101]. Siekiant sukurti metodą, kuris padidintų tokių defektų aptikimo tikimybę, tyrimui buvo naudojami du komponentai iš klįjais sujungtų skirtingų medžiagų. Tiriamieji komponentai yra plokštė su storesniais skirtingų medžiagų sluoksniais ir viena persidengianti sujungimo detalė su plonesniais sluoksniais, dėl kurių defektus aptikti gali būti daug sunkiau.

Siekiant įgyvendinti darbo tikslą, buvo atliktas tyrimas, kurio eigos blokinė schema pateikta 2.1 paveiksle.



2.1 pav. Tyrimo metodo etapai

Siekiant aptikti klįjavimo defektus skirtingų medžiagų sujungimuose ir padidinti aptikimo tikimybę, buvo ištirti ribos charakteristikos teoriniai įvertinimai ir energijos kiekis, gautas iš keitiklio po ultragarsinės bangos sklidimo struktūrose. Taip pat atlikta defektų aptikimo jautrumo analizė, norint nustatyti didžiausią įtaką patikrinimui turėjusius parametrus, siekiant toliau tobulinti metodą ir padidinti defekto aptikimo galimybes. Naudojant pusiau analitinius baigtinius elementus atliktas patikrinimo modeliavimas, siekiant ištirti ultragarso bangų elgseną ir

sklidimą per skirtingos klijų būklės bandinių sluoksnius ir defektus klijuose. Be to, buvo atliktas zondojuančio signalo atspindžių amplitudės palyginimas ir įvertinimas skirtingais defektų lokacijos atvejais klijų sluoksnyje. Siekiant nustatyti galimus metodus, leidžiančius padidinti defektų aptikimo tikimybę skirtingų medžiagų sujungimuose, ir sukurti apdorojimo algoritmą tam pačiam tikslui pasiekti, reikia atlikti aprašyta analizę. Signalui modeliuoti buvo sukurtas algoritmas, kuris buvo realizuotas MatLab programiniu paketu. Jo tikslas – suskaičiuoti ir sugeneruoti eksperimentiniams bandymams artimą signalą. Išnagrinėti visi teoriniai ribinių charakteristikų vertinimai ir apskaičiuotas keitiklio gautos energijos kiekis, ultragarso bangoms sklindant sujungimo konstrukcijose. Atlikus skirtingos medžiagos sujungimų analizę ir sukūrus defektų aptikimo galimybes didinančią techniką, siūlomus metodus reikėtų patvirtinti atliekant eksperimentinius tyrimus, taikant sukurtus signalų apdorojimo algoritmus. Pagal modelį apskaičiuota aptikimo tikimybė rodo minimalų defekto dydį, kurį galima aptikti pasirinktu ultragarsiniu metodu 90 % patikros atvejų, esant 95 % patikimumo lygiui. Be to, buvo apskaičiuota išmatuotų defektų dydžių neapibrėžtis.

2.2.1. Daugkartinių atspindžių ir ribinių charakteristikų teorinė analizė

Šio skyriaus tikslai: 1) įvertinti skirtingos medžiagos sujungimų ribines charakteristikas, siekiant sužinoti ultragarso bangų elgseną daugiasluoksniėje struktūroje, 2) ištirti sklidimo ir atspindžio nuo bandinio ribų kelius, 3) nustatyti kiekvieno iš jų laiko atvejus ir 4) apskaičiuoti daugkartinių signalų, atsispindėjusių nuo tam tikrų ribų, amplitudžių vertes, esant skirtingoms defektų vietoms klijų sluoksnyje. Norint pasiekti nustatytus tikslus, tyrimui atlikti naudotas aliuminio ir CFRP bandinys iš klijais sujungtų medžiagų. Komponentą sudaro 3 sluoksniai: 1,6 mm aliuminio, 0,22 mm klijų ir 5,11 mm CFRP. Anglies pluoštu armuoto plastiko plokštę sudaro 41 sluoksnis, iš kurių pirmasis ir paskutinis yra stiklo pluoštu armuoti polimerai (angl. GFRP), o likusieji – CFRP. Kadangi GFRP posluoksniai yra gana ploni, visa kompozitinė plokštė vadinama CFRP.

Siekiant apskaičiuoti ir toliau palyginti keitiklio gaunamą energiją sklindant ultragarso bangoms ir daugkartiniams atspindžiams nuo tam tikrų sujungimo sluoksnių, buvo sukurti trys konstrukciniai modeliai su skirtinga defekto padėtimi klijų sluoksnyje. Pirmu atveju defektas įterptas tarp aliuminio ir klijų, antru – defektas klijų sluoksniu viduryje, trečiu atveju klijavimas be defekto („tobulas klijavimas“). Pradžioje buvo apskaičiuotos kiekvienos medžiagos ribinės charakteristikos: akustinė varža (Z_k), atspindžio (K_R) ir perdavimo K_R koeficientai.

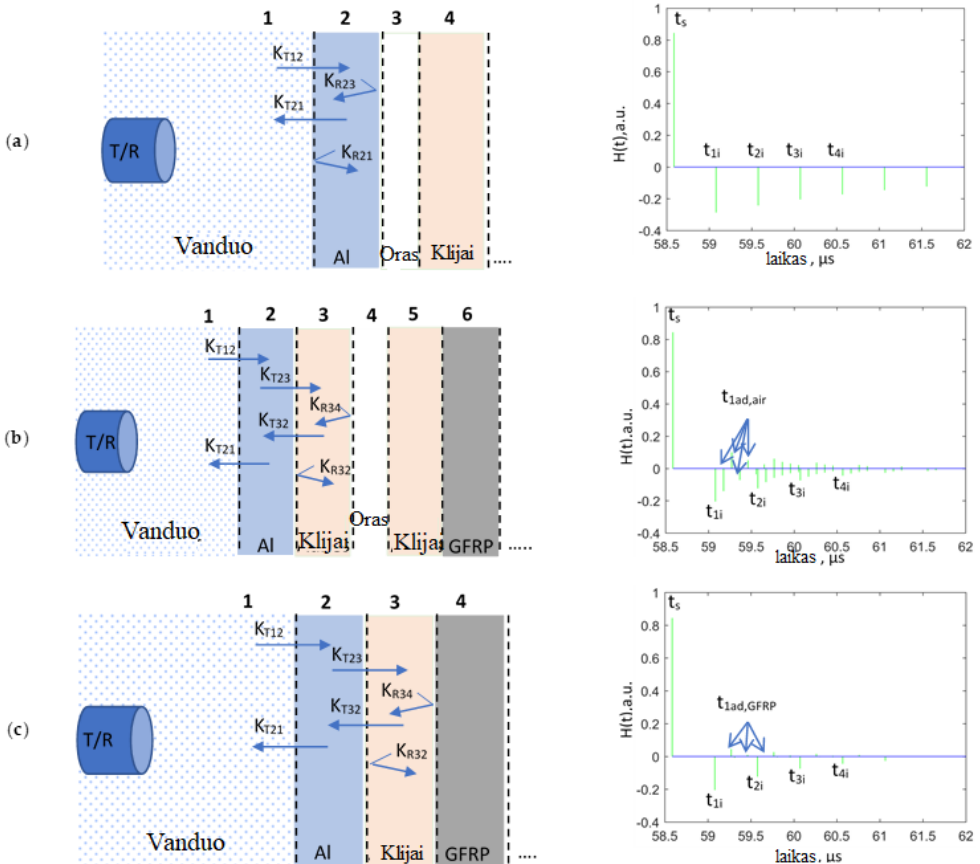
Signalų atspindžių ir daugkartinių atspindžių nuo bandinių ribų amplitudės vertės buvo apskaičiuotos pagal 2.1 ir 2.2 išraiškas. Modeliui su defektu tarp aliuminio ir klijų (aliuminio ir klijų riba) pagal 2.1 išraišką, o modeliams su defektais klijų sluoksniu viduryje (klijų ir oro riba) ir tobulam sukibimui (klijų ir GFRP riba) pagal 2.2 išraišką [9].

$$A_{1n} = K_{T12} \cdot K_{T21} \cdot K_{R23}^n \cdot K_{R21}^{n-1}; \quad 2.1$$

$$A_{2n} = K_{T12} \cdot K_{T23} \cdot K_{T32} \cdot K_{T21} \cdot K_{R34}^n \cdot K_{R32}^{n-1}; \quad 2.2$$

kur n – daugkartinių atspindžių nuo tam tikros ribos laipsnis arba skaičius, K_T – perdavimo koeficientas, K_R – atspindžio koeficientas, o skaitmeniniai indeksai – sudedamųjų sluoksnių numeriai.

Trys modeliai, sukurti skirtingoms ribinėms sąlygoms tirti, parodyti 2.2 pav. Atlikti teoriniai skaičiavimai, siekiant įvertinti atspindėtų signalų amplitudes. Gauti impulsų grafikai apibūdina signalų, atsispindėjusių nuo skirtingų bandinių ribų, priėmimo laiką. $H(t)$ apibūdina perdavimo funkciją, amplitudės vertę, taip pat fazės pokytį. Sudaryti daugkartinių atspindžių t_{1i} - t_{4i} , $t_{1ad,air}$ ir $t_{1ad,GFRP}$ grafikai kiekvienam ribinės sąlygos atvejui: aluminis-defektas, klįjai-defektas ir klįjai-GFRP (tobulas sukibimas). Teigiamą ir neigiamą impulsų poliškumą apibūdina skirtingi konstrukcijos medžiagų akustiniai impedansai ir fazės pokyčiai.



2.2 pav. Modeliai su skirtingomis medžiagų sujungimo ribų būsenomis: (a) defektas tarp aluminio ir klįjų, (b) defektas tarp dviejų klįjų juostų, (c) tobulas sukibimas [9]

Buvo apskaičiuotos ir 2.1 lentelėje pateiktos kiekvieno modelinio atvejo – aliuminio-defekto, klijų-defekto ir klijų-GFRP – daugkartinių atspindžių amplitudės vertės.

2.1 lentelė Apskaičiuotos daugkartinių atspindžių amplitudės vertės

Daugkartinių atspindžių amplitudė	Aliuminis-defektas	Klijai-defektas	Klijai-GFRP
A ₁	-0,2915	-0,1451	0,0468
A ₂	-0,2424	0,1020	0,0106
A ₃	-0,2016	-0,0717	0,0024
A ₄	-0,1676	-0,0504	0,00054

Remiantis lentelėje pateiktais rezultatais padaryta išvada, kad patikimiau įvertinti defektus leistų aukštesnės eilės atspindžiai. Taikant šį metodą galima padidinti defektų aptikimo galimybes sluoksniuotose struktūrose.

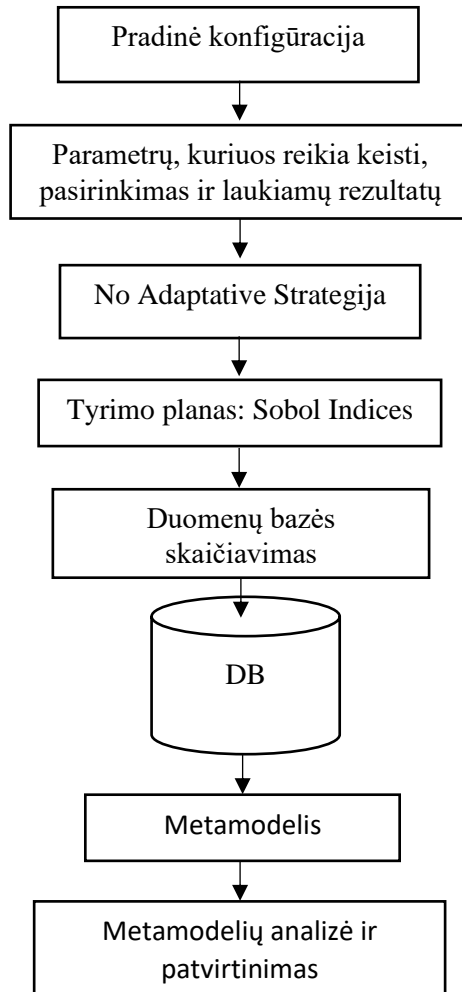
2.1.2. Jautrumo analizė

Šio skyriaus tikslas – ištirti įtaką turinčius parametrus ir nustatyti, kurie iš jų daro didžiausią įtaką pasirinktam tikrinimo metodui ir jo rezultatams. Žinios apie pagrindinius parametrus, turinčius įtakos sujungtų skirtingų medžiagų struktūros defektų aptikimui, gali būti panaudotos signalų apdorojimo algoritmo kūrimo etape ir suteikti informacijos, į ką reikėtų sutelkti dėmesį tikrinimo metu, siekiant pagerinti sujungtų medžiagų defektų aptikimo patikimumą. Šiems parametrams identifikuoti buvo atlikta jautrumo analizė naudojant pusiau analitinę baigtinių elementų programinę įrangą CIVA.

Jautrumo analizę sudaro du pagrindiniai etapai: kalibravimas ir metamodelio skaičiavimas. Siekiant gauti atraminio signalo amplitudę, buvo nustatyta kalibravimo konfigūracija. Buvo sukurtas klijais sujungtų aliuminio su CFRP plokščių modelis, kurio geometriniai parametrai buvo tokie patys kaip ir tiriamo pagaminto bandinio ir kurio išsamios charakteristikos pateikiamos 3 skyriuje. Vienakrypčių pluoštų skaičius – 41, kiekvieno jų storis ir laminatų orientacija atitinka bandinio charakteristikas. Modeliavimo patikrinimui taikytas ultragarsinis impulsų atspindžio metodas imersijos režimu ir 10 MHz fokusuotas keitiklis. Keitiklis buvo sumontuotas tokiu atstumu nuo komponento, kad ultragarso spindulys būtų nukreiptas į sluoksniuotos struktūros ribą. Maksimaliai nuo defekto atsispindėjusio signalo amplitudė buvo naudojama kaip atraminė amplitudės vertė metamodeliui kurti. Metamodelio metodas leidžia nuodugniai ištirti įtaką darančius parametrus defekto aptikimui. Metamodelio generavimo proceso schema pateikta 2.3 paveiksle.

Neapibrėžties parametų analizė atlikta atsižvelgiant į pasirinktą tikrinimo metodą ir bandinio struktūrą. Kitas svarbus metamodelio kūrimo etapas, siekiant

atlikti kiekvieno įtaką turinčio parametro jautrumo analizę, yra statistinio pasiskirstymo dėsnio priskyrimas kiekvienam parametrai, kuris gali būti normalusis, tolygusis ir kitoks, taip pat variacijos intervalų nustatymas [78]. Neapibrėžtieji parametrai su nustatytais variacijos intervalais ir pasiskirstymo dėsniais pateikti 2.2 lentelėje.



2.3 pav. Metamodelio kūrimo proceso schema (DB – duomenų bazė)

Taikytas statistinis Sobolio indeksų metodas ir pasirinktas Krigingo interpoliatorius. Sobolio indeksai apibūdina dispersijos dalį, susijusią su kiekvienu įėjimo parametru arba jų pogrūpiu. Be to, pasirinkus Krigingo interpoliatorių, sumažėja santykinė paklaida. Siekiant sukurti nuoseklų metamodelį, atlikta 768 modeliavimo atvejų.

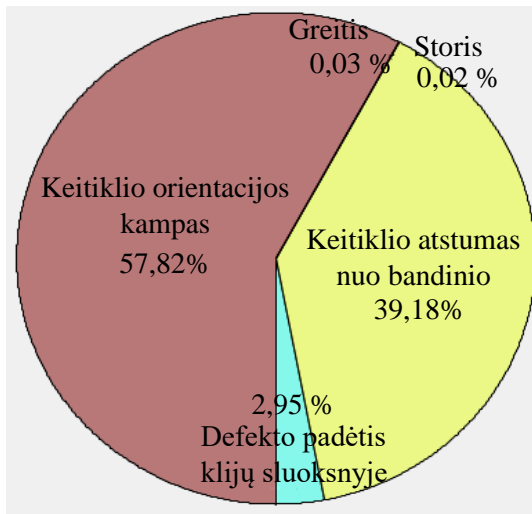
2.2 lentelė. Neapibrėžtų parametų variacijos intervalai ir pasiskirstymo dėsniai

Parametrai	Vidutinė vertė	Variacijos intervalas	Statistinis pasiskirstymo dėsnis
Išilginės ultragarso bangos greitis aliuminyje	6 363 m/s	[6 313 m/s; 6 500 m/s]	Normalusis
Defekto ilgis išilgai X ašies	2,625 mm	[0,25 mm; 5 mm]	Konstanta / Charakteristinė vertė
Defekto padėtis klijų sluoksnyje	1,72 mm	[1,61 mm; 1,82 mm]	Tolygusis
Vandens kelias tarp bandinio paviršiaus ir keitiklio	44,03 mm	[43,5 mm; 44,03 mm]	Tolygusis
Aliuminio storis	1,61 mm	[1,60 mm; 1,61 mm]	Normalusis
Zonduojančios bangos kritimo kampas	0°	[-6°; 0°]	Tolygusis

2.3 lentelėje pateikiamos kiekvieno neapibrėžto parametro jautrumo ir poveikio dalies vertės. Sobolio indeksų diagrama pateikta 2.4 pav.

2.3 lentelė. Kiekvieno neapibrėžto parametro jautrumo vertės ir įtakos dalis

Neapibrėžtieji parametrai	Jautrumas, Sobolio indeksai	Proporcijos vertė, %
Išilginės bangos greitis	0,04	0,03
Defekto padėtis klijų sluoksnyje	3,53	2,95
Keitiklio atstumas nuo bandinio	46,90	39,18
Aliuminio plokštės storis	0,03	0,02
Keitiklio orientacijos kampas	69,21	57,82



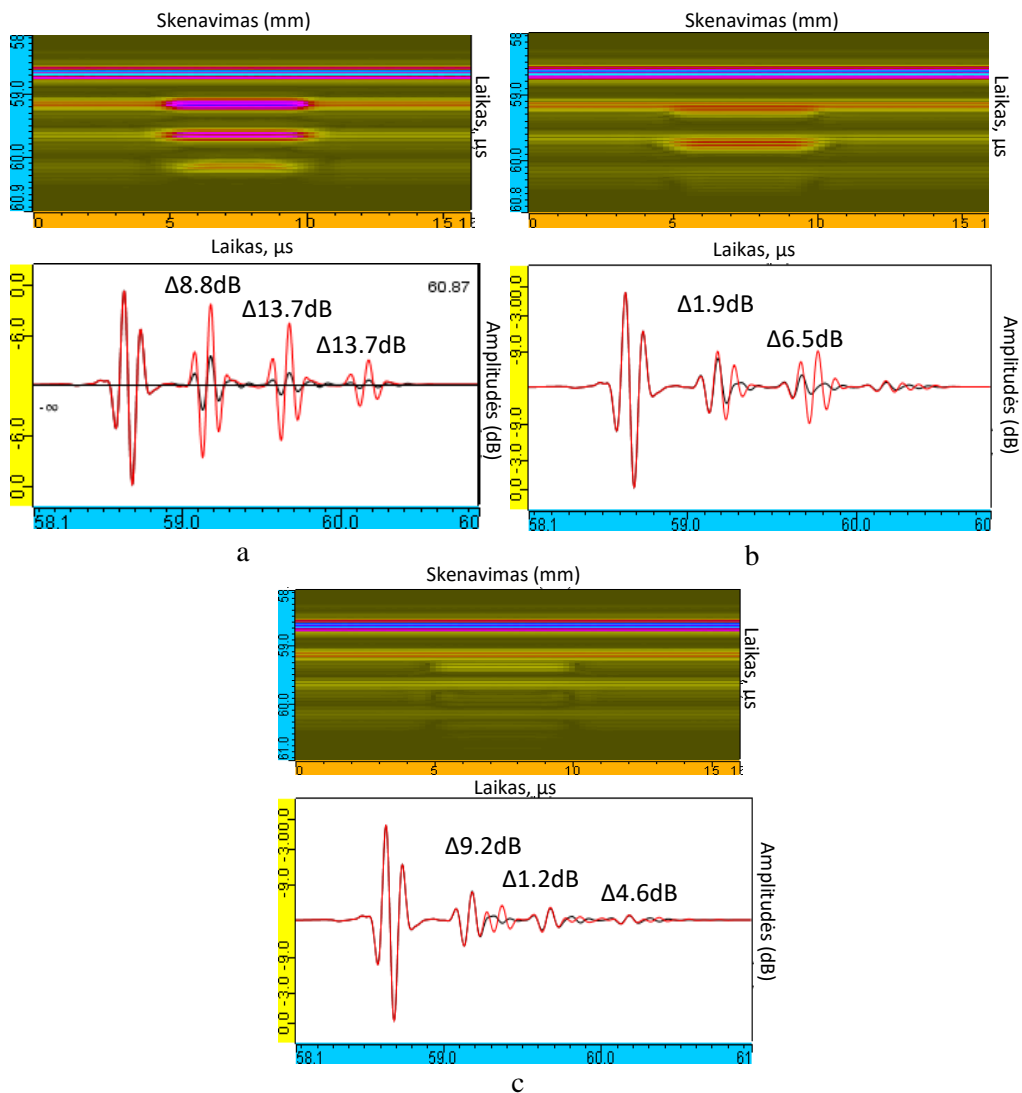
2.4 pav. Jautrumo analizės Sobolio indeksų diagrama

Iš jautrumo analizės diagramos matyti, kad yra du kritiniai neapibrėžties parametrai, kurie labiausiai įtakoja ultragarsinės kontrolės rezultatus: vandens kelias tarp keitiklio ir detalės paviršiaus bei keitiklio kritimo kampas. Defekto padėtis klijų sluoksnyje taip pat turi įtakos rezultatui. Tačiau, palyginus su vandens trajektorija ir kritimo kampu, įtaka yra daug mažesnė. Neapibrėžti parametrai, pavyzdžiui, vandens kelias ir keitiklio kritimo kampas, yra susiję su patikros nustatymu. Be to, vandens kelias ir keitiklio kritimo kampas priklauso nuo paviršiaus kreivumo. Kai keičiasi spindulių kritimo kampas, keičiasi ir ultragarso bangų sklaidimo laikas. Kadangi kritimo kampas ir vandens kelio faktorius turi didelę įtaką patikros rezultatams, daugiausia dėmesio reikia skirti eksperimento rengimui arba konkrečios patikros metodikos kūrimui. Todėl, suderinus signalus pagal jų atvykimo laiką, galima pašalinti kreivumo poveikį ir padidinti defektų aptikimo tikimybę.

2.1.3. Ultragarso patikrinimo modeliavimas

Šio skyriaus tikslas – atlikti skirtingų medžiagų sujungimų ultragarso patikrinimo modeliavimą, siekiant ištirti ultragarso bangų sklaidimo parametrus, parinkti bandinio testavimo kryptį, įvertinti signalų, atsispindėjusių nuo defektuotų ir nedefektuotų sričių, amplitudės vertes. Taip pat palyginti rezultatus, siekiant atrinkti metodus, kurie leistų pagerinti sujungimuose esančių defektų aptikimo galimybes.

Atliekant patikros modeliavimą buvo modeliuojami aliuminio ir CFRP bei plieno ir CFRP plokščių klijuoti sujungimai. Siekiant ištirti ir palyginti defekto padėties įtaką defekto aptikimo galimybei sujungto aliuminio ir CFRP struktūroje, buvo sumodeliuotos trys skirtingos defekto vietos klijų sluoksnyje. Modeliuojamų defektų vieta klijų sluoksnyje yra tokia: tarp aliuminio ir klijų, klijų viduryje ir tarp klijų ir CFRP. Skirtingų medžiagų tyrimams buvo pasirinktas ultragarso impulsų aido metodas panardinimo režimu, taip pat fokusuojantis keitikliai. Ultragarso bangos ilgis buvo apskaičiuotas siekiant parinkti tinkamą keitiklio dažnių diapazoną kiekvienam komponentui patikrinti. Patikros modeliavimui pasirinktas 10 MHz dažnis, kuris vėliau bus naudojamas atliekant eksperimentinius tyrimus. Šis dažnių diapazonas leidžia kontroliuoti skirtingų medžiagų sujungimus ir išvengti slopinimo medžiagose. Gautos daugybinių atspindžių nuo konstrukcijos A ir B projekcijos pavaizduotos 2.5 pav.



2.5 pav. A ir B tipo skenų modeliavimas iš metalo pusės, klijų defektui esant: (a) tarp aliuminio ir klijų, (b) klijų viduryje, (c) tarp klijų ir CFRP

Iš modelyje gautų A ir B tipo skenų rezultatų matyti, kad defekto aptikimo tikimybė mažėja defektui esant gilesniame klijų sluoksnyje. Jei defektas yra klijų sluoksniu viduryje arba klijų ir kompozito riboje, aliuminio-klijų, defekto ir klijų-kompozito atspindėti signalai sutampa. Tai lemia plonas klijų sluoksniu ir didelis signalo slopinimas epoksidinėje medžiagoje, kuris taip pat apsunkina defekto aptikimą. Lyginant signalų, daug kartų atsispindėjusių nuo defektuotų (raudonos spalvos signalas A-skenuose) ir nedefektuotų (juodos spalvos signalas A-skenuose) sričių, pastebėta, kad amplitudžių skirtumo vertė didėja su kiekvienu daugkartiniu

atspindžių. Remiantis gautais patikrinimo modeliavimo duomenimis, perspektyviausias defektų aptikimo vertinimas skirtingų medžiagų sujungimuose turėtų būti pagrįstas daugkartinių atspindžių nuo konstrukcijos ribos analize ir naudojamas kuriant defektų aptikimo tikimybės didinimo algoritmą. Tokie patys rezultatai gauti tikrinant plieno-CFRP sujungimus. Analizuojant bandinio patikros atlikimo pusės pasirinkimą, pastebėta, kad defekto aptikimo galimybė testuojant iš kompozito pusės yra mažesnė nei tikrinant iš plieno pusės. Taip pat dėl didelio kompozitinės medžiagos slopinimo ir iškraipymų sudėtinga taikyti daugybinių atspindžių analizę. Todėl buvo pasirinkta patikra iš metalo pusės.

2.1.4. Sluoksniuotos struktūros signalų modeliavimas ir parametru optimizavimas

Šio skirsnio tikslas – aptikti laiko momentus signale, kur stebimas didžiausias amplitudės pokytis, signalizuojantis apie struktūroje esančius defektus. Šiam tikslui pasiekti signalai, atsispindintys nuo tobulo sujungimo ir sujungimo su defektais, buvo modeliuojami pagal specialiai tam sukurtą ir realizuotą algoritmą. Pagrindinė idėja – išgauti signalus, kurie būtų kuo artimesni eksperimentuose išduotiems signalams. Tam buvo naudojamas etaloninis signalas. Eksperimentiniam etaloniniam signalui gauti buvo naudojamas aliuminio blokas ir 10 MHz fokusuotas keitiklis. Tyrimas atliktas imersiniu impulsinio aido režimu. Be to, norint pasiekti geriausią eksperimentinių ir sumodeliuotų signalų sutapimą, reikėjo optimizuoti modelio parametrus. Siekiant geresnio sutapimo, programoje rankiniu būdu buvo optimizuoti šie parametrai: ultragarso greitis konstrukcijos medžiagose, sluoksnių storio vertės ir medžiagų tankiai. Norint aptikti laiko momentus, kai signale stebimas didžiausias amplitudės pokytis, reikia palyginti signalus, atsispindinčius nuo defektuotų ir nedefektuotų sujungimų. Tam buvo sukurti tobulo sukibimo (aliuminio-klijų-kompozito) ir defekto klijų sluoksniuotos struktūros (aliuminio-klijų-defekto) modeliai ir signalai $u(t)$ sumodeliuoti pagal lygtį [9]:

$$u(t) = y_{ref}(t) \otimes h(t); \quad 2.3$$

kur y_{ref} – eksperimentinis etaloninis signalas, įrašytas naudojant etaloninį bloką, $h(t)$ – teoriškai apskaičiuotas impulsų atspindys sluoksniuotos struktūros bandinyje.

Atlikus tyrimą, parametrai buvo optimizuoti ir tolesniam palyginimui sumodeliuoti signalai, atsispindintys nuo defektuotų ir bedefekčių sujungimų.

2.2. Apdorojimo algoritmo sukūrimas, siekiant padidinti aptikimo galimybes

Sukurti matavimo signalų apdorojimo algoritmai leidžia pagerinti NDT technikos efektyvumą. Todėl šiame darbe daugiausia dėmesio buvo skiriama algoritmų kūrimui. Šio skyriaus tikslas – sukurti metodą, kuris padidintų sukibimo defektų aptikimo tikimybę skirtingų medžiagų sujungimuose. Metodas pagrįstas teorinių skaičiavimų, įvairių skirtingų medžiagų bandinių tyrimų rezultatais, modeliavimo rezultatais ir tikrinimo modeliavimu, atsižvelgiant į visus galimus apribojimus ir įtakos faktorius patikrinimo metodui ir rezultatams.

Šio darbo tyrimo objektas – aliuminio ir CFRP plokščių sujungimas panaudojant klijus. Siekiant padidinti defektų aptikimo galimybes bei suklijavimo

kokybei įvertinti buvo sukurtas signalų apdorojimo algoritmas. Sudarant algoritmą buvo atlikti šie pagrindiniai veiksmai:

1. Išėjimo duomenų surinkimas po eksperimentinio patikrinimo.
 2. Signalo filtravimas filtru, išsaugant svarbią, informatyvią, signalo dalį.
- Pirmiausia buvo apskaičiuoti signalo dažnių spektrai:

$$U(f) = \text{FT}[u(t)]; \quad 2.4$$

kur FT žymi Furjė transformaciją.

Dažnių spektro filtravimas naudojant juostinį filtrą.

$$U_F(f) = U(f) \cdot H(f); \quad 2.5$$

kur $H(f)$ – filtro perdavimo funkcija.

Signalų rekonstravimas naudojant atvirkštinę Furjė transformaciją.

$$u_F(t) = \text{Re}(\text{FT}^{-1}[U_F(f)]); \quad 2.6$$

kur Re žymi realiąją dalį, o FT^{-1} yra atvirkštinė Furjė transformacija.

3. Laiko momento nustatymas, siekiant suderinti visus signalus, atsispindėjusius nuo objekto paviršiaus laiko srityje.

Riba buvo nustatyta objekto paviršiaus atspindžiams. Tada buvo nustatyti kiekvieno nuo paviršiaus atsispindėjusio signalo priėmimo laiko atvejai ties nustatyta riba U_{th} [9].

$$t_{n_1,k} = \min\{\arg[u_k(t_{n_1}) > U_{th}]\}; \quad 2.7$$

kur $u_k(t_{n_1})$ – skaitmeninis signalas, $k = 1, 2, \dots, K$, K žymi nuo paviršiaus atsispindėjusių signalų skaičių, o t_{n_1} – pirmoji imtis, viršijanti U_{th} laiko momentą.

Buvo nustatyti pirmojo signalo perėjimo per nulio kirtimo tašką, viršijantį t_{n_1} laiko momentą.

$$t_{0,k} = \min\{\arg[u_k(t_n) = 0]\}; \quad 2.8$$

kur $t_n > t_{n_1}$, t_n – visi laiko momentai, o $u_k(t_n)$ – visi skaitmeniniai signalai, atsispindėti laiko momentais t_n didesniais už t_{n_1} .

Visų signalų suderinimas laike buvo atliekamas perstumiant signalą pagal nustatytus laiko intervalus, apibūdinančius signalo vėlavimą [9].

$$u'_k(t_n) = u_k(t_n + t_{0,k}); \quad 2.9$$

4. Daugkartinių atspindžių nuo bandinio ribos (metalo-klijai) laiko intervalų nustatymas, kai stebimas didžiausias amplitudės pokytis.

5. Apskaičiuota signalo amplitudė laiko srityje nuo taško, kuriame pastebimas didžiausias amplitudės pokytis esant defektui. Amplitudė buvo apskaičiuota kiekvienam daugkartinių signalo atspindžių nuo aliuminio ir klijų jungties laiko intervalui.

$$M_n = \max(u(t)) - \min(u(t)); \quad 2.10$$

kur n – daugkartinių atspindžių nuo sujungimo skaičius, $n = [1, 2, \dots, N]$, t nustatyti daugkartinių atspindžių laiko intervalai.

6. Daugkartinių atspindžių amplitudžių santykio apskaičiavimas.

$$K_1 = \frac{M_n}{M_{n+1}}; \quad 2.11$$

$$K_2 = \frac{M_{n+1}}{M_n}; \quad 2.12$$

kur M_n yra daugkartinių atspindžių amplitudės maksimumo vertė nustatytuose laiko intervaluose, o n yra ribinių daugkartinių atspindžių skaičius, kur $n = [1, 2, \dots, N]$.

Algoritmo taikymas demonstruojamas tolesniame eksperimentinių rezultatų ir sukurto algoritmo taikymo skyriuje.

3. EKSPERIMENTINIAI TYRIMAI IR SUKURTO ALGORITMO TAIKYMAS

Šiame skyriuje pateikiami eksperimentinių tyrimų rezultatai, eksperimentinių ir sumodeliuotų duomenų palyginimo rezultatai, siūloma metodika ir demonstruojamas sukurto algoritmo taikymas.

3.1. Skirtingų medžiagų sujungimų eksperimentiniai tyrimai ir rezultatai

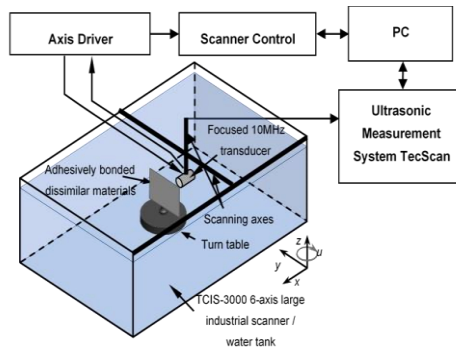
Šio skyriaus tikslas – pademonstruoti gautus eksperimentinės skirtingos medžiagos sujungimų patikros rezultatus naudojant ultragarsinius neardomuosius metodus.

3.1.1. Sujungto plieno ir CFRP komponento aprašymas ir eksperimentinis tyrimas

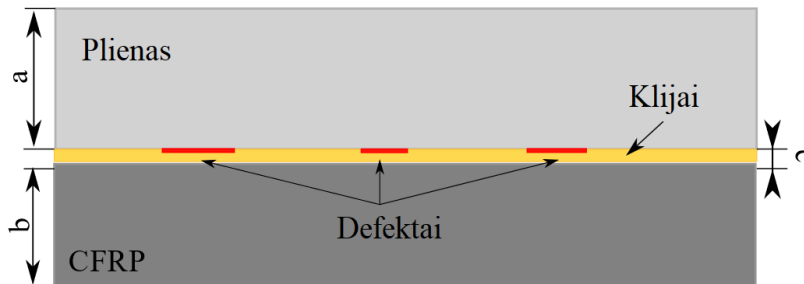
Šiame skyriuje buvo tiriamas plieno ir anglies pluošto sukibimo komponentas, kai abi plokštės turi storus skirtingų medžiagų sluoksnius. Plieno ir CFRP bandinys yra plokščios stačiakampio formos. Jungtyje taip pat yra 3 dirbtiniai defektai, esantys tarp klijų ir plieno. Defektai buvo padaryti iš polietileno (PE) juostos, naudojant alyvą, kad būtų išvengta plokštelių ir epoksidinės medžiagos sukibimo. CFRP kompozitinę medžiagą sudaro 4 vienkrypčiai anglies epoksidinio pluošto (plieno ir CFRP junginio) sluoksniai, išdėstyti skirtingais kampais (90° , 45° , 0° , -45°). Bandinių geometrinės charakteristikos pateiktos 3.1 lentelėje ir 3.1 paveiksle.

3.1 lentelė. Tiriamų skirtingų medžiagų sujungimų plienas-CFRP geometrinės charakteristikos

Nr.	Charakteristikos	Plienas-CFRP
1	Storis	9,32 mm
2	Metalo storis	6,14 mm
3	Kompozito storis	3,18 mm
4	Klijų storis	0,1 mm
5	Bandinio matmuo	300 mm × 300 mm
6	Defektų kiekis	3
7	Defektų matmuo	20 mm × 20 mm; 15 mm × 15 mm; 25 mm × 25 mm;
8	Metalo ir kompozito plokštės matmenys	300 mm × 300 mm
9	Prikljuotos dalies matmenys	300 mm × 300 mm
10	Defekto vieta	Tarp epoksidinės ir metalinės plokštės
11	Vienakrypčiai pluoštai	4 sluoksniai CFRP pluoštų



a

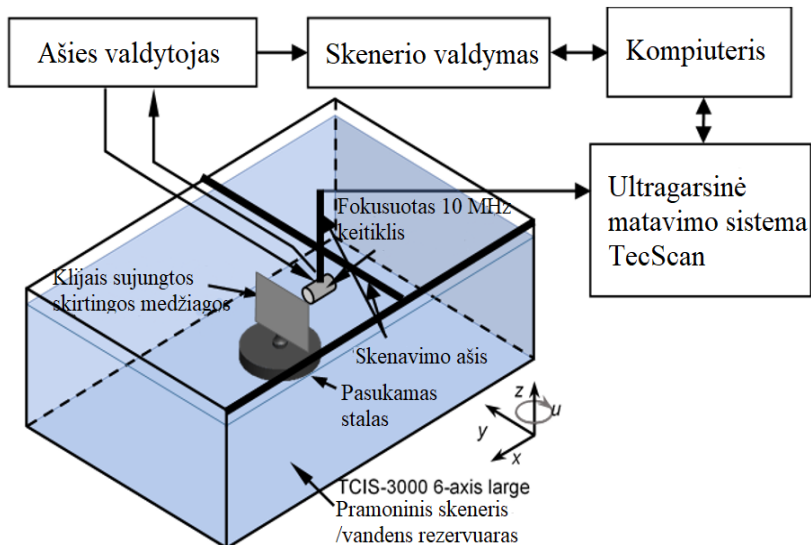


b

3.1 pav. Skirtingų medžiagų sujungimas plieno-CFRP jungtis: (a) bandinių struktūra plokštumoje, (b) bandinių struktūra skerspjūvyje, kur a = plieno storis, b = CFRP storis, c = klijų sluoksnio storis

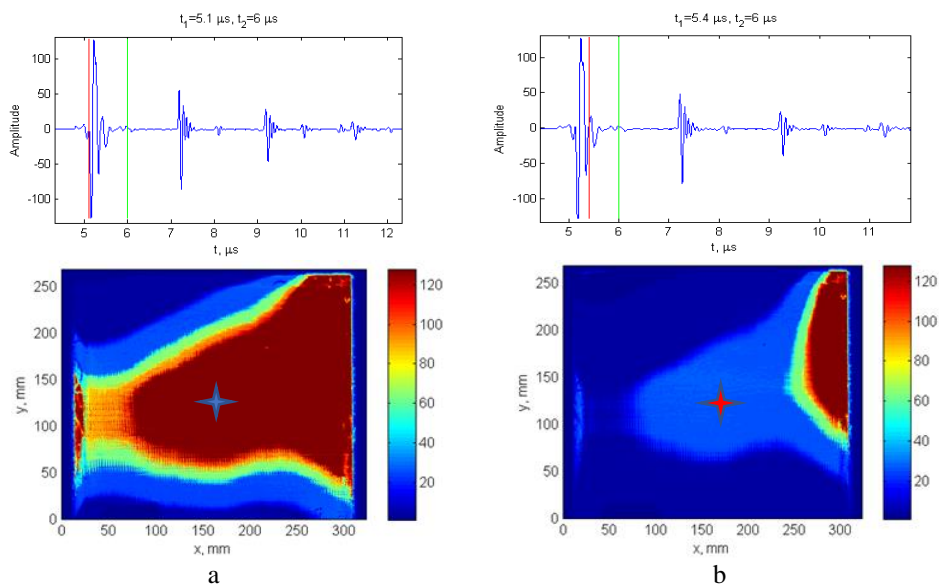
Iš skirtingų medžiagų suklijuotų konstrukcijų ultragarsiniam patikrinimui buvo naudojama „TecScan“ matavimo sistema („TecScan Systems Inc.“) su 10 MHz

fokusuotu keitikliu, taikant ultragarsinį impulsinį atspindžio metodą. Tiriamas bandinys buvo panardintas į vandens rezervuarą ir pritvirtintas prie sistemos sukamojo stalo, o keitiklis buvo fokusuotas į vidinę plokščių suklijavimo ribą. Skenavimo sritis buvo nustatyta išilgai y ir z ašių su 1 mm (plienas-CFRP) skenavimo žingsniu. Patikrinimo atlikimo schema pavaizduota 3.2 paveiksle.



3.2 pav. Plieno-CFRP ir aliuminio-CFRP klijuotų konstrukcijų iš skirtingų medžiagų sujungimų ultragarsinės impulsinės echoskopinės patikros imersiniu metodu parengimas [9]

Gauti rezultatai apibūdina klijuotų skirtingų medžiagų apžiūros problematiką ir įtaką darantį faktorių – objekto paviršiaus kreivumą. Plieno-CFRP konstrukcijos eksperimentinio tyrimo C-skenai, atlikti naudojant 10 MHz fokusuotą keitiklį impulsiniu atspindžio režimu, pateikti 3.3 paveiksle. Gauti C-skenai rodo bandinio paviršiaus kreivumą. Šis faktorius turi didelę įtaką defektų nustatymui dėl skirtingo ultragarso bangų sklaidimo laiko.



3.3 pav. Plieno ir CFRP konstrukcijos A ir C skenavimas, rodantis signalus, prasidedančius skirtingais laiko momentais: (a) 5,1-6 μ s laiko intervalui, (b) 5,4-6 μ s laiko intervalui

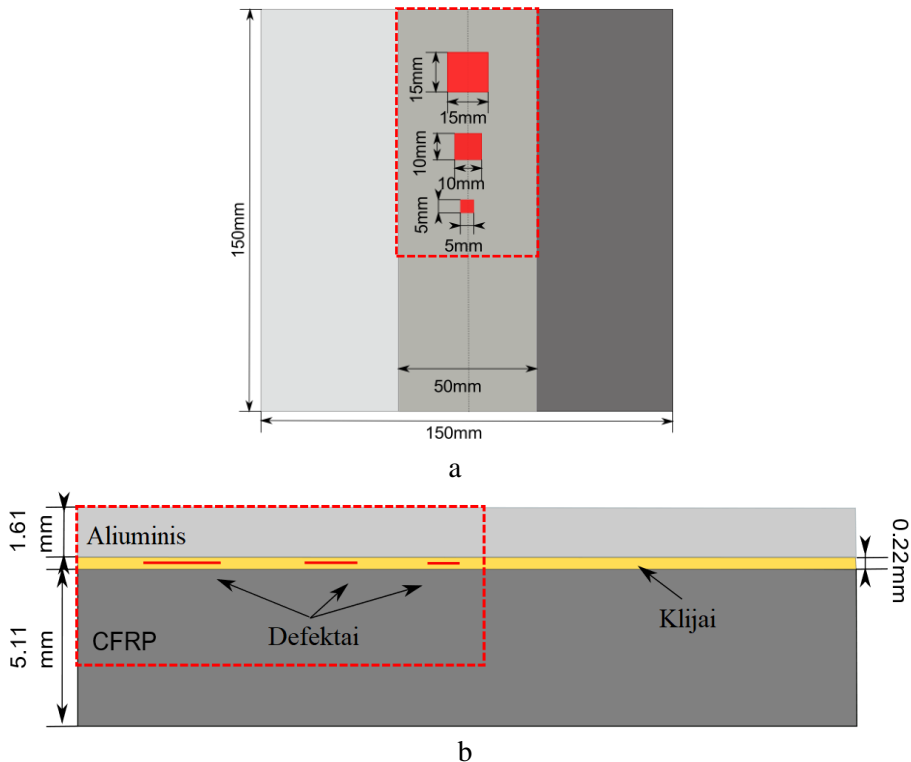
Remiantis modeliavimo rezultatais, analizuojant daugkartinius atspindžius turėtų padidėti tikimybė aptikti sukibimo defektus. Todėl daugkartinių atspindžių nuo metalo ir klijų sandūros ribos analizei buvo nustatyti laiko ribos. Geriausi defektų aptikimo rezultatai gauti tiriant 3-įjį atspindį nuo plieno ir klijų jungties.

3.1.2. Sujungto aliuminio-CFRP komponento aprašymas ir eksperimentinis tyrimas

Taip pat tiriamas aliuminio ir anglies pluoštu sutvirtinto plastiko vienasluoksnis sujungimas. Dėl plonesnių detalių medžiagų sluoksnių gali būti sunkiau nustatyti defektus. Aliuminis ir CFRP buvo suklijuoti naudojant du sluoksnius struktūrinės klijų plėvelės „3M Scotch-Weld AF163-2 K red“. Sujungime tarp dviejų klijų plėvelės sluoksnių buvo įterpti trys dirbtiniai defektai. Atsiloksniavimo defektai buvo pagaminti iš dviejų sluoksnių „Wrightlon® 4600“ poliolefino kopolimero plėvelės. Bandinio CFRP plokštė sudaryta iš 41 vienkrypčio pluošto sluoksnio, kur pirmasis ir paskutinis sluoksniai yra GFRP pluoštas. Laminatų orientacija yra tokia: 45°, -45°, 0°, 90°. Bandinio geometrinės charakteristikos pateiktos 3.2 lentelėje ir 3.4 paveiksle.

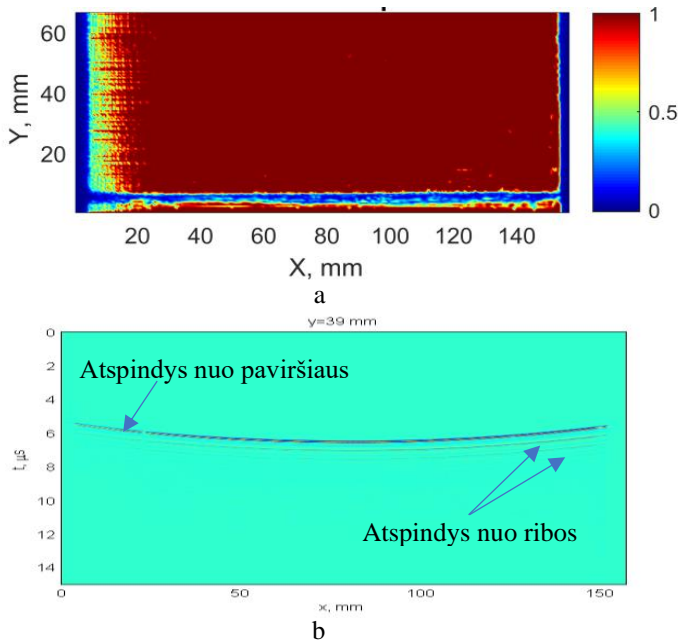
3.2 lentelė. Tiriamų skirtingų medžiagų sujungimų plienas-CFRP geometrinės charakteristikos

Nr.	Charakteristikos	Plienas-CFRP
1	Storis	6,94 mm
2	Metalo storis	1,61 mm
3	Kompozito storis	5,11 mm
4	Klijų storis	0,22 mm
5	Bandinio matmuo	150 mm × 150 mm
6	Defektų kiekis	3
7	Defektų matmuo	5 mm × 5 mm; 10 mm × 10 mm; 15 mm × 15 mm;
8	Metalo ir kompozito plokštės matmenys	100 mm × 150 mm
9	Prikljuotos dalies matmenys	50 mm × 150 mm
10	Defekto vieta	Tarp 2 sluoksnių klijų plėvelės
11	Vienakrypčiai pluoštai	41 sluoksnis (0–41): 40 CFRP pluoštų, 2 GFRP pluoštai



3.4 pav. Skirtingų medžiagų sujungimas iš aliuminio ir CFRP: (a) bandinių struktūra plokštumoje, (b) bandinių struktūra skerspjūvyje, kur a = plieno storis, b = CFRP storis, c = klijų sluoksnio storis

Taip pat buvo naudojama „TecScan“ matavimo sistema („TecScan Systems Inc.“) ir 10 MHz fokusuotas keitiklis, skirtas aliuminio-SFRP konstrukcijai patikrinti ultragarso impulso-echo metodu. Keitiklis buvo nukreiptas į metalo ir klijų sujungimo vietą. Skenavimo sritis išilgai y ir z ašių buvo nustatyta 0,5 mm skenavimo žingsniu. Patikrinimo schema parodyta 3.2 pav. Aliuminio ir anglies pluoštu armuoto plastiko sujungimo eksperimentinio tyrimo C ir B skenavimas parodytas 3.5 paveiksle.



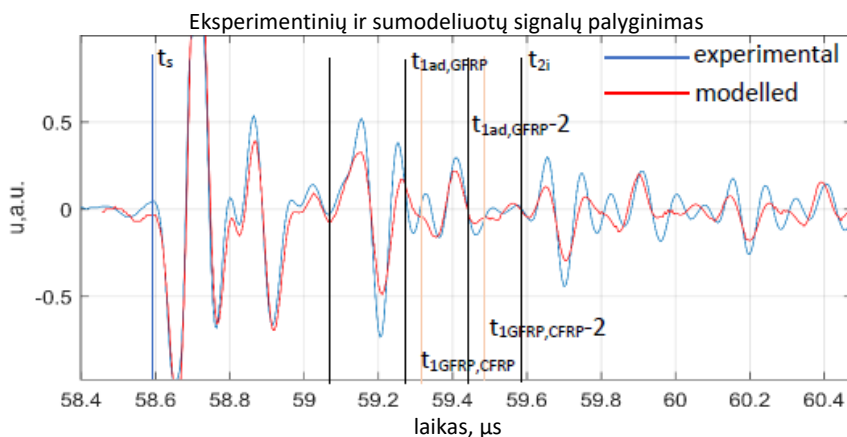
3.5 pav. Aliuminio ir CFRP klijuotos konstrukcijos B ir C skenai: (a) C-skenas, (b) B-skenas, rodantis komponentų kreivumą

Dėl įtakingo bandinio kreivumo veiksnio buvo sudėtinga aptikti sukibimo defektus struktūros riboje. Didžiausias laiko skirtumas, pastebėtas dėl paviršiaus kreivumo, yra 1 μ s. Defektų ir jų dydžių neįmanoma išmatuoti. Taigi, reikia sukurti ir taikyti vieną metodą visų tipų bandiniams iš skirtingų medžiagų, turinčių sluoksniuotą struktūrą, siekiant pašalinti bandinių kreivumo (o ne idealios geometrijos) įtaką.

Apibendrinant galima teigti, kad visi eksperimentų rezultatai, gauti tiriant skirtingų nelygiaverčių medžiagų bandinius, rodo pagrindinę defektų nustatymo problemą, kurią lemia skirtingas nelygiaverčių medžiagų akustinis impedansas ir įtakos turintis paviršiaus kreivumo faktorai.

3.2. Modeliavimo ir eksperimentinių rezultatų palyginimas

Šio skyriaus tikslas – nustatyti daugkartinių atspindžių laiko momentus ir laiko intervalus su didžiausiu amplitudės pokyčiu, kurį sukelia defektas, taikant 2.1.4 skyriuje aprašytą metodą. Pirmasis atliktas metodo etapas – optimizuoti parametrus (ultragarso greitį, sluoksnio storį ir tankį), siekiant gauti modeliuojamą signalą, sklindantį per aliuminio ir CFRP medžiagų sluoksniuotą struktūrą, kuo artimesnį eksperimentiniu būdu gautam signalui. Optimizavus parametrus, buvo pasiektas geriausias modeliavimo ir eksperimentinio signalo atitikimas. Šių signalų, atsispindėjusių nuo defektų neturinčios ribos, modelio ir eksperimento A-skenavimo palyginimas parodytas 3.6 pav.



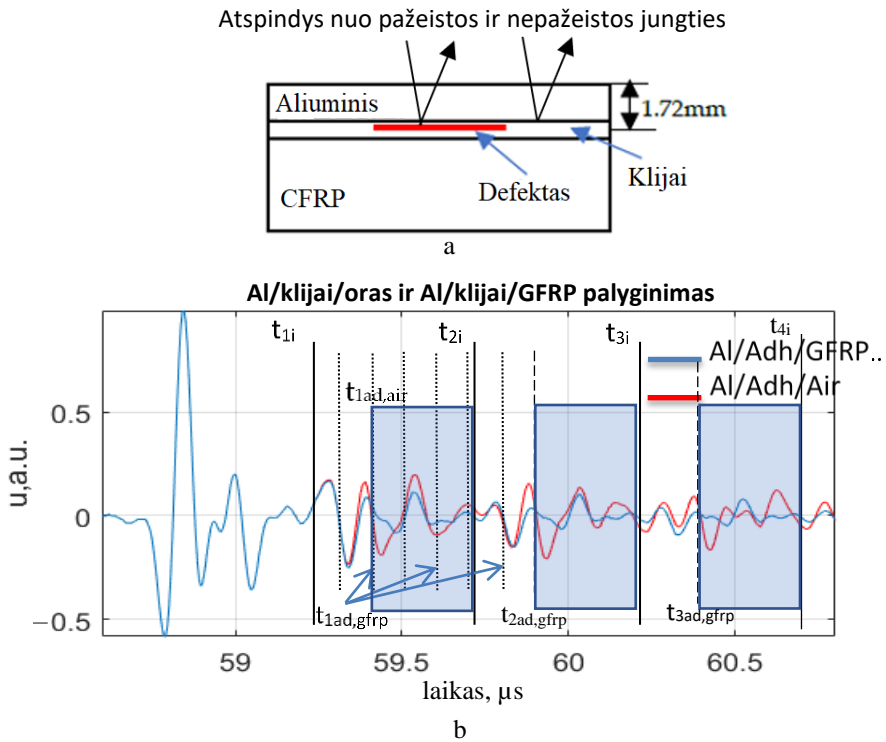
3.6 pav. A skenavimo modelio ir eksperimentinių signalų palyginimas (mėlyna spalva apibūdina sumodeliuotą signalą, raudona – eksperimentiškai gautą signalą) [9]

Tyrimas parodė, kad reverberacija pasireiškia paviršiaus ir vidinio sujungimo atspindžiuose abiejuose signaluose (modeliuojamuose ir eksperimentiniu būdu gautuose signaluose). A skenas, pateiktas 3.6 paveiksle, iliustruoja, kaip signalai, kurie atsispindi nuo aliuminio ir klijų jungties t_{1i} , ir signalai, atsispindintys nuo klijų-GFRP $t_{1ad,GFRP}$ ir GFRP-CFRP $t_{1GFRP,CFRP}$ ribų, taip pat jų daugkartiniai atspindžiai persidengia dėl plonų sluoksnių storių. Dėl šio persidengimo efekto defektus aptikti sunkiau, nes signalų, atsispindėjusių nuo defektų turinčių ir defektų neturinčių sričių, amplitudės skirtumas gali būti neakivaizdus ir jo nepavyks nustatyti.

Modeliuojamo signalo, atsispindėjusio nuo daugiasluoksnės aliuminio ir anglies plastiko konstrukcijos, esant idealiam sujungimui su klijais (aliuminis-klijai-kompozitas) ir defektiniam sujungimui (aliuminis-klijai-defektas), A-skenavimo palyginimas pateiktas 3.7 pav.

Palyginus A skeno modeliuotus signalus, atsispindėjusius nuo tobulo sujungimo jungties (aliuminis-klijai-kompozitas) ir defektinės jungties (aliuminis-klijai-defektas), buvo nustatytas atitinkamo atspindžio laikas. Atsižvelgiant į pirmojo atspindžio nuo aliuminis-klijai ribos laiko intervalą, didžiausias amplitudės pokytis pastebėtas po antrojo atspindžio nuo defekto $t_{1ad,air}$ arba pirmojo atspindžio

nuo apatinės klėjai-kompozitas ribos $t_{1ad,gfrp}$ metu laiko intervale $t_{1i}:t_{2i}$. Signalo, atsispindėjusio nuo dugno arba klijų ir kompozito jungties, laiko momentas sutampa su dvigubai ilgesniu signalo laiku, atsispindėjusiu nuo defekto. Kadangi daugkartinių atspindžių tyrimas turi didelę įtaką defektų aptikimo tikimybei, kiekvienam daugkartinių atspindžių nuo tarpinės ribos (aliuminis-klėjai) laiko intervalui ($t_{1i}:t_{2i}$, $t_{2i}:t_{3i}$, $t_{3i}:t_{4i}$, $t_{4i}:t_{5i}$) atitinkamai buvo nustatyti laiko momentai ir laiko intervalai su dideliais amplitudės pokyčiais. 3.3 lentelėje pateikiami laiko intervalai, kuriuose amplitudės vertės keitėsi labiausiai.



3.7 pav. Sumodeliuotų signalų palyginimas: (a) struktūros pjūvio vaizdas, (b) A skenavimo palyginimas [9]

3.3 lentelė. Pasirinkti laiko intervalai ir amplitudės vertės

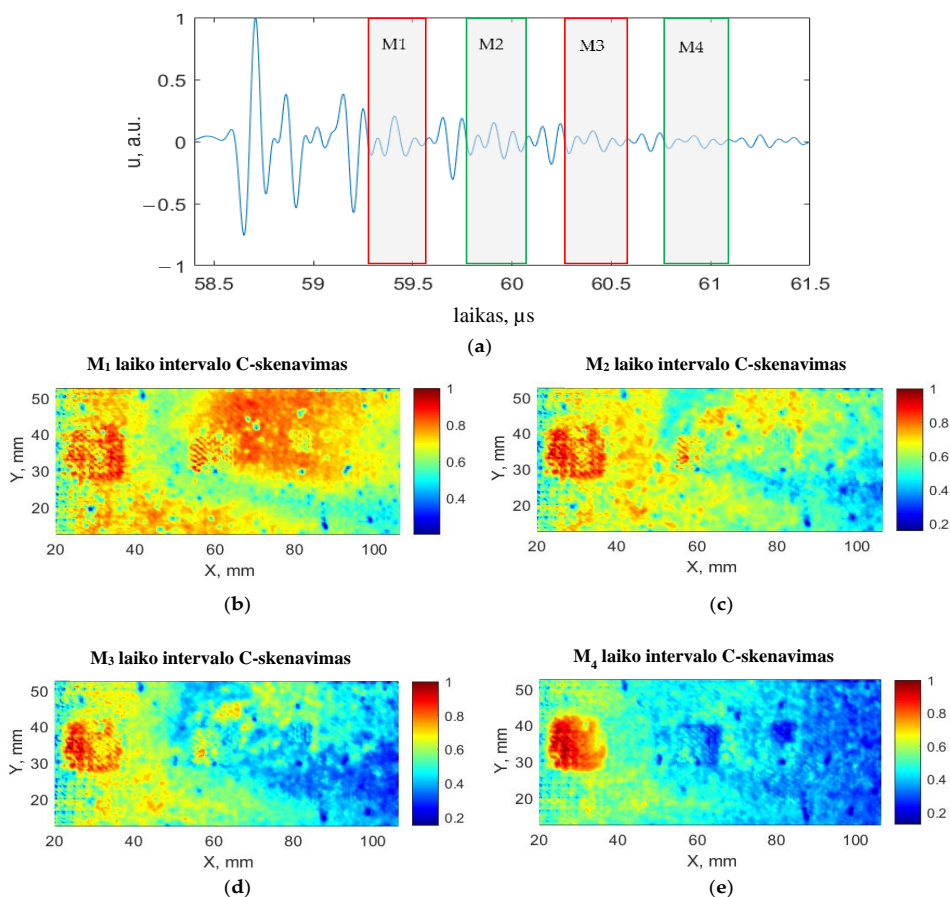
Amplitudės vertės	Laiko intervalai su didžiausiu amplitudės pokyčiu
M_1	$t_{1ad,GFRP}:t_{2i}$
M_2	$t_{2ad,GFRP}:t_{3i}$
M_3	$t_{3ad,GFRP}:t_{4i}$
M_4	$t_{4ad,GFRP}:t_{5i}$

Nustatyti laiko intervalai ir amplitudžių apskaičiavimas buvo naudojami sukurtame apdorojimo algoritme siekiant padidinti defekto aptikimo tikimybę.

3.3. Sukurto signalo apdorojimo algoritmo taikymas ir rezultatų aptarimas

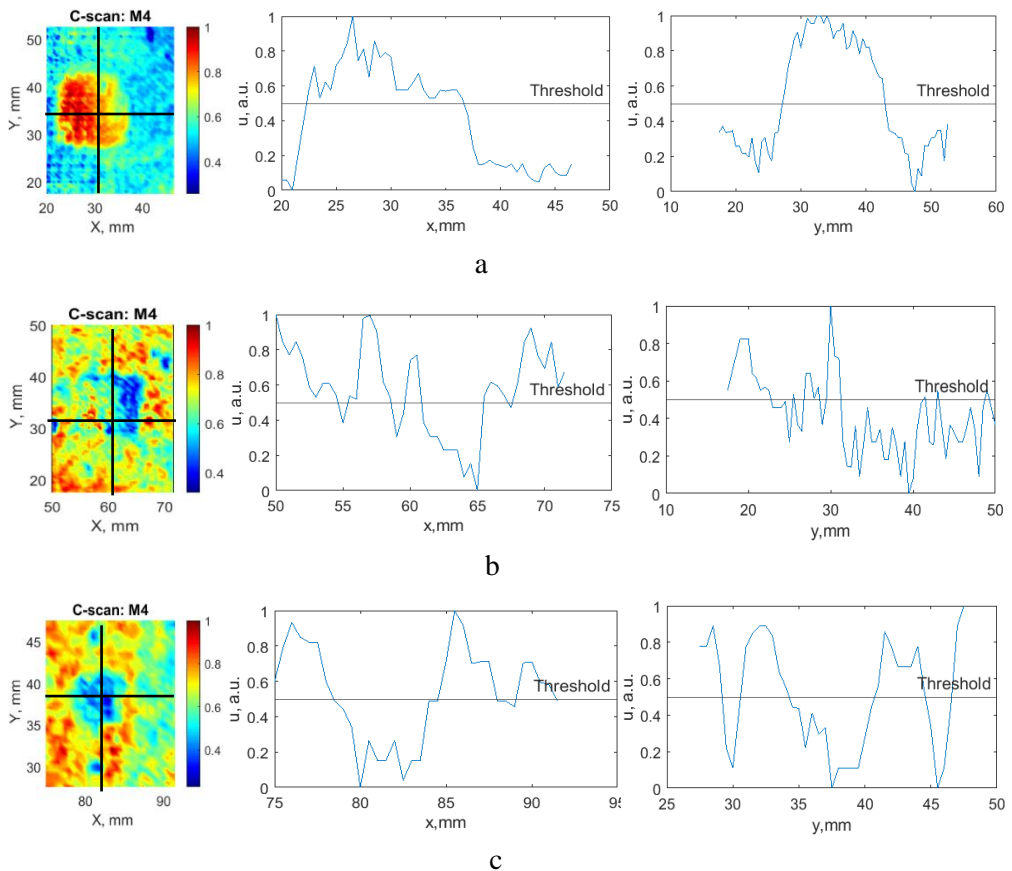
Šio skyriaus tikslas – pritaikyti sukurtą signalo apdorojimo algoritmą siekiant pagerinti defektų aptikimo galimybes klįjais sujungtuose skirtingų medžiagų sujungimuose. Šiam tikslui pasiekti eksperimentinių aliuminio ir CFRP sluoksniuotos konstrukcijos tyrimo metu įrašyti matavimo signalai buvo apdoroti pagal sukurtą algoritmą.

Pirmausia buvo naudojamas juostinis filtras, kad būtų pašalintas triukšmas iš signalų. Tada buvo taikomas nulinio kirtimo metodas norint suvienodinti nuo objekto paviršiaus atsispindėjusių signalų atvykimo laiką. Po to buvo nustatytas paviršiaus atspindžių laikas ir numatyti tinkami laiko intervalai daugkartiniams atspindžiams nuo vidinio klįjų sluoksniu (aliuminio ir klįjų sujungimas) analizei atlikti. Tuomet buvo apskaičiuotos amplitudės vertės pasirinktais laiko intervalais (M_1 - M_4) C skenui atvaizduoti (3.8 pav.).



3.8 pav. Pasirinktų daugkartinių atspindžių A ir C skenai: (a) A-skenas, (b) C-skenas M_1 laiko intervalu, (c) C-skenas M_2 laiko intervalu, (d) C-skenas M_3 laiko intervalu, (e) C-skenas M_4 laiko intervalu [9]

Taikant pasirinktus laiko intervalus C skenavimo vizualizacijai, buvo galima aptikti visus struktūroje esančius defektus. Du mažesni defektai pastebimi aiškiau. Pirmasis ir ketvirtasis atspindžiai iš aliuminio ir klijų jungties M_1 ir M_4 laiko intervaluose suteikia ryškesnius visų trijų defektų formos kontūrus. Be to, defektų aptikimo pagerėjimas buvo kiekybiškai įvertintas taikant -6 dB kritimo metodą M_4 intervalui. C skenavimas ir intensyvumo pokyčio pjūviai pasirinktoje defekto koordinatėje išilgai x ir y ašių pavaizduoti 3.9 pav. Defektų matmenys pateikti 3.4 lentelėje.

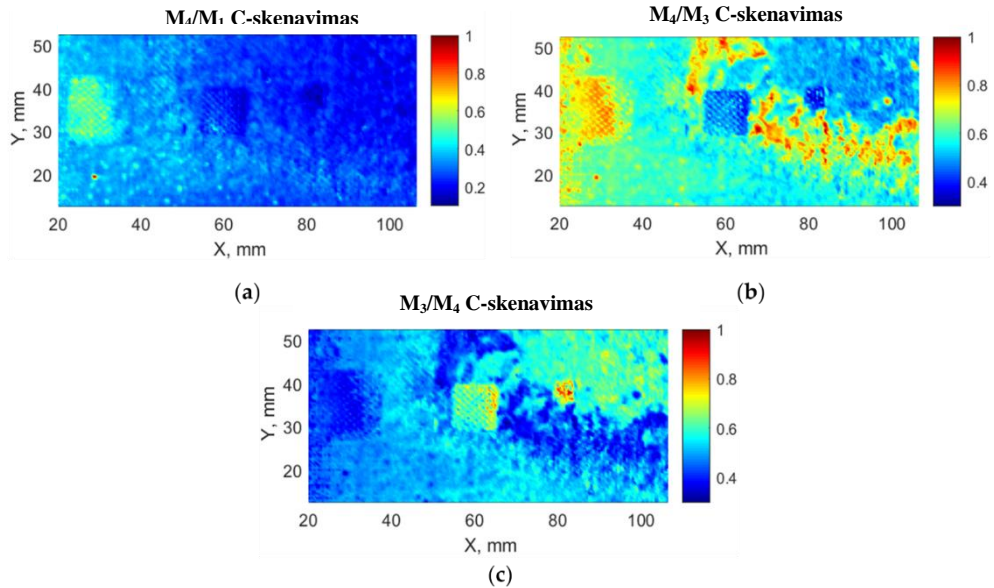


3.9 pav. C skenavimas ir intensyvumo pokyčio pjūviai x ir y ašyse (-6 dB kritimo metodas):
 (a) didžiausias defektas, (b) vidutinio dydžio defektas, (c) mažiausias defektas

3.4 lentelė. Defektų matmenys, išmatuoti taikant -6 dB kritimo metodą

Atspindys	Pokyčio pjūviai	Didžiausias defektas, mm	Vidutinio dydžio defektas, mm	Mažiausias defektas, mm
M_4	X ašis	14,3	4,7	6
	Y ašis	15,7	10,2	6,4

Šiuo atveju išmatuoti defektų dydžiai yra artimesni etaloniniams defektams, palyginus su aliuminio ir klijų sukibimo atspindžių rezultatais, kai laiko intervalai yra $t_{1i}; t_{2i}$ ir kiti. Be to, buvo apskaičiuotas nustatytų laiko intervalų M_1 - M_4 amplitudžių santykis (lygtys 2.11, 2.12), kuris atitinka sukurto apdorojimo algoritmo 6 žingsnį. Geriausi amplitudžių santykio koeficientai, užtikrinantys geriausią defektų aptikimo galimybę, parodyti 3.10 pav. Pagal C skeną galima matyti visus struktūros defektus, kurie buvo aptikti su geresniu aptikimo patikimumu.



3.10 pav. Amplitudės santykio koeficientų C skenai: (a) M_4/M_1 , (b) M_4/M_3 , (c) M_3/M_4 [9]

M_4/M_1 laiko intervalo santykio C skenavimas rodo aptiktą didžiausią defektą. M_4/M_3 ir M_3/M_4 C skenavimas rodo didesnę tikimybę aptikti du mažesnius defektus su ryškesniais defekto geometrijos kontūrais. Defektų dydžiai buvo išmatuoti taikant -6 dB kritimo metodą ir pateikti 3.5 lentelėje.

3.5 lentelė. Defektų matmenys, išmatuoti taikant -6 dB kritimo metodą

Atspindys	Pokyčio pjūviai	Didžiausias defektas, mm	Vidutinio dydžio defektas, mm	Mažiausias defektas, mm
M4/M1	X ašis	9,8	-	-
	Y ašis	13,5	-	-
M4/M3	X ašis	11,6	11,5	4,9
	Y ašis	11,6	13,5	6,2
M3/M4	X ašis	13,6	10,3	3,8
	Y ašis	11,8	11,4	3,9

Geriausius didžiausio defekto aptikimo rezultatus rodo M_4 laiko intervalo C skenavimas, kurio matmenys – 14,3 x 15,7 mm. Vidutinio defekto atveju geriausius

rezultatus rodo M3/M4 C-skenavimas, kurio matmenys yra 10,3 x 11,4 mm, o mažiausio defekto atveju – M4/M3 C-skenavimas, kurio matmenys yra 4,9 x 6,2 mm.

4. ULTRAGARSINIO NDT METODO PATIKIMUMAS IR NEAPIBRĖŽTIES MATAVIMAS

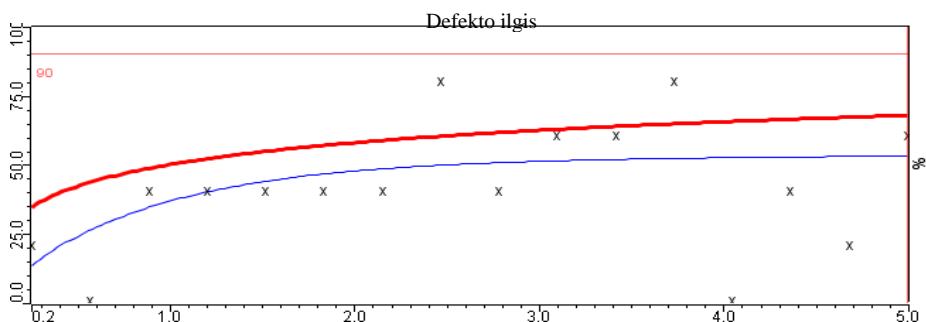
Ultragarsinio neardomojo metodo patikimumą, siekiant aptikti defektus skirtingų medžiagų sujungimuose, galima kiekybiškai įvertinti taikant aptikimo tikimybės metodą [76, 83]. Šio skyriaus tikslas – įvertinti sukibimo defekto, kurį galima aptikti naudojant pasirinktą ultragarsinį NDT metodą, dydį sluoksniuotosios struktūros skirtingų medžiagų sujungimuose prieš ir po to, kai panaudojamas sukurtas signalo apdorojimo algoritmas.

4.1. Modeliu pagrįstos aptikimo tikimybės vertinimas

POD kreivėms vertinti naudotas 2 skyriuje aprašytas metamodelio metodas. Nustatyta pradinė konfigūracija, kurioje aprašyta visa būtina patikrinimo informacija. Tada buvo nustatyti ir apibūdinti kintamumo šaltiniai bei jų statistiniai pasiskirstymai. Nustatytų kintamųjų parametru statistinių pasiskirstymų atranka atlikta taikant Monte Karlo algoritmą. Buvo apskaičiuoti atitinkami modeliavimo rezultatai. Pagal gautus rezultatus apskaičiuotos POD kreivės. Ultragarsinio NDT metodo patikimumas prieš ir po sukurto signalo apdorojimo algoritmo panaudojimo buvo įvertintas nustatant defektų POD ir pateiktas [78]. Sukurto algoritmo veiksmingumas gerinant defektų aptikimą buvo įvertintas lyginant šiuos rezultatus. Statistiniam apdorojimui buvo pasirinktas signalo atsako metodas. Defekto ilgis (charakteristikų reikšmė) laikomas POD kreivės abscisių ašimi.

4.1.1. Sukibimo defektų aptikimo signalo atsako analizė prieš taikant signalo apdorojimo algoritmą

Pirma, POD kreivė buvo įvertinta defektams aptikti naudojant ultragarsinę patikrą prieš taikant signalų apdorojimo algoritmą. Aptikimo riba yra -9,1 dB, o tai yra aukščiausias foninio triukšmo lygis (atspindys nuo defektų neturinčios jungties). Gauta signalo atsako POD kreivė pavaizduota 4.1 pav.

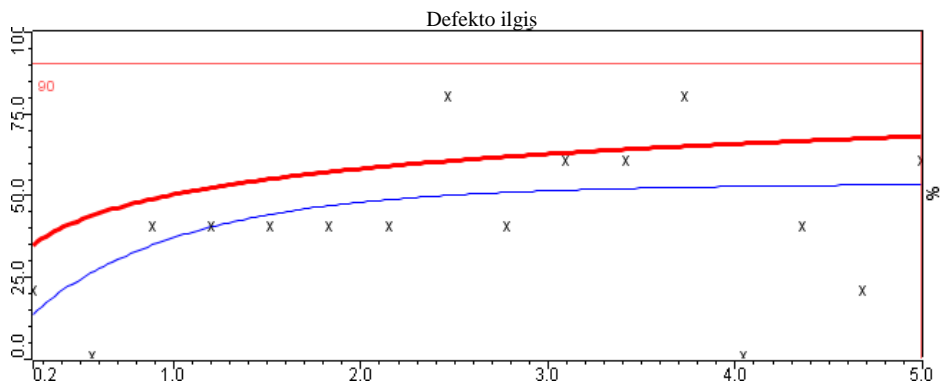


4.1 pav. Signalo atsako POD kreivė su Log/Lin duomenimis patikrinimui prieš algoritmo taikymą (defekto ilgis)

90 % atliktų patikrinimų, kai patikimumo lygis yra 95 %, neįmanoma aptikti jokio defekto komponento sukibimo sluoksnyje. Tikimybių kreivės, kurios nesiekia 100 % aptikimo tikimybės, nėra nuoseklios. Tačiau, analizuojant gautą POD kreivę, yra maždaug 53 % tikimybė, kad 5 mm dydžio defektą galima aptikti. Ši tikimybė yra labai maža ir neatitinka matavimo reikalavimų, ypač aviacijos ir kosmoso pramonėje. Tai gali lemti faktoriai, kurie daro didelę įtaką defektų aptikimui naudojant patikrinimo techniką.

4.1.2. Sukibimo defekto aptikimo signalo atsako analizė pritaikius signalo apdorojimo algoritmą

Šioje dalyje sukurto metodo efektyvumas buvo įvertintas pagal POD kreivės vertinimą, siekiant nustatyti klįjavimo defektus. Pagrindiniai faktoriai, tokie kaip kritimo kampas ir vandens kelias, buvo pašalinti taikant šį metodą, todėl šie faktoriai nebuvo įtraukti kaip neapibrėžtieji parametrai POD vertinimui. Be to, laiko intervalas buvo nustatytas taip, kad apimtų daugkartinį atspindį nuo ribos. Defekto ilgis pasirinktas kaip charakteristinė reikšmė ir laikomas POD kreivės abscisių ašimi. Įvertinta POD kreivė pateikta 4.2 pav.



4.2 pav. Signalo atsako POD kreivė su Log/Log duomenimis patikrinimui po algoritmo pritaikymo (defekto ilgis)

Todėl, pašalinus didžiausią įtaką darančius faktorius, buvo gauta nuosekli POD kreivė. Defekto a_{90} ilgis yra 3,26 mm ir jį galima aptikti su 90 % tikimybe. Defekto $a_{90/95}$ ilgis yra 4,64 mm, jį galima aptikti 90 % atliktų patikrinimų su 95 % patikimumo lygiu. Neapibrėžtis pagal pasikliautinius intervalus yra 1,38 mm.

4.2. Neapibrėžties matavimas

Šiame skyriuje buvo vertinama išmatuotų defektų dydžių neapibrėžtis, pritaikius sukurta signalo apdorojimo algoritmą defektams aptikti ir pagerinus jų aptikimo tikimybę. Neapibrėžčiai matuoti buvo nustatytas matematinis modelis. Norint apskaičiuoti defekto ilgio neapibrėžtį išilgai x ir y ašių, formulė išreiškiama taip [112]:

$$Y = f(X_1, X_2, \dots, X_n); \quad 4.1$$

kur Y yra matuojamasis dydis arba defekto ilgis, X_i – įėjimo dydžiai (paklaidų šaltiniai), nuo kurių priklauso išėjimo dydis Y , kur $i=1, 2, \dots, n$, f – matavimo proceso funkcija.

Pagrindiniai veiksniai, turintys įtakos defektų aptikimui ir jų dydžio nustatymui, buvo nustatyti 2 skyriaus jautrumo analizės poskyryje ir yra šie: ultragarso greitis aliuminyje, defekto padėtis klijų sluoksnyje, vandens kelias tarp keitiklio ir detalės paviršiaus, aliuminio storis ir paviršiaus kreivumas. Kiekvieno įtaką darančio faktoriaus standartinė neapibrėžtis buvo kiekybiškai įvertinta taikant A ir B tipo neapibrėžties vertinimą. Įtaką darantys faktoriai, arba paklaidų šaltiniai, jų išvestiniai faktoriai, taip pat kiekvienam iš jų tinkamas neapibrėžties tipas ir matavimo modelis pateikiami 4.1 lentelėje.

4.1 lentelė. Įtakoiantys faktoriai ir matematiniai modeliai

Nr .	Įtakoiantys faktoriai	Neapibrėžties tipas	Modelis
1	Ultragarso greitis aliuminyje, V_{al}	B	$V_{al} = \left(\frac{2H_{al}}{t_{al}}\right);$
2	Aliuminio storis, H_{al}	A	Statistinė analizė
3	Matuoklio skiriamoji geba, r_c	B	Instrumento vertės, $r_c=0.01$
4	Skridimo iki aliuminio klijų jungties ir atgal laikas, t_{al}	A	Statistinė analizė
5	Ultragarso bangos ilgis aliuminyje, λ_{al}	B	$\lambda_{al} = \left(\frac{V_{al}}{f_{freq}}\right);$
6	Keitiklio dažnis, f_{freq}	B	Techniniai dokumentai
7	Defekto padėtis klijų sluoksnyje, D_d	A	Statistinė analizė
8	Vandens kelias tarp keitiklio ir paviršiaus, W_p	B	$W_p = F - M_D \left(\frac{V_{al}}{V_w}\right);$
9	Fokusavimo atstumas, F	B	Techniniai dokumentai
10	Ultragarso greitis vandenyje, V_w	B	$V_w = \left(\frac{2H_w}{t_w}\right);$
11	Vandens terpės storis, H_w	A	Statistinė analizė
12	Skridimo iki vandens ir aliuminio jungties ir atgal laikas, t_w	A	Statistinė analizė

A ir B tipo matavimo standartinė neapibrėžtis nustatyta pagal 4.2 ir 4.3 lygtis. Kombinuota neapibrėžtis buvo išplėsta iki 95 % patikimumo lygio (4.4 lygtis).

$$u(x_i) = \sqrt{\frac{1}{N(N-1)} \sum_{i=1}^N (x_i - \bar{x})^2}; \quad 4.2$$

kur N yra nepriklausomų matavimų skaičius, x_i – išmatuota vertė, \bar{x} – kelių nepriklausomų matavimų vidutinės vertės.

$$u(y) = \sqrt{\sum_{i=1}^n u(x_i)^2 \cdot W(x_i)^2}; \quad 4.3$$

kur $W(x)$ – įtakos koeficientas.

$$u_{exp} = k \cdot u(y); \quad 4.4$$

kur $k = 2$ – apimties skaičius, parinktas iš Stjudento lentelės (normaliojo pasiskirstymo dėsnis).

Aptikto defekto ilgio išilgai x ir y ašių išplėstinė neapibrėžtis yra 0,88 mm.

IŠVADOS

1. Ultragarsinis neardomasis tyrimų metodas, atspindžio ir perdavimo koeficientų įvertinimas, duomenų apdorojimas, taip pat įtakojančių veiksnių tyrimas ir aptikimo tikimybės įvertinimas buvo pasirinkti siekiant sukurti metodiką, kuri leistų geriau aptikti sukibimo defektus skirtingų medžiagų sujungimuose.

2. Analizuojant daugkartinius atspindžius nuo ribos tarp skirtingų medžiagų, tikimybė aptikti sukibimo defektus padidėja, nes išauga amplitudės skirtumas tarp signalų, atsispindėjusių nuo sričių be defektų ir su defektais. Pagrindinis faktorius, turintis įtakos defektų aptikimui komponentuose su sluoksniuotomis struktūromis, yra paviršiaus (jungiamojo sluoksnio) kreivumas, kuris apibūdinamas tokiais neapibrėžtais parametrais kaip ultragarso spindulio kritimo kampas ir atstumas vandenyje. Šie parametrai turi atitinkamai 57 % ir 39 % įtakos.

3. Ultragarso bangų sklidimo trukmės modeliavimas leido nustatyti laiko intervalus, per kuriuos buvo pastebėtas didžiausias amplitudės pokytis, lyginant sumodeliuotus signalus, atsispindėjusius nuo defektinių ir nedefektinių sričių. Klįjais sujungtų skirtingų medžiagų sujungimų tyrimo metodas buvo sukurtas siekiant išgauti vertingus kriterijus, reikalingus signalo apdorojimo algoritmui sukurti, kad būtų padidinta defektų aptikimo klįjų sluoksnyje tikimybė. Išskiriami šie kriterijai: sklidimo laiko momentai ir atspindėtų signalų laiko intervalai, atsižvelgiant į daugkartinius atspindžius, amplitudės pokytis ir pasirinktų laiko intervalų amplitudžių santykio koeficientai. Tyrimo metodą sudaro šie etapai: daugkartinių atspindžių ir ribos charakteristikų analizė, jautrumo analizė, skaitinis tyrimas ir parametru optimizavimas.

4. Sukurtas apdorojimo algoritmas apima perėjimo per nulį metodą nuo bandinio paviršiaus atsispindėjusiems signalams išlyginti laike, daugkartinių atspindžių analizę, reikiamų laiko momentų nustatymą, kad būtų galima teisingai nustatyti laiko intervalus ir amplitudžių santykio koeficientus.

5. Naudojant sukurtą algoritmą buvo aptikti visi sukibimo defektai ir (arba) atsisluoksniavimai skirtingų medžiagų sujungimų sluoksnyje (nenaudojant algoritmo aptikimas apskritai neįmanomas) ir nustatyti jų dydžiai: 14,3 x 15,7 mm ±0,88 mm (didžiausias defektas), 10,3 x 11,4 mm ±0,88 mm (vidutinis defektas), 4,9 x 6,2 mm ±0,88 mm (mažiausias defektas). Pagal sukurtą metodiką, remiantis MAPOD vertinimu, taikant sukurtą algoritmą galima aptikti klįjų sluoksnio sukibimo ir (arba)

delaminacijos defektus atliekant 90 % patikrinimų, kai patikimumo lygis yra 95 %. Primintina, kad atliekant ultragarsinę patikrą ir netaikant algoritmo, iš viso nebuvo įmanoma aptikti defektų skirtingų medžiagų sujungimų bandinyje.

REFERENCES

- [1] N. Toyama, T. Yamamoto, K. Urabe, and H. Tsuda, "Ultrasonic inspection of adhesively bonded CFRP/aluminum joints using pulsed laser scanning," *Advanced Composite Materials*, vol. 28, no. 1, pp. 27–35, 2019.
- [2] L. Attar, D. Leduc, M. Ech Cherif El Kettani, M. V. Predoi, J. Galy, and P. Pareige, "Detection of the degraded interface in dissymmetrical glued structures using Lamb waves," *NDT & E International*, vol. 111, no. January, p. 102213, 2020.
- [3] K. Dröder, F. Dietrich, A. Fricke, C. Gerhard, and M. Schäfer, "Automated Non-destructive Testing of Hybrid Structures," *NDT.net Issue: 2016-07*, pp. 1–4, 2016.
- [4] H. Towsyfyian, A. Biguri, R. Boardman, and T. Blumensath, "Successes and challenges in non-destructive testing of aircraft composite structures," *Chinese Journal of Aeronautics*, vol. 22, issue 3, pp. 771-791, 2020.
- [5] D. Smagulova and E. Jasiuniene, "Inspection of Dissimilar Material Joints Using Ultrasonic Phased Arrays," *Elektronika Ir Elektrotechnika*, vol. 24(6), pp. 28–32, 2018.
- [6] D. Smagulova and E. Jasiuniene, "High quality process of ultrasonic nondestructive testing of adhesively bonded dissimilar materials," *2020 IEEE International Workshop on Metrology for AeroSpace, Metroaerospace 2020 - Proceedings, IEEE Xplore*, pp. 475–479, 2020.
- [7] J. Ahamed, M. Joosten, P. Callus, M. R. Wisnom, and C. H. Wang, "Ply-overlap hybrid technique for joining dissimilar composite materials," *Materials and Design*, vol. 100, pp. 157–167, 2016.
- [8] P. Daryabor and M. S. Sa, "Image fusion of ultrasonic and thermographic inspection of carbon / epoxy patches bonded to an aluminum plate," *NDT and E International*, vol. 90, no. April, pp. 1–10, 2017.
- [9] D. Smagulova, L. Mazeika, and E. Jasiuniene, "Novel processing algorithm to improve detectability of disbonds in adhesive dissimilar material joints," *Sensors*, vol. 21, no. 9: 3048, 2021.
- [10] K. Martinsen, S. J. Hu, and B. E. Carlson, "Joining of dissimilar materials," *CIRP Annals - Manufacturing Technology*, vol. 64, no. 2, pp. 679–699, 2015.
- [11] J. Jahn, M. Weber, J. Boehner, and R. Steinhilper, "Assessment Strategies for Composite-metal Joining Technologies-A Review," *Procedia CIRP*, vol. 50, pp. 689–694, 2016.
- [12] A. Y. Kanani, X. Hou, R. Laidlaw, and J. Ye, "The effect of joint configuration on the strength and stress distributions of dissimilar adhesively bonded joints," *Engineering Structures*, vol. 226, no. October 2020, p. 111322, 2021.
- [13] J. R and G. N. Naik, "Single and dual adhesive bond strength analysis of single lap joint between dissimilar adherends," *International Journal of Adhesion and Adhesives*, vol. 92, no. April, pp. 142–153, 2019.
- [14] S. Bayramoglu, K. Demir, and S. Akpınar, "Investigation of internal step and

- metal part reinforcement on joint strength in the adhesively bonded joint: Experimental and numerical analysis,” *Theoretical and Applied Fracture Mechanics*, vol. 108, no. January, p. 102613, 2020.
- [15] N. G. C. Barbosa, R. D. S. G. Campilho, F. J. G. Silva, and R. D. F. Moreira, “Comparison of different adhesively-bonded joint types for mechanical structures,” *Applied Adhesion Science*, vol. 6, no. 1, pp. 1–19, 2018.
- [16] R. Bai, S. Bao, Z. Lei, C. Yan, and X. Han, “Finite element inversion method for interfacial stress analysis of composite single-lap adhesively bonded joint based on full-field deformation,” *International Journal of Adhesion and Adhesives*, vol. 81, no. November 2017, pp. 48–55, 2018.
- [17] A. Kimiaefar, E. Lund, O. T. Thomsen, and J. D. Sørensen, “Asymptotic Sampling for reliability analysis of adhesive bonded stepped lap composite joints,” *Engineering Structures*, vol. 49, pp. 655–663, 2013.
- [18] U. A. Khashaba and I. M. R. Najjar, “Adhesive layer analysis for scarf bonded joint in CFRE composites modified with MWCNTs under tensile and fatigue loads,” *Composite Structures*, vol. 184, no. May 2017, pp. 411–427, 2018.
- [19] P. Saikaew, A. F. M. A. Chowdhury, M. Fukuyama, S. Kakuda, R. M. Carvalho, and H. Sano, “The effect of dentine surface preparation and reduced application time of adhesive on bonding strength,” *Journal of Dentistry*, vol. 47, pp. 63–70, 2016.
- [20] K. Bashandeh, A. Marchert, U. Takayuki, A. A. Polycarpou, J. Meyer, and P. Lan, “The effect of surface texturing on thin film reversible adhesive bond strength,” *International Journal of Adhesion and Adhesives*, vol. 107, p. 102829, 2021.
- [21] A. J. Harris, B. Vaughan, J. A. Yeomans, P. A. Smith, and S. T. Burnage, “Surface preparation of silicon carbide for improved adhesive bond strength in armour applications,” *Journal of the European Ceramic Society*, vol. 33, no. 15–16, pp. 2925–2934, 2013.
- [22] W. Xu and Y. Wei, “Influence of adhesive thickness on local interface fracture and overall strength of metallic adhesive bonding structures,” *International Journal of Adhesion and Adhesives*, vol. 40, pp. 158–167, 2013.
- [23] B. Watson, M. J. Worswick, and D. S. Cronin, “Quantification of mixed mode loading and bond line thickness on adhesive joint strength using novel test specimen geometry,” *International Journal of Adhesion and Adhesives*, vol. 102, no. July, p. 102682, 2020.
- [24] M. Elhannani, K. Madani, E. Legrand, S. Touzain, and X. Feaugas, “Numerical analysis of the effect of the presence, number and shape of bonding defect on the shear stresses distribution in an adhesive layer for the single-lap bonded joint; Part 1,” *Aerospace Science and Technology*, vol. 62, pp. 122–135, 2017.
- [25] W. Xu and Y. Wei, “Strength analysis of metallic bonded joints containing defects,” *Computational Materials Science*, vol. 53, no. 1, pp. 444–450, 2012.
- [26] M. Shishesaz and N. Bavi, “Shear stress distribution in adhesive layers of a

- double-lap joint with void or bond separation,” *Journal of Adhesion Science and Technology*, vol. 27, no. 11, pp. 1197–1225, 2013.
- [27] R. C. Tighe, J. M. Dulieu-Barton, and S. Quinn, “Identification of kissing defects in adhesive bonds using infrared thermography,” *International Journal of Adhesion and Adhesives*, vol. 64, pp. 168–178, 2016.
- [28] D. Yan, B. W. Drinkwater, and S. A. Neild, “Measurement of the ultrasonic nonlinearity of kissing bonds in adhesive joints,” *NDT & E International*, vol. 42, no. 5, pp. 459–466, 2009.
- [29] C. Jeenjitkaew and F. J. Guild, “The analysis of kissing bonds in adhesive joints,” *International Journal of Adhesion and Adhesives*, vol. 75, no. February, pp. 101–107, 2017.
- [30] B. Ehrhart, B. Valeske, and C. Bockenheimer, “Non-destructive evaluation (NDE) of aerospace composites: Methods for testing adhesively bonded composites,” *Non-Destructive Evaluation (NDE) of Polymer Matrix Composites*, Tech. Appl., pp. 220–237, 2013.
- [31] C. He, Y. Li, Y. Lyu, G. Song, and B. Wu, “Ultrasonic reflection characteristics of FRP-to-FRP bonded joints with thick adhesive layers for bonding evaluation: Theoretical analysis,” *Composite Structures*, vol. 246, no. January, p. 112402, 2020.
- [32] R. L. Vijaya Kumar, M. R. Bhat, and C. R. L. Murthy, “Some studies on evaluation of degradation in composite adhesive joints using ultrasonic techniques,” *Ultrasonics*, vol. 53, no. 6, pp. 1150–1162, 2013.
- [33] M. N, M. N, and K. T, “Effect of interfacial adhesion on the ultrasonic interaction with adhesive joints: A theoretical study using spring-type interfaces,” *Journal of the Acoustical Society of America*, vol. 145(6) 3541-3550, 2019.
- [34] A. J. Balvantín, J. A. Diosdado-De-la-Peña, P. A. Limon-Leyva, and E. Hernández-Rodríguez, “Study of guided wave propagation on a plate between two solid bodies with imperfect contact conditions,” *Ultrasonics*, vol. 83, pp. 137–145, 2018.
- [35] R. Leiderman, J. C. Figueroa, A. M. B. Braga, and F. A. Rochinha, “Scattering of ultrasonic guided waves by heterogeneous interfaces in elastic multi-layered structures,” *Wave Motion*, vol. 63, pp. 68–82, 2016.
- [36] S. Mustapha and L. Ye, “Propagation behaviour of guided waves in tapered sandwich structures and debonding identification using time reversal,” *Wave Motion*, vol. 57, pp. 154–170, 2015.
- [37] J. Ding, B. Wu, and C. He, “Reflection and transmission coefficients of the SH₀ mode in the adhesive structures with imperfect interface,” *Ultrasonics*, vol. 70, pp. 248–257, 2016.
- [38] A. Loukkal, M. Lematre, M. Bavencoffe, and M. Lethiecq, “Modeling and numerical study of the influence of imperfect interface properties on the reflection coefficient for isotropic multilayered structures,” *Ultrasonics*, vol. 103, no. February, p. 106099, 2020.
- [39] A. Pilarski and J. L. Rose, “A transverse-wave ultrasonic oblique-incidence

- technique for interfacial weakness detection in adhesive bonds,” *Journal of Applied Physics*, vol. 63, no. 2, pp. 300–307, 1988.
- [40] P. Fraisse, F. Schmit, and A. Zarembowitch, “Ultrasonic inspection of very thin adhesive layers,” *Journal of Applied Physics*, vol. 72, no. 8, pp. 3264–3271, 1992.
- [41] P. B. Nagy, “Ultrasonic classification of imperfect interfaces,” *Journal of Nondestructive Evaluation*, vol. 11, no. 3–4, pp. 127–139, 1992.
- [42] H. Chen, X. Nie, S. Gan, Y. Zhao, and H. Qiu, “Interfacial imperfection detection for steel-concrete composite structures using NDT techniques: A state-of-the-art review,” *Engineering Structures*, vol. 245, no. June 2020, p. 112778, 2021.
- [43] D. Li, J. Zhou, and J. Ou, “Damage, nondestructive evaluation and rehabilitation of FRP composite-RC structure: A review,” *Construction and Building Materials*, vol. 271, p. 121551, 2021.
- [44] S. Deane et al., “Application of NDT thermographic imaging of aerospace structures,” *Infrared Physics & Technology*, vol. 97, no. December 2018, pp. 456–466, 2019.
- [45] M. Barus et al., “NDT-based design of joint material for the detection of bonding defects by infrared thermography,” *NDT & E International*, vol. 93, no. October 2017, pp. 157–163, 2018.
- [46] W. S. Na, “Low cost technique for detecting adhesive debonding damage of glass epoxy composite plate using an impedance based non-destructive testing method,” *Composite Structures*, vol. 189, no. March 2017, pp. 99–106, 2018.
- [47] R. A. Pethrick, *Non-destructive evaluation (NDE) of composites: Dielectric methods for testing adhesive bonds in composites*. Woodhead Publishing Limited, 2013.
- [48] R. L. Vijaya Kumar, M. R. Bhat, and C. R. L. Murthy, “Evaluation of kissing bond in composite adhesive lap joints using digital image correlation: Preliminary studies,” *International Journal of Adhesion and Adhesives*, vol. 42, pp. 60–68, 2013.
- [49] K. Zhang, S. Li, and Z. Zhou, “Detection of disbonds in multi-layer bonded structures using the laser ultrasonic pulse-echo mode,” *Ultrasonics*, vol. 94, no. June 2018, pp. 411–418, 2019.
- [50] S. A. Titov, R. G. Maev, and A. N. Bogachenkov, “Pulse-echo NDT of adhesively bonded joints in automotive assemblies,” *Ultrasonics*, vol. 48, no. 6–7, pp. 537–546, 2008.
- [51] H. Gao, S. Ali, and B. Lopez, “Efficient detection of delamination in multilayered structures using ultrasonic guided wave EMATs,” *NDT & E International*, vol. 43, no. 4, pp. 316–322, 2010.
- [52] P. Daryabor and M. S. Safizadeh, “Image fusion of ultrasonic and thermographic inspection of carbon/epoxy patches bonded to an aluminum plate,” *NDT & E International*, vol. 90, no. April, pp. 1–10, 2017.
- [53] Q. Yi et al., “Evaluation of debonding in CFRP-epoxy adhesive single-lap joints using eddy current pulse-compression thermography,” *Composites Part*

- B Engineering, vol. 178, no. September, 2019.
- [54] V. K. Nadimpalli, L. Yang, and P. B. Nagy, "In-situ interfacial quality assessment of Ultrasonic Additive Manufacturing components using ultrasonic NDE," *NDT & E International*, vol. 93, no. October 2017, pp. 117–130, 2018.
- [55] T. Stepinski and M. Jonsson, "Narrowband ultrasonic spectroscopy for NDE of layered structures," *Insight - Non-Destructive Testing and Condition Monitoring*, The British Institute of Non-Destructive Testing, Volume 47, Number 4, 1 April 2005, pp. 220-225(6)
- [56] M. Engholm and T. Stepinski, "Designing and evaluating transducers for narrowband ultrasonic spectroscopy," *NDT & E International*, vol. 40, no. 1, pp. 49–56, 2007.
- [57] "the Non-Destructive Testing of Adhesively Bonded," no. November, 1986.
- [58] B. Yılmaz and E. Jasiūnienė, "Advanced ultrasonic NDT for weak bond detection in composite-adhesive bonded structures," *International Journal of Adhesion and Adhesives*, vol. 102, 2020.
- [59] F. Nicassio, S. Carrino, and G. Scarselli, "Elastic waves interference for the analysis of disbonds in single lap joints," *Mechanical Systems and Signal Processing*, vol. 128, pp. 340–351, 2019.
- [60] K. Zhang and Z. Zhou, "Quantitative characterization of disbonds in multilayered bonded composites using laser ultrasonic guided waves," *NDT & E International*, vol. 97, no. November 2017, pp. 42–50, 2018.
- [61] P. Pyzik, A. Ziaja-Sujdak, J. Spytek, M. O'Donnell, I. Pelivanov, and L. Ambrozinski, "Detection of disbonds in adhesively bonded aluminum plates using laser-generated shear acoustic waves," *Photoacoustics*, vol. 21, p. 100226, 2021.
- [62] D. Palumbo, R. Tamborrino, U. Galietti, P. Aversa, A. Tatì, and V. A. M. Luprano, "Ultrasonic analysis and lock-in thermography for debonding evaluation of composite adhesive joints," *NDT & E International*, vol. 78, pp. 1–9, 2016.
- [63] C. V. Katsiropoulos and S. G. Pantelakis, "Assessment of imperfect bonding of adhesively bonded U-joints using ultrasonic inspection," *Plastic Rubber and Composites*, vol. 43, no. 10, pp. 316–321, 2014.
- [64] B. Ehrhart, U. Netzelmann, G. Walle, and B. Valeske, "Quality assessment of CFRP bonded structures with active thermography techniques," *5th Int. Symp. on NDT in AerospaceAt: Singapore* Volume: *NDT-Net e-journal of Non-destructive Testing* ISSN 1435-4934, no. November, pp. 13–15, 2013.
- [65] Pierre Noël Marty , N. Desai, and J. Andersson, "NDT of kissing bond in aerotautical structures", *Material Science*, CSM Materialteknik AB, Linköping, Sweden, 2004.
- [66] J. Alston, A. Croxford, J. Potter, and P. Blanloeuil, "Nonlinear non-collinear ultrasonic detection and characterisation of kissing bonds," *NDT & E International*, vol. 99, no. January, pp. 105–116, 2018.
- [67] P. Zabbal, G. Ribay, and J. Jumel, "Evaluation of metallic bonded plates with

- nonlinear ultrasound and comparison with destructive testing,” *NDT & E International*, vol. 123, no. June 2020, p. 102514, 2021.
- [68] S. Kumar and M. R. Sunny, “A novel nonlinear Lamb wave based approach for detection of multiple disbonds in adhesive joints,” *International Journal of Adhesion and Adhesives*, vol. 107, no. February, p. 102842, 2021.
- [69] G. Shui, Y. S. Wang, P. Huang, and J. Qu, “Nonlinear ultrasonic evaluation of the fatigue damage of adhesive joints,” *NDT & E International*, vol. 70, pp. 9–15, 2015.
- [70] G. Sun, L. Zhao, M. Dong, X. Lou, and L. Zhu, “Non-contact characterization of debonding in lead-alloy steel bonding structure with laser ultrasound,” *Optik (Stuttg.)*, vol. 164, pp. 734–744, 2018.
- [71] K. Zhang, Z. Zhou, J. Zhou, and G. Sun, “Characteristics of laser ultrasound interaction with multi-layered dissimilar metals adhesive interface by numerical simulation,” *Applied Surface Science*, vol. 353, pp. 284–290, 2015.
- [72] E. Jasiūnienė, L. Mažeika, V. Samaitis, V. Cicėnas, and D. Mattsson, “Ultrasonic non-destructive testing of complex titanium/carbon fibre composite joints,” *Ultrasonics*, vol. 95, no. December 2017, pp. 13–21, 2019.
- [73] J. Summa, M. Becker, F. Grossmann, M. Pohl, M. Stommel, and H. G. Herrmann, “Fracture analysis of a metal to CFRP hybrid with thermoplastic interlayers for interfacial stress relaxation using in situ thermography,” *Composite Structures*, vol. 193, no. September 2017, pp. 19–28, 2018.
- [74] M. Moradi and M. S. Safizadeh, “Edge disbond detection of carbon/epoxy repair patch on aluminum using thermography,” *Composite Science and Technology*, vol. 179, no. January, pp. 41–53, 2019.
- [75] H. Sun, H. Kosukegawa, M. Hashimoto, T. Uchimoto, and T. Takagi, “Electromagnetic-pulse-induced acoustic testing for nondestructive testing of plastic composite/metal adhesive bonding,” *International Journal of Hydrogen Energy*, vol. 45, no. 55, pp. 31303–31314, 2020.
- [76] G. Ribay, X. Artusi, F. Jenson, C. Reece, and P. Lhuillier, “Model-based POD study of manual ultrasound inspection and sensitivity analysis using metamodel Model-Based POD Study of Manual Ultrasound Inspection and Sensitivity Analysis Using Metamodel,” vol. 200006, no. February, 2016.
- [77] V. K. Rentala, P. Mylavarapu, and J. P. Gautam, “Issues in estimating probability of detection of NDT techniques – A model assisted approach,” *Ultrasonics*, vol. 87, pp. 59–70, 2018.
- [78] B. Chapuis, P. Calmon, and F. Jenson, *Best Practices for the Use of Simulation in POD Curves Estimation* No Title, 1st ed. Springer International Publishing, 2018.
- [79] I. Virkkunen, T. Koskinen, S. Papula, T. Sarikka, and H. Hänninen, “Comparison of \hat{a} Versus a and Hit/Miss POD-Estimation Methods: A European Viewpoint,” *Journal of Nondestructive Evaluation*, vol. 38, no. 4, pp. 1–13, 2019.
- [80] US Department of Defense. MIL HDBK 1823A. Nondestructive Evaluation System Reliability Assessment; Department of Defense Handbook; US

- Department of Defense: Arlington, VA, USA, no. April, 2009.
- [81] E. O. Connor, and W. Q. Meeker, "Quantifying Method Differences in Predicting the Probability of Detection for Structural Health Monitoring Applications," Department of Statistics, Iowa State University, April, p. 27, 2019.
 - [82] T. Stepinski, T. Uhl, and W. Staszewski, "Model Assisted Probability of Detection in Structural Health Monitoring," *Adv. Struct. Damage Detect. From Theory to Eng. Appl.*, pp. 57–72, 2013.
 - [83] G. Ribay et al., "Simulation-based POD study for welded pipe inspection," *NDT.net Issue: 2018-08, 12th European Conference on Non-Destructive Testing (ECNDT 2018), Gothenburg 2018, June 11-15 (ECNDT 2018)*, pp. 2–4.
 - [84] J. Knopp, R. Grandhi, L. Zeng, and J. Aldrin, "Considerations for Statistical Analysis of Nondestructive Evaluation Data: Hit/Miss Analysis," *E-Journal of Advanced Maintenance*, vol.4, No.3 (2012), Japan Society of Maintenology, pp. 105–115, 2012.
 - [85] F. Foucher, R. Fernandez, S. Leberre, and P. Calmon, "New Tools in CIVA for Model Assisted Probability of Detection (MAPOD) to Support NDE Reliability Studies," *NDE Aerosp. Mater. Struct.* 2018, pp. 32–43, 2018.
 - [86] W. Q. Meeker, D. Roach, and S. S. Kessler, "Statistical methods for probability of detection in structural health monitoring," *Struct. Heal. Monit.* 2019 *Enabling Intell. Life-Cycle Heal. Manag. Ind. Internet Things - Proceedings. 12th Int. Work. Struct. Heal. Monit.*, vol. 1, pp. 24–35, 2019.
 - [87] J. Fisher, A. Cobb, and J. E. Michaels, "Model-Assisted Probability of Detection for Ultrasonic Structural Health Monitoring," *4th European-American Workshop on Reliability of NDE - Th.2.A.2*, no. January, 2009.
 - [88] A. C. Cobb, J. E. Michaels, and T. E. Michaels, "Ultrasonic structural health monitoring: A probability of detection case study," *AIP Conference Proceedings*, vol. 1096, no. January, pp. 1800–1807, 2009.
 - [89] F. Schoefs, O. Abraham, and J. S. Popovics, "Quantitative evaluation of contactless impact echo for non-destructive assessment of void detection within tendon ducts," *Construction and Building Materials*, vol. 37, pp. 885–892, 2012.
 - [90] M. R. Bato, A. Hor, A. Rautureau, and C. Bes, "Experimental and numerical methodology to obtain the probability of detection in eddy current NDT method," *NDT & E International*, vol. 114, no. March, p. 102300, 2020.
 - [91] J. H. Kurz, A. Jüngert, S. Dugan, G. Dobmann, and C. Boller, "Reliability considerations of NDT by probability of detection (POD) determination using ultrasound phased array," *Engineering Failure Analysis*, vol. 35, pp. 609–617, 2013.
 - [92] J. H. Kurz, A. Jüngert, S. Dugan, G. Dobmann, and C. Boller, "Reliability considerations of NDT by probability of detection (POD) determination using ultrasound phased array," *Engineering Failure Analysis*, vol. 35, pp. 609–6617, 2013.

- [93] M. S. Syed Akbar Ali, A. Kumar, P. B. Rao, J. Tammana, K. Balasubramaniam, and P. Rajagopal, "Bayesian synthesis for simulation-based generation of probability of detection (PoD) curves," *Ultrasonics*, vol. 84, pp. 210–222, 2018.
- [94] M. R. Bato, A. Hor, A. Rautureau, and C. Bes, "Experimental and numerical methodology to obtain the probability of detection in eddy current NDT method," *NDT & E International*, vol. 114, no. February 2018, p. 102300, 2020.
- [95] Y. Duan et al., "Reliability assessment of pulsed thermography and ultrasonic testing for impact damage of CFRP panels," *NDT & E International*, vol. 102, no. May 2018, pp. 77–83, 2019.
- [96] F. H. Kim, A. L. Pintar, J. Fox, and A. M. Donmez, "QNDE2019-1234," pp. 1–3, 2019.
- [97] L. Junyan, L. Yang, W. Fei, and W. Yang, "Study on probability of detection (POD) determination using lock-in thermography for nondestructive inspection (NDI) of CFRP composite materials," *Infrared Physics and Technology*, vol. 71, pp. 448–456, 2015.
- [98] S. M. Subair, K. Balasubramaniam, P. Rajagopal, A. Kumar, B. P. Rao, and T. Jayakumar, "Finite element simulations to predict Probability of Detection (PoD) curves for ultrasonic inspection of nuclear components," *Procedia Engineering*, vol. 86, pp. 461–468, 2014.
- [99] L. Le Gratiet, B. Iooss, G. Blatman, T. Browne, S. Cordeiro, and B. Goursaud, "Model Assisted Probability of Detection Curves: New Statistical Tools and Progressive Methodology," *Journal of Nondestructive Evaluation*, vol. 36, no. 1, pp. 1–12, 2017.
- [100] F. Möller, C. Thomy, F. Vollertsen, P. Schiebel, C. Hoffmeister, and A. S. Herrmann, "Novel method for joining CFRP to aluminium," *Physics Procedia*, vol. 5, no. PART 2, pp. 37–45, 2010.
- [101] M. A. Caminero, S. Pavlopoulou, M. Lopez-Pedrosa, B. G. Nicolaisson, C. Pinna, and C. Soutis, "Analysis of adhesively bonded repairs in composites: Damage detection and prognosis," *Composite Structures*, vol. 95, pp. 500–517, 2013.
- [102] R. L. Smith, "Materials Characterization by Ultrasonic Attenuation Spectral Analysis," *Review of Progress in Quantitative Nondestructive Evaluation*, pp. 1475–1483, 1987.
- [103] V. R. Amin, "Ultrasonic attenuation estimation for tissue characterization," *Retrospect. Theses Diss.*, 1989.
- [104] X. Bai, Y. Zhao, J. Ma, Y. Liu, and Q. Wang, "Grain-size distribution effects on the attenuation of laser-generated ultrasound in α -titanium alloy," *Materials (Basel)*, vol. 12, no. 1, pp. 1–14, 2018.
- [105] B. Yilmaz, A. Ba, E. Jasiuniene, H. K. Bui, and G. Berthiau, "Evaluation of bonding quality with advanced nondestructive testing (Ndt) and data fusion," *Sensors (Switzerland)*, vol. 20, no. 18, pp. 1–17, 2020.
- [106] L. Draudviliene, H. Ait Aider, O. Tumsys, and L. Mazeika, "The Lamb waves

- phase velocity dispersion evaluation using an hybrid measurement technique,” *Composite Structures*, vol. 184, no. October 2017, pp. 1156–1164, 2018.
- [107] L. Mazeika and L. Draudviliene, “Analysis of the zero-crossing technique in relation to measurements of phase velocities of the Lamb waves L,” *J. Ultragarsas*, vol. 9, no. 4, pp. 293–295, 2010.
- [108] E. Salernitano, C. Migliaresi, "Composite Materials for Biomedical Applications: A Review," *Journal of applied biomaterials & biomechanics (JABB)*, vol. 1(1):3-18, 2003.
- [109] V. Krishna, P. Mylavarapu, and J. Prakash, “Issues in estimating probability of detection of NDT techniques – A model assisted approach,” *Ultrasonics*, vol. 87, pp. 59–70, 2018.
- [110] J. Moriot et al., "A model-based approach for statistical assessment of detection and localization performance of guided wave – based imaging techniques" *Structural Health Monitoring* 17(2):147592171774467, 2018.
- [111] E. Lindgren, C. Buynak, J. Aldrin, E. Medina, and M. Derriso, “Model-assisted Methods for Validation of Structural Health Monitoring Systems,” 2009.
- [112] J. A. Roberti, M. D. SanClements, H. W. Loescher, and E. Ayres, “Traceable calibration, performance metrics, and uncertainty estimates of minirhizotron digital imagery for fine-root measurements,” *PLoS One*, vol. 9, no. 11, 2014.
- [113] A. National Association of Testing Authorities, “Guidance Infrastructure and Asset Integrity Measurement Uncertainty in Geotechnical Testing,” NATA, National Association of Testing Authorities, Australia 2018.
- [114] A. Wronkowitz, K. Dragan, and K. Lis, “Assessment of uncertainty in damage evaluation by ultrasonic testing of composite structures,” *Composite Structures*, vol. 203, no. March, pp. 71–84, 2018.
- [115] D. Neudecker, R. Capote, and H. Leeb, “Impact of model defect and experimental uncertainties on evaluated output,” *Nuclear Instruments and Methods in Physics Research Section A Accelerators Spectrometers Detectors and Associated Equipment*, vol. 723:163–172, 2013.
- [116] B. Wang, H. De Backer, and A. Chen, “An XFEM based uncertainty study on crack growth in welded joints with defects,” *Theoretical and Applied Fracture Mechanics*, vol. 86, pp. 125–142, 2016.

INFORMATION ABOUT AUTHOR

Education

- 2017–2022 – PhD in Measurement Engineering (T 010), Kaunas University of Technology, Lithuania.
- 2015 – Master of Science degree in Measurement Engineering, Kaunas University of Technology, Lithuania.
- 2012 – Bachelor of Science degree in Electronics, Electrical Engineering and Telecommunications, Karaganda State Technical University, Kazakhstan.

Fields of research interest

Non-destructive ultrasonic testing of joints in multilayer structures; ultrasonic signal and image post-processing; calculation and evaluation of probability of detection curves and uncertainty measurement.

Work experience

- 2018–2020 – Kaunas University of Technology, Prof. K. Baršauskas Ultrasound Research Institute, junior researcher.
- 2015–2018 – Caspian Logistic and Procurement LLP, Kazakhstan, Business Development Coordinator / Project Supervisor in Logistics and Procurement Department / Senior Project Supervisor in Logistics and Procurement Department.
- 2015–2015 – Kaunas University of Technology, Prof. K. Baršauskas Ultrasound Research Institute, engineering intern .
- 2013–2013 – PSP System LLP, Kazakhstan, Sales Manager of Relay Security and Automation Equipment.

LIST OF PUBLICATIONS

List of publications in journals of the *Thomson Reuters* database indexed in the *Web of Science* with the Impact Factor:

1. Smagulova, Damira; Mažeika, Liudas; Jasiūnienė, Elena. Novel processing algorithm to improve detectability of disbands in adhesive dissimilar material joints // *Sensors*. Basel: MDPI. ISSN 1424-8220. 2021, vol. 21, iss. 9, art. no. 3048, p. 1-22. DOI: 10.3390/s21093048. [Science Citation Index Expanded (Web of Science); Scopus; MEDLINE] [CiteScore: 5.80; SNIP: 1.555; SJR: 0.636; Q1 (2020, Scopus Sources)] [Field: T010, T 001] [Input: 0.334]

2. Smagulova, Damira; Jasiūnienė, Elena. Inspection of dissimilar material joints using ultrasonic phased arrays // *Elektronika ir elektrotechnika*. Kaunas: KTU. ISSN 1392-1215. eISSN 2029-5731. 2018, vol. 24, no. 6, p. 28-32. DOI: 10.5755/j01.eie.24.6.22286. [Science Citation Index Expanded (Web of Science); Scopus] [CiteScore: 0.81; SNIP: 0.554; SJR: 0.182; Q3 (2018, Scopus Sources)] [Field: T 001, T 010] [Input: 0.500]

3. Yilmaz, Bengisu; Smagulova, Damira; Jasiūnienė, Elena. Model-assisted reliability assessment for adhesive bonding quality evaluation with ultrasonic NDT // *NDT & E international*. Oxford: Elsevier. ISSN 0963-8695. eISSN 1879-1174. 2022, vol. 126, art. No. 102596, p. 1-14. DOI: 10.1016/j.ndteint.2021.102596. [Science Citation Index Expanded (Web of Science); Scopus] [IF: 3.739; AIF: 2.884; IF/AIF: 1.296; Q1 (2020, InCites JCR SCIE)] [M.kr.: T 001, T 010] [Input: 0.333]

List of publications in journals of the *Thomson Reuters* database indexed in the *Web of Science* without the Impact Factor:

1. Smagulova, Damira; Jasiūnienė, Elena. High quality process of ultrasonic nondestructive testing of adhesively bonded dissimilar materials // 2020 IEEE 7th International Workshop on Metrology for AeroSpace (MetroAeroSpace): virtual conference, 22-24 June, 2020, Pisa, Italy: proceedings. Piscataway, NJ: IEEE, 2020. ISBN 9781728166377. eISBN 9781728166360. ISSN 2575-7482. eISSN 2575-7490. p. 484-488. DOI: 10.1109/MetroAeroSpace48742.2020.9160095. [Conference Proceedings Citation Index - Science (Web of Science); Scopus; INSPEC] [Field: T 010] [Input: 0.500]

Articles published in peer-reviewed scientific conference proceedings:

1. Smagulova, Damira; Yilmaz, Bengisu; Papanaboina, Mastan Raja; Jasiūnienė, Elena. Investigation on complex shaped aerospace structure: reliability and cost balance // *AeroNDT 2019: 11th international symposium on NDT in aerospace*, November 2019, Paris-Saclay, France. Bad Breisig: NDT.net. 2020, iss. 2, p. 1-9. [Field: T 010, T 001] [Input: 0.250]

2. Smagulova, Damira; Jasiūnienė, Elena. Non-destructive evaluation of dissimilar material joints // 12th European Conference on Non-Destructive Testing

(ECNDT 2018): Gothenburg, Sweden, 2018, June 11-15: proceedings / European Federation for Non-Destructive Testing (EFNDT). Bad Breisig: EFNDT, 2018. ISBN 9789163962172. ISSN 1435-4934. p. 1-4. [Field: T 001, T 010] [Input: 0.500]

Abstracts of scientific conferences:

1. Yilmaz, B.; Smagulova, D.; Jasiūnienė, E. Model assisted probability of detection in adhesive joints // 6th international conference on structural adhesive bonding AB2021: 8-9 July 2021, Faculty of Engineering – University of Porto, Porto, Portugal: book of abstracts. Porto: Quântica Editora, 2021. ISBN 9789899017641. p. 181. [Field: T 010]

2. Smagulova, Damira; Samaitis, Vyktintas; Papanaboina, Mastan Raja; Jasiūnienė, Elena. A case study on ultrasonic guided wave inspection of aerospace components – is ‘in-situ’ feasible? // 10th EASN virtual international conference on innovation in aviation & space to the satisfaction of the European citizens, 2-4 September 2020: book of abstracts. [S.l.]: EASN. 2020, p. 76. [Field: T 010]

3. Smagulova, Damira. Ultrasonic NDT and numerical simulation of adhesively bonded aluminium to CFRP materials // 11th international symposium on NDT in aerospace, 13-15, November, 2019, Paris, France: catalog of abstracts. Paris: COFREND. 2019, p. 41. [Field: T 010]

4. Smagulova, Damira; Jasiūniene, Elena. Disbond detection of adhesively bonded metal to composite joints using different ultrasonic techniques // 9th EASN international conference on innovation in aviation & space, 3 to 6 September, 2019, Athens, Greece: booklet of abstracts / organised by European Aeronautics Science Network. Athens: EASN. 2019, p. 97. [Field: T 010]

5. Smagulova, Damira; Jasiūnienė, Elena. Delamination detection in adhesively bonded dissimilar materials using ultrasound // Open readings 2019: 62nd international conference for students of physics and natural sciences, March 19-22, Vilnius, Lithuania: abstract book. Vilnius: Vilnius University, 2019, P3-39. ISBN 9786090701379. p. 315. [Field: T 010]

UDK 620.179.4[+539.61+665.93] (043.3)

SL 344. 2022-**-*, * leidyb. apsk. I. Tiražas 14 egz. Užsakymas * .
Išleido Kauno technologijos universitetas, K. Donelaičio g. 73, 44249 Kaunas
Spausdino leidykla „Technologija“ spaustuvė, Studentų g. 54, 51424 Kaunas